

Transport Phenomena in Thermoelectric and Ferromagnetic Nanostructures

Dissertation

zur Erlangung des Doktorgrades
des Fachbereichs Physik
der Universität Hamburg

vorgelegt von

Johannes Georg Kimling

geb. in

Heidenheim an der Brenz

Hamburg
2013

Bibliografische Information der Deutschen Nationalbibliothek
Die Deutsche Nationalbibliothek verzeichnet diese Publikation in der
Deutschen Nationalbibliografie; detaillierte bibliografische Daten
sind im Internet über <http://dnb.d-nb.de> abrufbar.

1. Aufl. - Göttingen: Cuvillier, 2013

Zugl.: Hamburg, Univ., Diss., 2013

978-3-95404-519-8

Gutachter der Dissertation:	Prof. Dr. Kornelius Nielsch Prof. Dr. Günter Reiss Prof. Dr. Gerrit E.-W. Bauer
Gutachter der Disputation:	Prof. Dr. Kornelius Nielsch PD Dr. habil. Guido Meier
Datum der Disputation:	21. Juni 2013
Vorsitzender des Prüfungsausschusses:	Dr. Stefan Mendach
Vorsitzender des Promotionsausschusses:	Prof. Dr. Peter Hauschildt
Dekan der MIN Fakultät:	Prof. Dr. Heinrich Graener

© CUVILLIER VERLAG, Göttingen 2013
Nonnenstieg 8, 37075 Göttingen
Telefon: 0551-54724-0
Telefax: 0551-54724-21
www.cuvillier.de

Alle Rechte vorbehalten. Ohne ausdrückliche Genehmigung
des Verlages ist es nicht gestattet, das Buch oder Teile
daraus auf fotomechanischem Weg (Fotokopie, Mikrokopie)
zu vervielfältigen.

1. Auflage, 2013

Gedruckt auf umweltfreundlichem, säurefreiem Papier
aus nachhaltiger Forstwirtschaft.

978-3-95404-519-8

Abstract

This thesis deals with transport phenomena in nanoscale systems: The Seebeck effect is explored in Bi_2Te_2 nanowires, the anisotropic magnetothermal resistance effect in Ni nanowires, and the giant magnetothermal resistance effect in Co/Cu multilayers. Research on transport phenomena in a variety of materials has played a decisive role in the development of solid-state physics and has led to important applications of functional materials, e.g. for the conversion and storage of energy or in the field of storage and processing of data.

We introduce a synthesis route for creating single-crystalline and nearly intrinsic Bi_2Te_3 nanowires. In the first step of the process, single-crystalline nanowires are formed with stoichiometries that deviate from the Bi_2Te_3 phase due to an increased Bi content. In the second step, the nanowires are transformed to the desired Bi_2Te_3 phase by annealing in a Te-rich atmosphere. We present measurements of the electrical resistance and the Seebeck coefficient on individual nanowires in the temperature range between 300 and 430 K. The results confirm the intrinsic behavior of the annealed nanowires in comparison to the metallic behavior of the as-grown nanowires. Before we deal with the magnetothermal effects, we introduce the 3ω method – a prevalent method for measuring thermal properties of bulk materials, thin films, and nanowires. We analyze this method for the case that the current source presupposed by the formalism of the method is replaced by a voltage source. By calculating the Fourier coefficients of the current and the measuring voltage, we demonstrate that a correction factor suggested in the literature is only required for direct 3ω measurements, but not for 3ω measurements after subtraction of the 1ω voltage, and also not for 1ω measurements. The theoretical results are confirmed by experiments. In addition to that, we present measurements of the electrical resistance, the thermal conductivity, and the Lorenz number on individual, electrochemically synthesized Ni nanowires under applied magnetic fields in the temperature range between 78 and 380 K. In analogy to the anisotropic magnetoresistance effect we introduce a simple theoretical model to describe the anisotropic magnetothermal resistance effect observed. We report on experimental results on this new effect that were achieved with the help of a slightly modified 3ω method. Finally, we analyze the Wiedemann-Franz law in magnetic multilayers. Among others, we demonstrate that the usual inference from violations of the Wiedemann-Franz law to inelastic scattering processes is not necessarily valid in the context of the magnetic-field dependence of electrical and thermal transport in magnetic multilayers. Vice versa, we demonstrate that a constant Lorenz number with respect to an applied magnetic field not necessarily excludes contributions from inelastic scattering processes to field-dependent transport properties. We present measurements of the giant magnetoresistance, the giant magnetothermal resistance, and the Lorenz number in Co/Cu multilayers in the temperature range between 10 and 300 K. The thermal measurements are again based on a modified 3ω method. We find that electron-magnon scattering is insignificant for the giant magnetoresistance and the giant magnetothermal resistance in the samples investigated. Furthermore, we conclude that electron-phonon scattering exhibits the same spin asymmetry as the predominant elastic scattering of electrons at the interfaces of the multilayer.

Inhaltsangabe

Diese Arbeit behandelt Transportphänomene in nanoskaligen Systemen: Der Seebeck effect wird in Bi_2Te_3 -Nanodrähten untersucht, der anisotrope magnetothermische Widerstandseffekt in Ni-Nanodrähten und der riesenmagnetothermische Widerstandseffekt in Co/Cu-Multischichten. Die Erforschung von Transportphänomenen in unterschiedlichsten Materialien hat in der Vergangenheit wesentlich zur Entwicklung der Festkörperphysik beigetragen und führte zu wichtigen Anwendungen funktionaler Materialien, z.B. zur Umwandlung und Speicherung von Energie oder im Bereich der Speicherung und Verarbeitung von Daten.

Wir stellen ein Syntheseverfahren zur Herstellung von einkristallinen und nahezu intrinsischen Bi_2Te_3 Nanodrähten vor. Im ersten Schritt des Verfahrens entstehen einkristalline Nanodrähte, deren Stöchiometrie aufgrund eines erhöhten Bi-Anteils von der Bi_2Te_3 -Phase abweicht. Im zweiten Schritt werden die Nanodrähte durch Ausheizen in einer Te-reichen Atmosphäre in die gewünschte Bi_2Te_3 -Phase überführt. Das intrinsische Verhalten wird durch Messungen des elektrischen Widerstands und des Seebeck-Koeffizienten an einzelnen Nanodrähten über einen Temperaturbereich von 300 bis 430 K nachgewiesen und mit dem metallischen Verhalten der unbehandelten Nanodrähte verglichen. Bevor wir die magnetothermischen Effekte behandeln, stellen wir die 3ω -Methode vor - eine vielfach verwendete Methode zur Messung der thermischen Eigenschaften von Bulkmaterialien, Dünnschichten und Nanodrähten. Wir untersuchen diese Messmethode für den Fall, dass die im Formalismus der Methode vorausgesetzte Stromquelle des Versuchsaufbaus durch eine Spannungsquelle ersetzt wird. Durch Berechnung der Fourier-Koeffizienten des Stroms und der Messspannung zeigen wir, dass ein für diesen Fall in der Literatur vorgeschlagener Korrekturfaktor nur für direkte 3ω -Messungen benötigt wird, nicht aber für 3ω -Messungen nach Subtraktion der 1ω -Spannung, und auch nicht für 1ω -Messungen. Die theoretischen Ergebnisse werden durch Experimente bestätigt. Darüber hinaus präsentieren wir Messungen des elektrischen Widerstandes, der Wärmeleitfähigkeit und der Lorenz-Zahl an einzelnen, elektrochemisch hergestellten Ni-Nanodrähten unter dem Einfluss von Magnetfeldern, im Temperaturbereich zwischen 78 und 380 K. In Analogie zum anisotropen Magnetowiderstand stellen wir ein einfaches theoretisches Modell zur Beschreibung des anisotropen magnetothermischen Widerstandes vor, und berichten über experimentelle Ergebnisse zu diesem neuen Effekt, die wir mit Hilfe einer leicht modifizierten 3ω -Methode erzielt haben. Schließlich analysieren wir das Wiedemann-Franz-Gesetz in magnetischen Multischichten. Unter anderem zeigen wir, dass der in der Literatur üblicherweise vorgenommene Schluss von Verletzungen des Wiedemann-Franz-Gesetzes auf inelastische Streuprozesse im Falle des Magnetfeld-abhängigen elektrischen und thermischen Transports in magnetischen Multischichten nicht notwendigerweise Gültigkeit besitzt. Umgekehrt zeigen wir, dass eine magnetfeldunabhängige Lorenz Zahl nicht notwendigerweise Beiträge von inelastischen Streuprozessen zu magnetfeldabhängigen Transportgrößen ausschließt. In diesem Zusammenhang präsentieren wir Messungen des Riesemagnetowiderstands, des riesenmagnetothermischen Widerstands und der Lorenz-Zahl in Co/Cu-Multischichten über einen Temperaturbereich von 10 bis 300 K. Die thermischen Messungen basieren ebenfalls auf einer Variante der 3ω Methode. Wir stellen fest, dass sich Elektron-Magnon-Streuung in den untersuchten Proben nur unwesentlich auf den Riesemagnetowiderstand und den riesenmagnetothermischen Widerstand auswirkt. Außerdem folgern wir, dass Elektron-Phonon Streuung die gleiche Spin-Asymmetrie aufweist wie der vorherrschende elastische Streuprozess von Elektronen an den Grenzflächen der Multischicht.

List of Constants

The following table lists physical constants used in this thesis without explicit specifications in the main text. The values are taken from Ref. [Chen 05].

Table 0.1: Physical constants.

Physical Constant	Symbol	Value	Units
Boltzmann constant	k_{B}	1.38×10^{-23}	JK^{-1}
Electron rest mass	m_{e}	9.1096×10^{-31}	kg
Elementary charge	e	1.6022×10^{-19}	As
Planck constant divided by 2π	\hbar	1.0546×10^{-34}	Js

Contents

1	Introduction	1
2	Theoretical Foundations	5
2.1	Magnetism	5
2.2	Boltzmann Equation and Relaxation-Time Approximation	8
2.3	Thermoelectric Effects	9
2.4	Thermoelectric Figure of Merit	10
2.5	Optimization of Thermoelectric Materials	11
2.6	Scattering Mechanisms	12
2.7	Matthiessen Rule	13
2.8	Wiedemann-Franz Law and Lorenz Number	14
2.9	Resistivity of Ferromagnetic Metals	15
2.10	Anisotropic Magnetoresistance	15
2.11	Spin-dependent Diffusive Transport Theory	16
2.12	Giant Magnetoresistance	17
2.13	Size Effects	18
3	Thermoelectric Nanowires	21
3.1	Seebeck Microdevice	21
3.2	Influence of the Substrate	23
3.3	Intrinsic Bismuth Telluride	26
3.4	What about Quantum Confinement Effects?	26
3.5	Growth and Characterization of Bi ₂ Te ₃ Nanowires	27
4	3ω Method	35
4.1	Concept of the 3 ω Method	35
4.2	Bulk Model	36
4.3	Thin-Film Model	37
4.4	Wire Model	39
4.5	Characteristic Length- and Time-scales	39
4.6	Thermal Radiation	39
4.7	1 ω and 3 ω Methods Revisited for Voltage-Driven Setups	40
5	Ferromagnetic Nanowires	53
5.1	3 ω Microdevice	53
5.2	Contact Issue	55
5.3	Spurious 3 ω Currents	57
5.4	Classical Size Effects in Ni Nanowires	58
5.5	Anisotropic Magnetothermal Resistance in Ni Nanowires	59
6	Magnetic Multilayers	69
6.1	Sample Design and Measuring Setup	69
6.2	Lorenz Number in Co/Cu Multilayers	70
7	Conclusion	81

A Review Article	83
B Philosophical Article	103
C Supporting Information [Hamd 13]	109
D Supplemental Material [Kiml 13a]	113
E Experimental Details	117
Bibliography	131

1 Introduction

Life, as we know it, is based on the capability of problem solving [Popp 96]. The problems or questions studied by natural scientists today are usually highly specialized. This is because the solution of a problem typically opens the view on deeper problems that have not been realized before. Thanks to the strong methodology of the natural sciences [Popp 05] this process of basic research increases our knowledge about the nature or better the reality, and gives the impulses for new technological applications. A basic research field that has led to many important technological applications, e.g. of transistors and semiconductors, is solid-state physics, which forms the theoretical foundation of materials science. The topics covered in this thesis can be allocated to two branches of solid-state physics: thermoelectrics and thermal spintronics or spin caloritronics.

Research in the field of **thermoelectrics** explores the non-equilibrium transport of charge and heat in conducting materials and devices [Nola 01]. The basic thermoelectric phenomena, which are the Seebeck effect and the Peltier effect (see Table 1.1), were discovered already in the 19th century. It was soon recognized that these effects are useful for applications, such as thermometry, refrigeration, and power generation. With the rise of quantum mechanics in the first half of the 20th century the understanding of thermoelectricity increased significantly, so that the most promising natural materials for thermoelectric applications had been figured out before 1960. These are alloys of the three compounds Bi_2Te_3 , Sb_2Te_3 , and Bi_2Se_3 , which are semiconductors with rather small bandgaps ($E_g \approx 0.1$ eV) and carrier concentrations of the order of $1 \times 10^{19} \text{ cm}^{-3}$ at room temperature. In the 30 years that followed, thermoelectricity had found some small but important applications, e.g. in radioisotope-thermoelectric generators that supply thermal and electrical power during space missions [Furl 99]. However, the efficiency of thermoelectric refrigerators remained too small for making them competitive with conventional cooling devices. Within the last 20 years, new strategies have been developed for enhancing the thermoelectric efficiency, for example by synthesizing materials with greater chemical complexity [Snyd 08], or by nanostructuring of thermoelectric materials [Dres 07, Minn 09, Vine 10, Pich 10, Kana 10]. The latter approach endeavors to make use of quantum confinement effects that can modify the energy dependence of the density of electronic states and can increase their effective band gap [Pich 10]. Furthermore, it is possible to reduce the phonon contributions to the thermal conductivity by nanostructuring [Kana 10]. A low thermal conductivity is crucial for thermal refrigeration to maintain the temperature gradient during cooling, but can be less important in the context of waste-heat recovery using thermoelectric generators [Nard 11]. Although the great promises of nanotechnology have unfortunately not materialized to date, it is very likely that the recent interest in waste-heat recovery [Rowe 06], as well as new applications, such as chip-scale thermoelectric cooling of transistors [Chow 09], may lead to an increased demand for thermoelectric devices. In recent years renewed interest in thermoelectric materials has been initiated by the prediction and subsequent demonstrations that many established thermoelectric materials (e.g. $\text{Bi}_x\text{Sb}_{1-x}$, Bi_2Te_3 , Bi_2Se_3) can exhibit signatures of topological insulators [Moor 10].

Some of the basic non-equilibrium transport phenomena are listed in Table 1.1. These phenomena may be separated into thermoelectric effects (Seebeck, Peltier, Thomson), galvanomagnetic effects (Hall, Ettingshausen), and thermomagnetic effects (Nernst, Righi-Leduc). Furthermore, in ferromagnetic conductors there are magnetoresistive effects, such as the anisotropic magnetoresistance effect and the giant magnetoresistance effect, as well as so-called anomalous (planar) effects that are observed if the magnetization is aligned perpendicular (parallel) to the currents, such as the anomalous- (planar-) Hall effect and the anomalous- (planar-) Nernst effect. The physical mechanisms behind the anomalous and planar effects are completely different from the respective ‘normal’ effects [Naga 10]. The common grounds that may justify the shared names are the related experimental geometries.

The anomalous and planar effects that involve temperature gradients, as well as the thermal and thermoelectric analogues of the magnetoresistive effects, such as the giant magnetothermal resistance effect and the giant magneto-Seebeck effect, may be counted to the new field of **thermal spintronics** or **spin caloritronics**, which explores non-equilibrium transport phenomena of spin, charge, and heat transport in ferromagnetic materials and ferromagnetic/non-magnetic hybrid structures [Baue 10, Baue 12]. Considering the spin degree of freedom further increases the zoo of non-equilibrium transport phenomena. Effects that are denoted by ‘spin dependent’, such as the spin-dependent Seebeck effect and the spin-dependent Peltier effect, rely on spin currents carried by spin polarized conduction electrons, while those denoted by ‘spin’, such as the spin-Hall effect, the spin-Nernst effect, and the spin-Seebeck effect, are thought to be based on pure spin currents. Another effect that involves pure spin currents is the thermal spin transfer torque [Hata 07, Yu 10]. Spin currents are a major issue in the field of spintronics. This research area has made a tremendous impact with the commercialization of magnetic hard disk drives that use spin-valves for data reading, and is coming up with many future applications [Bade 10]. Particular attention on thermal spintronics has been triggered by the spin-Seebeck effect – the evolution of a transverse voltage in a paramagnetic metal that is in thermal contact with the spin-Seebeck material under the influence of a temperature gradient and external magnetic fields. To explain the spin-Seebeck voltage it is assumed that the temperature gradient is associated with a spin current, which flows into the paramagnetic metal and causes a voltage due to the inverse spin-Hall effect [Uchi 08]. This interpretation suggests that pure spin currents may propagate over macroscopic length scales. Soon later the spin-Seebeck effect was also found, e.g., in electrically insulating yttrium iron garnet [Uchi 10] and even in a non-magnetic semiconductor [Jawo 12]. Perhaps over-motivated by the technological importance of spin currents, serious efforts have been undertaken to find a theory that explains the physical origin of the presupposed spin current in the spin-Seebeck effect [Xiao 10, Adac 13], although this spin current has only been measured indirectly. There is an ongoing debate about this topic and it could be possible that the spin-Seebeck effect will be explained in the light of a much simpler theory. This view is supported by the recent work of Avery *et al.*, who explained the signatures of the spin-Seebeck effect in their experiments in terms of the planar-Nernst effect [Aver 12].

So much for the problem situations of thermoelectrics and thermal spintronics. It is the objective of this thesis to make some small contributions to these research fields. The thesis is organized as follows:

Chapter 2 provides theoretical foundations that may be required for the discussion of our experiments. Chapter 3 demonstrates a synthesis route to nearly intrinsic Bi_2Te_3 nanowires, discusses the measuring microdevice used for determining the Seebeck coefficient, and presents a structural and compositional analysis as well as thermoelectric transport measurements on individual Bi_2Te_3 nanowires. Chapter 4 deals with the 3ω method, which is a prevalent measuring technique of thermal properties of bulk materials, thin films and nanowires. The concept of the 3ω method is revisited for voltage-driven measurement setups. Chapter 5 focuses on the electrical and thermal transport in individual Ni nanowires. A simple model is proposed to describe a new effect, the anisotropic magnetothermal resistance effect. Experimental results on this effect are presented. Chapter 6 is concerned with the electrical and thermal transport in Co/Cu multilayers. The Wiedemann-Franz law is revisited, which is complemented by measurements of the giant magnetoresistance effect and the giant magnetothermal resistance effect. Chapter 7 closes the thesis with a conclusion that summarizes our main results and suggests further experiments. In Appendix A our review article “Thermoelectric Nanostructures: From Physical Model Systems towards Nanograined Composites” is reprinted, which may be of interest for the reader in connection with Chapter 4. In Appendix B a philosophical article is reprinted. In particular natural scientists, who often get lost in highly specialized technical problems, should show an open-mindedness toward philosophical problems, perhaps in particular toward those related to the scientific method and the history of science (compare Ref. [Lder 12]).

Table 1.1: Basic non-equilibrium transport phenomena [Nola 01]. \mathbf{E} : Electric field, T : Temperature, \mathbf{q} : Heat current density, \mathbf{j} : Current density, p : Power density, ρ : Resistivity, H_z : Magnetic field strength.

Phenomenon	Phenomenological description	Formula
Seebeck effect	A temperature gradient imposed on a conductor generates a diffusion current. Under open circuit conditions an electric field acting against the temperature gradient develops and finally balances the diffusion current.	$\mathbf{E} = S \nabla T$; S : Seebeck coefficient.
Peltier effect	A voltage imposed on a conductor generates a charge current that is associated with a heat current. The change of the total energy flow at a junction of two conductors is accompanied by evolution of heat at the junction.	$\mathbf{q} = \Pi \mathbf{j}$; Π : Peltier coefficient.
Thomson effect	A current traversing a temperature gradient in a conductor is accompanied by evolution of Thomson heat in addition to the Joule heat.	$p = \rho \mathbf{j}^2 - \mu \mathbf{j} \nabla T$; μ : Thomson coefficient.
Hall effect	A current-carrying conductor placed in a transverse magnetic field develops an electric field perpendicular to the current and magnetic field directions.	$E_y = R_H H_z j_x$; R_H : Hall coefficient.
Ettingshausen effect	A current-carrying conductor placed in a transverse magnetic field develops a temperature gradient perpendicular to the current and magnetic field directions.	$\frac{dT}{dx} = R_E H_z j_x$; R_E : Ettingshausen coefficient.
Nernst effect	A heat current carrying conductor placed in a transverse magnetic field develops an electric field perpendicular to the heat current and magnetic-field directions.	$E_y = R_N H_z \frac{dT}{dx}$; R_N : Nernst coefficient.
Righi-Leduc effect	A heat current carrying conductor placed in a transverse magnetic field develops a temperature gradient perpendicular to the current and magnetic field directions.	$\frac{dT}{dy} = R_{RL} H_z \frac{dT}{dx}$; R_{RL} : Righi-Leduc coefficient.

2 Theoretical Foundations

This chapter deals with the basic physics relevant for this thesis. The main focus is on electronic transport phenomena in conducting materials, in particular ferromagnets. Section 2.1 briefly recapitulates the main magnetic interactions in electron systems. Section 2.2 introduces the Boltzmann-transport theory, which is used in Sec. 2.3 to quickly arrive at the basic thermoelectric effects. Since it is a major issue of thermoelectrics to find strategies for enhancing the efficiency of thermoelectric devices, Sec. 2.4 introduces the thermoelectric figure of merit. In Sec. 2.5, a discussion of the basic bulk optimization strategies that are based on tuning of the carrier concentration and looking for high carrier mobilities follows. Section 2.6 briefly summarizes the dominant scattering mechanisms of electrons. The two subsequent sections introduce two famous laws in solid state physics: the Matthiessen law in Section 2.7 and the Wiedemann-Franz law in Sec. 2.8. Coming back to magnetism, Sec. 2.9 discusses the peculiarities of electronic transport in ferromagnets and Sec. 2.10 introduces the anisotropic magnetoresistance effect. Section 2.11 addresses the spin-dependent diffusive transport theory that leads to the concepts of spin- and spin-heat-accumulation, followed by a discussion of the giant magnetoresistance effect in Sec. 2.12. The last section of this chapter deals with classical size effects, which are always present in nanostructures, and quantum confinement effects, which can play a significant role in nanostructures.

2.1 Magnetism

There are three main magnetic interactions in electron systems [Sthr 06]: The exchange interaction that is responsible for the alignment of spins, the spin-orbit interaction that creates orbital magnetism and couples the spin system to the lattice, and the Zeeman interaction that enables us to manipulate the alignment of magnetic moments.

2.1.1 Exchange Interaction

The exchange interaction is a quantum-mechanical effect between identical particles. It arises from the symmetrization postulate. According to this postulate, the total wavefunction of an electron system is antisymmetric under exchange of any two electrons. Due to the antisymmetric wavefunction the Coulomb potential between the electrons in the system acts as if it was spin-dependent [Gasi 02]. The resulting change of the expectation value of the energy favors either parallel or antiparallel spins. The fact that the exchange interaction arises from the wavefunctions imposes big challenges on the theoretical description, in particular for macroscopic systems. Therefore, one often uses a model Hamiltonian, e.g. the Heisenberg Hamiltonian or the Hubbard Hamiltonian, which are designed to give suitable results for well-known problems, in combination with one-particle wavefunctions [Sthr 06]. One distinguishes several forms of exchange. Important examples are given in the following.

Direct exchange is due to direct overlap of the wavefunctions considered for exchange. In He atoms direct exchange between the two electrons favors parallel spins. The exchange energy split between triplet and singlet states of excited He atoms is observable

in the spectrum of He. In H_2 molecules direct exchange between the two electrons favors antiparallel spins. Due to the wavefunction overlap between the H^+ ions a bonding orbital is formed. In that way, the exchange interaction gives a physical explanation of the covalent chemical bond.

Indirect exchange between two magnetic atoms can be mediated by a nonmagnetic atom. It leads to antiferromagnetic coupling and occurs for example in transition metal oxides, such as NiO. This kind of indirect exchange is called superexchange, because it extends the short-ranging direct exchange interaction to longer distances. Another important example for indirect exchange is the RKKY interaction¹ that describes the exchange over the distance between two localized magnetic electrons mediated by conduction electrons. Scattering of conduction electrons at the localized magnetic electrons generates spin-density waves in the itinerant electron system that screen the disturbing localized magnetic moment. This leads to an oscillatory behavior of the RKKY-exchange interaction. Depending on the distance between the localized magnetic electrons, their magnetic coupling can be ferromagnetic or antiferromagnetic. The RKKY interaction works over relatively large distances of a few nanometers. It can be used to couple magnetic layers that are separated by a nonmagnetic spacer layer. As discussed in Sec. 2.12, this possibility is of highest practical interest.

Itinerant exchange means exchange between itinerant electrons. In the ferromagnetic transition metals Fe, Co, and Ni, the exchange interaction causes a spontaneous magnetization, i.e. a parallel alignment of spins over macroscopic regions or domains, even in the absence of external magnetic fields. The main source of the spontaneous magnetization in transition metals are the spin moments of partly occupied $3d$ states at the Fermi energy that generate a sizeable magnetization at room temperature. A general theory of ferromagnetic transition metals should describe simultaneously the characteristic electron correlation effects that lead to the spontaneous magnetization, as well as the electronic transport properties predicted by band theories [Sthr 06].² The formulation of such a theory is a topic of contemporary research in magnetism. Instead of such a theory, a widely supported description is given by the Stoner model that is based on band theory [Sthr 06]. This model assumes that an exchange interaction of $3d$ electrons generates an exchange-energy splitting of the $3d$ bands. As the $3d$ bands are not fully occupied, the exchange splitting increases the number of electrons in the energetically favored band, and vice versa. The spin-polarized $3d$ bands give rise to a spontaneous magnetization that is determined by the difference of the occupation numbers of both bands. Due to the filling of the bands up to the Fermi surface the magnetic moment per atom is a noninteger multiple of the Bohr magneton. Electrons with spin orientation antiparallel to the magnetization vector are called majority-spin electrons. The others are called minority-spin electrons. In Fig. 2.1, the Stoner model is illustrated for Ni. The exchange interaction is the strongest among the three magnetic interactions, because it arises from the Coulomb interaction. In the $3d$ transition metals, the exchange energy is of the order of 1 eV.

¹Named after the scientists involved in the discovery of this effect: Ruderman, Kittel, Kasuya, and Yosida.

²The behavior of electrons in solids has largely remained a mystery. One distinguishes two important concepts: localized or correlated and independent, delocalized, itinerant, or band-like electron behavior [Sthr 06]. Correlated electrons remain localized on different atomic sites due to dominating Coulomb repulsion, whereas the wavefunctions of independent electrons in a solid are spread over the entire crystal. Such delocalized electrons are itinerant and can be well described by band-theoretical models.

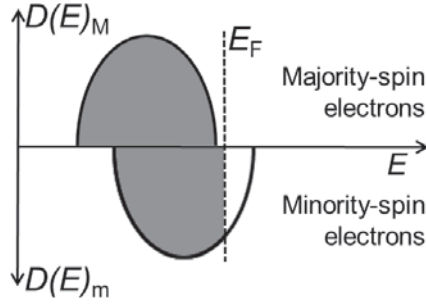


Figure 2.1: Illustration of the spin-polarized 3d band of Ni in the Stoner model. Minority spins point in the direction of the spontaneous magnetization. The bands are separated due to the exchange energy splitting. Filled electron states below the Fermi energy E_F are indicated by the shaded area. This figure is based on Fig. 7.6 in Ref. [Sthr 06].

2.1.2 Spin-Orbit Interaction

The spin \mathbf{S} of an electron couples with the orbital angular momentum \mathbf{L} of the electron to the total angular momentum $\mathbf{J} = \mathbf{S} + \mathbf{L}$. This effect is described by the spin-orbit Hamiltonian H_{so} , which follows from the relativistic Dirac equation [Sthr 06]:

$$H_{so} = \xi \mathbf{L} \cdot \mathbf{S}, \quad (2.1)$$

where ξ is the spin orbit coupling constant. In a crystal, electron orbitals are linked to the lattice due to bonding with adjacent atoms, i.e. the orbital angular momentum favors certain crystallographic directions. This anisotropy combined with the spin-orbit interaction leads to the magnetocrystalline anisotropy in ferromagnetic materials. On the other hand, the presence of a spontaneous magnetization coupled to the lattice breaks the time-reversal symmetry and allows for a net orbital magnetization. Applied to 3d orbitals of ferromagnetic transition metals with an energy splitting due to a ligand field of cubic symmetry, the spin-orbit interaction generates mixing of states with the same spin and mixing of states with opposite spin [Sthr 06]. It turns out that this intermixing effect is anisotropic. We come back to this point in Sec. 2.10, where the anisotropic magnetoresistance is discussed. The spin-orbit interaction energy in the 3d transition metals is of the order of 10 to 100 meV.

2.1.3 Zeeman Interaction

The Zeeman interaction describes the coupling of angular momentum to an external magnetic field \mathbf{H} . The total angular momentum $\mathbf{J} = \mathbf{L} + \mathbf{S}$ generates a magnetic moment $\mathbf{m} = -\frac{\mu_B}{\hbar}(\mathbf{L} + 2\mathbf{S})$. The Zeeman Hamiltonian is given by [Sthr 06]

$$H_{ZI} = \frac{\mu_B}{\hbar}(\mathbf{L} + 2\mathbf{S}) \cdot \mathbf{H}. \quad (2.2)$$

In atoms, the Zeeman interaction lifts the degeneracy of electronic states. In ferromagnetic materials, the Zeeman interaction allows for the alignment of magnetic domains by applying magnetic fields.

2.2 Boltzmann Equation and Relaxation-Time Approximation

A system of noninteracting identical fermions can be described using Fermi-Dirac statistics. Application of Fermi-Dirac statistics to electrons in metals is known as the Sommerfeld theory of metals. The average number of electrons in a single-particle state of energy E at equilibrium is described by the Fermi-Dirac function

$$f_0(E, T) = \frac{1}{e^{(E-\zeta)/k_B T} + 1}, \quad (2.3)$$

where ζ is the chemical potential, which at $T = 0$ is equal to the Fermi energy. Within the semi-classical transport theory, the nonequilibrium distribution function f is defined to depend on the wave vector \mathbf{k} , the spatial coordinate \mathbf{r} , and the time t . To justify the assumption of a classical position-momentum space, it is assumed that the chemical potential and the temperature vary over a scale that is large compared to atomic dimensions. The differential equation for $f(\mathbf{k}, \mathbf{r}, t)$ is the Boltzmann equation, a continuity equation for particle flow:

$$\frac{df(\mathbf{k}, \mathbf{r}, t)}{dt} = \frac{\partial f(\mathbf{k}, \mathbf{r}, t)}{\partial t} + \nabla_r f(\mathbf{k}, \mathbf{r}, t) \frac{d\mathbf{r}}{dt} + \nabla_k f(\mathbf{k}, \mathbf{r}, t) \frac{d\mathbf{k}}{dt} = \left(\frac{\partial f(\mathbf{k}, \mathbf{r}, t)}{\partial t} \right)_{\text{coll}}, \quad (2.4)$$

where the collision term on the right hand side contains the information about the microscopic scattering mechanisms. The linearized Boltzmann equation for steady-state distribution functions ($\frac{\partial f}{\partial t} = 0$) is obtained by replacing f with f_0 in the left hand side of Eq. (2.4). This is reasonable for weak external fields, so that the system is not too far from equilibrium. The simplest approximation of the right hand side is the relaxation time approximation. For this approach it is assumed that the collision term, which is responsible for the system to approach thermal equilibrium, is proportional to the deviation of the distribution function from its equilibrium value. The linearized Boltzmann equation in the relaxation time approximation then reads [Uher 04]:

$$\left(\frac{df_0(\mathbf{k})}{dE} \right) \left[\frac{E(\mathbf{k}) - \zeta}{T} \nabla_r T + \nabla_r \zeta - e\mathbf{E} \right] \mathbf{v} = -\frac{f(\mathbf{k}, \mathbf{r}) - f_0(\mathbf{k})}{\tau(\mathbf{k})}, \quad (2.5)$$

where $\tau(\mathbf{k})$ is the relaxation time and $\mathbf{E} = \frac{\hbar}{e} \frac{d\mathbf{k}}{dt}$ the electrostatic field.³ The validity of the relaxation-time approximation is a critical issue [Ashc 76]. Inelastic scattering processes for example can be very effective in relaxing a thermal current without degrading an electric current. As a consequence of the relaxation-time approximation, τ would be different for heat- and charge-currents. Consequently, the interpretation of the relaxation time as a measure of the time between two collisions is not valid anymore. Before we come back to this point in Sec. 2.8, Eq. (2.5) is used to define the current densities that are caused by an electric field and a temperature gradient.

³The effective field that drives the current is given by $\epsilon = \mathbf{E} - \nabla_r \zeta / e = -\nabla_r(\varphi + \zeta/e) \equiv -\nabla_r \Phi / e$, where $\Phi = \zeta + e\varphi$ is the electrochemical potential. Throughout the text the elementary charge e is defined as a parameter (compare Table 0.1), i.e. the charge of an electron is $-e$.

2.3 Thermoelectric Effects

The nonequilibrium distribution described by Eq. (2.5) results in nonvanishing charge- and heat-current densities that are given by

$$\mathbf{j}(\mathbf{r}) = \frac{2e}{V} \sum_{\mathbf{k}} \mathbf{v}(\mathbf{k}) f(\mathbf{k}, \mathbf{r}), \quad (2.6)$$

and

$$\mathbf{q}(\mathbf{r}) = \frac{2}{V} \sum_{\mathbf{k}} \mathbf{v}(\mathbf{k}) (E(\mathbf{k}) - \zeta) f(\mathbf{k}, \mathbf{r}). \quad (2.7)$$

Substituting Eq. (2.5) into Eqs. (2.6) and (2.7) results in a linear relation between the external fields and their associated currents⁴ [Uher 04],

$$\mathbf{j}(\mathbf{r}) = e^2 K_0 \mathbf{E} + \frac{eK_1}{T} (-\nabla_r T), \quad (2.8)$$

$$\mathbf{q}(\mathbf{r}) = eK_1 \mathbf{E} + \frac{K_2}{T} (-\nabla_r T), \quad (2.9)$$

where the transport coefficients K_n are in general tensors:

$$K_{n,(i,j)} = \frac{2}{V} \sum_{\mathbf{k}} v_i(\mathbf{k}) v_j(\mathbf{k}) [E(\mathbf{k}) - \zeta]^n \tau(\mathbf{k}) \left(-\frac{df_0(\mathbf{k})}{dE} \right). \quad (2.10)$$

For isotropic materials the tensors reduce to scalars. Assuming zero temperature gradient, Eq. (2.8) reduces to the Ohm law:

$$\mathbf{j} = e^2 K_0 \mathbf{E} \equiv \sigma \mathbf{E}, \quad (2.11)$$

where σ is the electrical conductivity. Under open-circuit conditions ($\mathbf{j} = 0$), Eq. (2.8) describes the generation of an electric field by a temperature gradient:

$$\mathbf{E} = \frac{K_0^{-1} K_1}{eT} \nabla_r T \equiv S \nabla_r T, \quad (2.12)$$

where S is the Seebeck coefficient. An important application of this so-called Seebeck effect is the thermocouple (see Fig. 2.2). The two legs of a thermocouple consist of two materials with different Seebeck coefficients, S_A and S_B . According to Eq. (2.12), the temperature difference across the legs of the thermocouple generates the voltage

$$U_{ac} = \int_a^b S_A \nabla_r T d\mathbf{r} + \int_b^c S_B \nabla_r T d\mathbf{r} = (S_A - S_B)(T_2 - T_1), \quad (2.13)$$

which can be used for temperature measurements (compare Fig. 2.2). In the absence of a temperature gradient, it follows from Eqs. (2.8) and (2.9) that the heat current generated by a voltage is proportional to the charge current:

$$\mathbf{q} = \frac{K_1 K_0^{-1}}{e} \mathbf{j} \equiv \Pi \mathbf{j}, \quad (2.14)$$

⁴In metals the chemical potential is not affected by the transport process and can be assumed constant, i.e. $\nabla_r \zeta = 0$. This is because of their large carrier concentrations.

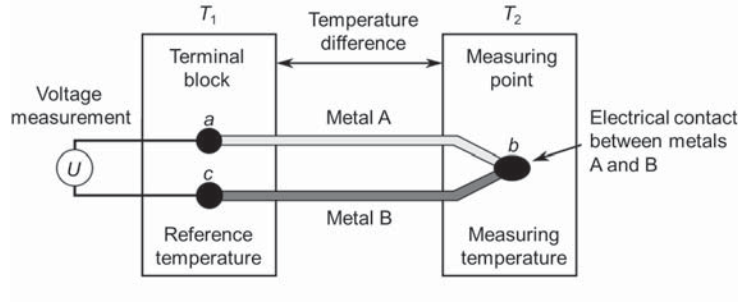


Figure 2.2: Basic thermoelement that can be used to measure temperatures. The figure is based on a public file [wwwc 08].

where Π is called the Peltier coefficient. A current that flows through a thermocouple is accompanied by the evolution of heat at the junction of the two materials. This so-called Peltier effect has its application in thermoelectric refrigeration.

The thermal conductivity is typically measured under open-circuit conditions ($\mathbf{j} = 0$). Then, substituting Eq. (2.12) into Eq. (2.9) yields

$$\mathbf{q} = \frac{K_2 - K_1 K_0^{-1} K_1}{T} (-\nabla_r T) \equiv \kappa (-\nabla_r T), \quad (2.15)$$

where κ is the electronic thermal conductivity. For metals, the term $K_1 K_0^{-1} K_1 \ll K_2$ and can therefore be neglected in Eq. (2.15).

Using Eqs. (2.8) and (2.9) the entropy current density $\mathbf{s} = \mathbf{q}/T$ can be expressed in terms of the current density and the temperature gradient:

$$\mathbf{s} = \frac{K_1 K_0^{-1}}{eT} \mathbf{j} + \frac{K_2 - K_1 K_0^{-1} K_1}{T^2} (-\nabla_r T). \quad (2.16)$$

According to this equation, the Seebeck coefficient defined in Eq. (2.12) is equal to the entropy per charge carried by a current in a conductor.

2.4 Thermoelectric Figure of Merit

It can be shown that both the power generation efficiency and the cooling coefficient of performance of a thermoelement (see Fig. 2.2) are maximized by maximizing the figure of merit [Nola 01]

$$ZT = \frac{(S_A - S_B)^2}{\left(\sqrt{\kappa_A \rho_A} + \sqrt{\kappa_B \rho_B}\right)^2} T, \quad (2.17)$$

where $\rho = 1/\sigma$ is the electrical resistivity. In typical applications, the absolute thermoelectric properties of the two materials are similar, and Z approximately equals the average of the individual figures of merit. Multiplied with the temperature, the dimensionless individual figure of merit is defined to be

$$zT = \frac{S^2}{\kappa \rho} T = \frac{S^2 \sigma}{\kappa} T. \quad (2.18)$$

2.5 Optimization of Thermoelectric Materials

Assuming one parabolic band and a relaxation time of the form $\tau \equiv \tau_0 E^r$, Eq. (2.10) can be expressed in the following form [Nola 01]:

$$K_n = A \int E^{r+3/2} (E - \zeta)^n \left(-\frac{df_0}{dE} \right) dE, \quad A \equiv \frac{m^{*1/2}}{3\pi^2} \left(\frac{2}{\hbar^2} \right)^{3/2} \tau_0, \quad (2.19)$$

where m^* denotes the effective electron mass. Further, we have used the density of states per energy interval defined in Eq. (2.43) and the velocity was replaced using the average thermal energy: $\langle v \rangle = \sqrt{2E/(3m^*)}$. It is convenient to express Eq. (2.19) in terms of the Fermi-Dirac integrals

$$F_j(\eta) = \int \frac{e^j}{e^{\epsilon-\eta} + 1} dt, \quad (2.20)$$

where $\eta \equiv \zeta/(k_B T)$ is the reduced chemical potential and $\epsilon \equiv E/(k_B T)$ is the reduced energy. Then, the carrier concentration and the transport quantities become:

$$n = \frac{1}{2\pi^2} \left(\frac{2m^* k_B T}{\hbar^2} \right)^{3/2} F_{1/2}(\eta); \quad (2.21)$$

$$\sigma = e^2 A (r + 3/2) (k_B T)^{3/2} F_{r+1/2}(\eta); \quad (2.22)$$

$$S = \frac{k_B}{e} \left(\frac{(r + 5/2) F_{r+3/2}(\eta)}{(r + 3/2) F_{r+1/2}(\eta)} - \eta \right); \quad (2.23)$$

$$\kappa = \frac{(k_B T)^{7/2}}{T} \left(A (r + 7/2) F_{r+5/2}(\eta) - \frac{(A (r + 5/2) F_{r+3/2}(\eta))^2}{A (r + 3/2) F_{r+1/2}(\eta)} \right). \quad (2.24)$$

Figure 2.3 depicts the various thermoelectric transport properties calculated using Eqs. (2.22) to (2.24) for Fermi energies⁵ between -0.2 eV and 0.4 eV and a temperature of $T = 293$ K. For the calculations we have assumed $r = -1/2$ and $m^* = m_e$. As can be seen in Fig. 2.3(c) at small Fermi energies, we have considered a lattice thermal conductivity of 2 W/mK. The behavior of the electronic Lorenz number $L = \kappa_{\text{el}}/\rho T$ is shown in Fig. 2.3(d). For metals, i.e. in the limit of large Fermi energies, L approaches the Sommerfeld value, a universal constant that does not depend on the material properties (compare Sec. 2.8). Thermoelectric materials are usually optimized by enhancing the powerfactor $S^2\sigma$ and the thermoelectric figure of merit zT . The respective dependencies on the Fermi energy are plotted in Figs. 2.3(e) and 2.3(f). The gray areas shown in each graph of Fig. 2.3 separate the nondegenerate electron gas regime of semiconductors ($k_B T \gg E_F$) from the degenerate electron gas regime of metals ($k_B T \ll E_F$). Obviously, this Fermi-energy range is of special interest for thermoelectric applications. In addition to the carrier concentration, the thermoelectric performance is governed by the carrier mobility [Nola 01]. In nondegenerate conductors Eq. (2.22) can be expressed in the form [Nola 01]

$$\sigma = ne\mu, \quad (2.25)$$

where μ is the carrier mobility. Combined with Eq. (2.21) it follows that for achieving efficient thermoelectric materials $\mu(m^*)^{3/2}$ should be as large as possible [Nola 01].

⁵At this point we assume $\zeta = E_F$.

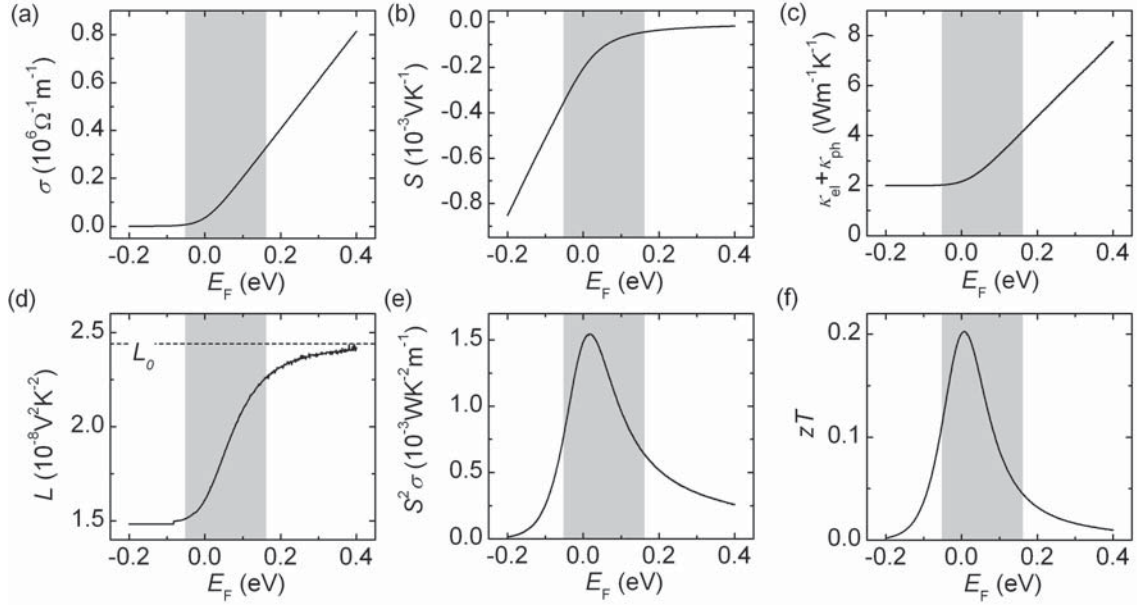


Figure 2.3: Thermoelectric transport properties plotted against the Fermi energy according to Eqs. (2.22) to (2.24); (a) electrical conductivity σ , (b) Seebeck coefficient S , (c) total (electronic and phonon) thermal conductivity $\kappa_{\text{el}} + \kappa_{\text{ph}}$, (d) Lorenz number L , (e) powerfactor $S^2\sigma$, (f) figure of merit zT . For calculating the Fermi-Dirac integrals we used the Matlab program developed by Raseong Kim and Mark Lundstrom [http 11].

2.6 Scattering Mechanisms

In Eq. (2.5), the relaxation time τ was introduced as a phenomenological parameter. However, to justify the relaxation time approximation, it must be possible to deduce relaxation times from microscopic theories. The general form of the collision term in Eq. (2.4) consists of scattering-in and scattering-out terms [Uher 04]:

$$\frac{df(\mathbf{k}, \mathbf{r}, t)}{dt} = \sum_{\mathbf{k}_i} [w_{\mathbf{k}_i \rightarrow \mathbf{k}} f(\mathbf{k}_i, \mathbf{r}, t) (1 - f(\mathbf{k}, \mathbf{r}, t)) - w_{\mathbf{k} \rightarrow \mathbf{k}_i} f(\mathbf{k}, \mathbf{r}, t) (1 - f(\mathbf{k}_i, \mathbf{r}, t))], \quad (2.26)$$

where $w_{\mathbf{k}_a \rightarrow \mathbf{k}_b}$ is the transition probability from state \mathbf{k}_a into state \mathbf{k}_b . The transition probabilities depend on the scattering mechanisms under consideration and are calculated using quantum mechanics, for example the Born approximation.

2.6.1 Electron-Impurity Scattering

In general, impurities are heavy objects on the scale of the electron mass. Therefore, the absorbed energy from colliding electrons is negligible. Scattering of electrons that is not accompanied by a change of the electron's energy is called **elastic scattering**, or sometimes large-angle scattering. Electron scattering at static impurities and lattice imperfections is independent of temperature and leads to the residual resistivity at zero temperature. In the simplest case of extremely short ranging interaction potentials, the inverse relaxation time of elastic scattering, and thus the residual resistivity, is proportional to the impurity concentration n_{imp} , the density of states at the Fermi energy $D(E_F)$, and the interaction potential V squared [Czyc 08]:

$$\rho_{\text{e-imp}} \sim n_{\text{imp}} D(E_F) V^2. \quad (2.27)$$

2.6.2 Electron-Phonon Scattering

The interaction between electrons and phonons involves absorption or emission of a phonon and results in a change of the electron energy. Therefore, electron-phonon scattering belongs to the group of **inelastic scattering**. A relaxation time for this scattering mechanism was derived by Bloch and Grüneisen [Bloc 28, Grne 33]. In the limits of low and high-temperatures, the Bloch-Grüneisen formula reveals the following asymptotic temperature dependencies [Czyc 08]:

$$\begin{aligned}\rho_{\text{e-p}}(T) &\sim T^5 \quad \text{for } T \ll T_{\text{Debye}}, \\ \rho_{\text{e-p}}(T) &\sim T \quad \text{for } T \geq T_{\text{Debye}}.\end{aligned}\tag{2.28}$$

2.6.3 Electron-Electron Scattering

Despite the high electron density in a metal, scattering of electrons by other electrons plays a negligible role for electronic transport properties.⁶ The reason for this is that two electrons in a metal experience a scattering potential that is strongly screened by the presence of all other charge carriers in the metal. Even for the purest specimens at very low temperatures ($T < 1$ K), the contribution from electron-electron scattering to the total resistance is of the order of 0.01% [Uher 04]. The electrical resistivity $\rho_{\text{e-e}}$ is predicted to vary with the square of the temperature [Uher 04]:

$$\rho_{\text{e-e}} \sim T^2.\tag{2.29}$$

2.6.4 Electron-Magnon Scattering

In a ferromagnetic metal, the exchange interaction between conduction electrons and localized magnetic moments gives rise to scattering of electrons at magnons. This scattering mechanism involves mixing of the two spin systems present in ferromagnets (compare Sec. 2.9): Majority- (minority-) spin electrons can be scattered into minority- (majority-) spin states by annihilation (excitation) of a magnon. At low temperatures model calculations indicate a squared temperature-dependence of the spin-disorder resistivity [Good 63]:

$$\rho_{\text{e-m}} \sim T^2 \quad \text{for } T < \sim 20 \text{ K}.\tag{2.30}$$

Experimental investigations in Fe-, Co-, and Ni-thin films indicate that at room temperature, the respective spin-disorder resistivities in these materials comprise 15%, 18%, and 30% of the respective total resistivities [Raqu 02].

2.7 Matthiessen Rule

The total resistivity of a material at temperature T is caused by various scattering mechanisms. In the simplest case, the respective scattering probabilities are assumed to be independent. Then, the individual scattering probabilities, and thus the inverse relaxation times, can simply be added. If the relaxation times are isotropic, one arrives at the Matthiessen rule:

$$\rho = \sum_i \rho_i.\tag{2.31}$$

⁶However, this does not hold in general for electron-electron interactions. For example, the exchange splitting of $3d$ bands in ferromagnetic transition metals strongly influences the transport properties due to s - d scattering (compare Secs. 2.1.1 and 2.9).

The Matthiessen rule is not generally valid [Ashc 76]. However, it is an important approximation, because it allows for discussing electron scattering in metals in terms of more or less independent scattering mechanisms, which can be treated separately.

2.8 Wiedemann-Franz Law and Lorenz Number

The Wiedemann-Franz (WF) law states that the ratio of electronic thermal conductivity to electrical conductivity is the same for all metals, and that this ratio is proportional to the temperature [Wied 53, Lore 72]. The validity of this law is based on the concept that in metals most of the heat is carried by electrons. The WF law can be deduced by applying the Sommerfeld expansion of the transport coefficients K_n [see Eq. (2.10)], which is valid at low temperatures ($k_B T \ll E_F$), to the Fermi-Dirac statistics discussed in Secs. 2.2 and 2.3. The result reads [Czyc 08]

$$\frac{\kappa}{\sigma} = \frac{3k_B^2}{2e^2} T \equiv L^0 T, \quad (2.32)$$

where $L^0 = 2.45 \times 10^{-8} \text{V}^2 \text{K}^{-2}$ is the Sommerfeld value of the Lorenz number L . It can be shown that the WF law only holds for a highly degenerate electron gas [compare Fig. 2.3(d)] under the assumption that all scattering processes are elastic⁷ [Ashc 76]. Then, electrical and thermal relaxation processes can be characterized by the same relaxation time. Deviations from the WF law occur at temperatures roughly between 10 K and 300 K due to inelastic scattering of electrons in combination with a small change in the electron wave vector. In this temperature range the phonon energies are comparable to $k_B T$. Consequently, small-angle scattering involves a thermal relaxation time that is considerably shorter than the electrical relaxation time [Uher 04]. The relaxation time can be interpreted as a measure of the effectivity of the scattering mechanism to relax the system to equilibrium rather than a measure of the time between two collisions. An example of $L(T)$ for high-purity Cu is shown in Fig. 2.4. It can be seen that the WF law holds for $T \rightarrow 0$, where elastic electron-impurity scattering dominates. After reaching a minimum,

⁷In this context ‘elastic’ means that the energy of the scattered electron is conserved in the scattering process.

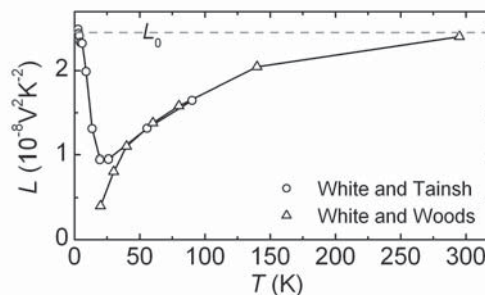


Figure 2.4: Deviations from Wiedemann-Franz law in high-purity Cu due to inelastic electron-phonon scattering. The data was derived using the bulk data of the electrical resistivity and of the thermal resistivity of high-purity Cu measured in Ref. [Whit 60] (circles) and in Ref. [Whit 59] (triangles). The solid lines are guides to the eyes; the dashed line indicates the Sommerfeld value L_0 .

L starts to increase with increasing temperature and approaches L^0 at $T \approx T_{\text{Debye}}$. For temperatures above T_{Debye} large-angle electron scattering at large-momentum phonons with wavevectors comparable to the Fermi wavelength dominates. A pronounced minimum of L can only be observed for high-purity metals. In alloys and nano-crystalline metals, this minimum is masked by the large residual resistivity of these materials.

The deviations from the WF law discussed so far are typically below 50%. Large violations of several orders of magnitude may occur in strongly-correlated materials, which cannot be described by conventional band-theoretical models (compare footnote 2) [Kane 96, Garg 09, Wake 11]. In a so-called Mott insulator, there can exist an efficient heat-conduction channel provided by spin fluctuations, while the electrical conductivity is exponentially small, resulting in $L \gg L_0$. On the other hand, the thermal conductivity of superconductors remains finite, while the electrical conductivity diverges, resulting in $L \approx 0$.

2.9 Resistivity of Ferromagnetic Metals

Assuming one parabolic band of an isotropic material in the limit $T \rightarrow 0$, the electrical conductivity defined in Eq. (2.11) reduces to the Drude formula [Czyc 08]

$$\sigma = \frac{ne^2\tau(E_F)}{m^*}, \quad (2.33)$$

where n is the charge carrier density. Mott developed a simple sd model to explain the resistivity of transition metals [Mott 36a, Mott 36b]. He assumed that the conductivity of transition metals is dominated by s electrons, because the effective mass of d electrons is much larger than that of s electrons. Due to the large density of states of the d band, Mott further suggested that a sizable contribution to the resistivity arises from scattering of s electrons into empty d states. In ferromagnetic metals with exchange split d bands, this effect results in a resistivity of the minority-spin channel that is larger compared to the one of the majority-spin channel (compare Fig. 2.1). Separation of the current into parallel contributions from majority and minority spins came to be known as the two-current model [Fert 68]. This model provides intuitive understanding of various transport phenomena in ferromagnetic metals and ferromagnetic metal/normal metal hybrid structures (e.g. resistance decrease upon ferromagnetic ordering, anisotropic magnetoresistance, giant magnetoresistance). Despite the success of the two-current model, its applicability has remained a critical issue [Banh 97]. One reason for this is the hybridization or mixing of conduction bands due to the spin-orbit interaction [Eber 97]. Moreover, the traditional semiclassical Boltzmann-transport theory (see Sec. 2.2) does not provide satisfactory explanations for quantum phenomena such as the anomalous-Hall effect that is observed in ferromagnetic conductors. To address these problems, new and fascinating concepts that are based on topology and geometry have been formulated in recent times [Naga 10].

2.10 Anisotropic Magnetoresistance

The resistivity of a ferromagnetic conductor depends on the direction of the current relative to the magnetization vector. This effect was discovered by William Thomson in 1856. Its today's common name is anisotropic magnetoresistance (AMR) effect. Spin-dependent scattering is indeed necessary for AMR. However, the symmetry breaking element enters via the spin-orbit interaction [Smit 51, Malo 86, Eber 00]. In Sec. 2.1.2, we

mentioned that the spin-orbit interaction gives rise to mixing or hybridization of the two spin subsystems. This mechanism permits majority-spin $4s$ electrons to be scattered to minority-spin $3d$ states. The anisotropy of the spin-orbit induced mixing of states results in a difference $\Delta\rho$ between the resistivities parallel and perpendicular to the spontaneous magnetization direction (see also footnote 8).

2.11 Spin-dependent Diffusive Transport Theory

In Sec. 2.3, it was shown that the Boltzmann-transport theory predicts a linear relation between external fields (\mathbf{E} , $\nabla_r T$) and their associated currents (\mathbf{j} , \mathbf{q}). In terms of generalized currents \mathbf{J} and generalized forces \mathbf{F} , Eqs. (2.8) and (2.9) can be written in the following form:

$$\mathbf{J} = \mathbf{C}\mathbf{F}, \quad (2.34)$$

where \mathbf{C} is the conductance matrix. Considering only charge transport in the absence of temperature gradients, the two-current model discussed in Sec. 2.9 can then be expressed by [Mott 36a, Vale 93]

$$\begin{pmatrix} \mathbf{j}_M \\ \mathbf{j}_m \end{pmatrix} = - \begin{pmatrix} \sigma_M & 0 \\ 0 & \sigma_m \end{pmatrix} \begin{pmatrix} \nabla_r \Phi_M/e \\ \nabla_r \Phi_m/e \end{pmatrix}, \quad (2.35)$$

where $\Phi_i = e\varphi + \zeta_i$ ($i \in \{M, m\}$) is the electrochemical potential. This means that at this point we consider the spin-dependent chemical potentials ζ_M and ζ_m , because they split and become position dependent in the presence of interfaces (compare Sec. 2.12 and footnotes 3 and 4). The spin accumulation $\Delta\zeta \equiv \zeta_M - \zeta_m$, which is related to divergences of the spin currents, is balanced by spin-flip scattering [Vale 93]:

$$\begin{pmatrix} \nabla_r \mathbf{j}_M \\ \nabla_r \mathbf{j}_m \end{pmatrix} = \begin{pmatrix} \sigma_M/\lambda_M^2 & -\sigma_M/\lambda_M^2 \\ -\sigma_m/\lambda_m^2 & \sigma_m/\lambda_m^2 \end{pmatrix} \begin{pmatrix} \Phi_M/e \\ \Phi_m/e \end{pmatrix}, \quad (2.36)$$

where λ_M and λ_m are characteristic lengths of the spin-diffusion processes. Combining Eq. (2.36) with the divergence of Eq. (2.35) yields a spin-diffusion equation in terms of chemical potentials [Vale 93]:

$$\nabla_r^2(\Delta\zeta) = \frac{\Delta\zeta}{\lambda_{\text{sf}}^2}, \quad (2.37)$$

where $\lambda_{\text{sf}} = ((1/\lambda_M)^2 + (1/\lambda_m)^2)^{-1/2}$ is the average spin diffusion length.

Spin-dependent heat models consider minority- and majority-spin subsystems that carry heat separately (\mathbf{q}_M , \mathbf{q}_m). Each spin subsystem is characterized by its own thermal conductivity (κ_M , κ_m) and temperature (T_M , T_m) [Giaz 07, Hata 07, Heik 10]. In such a spin-dependent heat model, Eq. (2.34) becomes [Slac 11]:

$$\begin{pmatrix} \mathbf{j}_M \\ \mathbf{j}_m \\ \mathbf{q}_M \\ \mathbf{q}_m \end{pmatrix} = \begin{pmatrix} \sigma_M & 0 & \sigma_M S_M & 0 \\ 0 & \sigma_m & 0 & \sigma_m S_m \\ \sigma_M \Pi_M & 0 & \kappa_M & 0 \\ 0 & \sigma_m \Pi_m & 0 & \kappa_m \end{pmatrix} \begin{pmatrix} \nabla_r \Phi_M/e \\ \nabla_r \Phi_m/e \\ \nabla_r T_M \\ \nabla_r T_m \end{pmatrix} \quad (2.38)$$

Analogue to spin accumulation, the concept of spin-heat accumulation $\Delta T = T_M - T_m$ was introduced [Hata 07, Heik 10]. The respective spin-heat diffusion equation that describes the relaxation of spin-heat accumulation is given by [Slac 11]

$$\nabla_r^2(\Delta T) = \frac{\Delta T}{\lambda_Q^2}, \quad (2.39)$$

where λ_Q is the relaxation length of the spin heat diffusion process. An effective relaxation mechanism for spin-heat accumulation is given through inelastic scattering at phonons, i.e. the temperature of each spin subsystem is equilibrated to the temperature of the phonon system [Heik 10].

2.12 Giant Magnetoresistance

Figure 2.5 shows a magnetoresistivity trace measured on a Co/Cu multilayer. The chosen thicknesses of the Cu layers is such that the coupling between adjacent Co layers is antiferromagnetic (see RKKY interaction in Sec. 2.1.1). Imposing an in-plane field leads to parallel alignment of the magnetization directions of adjacent Co layers. During the alignment process, the resistance of the multilayer drops significantly. This so-called giant magnetoresistance (GMR) effect discovered in 1988 [Baib 88, Bina 89] triggered the research field of spintronics [Wolf 01]. The GMR ratio is defined to be

$$\frac{\Delta R}{R_{AP}} = \frac{R_{AP} - R_P}{R_{AP}}, \quad (2.40)$$

where R_{AP} is the resistance of the antiparallel magnetization configuration, and R_P the typically lower resistance of the parallel configuration. The GMR ratio can reach values of the order of 50% at room temperature. This effect is observed for both current directions, for current flowing in the plane of the layers (CIP transport) and for current flowing perpendicular to the plane of the layers (CPP transport). However, there are significant differences between CIP and CPP transport [Tsym 01] as briefly discussed in the following.

2.12.1 CIP transport

The scaling length for CIP transport is the electron mean free path [Caml 89]. Assuming that the thicknesses of the individual layers are smaller than the mean free path, the scattering probabilities in adjacent layers simply add. Then, it can easily be seen that the resistance of the parallel configuration is governed by the lower resistance of the majority-

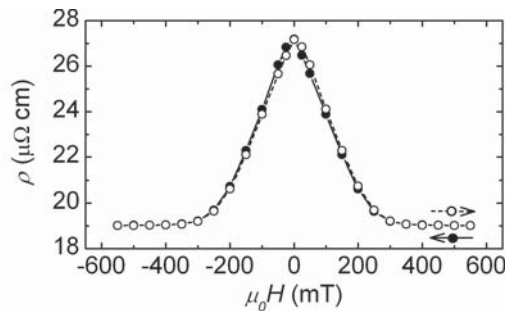


Figure 2.5: Magnetoresistivity trace measured on a Co/Cu multilayer (for details see Chapter 6). The resistivity change observed under applied fields is the giant magnetoresistance effect.

spin channel, while in the antiparallel configuration both spin channels have the same high resistance. The physical mechanism responsible for GMR is spin-dependent scattering, which however can have various microscopic origins. These can be separated into intrinsic and extrinsic origins [Tsymb 01]. Intrinsic spin-dependent scattering at the interfaces arises due to the spin-dependent band mismatch between magnetic and nonmagnetic layers. Moreover, the spin-polarized band structure of the magnetic layers generates spin-dependent bulk scattering in the layers. Extrinsic spin-dependent scattering is associated with impurities in the layers and with roughness at the interfaces.⁸

2.12.2 CPP transport

The scaling length for CPP transport is the spin-diffusion length [Vale 93]. The different microscopic origins of spin-dependent scattering of CIP transport are also present for CPP transport. The main difference are spin-accumulation effects that only appear for CPP transport [Vale 93]. If a current is imposed to flow through the interface between a ferromagnetic metal and a nonmagnetic metal, the spin-dependent chemical potentials split and become position dependent resulting in a spin-accumulation layer in the vicinity of the interface [John 87, Vale 93]. The spin accumulation decays exponentially with the distance from the interface [compare Eq. (2.37)]. The spin-diffusion length λ_{sf} depends on the spin-flip scattering rate. For Cu, $\lambda_{sf} = 44$ nm and for Co, $\lambda_{sf} = 5.8$ nm at 300 K [Sthr 06].

2.13 Size Effects

Reduction of the extension of a material in one, two or three dimensions can alter the transport properties of the material significantly. Below the micrometer-lengthscale, classical size effects are observed. At the nanometer-length scale and below, one enters the regime where quantum-confinement effects become sizeable.

2.13.1 Classical Size Effects

In nanocrystalline materials, thin films, and nanowires the mean free paths of carriers that contribute to the transport properties can become comparable to or larger than the grain sizes, the thickness of the thin film, or the diameter of the nanowire. The resulting transport properties can deviate significantly from the bulk properties. Enhanced scattering of electrons in metals for example leads to reduced electrical and thermal conductivities [Fuch 38, Maya 70, Sond 01, Stoj 10].

2.13.2 Quantum Confinement Effects

In a simple cubic crystal with lattice constant a , the Bloch wavevectors allowed are given by [Ashc 76]

$$k_x, k_y, k_z \in \left\{0, \pm \frac{2\pi}{Na}, \pm \frac{4\pi}{Na}, \dots, \pm \frac{\pi}{a}\right\}, \quad (2.41)$$

⁸In the context of spin-dependent scattering and anisotropic scattering it is helpful to consider Fermi's golden rule, which states that the scattering rate is proportional to the scattering matrix element squared times the density of final states [Gasi 02]. Spin-dependent scattering can arise from a spin-dependent density of states (intrinsic origin) and from spin-dependent scattering potentials in the matrix element (intrinsic or extrinsic origins). Anisotropic scattering can arise from anisotropic wavefunctions in the matrix element (usual explanation) and from anisotropic scattering potentials (e.g. magnons) [McGu 75].

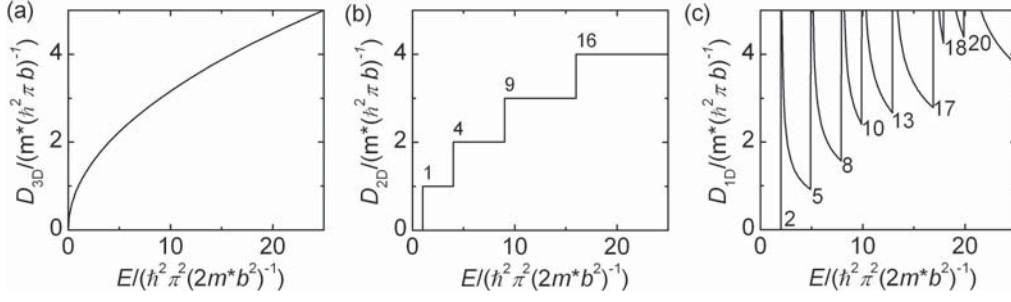


Figure 2.6: Energy dependence of the density of states of Bloch electrons in a simple cubic crystal. (a) The electrons are free to move in all three dimensions. (b) The electron gas is confined in a quantum well of width b . (c) The electron gas is confined in a quantum wire with quadratic cross-sectional area of width b .

where $Na = L_x = L_y = L_z$ is the extent of the crystal in each of the three directions of space, and $N \gg 1$ a large integer. Assume a spherical symmetric parabolic energy dispersion of the form

$$E(\mathbf{k}) = \frac{\hbar^2}{2m^*} (k_x^2 + k_y^2 + k_z^2). \quad (2.42)$$

Due to the large number of states in each of the three directions in reciprocal space, the energy separation between the quantized states is small compared to the Fermi energy, and a density of states can be defined. One finds the following density of states per energy interval [Ashc 76]:

$$D_{3D}(E) = \frac{1}{2\pi^2} \left(\frac{2m^*}{\hbar^2} \right)^{3/2} E^{1/2}. \quad (2.43)$$

Inside a quantum well, the electron gas is confined in the direction perpendicular to the plane of the well. If $b \ll Na$ is the thickness of the quantum well, Eq. (2.42) becomes

$$E(k_x, k_y, n) = \frac{\hbar^2}{2m^*} (k_x^2 + k_y^2) + n^2 \frac{\hbar^2 \pi^2}{2m^* b^2}, \quad (2.44)$$

where n indexes the subbands that arise from the confinement in the z -direction. The two-dimensional density of states is given by [Chen 05]

$$D_{2D} = \frac{m^*}{\hbar^2 \pi b} \sum_i \theta(E - E_i), \quad (2.45)$$

where θ denotes the Heaviside function, and E_i is the energy of subband i . Inside a quadratic quantum wire with cross-sectional area b^2 the electron gas is confined in two directions perpendicular to the wire axis. The energy-dispersion relation and its one-dimensional density of states are [Chen 05]

$$E(k_x, i, j) = \frac{\hbar^2}{2m^*} k_x^2 + (i^2 + j^2) \frac{\hbar^2 \pi^2}{2m^* b^2}, \quad (2.46)$$

and

$$D_{1D} = \frac{(2m^*)^{1/2}}{\hbar \pi b^2} \sum_{i,j} \frac{\theta(E - E_{i,j})}{(E - E_{i,j})^{1/2}}, \quad (2.47)$$

with the subband indices (i,j) . The energy dependence of the above densities of states is depicted in Fig. 2.6. The number of occupied subbands is large for Fermi energies $E_F \gg E_2$, where E_2 denotes the energy of the second subband. In that limit, D_{1D} and D_{2D} approach D_{3D} [Corn 11]. Quantum-confinement effects become sizeable if E_2 is comparable to or larger than E_F . This condition holds if the confinement length b is comparable to or smaller than the Fermi wavelength $\lambda_F = h/\sqrt{2m^*E_F}$. At finite temperatures quantum confinement effects can be destroyed by thermal fluctuations. Therefore, E_2 must be comparable to or larger than the thermal energy $k_B T$. This condition holds, if b is comparable to or smaller than the thermal de Broglie wavelength $\lambda_{th} = h/\sqrt{2\pi m^* k_B T}$. Scattering of electrons can destroy quantum-confinement effects. Therefore, b must be comparable to or smaller than the electron mean free path λ_{mfp} . The three conditions necessary for observing quantum-confinement effects are summarized in the following expression:

$$b < \sim \min\{\lambda_F, \lambda_{th}, \lambda_{mfp}\}. \quad (2.48)$$

3 Thermoelectric Nanowires

This chapter summarizes results on $\text{Bi}_x\text{Te}_{1-x}$ nanowires synthesized via a gold-nanoparticle assisted vapor-liquid-solid (VLS) mechanism. The synthesis of the nanowires was conducted and optimized by Bacel Hamdou during his diploma work in the group of Prof. Kornelius Nielsch [Hamd 11], and is described in Sec. 3.5. The beneficial collaboration with Bacel continued when he started his PhD work in 2012 in the same group. Structural and compositional analysis via transmission-electron microscopy was done by Dr. Eckard Pippel at the Max-Planck-Institut für Mikrostrukturphysik in Halle.

Section 3.1 introduces the microdevice used for Seebeck measurements on individual nanowires. Section 3.2 analyzes the influence of different substrates on the performance of the Seebeck microdevice. Section 3.3 briefly discusses the thermoelectric properties of $\text{Bi}_x\text{Te}_{1-x}$ in a sense that allows for motivating our research study on $\text{Bi}_x\text{Te}_{1-x}$ nanowires. Section 3.4 discusses the relevance of quantum confinement effects in the nanowires investigated and gives estimates of the Fermi wavelength and the thermal de Broglie wavelength. The chapter closes with a description of the synthesis method and a presentation of the experimental results obtained on several $\text{Bi}_x\text{Te}_{1-x}$ nanowires, which have been published in Ref. [Hamd 13] reprinted in Sec. 3.5. An extensive overview on research activities in the field of thermoelectric nanostructures and nanostructured materials is given in our review article [Niel 11] that is reprinted in Appendix A.

3.1 Seebeck Microdevice

After the growth process, Bi_2Te_3 nanowires are transferred to substrates by mechanical contact with the growth substrate. The substrate material used is either Si or glass. The Si substrates are electrically isolated by a 300-nm- SiO_2 layer. Microdevices that allow for Seebeck measurements on individual nanowires are prepared using laser lithography, sputter deposition, and lift-off processing. The native-oxide shell surrounding the nanowires is removed via Ar-sputter etching in the same sputter-chamber in which the metalization

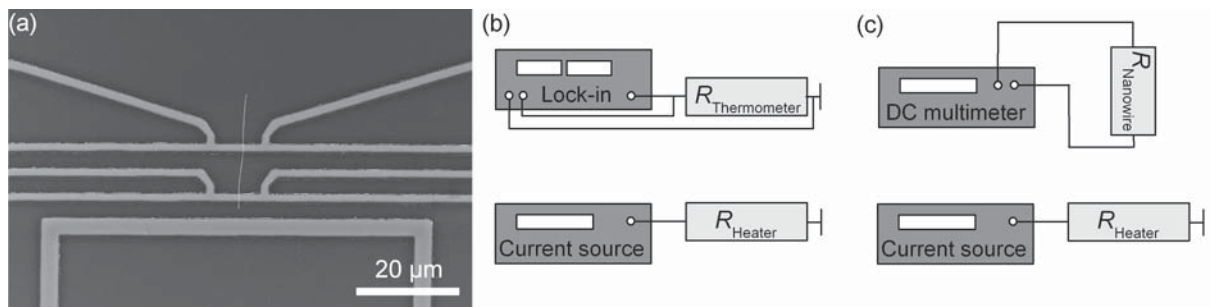


Figure 3.1: (a) Scanning electron micrograph of a typical microdevice used for Seebeck measurements on individual nanowires. (b) Experimental configuration for applying heating currents to the heater line and detecting temperature responses of one of the two thermometers. (c) Experimental configuration for applying heating currents to the heater line and detecting thermovoltages along the nanowire.

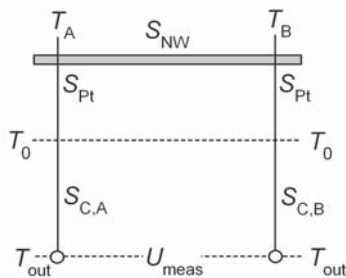


Figure 3.2: Illustration of the different contributions to the thermovoltage in a typical nanowire microdevice. S_{NW} , S_{Pt} , and S_{C} denote the Seebeck coefficients of the nanowire, the platinum leads, and the wiring, respectively; T_0 denotes the temperature of the substrate, T_{out} is the temperature of the measuring apparatus.

takes place. Preparation steps and process parameters used are summarized in Table E.7 in Appendix E. Figure 3.1(a) shows a typical microdevice used for Seebeck measurements. The device includes a heater line and two four-probe resistance thermometers attached to the nanowire. The three line-shaped structures are aligned perpendicular to the nanowire. A direct current is applied to the heater line generating a temperature gradient along the nanowire. Due to the geometry of the structures, the temperature gradient can be considered one-dimensional between the inner contacts of the thermometers. Similar devices have been used by others [Shap 07, Zuev 10]. Both thermometers are in electrical contact with the nanowire and can be used for voltage measurements. The measuring procedure is divided into four steps: (i) calibration of the two thermometers, (ii) measurement of the thermovoltage along the nanowire, (iii) measurement of the temperature response of thermometer A, (iv) measurement of the temperature response of thermometer B. During steps (ii)-(iv) the applied heating power is maintained constant, while for step (i) the heater is switched off. Steps (iii) and (iv) are measured consecutively because of the limited number of microprobes.⁹ For calibration and read-out of the thermometers we use a lock-in amplifier (Stanford Research Systems SR830). The thermovoltage along the nanowire is detected using a DC multimeter (Agilent 34401A); the heating current is supplied using a DC current source (Yokogawa GS200). The software for controlling the measurements is built using LabView. According to Eq. (2.12) the thermovoltage measured is given by (compare Fig. 3.2)

$$U_{\text{meas}} \approx (S_{\text{NW}} - S_{\text{Pt}})(T_{\text{B}} - T_{\text{A}}), \quad (3.1)$$

where S_{Pt} is the Seebeck coefficient of the Pt contacts. Due to the symmetry of the measuring device we can assume that the thermovoltages along probes and cables are canceled out ($S_{\text{C,A}} \approx S_{\text{C,B}}$). Using a resistance thermometer the temperature difference ($T_{\text{B}} - T_{\text{A}}$) can be deduced according to the linear approximation

$$T_i - T_0 = \frac{R_i(T_i) - R_i(T_0)}{\left(\frac{dR_i}{dT}\right)_{T_0}}, \quad i \in \{A, B\}, \quad (3.2)$$

⁹The micromanipulated probestation used is described in Appendix E.

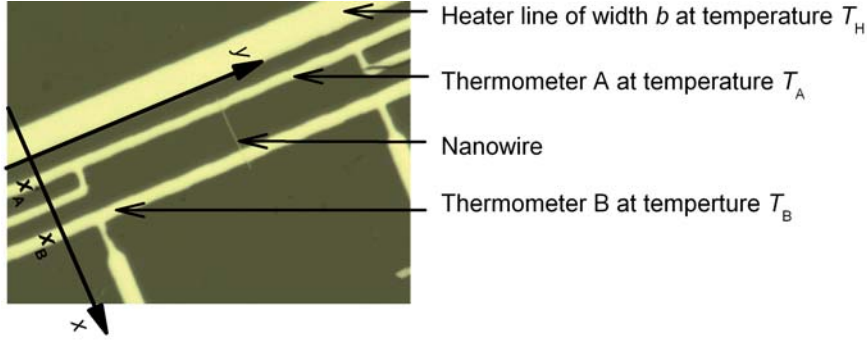


Figure 3.3: The heater line at temperature T_H generates a temperature difference $T_A - T_B$ between thermometer A and thermometer B along the nanowire.

where R_i is the resistance of thermometer i . The method employed for the determination of the Seebeck coefficient of individual nanowires has several drawbacks. Determining the temperature rise using Eq. (3.2) involves subtraction of two resistance values of similar magnitude $[R(T) - R(T_0)]$. Consequently, small errors of the resistance measurement result in large errors of the temperature rise of the thermometer. Given by the micrometer-sized length of the nanowires investigated, the outer nanowire end cannot be considered as the heat sink of the experiment (see Sec. 3.2). This means that this large error accounts twice, because the method employed involves two resistance thermometers and the temperature rise of each thermometer is of comparable magnitude.

An alternative Seebeck microdevice that uses a thermoelectric reference thin film with well known Seebeck coefficient to determine the temperature difference along the nanowire was demonstrated by Völklein *et al.* [Vlkl 09b]. An elaborate suspended microdevice that provides a heat sink at the cold side of the nanowire was fabricated by Shi *et al.* [Shi 05].

3.2 Influence of the Substrate

Creation of a well defined temperature gradient over a few micrometers is a nontrivial task. The choice of the substrate material for the Seebeck microdevice influences the attainable temperature gradient along the nanowire and its mean temperature rise significantly. We examined three different substrates: a 530- μm -Si substrate that has a 300-nm- SiO_2 layer on top, a 530- μm -glass substrate, and a 1.5- μm - Si_3N_4 membrane. The device geometry used in the following discussion is depicted in Fig. 3.3. The nanowire lies parallel to the x -axis and perpendicular to the heater line; the edge of the heater line facing to thermometer A is located at $x = 0$, thermometer A at x_A , and thermometer B at x_B ; we define the following dimensionless parameters:

$$\tau(x) \equiv \frac{T(x) - T_0}{T_H - T_0}, \quad \tau_1 \equiv \frac{T_A - T_B}{T_H - T_0}, \quad \tau_2 \equiv \frac{T_A - T_B}{T_A - T_0}, \quad (3.3)$$

where $\tau(x)$ is a measure of the temperature rise at position x , τ_1 is a measure of the temperature difference along the nanowire, and τ_2 is a measure of the mean temperature rise of the nanowire. The ideal device would require $\tau_1 = \tau_2 = 1$. For a real device, in particular for a nanowire device, we always have $\tau_1 < \tau_2 < 1$. This is because of the challenges to fabricate a nanowire device with a heat source at one side and a heat sink at the other side, both in the immediate vicinity to the nanowire.

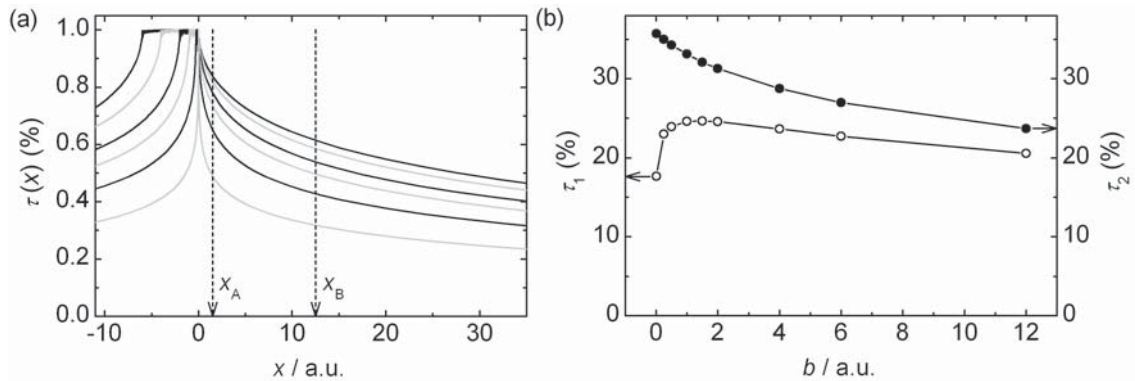


Figure 3.4: (a) Simulation of the normalized one-dimensional temperature profile $\tau(x)$ perpendicular to the heater line for different heater widths, as can be seen in the plot. For simplicity we have ignored heat conduction through the thermometers. (b) τ_1 and τ_2 for $\{x_A, x_B\} = \{1.5, 12.5\}$. The symbols are described in Fig. 3.3 and in Eq. (3.3).

3.2.1 Standard Substrates

For substrates much thicker than the length of the nanowire, the heat generated spreads in all directions below the heater line. Fig. 3.4(a) shows $\tau(x)$ simulated for different heater widths b .¹⁰ It can be seen that τ_1 and τ_2 are determined by the distances x_A between heater line and thermometer A, and by the distance $x_B - x_A$ between both thermometers, if the heating power remains constant. Figure 3.4(b) depicts τ_1 and τ_2 for $\{x_A, x_B\} = \{1.5, 12.5\}$. The units are arbitrary but can be thought as micrometers. It turns out that for each pair $\{x_A, x_B\}$ there exists an optimal heater width that maximizes τ_1 , while the curve for τ_2 monotonically decreases. The maximum τ_1 of $\sim 25\%$ is achieved for $b \approx 1.5$ (μm). This width is near the minimum linewidth for photo lithography. To obtain a homogeneous temperature profile we used heater widths between $3 \mu\text{m}$ and $5 \mu\text{m}$. Figure 3.5(a) shows the temperature rises of thermometers A and B as a function of the heating power per unit length measured on Si substrate; those for the glass substrate are depicted in Fig. 3.5(b). For homogeneous substrates τ , τ_1 , and τ_2 do not depend on materials properties. However, due to the influence of the insulating SiO_2 layer, τ_2 is larger for the Si substrate. Clearly, due to its high thermal conductivity the heating power to reach comparable absolute temperature differences $T_A - T_B$ is much larger for the Si substrate.

3.2.2 Membranes

Si_2N_3 membranes are fabricated as described in Table refATabPrepMembranes in Appendix E. For membranes much thinner than the length of the nanowire, we can consider a simple one-dimensional heat diffusion model (Fourier law):

$$q_x = -\kappa \frac{dT}{dx} \quad (3.4)$$

$$\Rightarrow \Delta T = \frac{P}{l d_m \kappa} \Delta x, \quad (3.5)$$

¹⁰The simulations were obtained using COMSOL Multiphysics, a commercially available software that is based on the finite element method. For simplicity we have ignored the influence of the thermometers on the temperature profile.

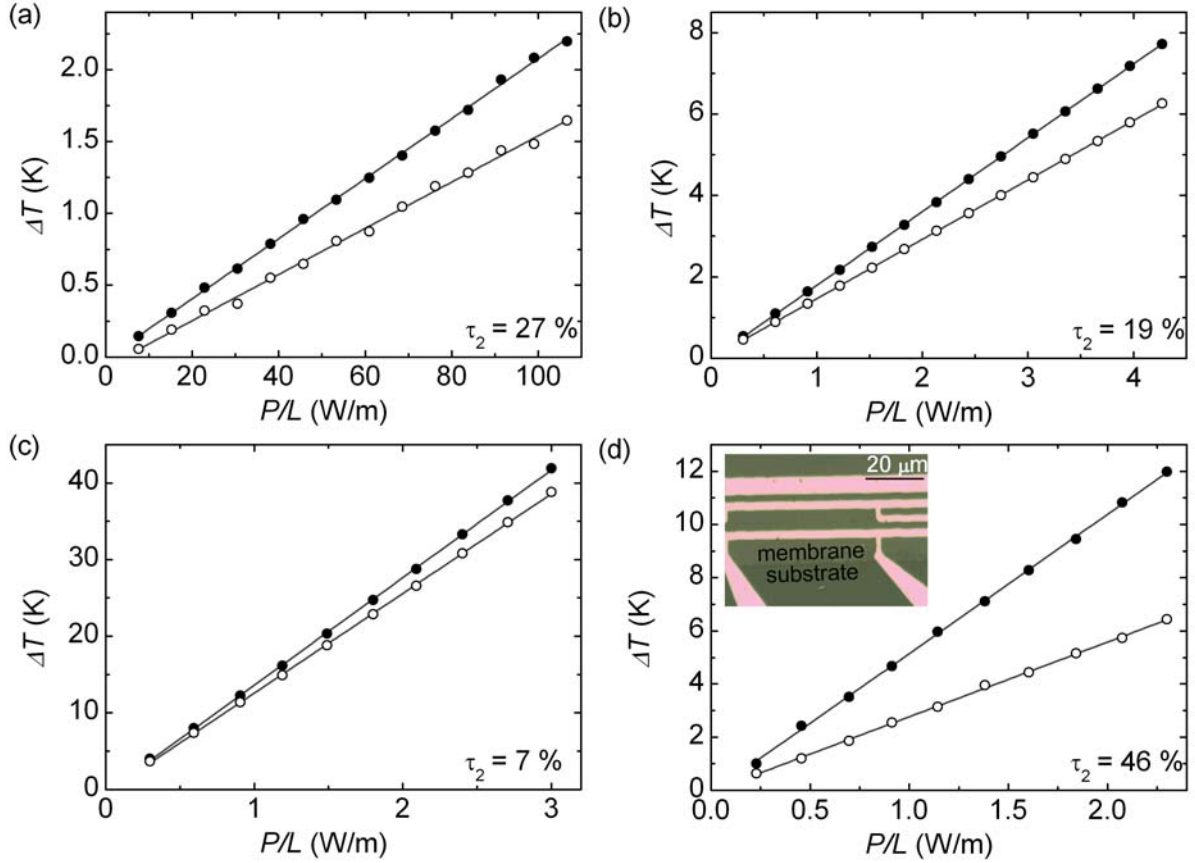


Figure 3.5: Temperature rises of thermometers A (full symbols) and B (open symbols) plotted against the heating power per unit length for the different substrates examined. (a) Si substrate with 300 nm SiO_2 on top; (b) glass substrate; (c) 1.5- μm - Si_3N_4 membrane, distance from thermometer B to the heat sink: $\sim 400 \mu\text{m}$; (d) 1.5- μm - Si_3N_4 membrane, distance from thermometer B to the heat sink: $\sim 10 \mu\text{m}$ as can be seen from the light micrography depicted in the inset.

where $q_x = \frac{P}{l d_m}$ is the heat flux along the membrane of thickness d_m , P/l is the power per unit length generated by the heater line, and κ the thermal conductivity of the membrane. In this case τ_2 is only determined by $x_B - x_A$. In reality, the membrane is suspended on a standard Si substrate that acts as a heat sink. Then, τ_2 strongly depends on the location of the nanowire on the membrane. This is demonstrated by the measurement data shown in Figs. 3.5(c) and 3.5(d). If the microdevice is located near the center of the membrane, τ_2 is very small [see Fig. 3.5(c)]. However, if the microdevice is located close to the edge of the membrane, τ_2 can reach rather high values [see Fig. 3.5(d)].

3.2.3 Conclusion

Sufficiently large temperature differences of ~ 1 K along nanowires with lengths of the order of $10 \mu\text{m}$ can be achieved for all three substrates discussed above. Using membranes can involve significant rising of the mean temperature of the nanowire during the measurements, unless the nanowire is, by coincidence, located close to the edge of the membrane and aligned perpendicular to it [see Fig. 3.5(d)]. Due to practical reasons most of the Seebeck measurements were conducted using Si- or glass-substrates.

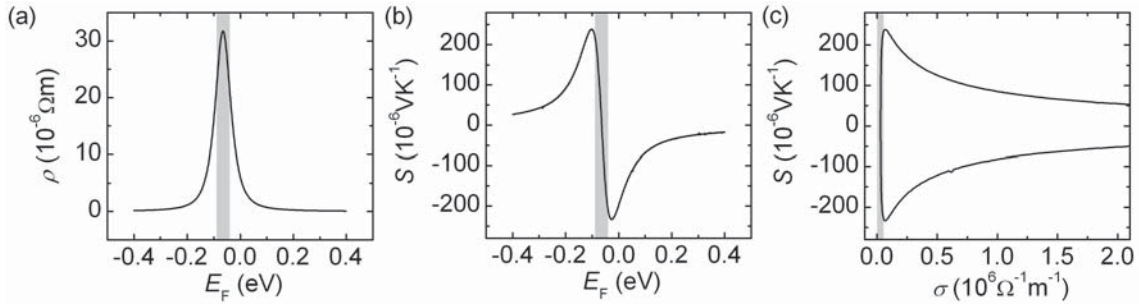


Figure 3.6: (a) Electrical resistivity ρ and (b) Seebeck coefficient S of Bi_2Te_3 plotted against the Fermi energy E_F ; (c) Seebeck coefficient as a function of the electrical conductivity $\sigma = 1/\rho$. The curves are calculated as described in the main text. The gray areas indicate the intrinsic region.

3.3 Intrinsic Bismuth Telluride

Bi_2Te_3 is among the best materials for thermoelectric applications at room temperature [Nola 01]. Figure 3.6 illustrates the electrical conductivity and the Seebeck coefficient of Bi_2Te_3 as functions of the Fermi energy. The curves are calculated using the room temperature bulk properties of Bi_2Te_3 listed in Table 3.1. Assuming bipolar conduction by electrons (e) and holes (h) in parabolic bands, the electrical conductivity σ is calculated using [Nola 01]

$$\sigma = \sigma_e + \sigma_h = n_e |e| \mu_e + n_h |e| \mu_h \quad (3.6)$$

and Eq. (2.21), with $\eta_e = E_F/(k_B T)$ and $\eta_h = -(E_F + E_g)/(k_B T)$. With this, the Seebeck coefficient S is calculated using [Nola 01]

$$S = \frac{S_e \sigma_e + S_h \sigma_h}{\sigma_e + \sigma_h} \quad (3.7)$$

and Eq. (2.23). Compared to group IV or group III-V semiconductors, the fabrication of stoichiometric Bi_2Te_3 showing intrinsic behavior at room temperature poses major challenges on the synthesis process [Satt 57, Gold 58]. This is because a wide solid solubility region (from ~ 45 at.% Te to ~ 75 at.% Te) exists yielding p -type behavior for excess Bi and n -type behavior for excess Te [Fleu 88]. It was found that the defects are essentially of the antistructure type, i.e. excess Bi atoms enter the lattice by replacement of Te atoms and vice versa [Mill 65]. The gray areas in each graph of Fig. 3.6 marks the vicinity of the center of the band gap and indicates the intrinsic region. This region corresponds to a very narrow compositional range (~ 2 at.%) somewhere close to stoichiometric Bi_2Te_3 .

3.4 What about Quantum Confinement Effects?

In Sec. 3.5, we find a mean Seebeck coefficient of $S = -122 \mu\text{V}/\text{K}$ and a mean electrical conductivity of $\sigma = 1.9 \times 10^4 \text{ 1}/(\Omega\text{m})$, which are averaged over the results from six annealed Bi_2Te_3 nanowires at room temperature. These values are clearly in the intrinsic range shown in Fig. 3.3. The mean Seebeck coefficient can be used to estimate the carrier concentrations from the bipolar model discussed in Sec. 3.3 [Mavr 09]. We obtain a Fermi level of $E_F \approx -0.053 \text{ eV}$ that corresponds to the following carrier concentrations at room temperature:

$$n_e \approx 1.35 \times 10^{18} \text{ cm}^{-3}, \quad n_h \approx 1.25 \times 10^{18} \text{ cm}^{-3}. \quad (3.8)$$

Table 3.1: Properties of Bi₂Te₃ at a temperature of 293 K. The values are taken from Ref. [Nola 01].

Property	Symbol	Value	Units
Effective electron mass	m_e	0.58	9.1×10^{-31} kg
Effective hole mass	m_h	1.07	9.1×10^{-31} kg
Electron mobility	μ_e	0.120	$\text{m}^2/(\text{Vs})$
Hole mobility	μ_h	0.051	$\text{m}^2/(\text{Vs})$
Band gap	E_g	0.13	eV

With this we can estimate the Fermi wavelength

$$\lambda_F = 2 \left(\frac{\pi}{3n_e} \right)^{1/3} \approx 18 \text{ nm}. \quad (3.9)$$

For the thermal-de Broglie wavelength we obtain

$$\lambda_{\text{th}} = h / \sqrt{2\pi m_e k_B T} \approx 6 \text{ nm}, \quad (3.10)$$

using the value for m_e listed in Table 3.1. Both wavelengths are well below the smallest confinement length present in the annealed nanowires investigated, which was ~ 50 nm. However, by using smaller gold colloids during VLS growth or by controlled sputter etching of the nanowire with Ar gas, the lateral size of the nanowires could be further reduced. Then, by performing similar measurements at liquid nitrogen or liquid helium temperatures, the investigation of quantum confinement effects in Bi₂Te₃ nanowires would become feasible.

3.5 Growth and Characterization of Bi₂Te₃ Nanowires

The challenges to achieve Bi₂Te₃ of well-defined stoichiometry and carrier concentration, in particular intrinsic Bi₂Te₃, seem to be even larger when it comes to nanowires [Zhou 05, Mavr 09]. However, intrinsic nanowires could be of interest for studying quantum confinement effects, because a low carrier concentration is associated with a large Fermi wavelength (compare Sec. 2.13.2). Moreover, in recent times it has been demonstrated that well known thermoelectric materials, including Bi₂Te₃, can exhibit a new quantum-phase of matter: the so-called topological insulating state [Moor 10]. This phase of matter is characterized by a bulk bandgap and gapless electronic surface states that are protected by time-reversal symmetry. Further explanation of this fascinating property would go beyond the scope of this thesis. Important in the context of our research study is that in order to investigate these surface states by means of transport measurements, the transport properties should not be dominated by the bulk. This could be achieved by intrinsic Bi₂Te₃ nanowires. We have grown Bi₂Te₃ nanowires that show metallic behavior at room temperature in the as-grown state. By annealing under a Te atmosphere these nanowires could be transformed to the single-crystalline Bi₂Te₃ phase. The experimental results have been published in Ref. [Hamd 13] reprinted in the following pages. The Supporting Information to this article is reprinted in Appendix C.

Thermoelectric Characterization of Bismuth Telluride Nanowires,
Synthesized Via Catalytic Growth and Post-Annealing

Reprinted with permission from

Bacel Hamdou*, Johannes Kimling*, August Dorn, Eckhard Pippel,
Raimar Rostek, Peter Woias, and Kornelius Nielsch

Advanced Materials, **25**, 239 (2013)

Copyright 2013 by the WILEY-VCH Verlag GmbH & Co. KGaA, Weinheim.

The contributions of each author to the research study are indicated in the table below using the following specifications: Conception of the research study (1), sample preparation (2), measurements (3), data analysis (4), interpretation (5), and composition of the manuscript (6).

BH*	JK*	AD	EP	RR	PW	KN
1,2,3,4,5	1,3,4,5,6	5	3,4,5	2	1	1

* Both authors contributed equally to the research study.

Thermoelectric Characterization of Bismuth Telluride Nanowires, Synthesized Via Catalytic Growth and Post-Annealing

Bacel Hamdou, Johannes Kimling,* August Dorn, Eckhard Pippel, Raimar Rostek, Peter Woias, and Kornelius Nielsch*

Bi_2Te_3 -based materials are among the most promising materials for thermoelectric applications with a figure of merit close to 1 near room temperature.^[1] Recently, it has been predicted and demonstrated that Bi_2Te_3 is a 3D topological insulator (a phase of matter that has a bulk bandgap and gapless electronic surface states that are protected by time-reversal symmetry).^[2–4] Nanostructured Bi_2Te_3 can be beneficial for both research areas. Regarding thermoelectrics, theoretical investigations predict that confinement effects in nanowires (NWs) can strongly enhance the thermoelectric powerfactor.^[5] On the other hand, the increased surface-to-volume ratio of NWs magnifies the contribution of surface states to electronic transport, which facilitates experimental access for studying topological insulating materials.^[6]

For thermoelectric applications, Bi_2Te_3 needs to be n-type or p-type with a carrier concentration on the order of 10^{19} cm^{-3} for optimal power factors.^[1] For studying topological insulator surface states, stoichiometric and therefore intrinsic Bi_2Te_3 is desirable to avoid unwanted bulk conductivity.^[2] However, small formation energies of antistructure-type defects pose an interesting materials challenge for achieving control over the structural and electronic properties of bismuth tellurides.^[7,8]

Recently, thermoelectric and structural properties have been correlated for the homologous series Bi_2Te_3 , Bi_4Te_5 , Bi_6Te_7 , Bi_8Te_9 , BiTe , Bi_4Te_3 , Bi_2Te , and Bi_7Te_3 .^[9] To our knowledge, a synthesis route to bismuth telluride nanowires of well-defined stoichiometry and crystal structure, as well as reproducible thermoelectric properties has not been established. Measurements on individual bismuth telluride NWs have only shown weak thermoelectric performances compared with bulk Bi_2Te_3 .^[10,11] The most-prominent method for synthesizing bismuth telluride

NWs is template-assisted electrodeposition.^[12–18] Solution-based chemical methods provide alternative routes to nanowires of group V–VI compounds.^[19–21] An efficient and competitive physical method for the fabrication of bismuth telluride nanowires was reported by Ham et al.^[22] The vapor-liquid-solid (VLS) method from the gaseous phase, which is a prevalent method for growing wires of a large variety of semiconducting materials (e.g., Si, Ge, and group III–IV compounds),^[23,24] has been less frequently applied to group V–VI compounds. Bi_2Se_3 , Sb_2Te_3 , and Sb_2S_3 NWs have been synthesized via physical^[25,26] and chemical^[27] vapor deposition. The growth of bismuth telluride nanorods and nanobelts by VLS has been reported by Wang et al.^[28] and by Wei et al.,^[29] however, no thermoelectric measurements have been performed. In the work of Wang et al.^[28] Bi_4Te_3 nanorods with a length on the order of $0.5 \mu\text{m}$ were grown using a molecular beam epitaxy system. Wei et al.^[29] employed thermal evaporation of Bi_2Te_3 powder inside a sealed evacuated quartz tube and obtained flat bismuth telluride nanobelts. Although they assumed that the nanobelts had the composition of Bi_2Te_3 , a compositional analysis confirming this assumption was not presented in their work. Recently, Han et al. have demonstrated that electrochemically grown Bi_2Te_3 NWs exhibit a reversible phase change from the crystalline to the amorphous phase, at a critical temperature of about $234 \text{ }^\circ\text{C}$.^[30] However, as uniaxial VLS-growth of nanowires is based on the growth of single-crystals, the absence of a crystalline phase for Bi_2Te_3 NWs, as observed by Han et al., indicates that this method is not suitable for growing Bi_2Te_3 NWs above $234 \text{ }^\circ\text{C}$. On the other hand, for NWs with bismuth contents above 40 at%, this phase change was not observed.^[30] A change in the composition from Bi_2Te_3 to Bi_4Te_3 after annealing under Ar atmosphere has been observed for electrodeposited bismuth telluride nanowires, and was attributed to the high vapor pressure of Te.^[31] For bismuth telluride thin films it has been demonstrated that Bi-rich phases can be transformed into Bi_2Te_3 by annealing in a Te atmosphere.^[32] In this work, we have performed gold-nanoparticle-assisted catalytic VLS-growth of bismuth telluride and obtained NWs with a reduced Te content below 60 at%. By post-annealing in a Te atmosphere, we were able to transform the as-grown NWs to the desired single-crystalline Bi_2Te_3 phase. The synthesis was performed in a single-heater zone tube furnace (Supporting Information, Figure S1). At the hot center of the furnace, the source material (Bi_2Te_3 powder with 99.99% purity) was thermally evaporated at $470 \text{ }^\circ\text{C}$. A constant flow of argon carrier-gas was used to transport the vapor to the substrate where the growth took place. The substrate was covered with gold

B. Hamdou, J. Kimling, Dr. A. Dorn, Prof. K. Nielsch
Institut für Angewandte Physik
Universität Hamburg
Jungiusstr. 11, 20355 Hamburg, Germany
E-mail: johannes.kimling@physik.uni-hamburg.de;
kornelius.nielsch@physik.uni-hamburg.de

Dr. E. Pippel
Max-Planck-Institut für Mikrostrukturphysik Halle
Weinberg 2, 06120 Halle, Germany
R. Rostek, Prof. P. Woias
Institut für Mikrosystemtechnik
Albert-Ludwigs-Universität Freiburg
Georges-Köhler-Allee 106, 79110 Freiburg, Germany



DOI: 10.1002/adma.201202474

nanoparticles (30 nm in diameter), which serve as catalysts for the growth of NWs. The base temperature of 470 °C decreases from the center of the furnace toward its ends. The position of the substrate should correspond to the temperature range within which VLS growth of nanowires occurs. As a reference point for determining this temperature range, the pseudobinary eutectic temperature T_e of the Au-Bi₂Te₃ system can be used, which is 475 °C.^[33] However it is known from other important VLS processes that uniaxial NW growth can proceed below T_e . For example, it has been shown for the Au-Ge system that below T_e NWs grow via VLS and vapor-solid-solid (VSS) processes.^[34] We observe nanowire growth at temperatures well below T_e . Conditions for uniaxial growth appear to be best at temperatures of about 420 °C. We note that for bulk systems, the crossing of the liquidus surface in this temperature range leads to the nucleation of crystals of the phase BiTe.^[33] We observe that the probability for uniaxial growth depends critically on the mass flow of evaporated source material and on the density of gold nanoparticles:

- *mass flow of educts*: The flow rate of evaporated source material through the tube at a given base temperature is determined by its vapor pressure, the surface area of the source material, and the flow rate of the Ar carrier-gas. For large flow rates vapor-solid (VS) growth dominates over uniaxial VLS growth. The growth of larger plates and crystallites, several micrometers in size, is observed.
- *density of gold nanoparticles*: Small distances between adjacent gold nanoparticles and agglomerations of several gold nanoparticles hinder uniaxial growth. The initially catalyzed growth at each seed particle combines to a single object.

Both parameters, the mass flow of educts and the gold-nanoparticle density, were optimized to enhance uniaxial growth of NWs. However, uniaxial growth was always accompanied by two-dimensional and three-dimensional VS-growth (Figure 1b,c). In the absence of catalyst particles we observe growth of nanoplates (Supporting Information, Figure S2). Few-layer nanoplates of Bi₂Te₃, synthesized by this method, could be of high importance for the field of topological insulating materials.^[35,36] The cross-sectional areas of most of the NWs appear polygonal (Supporting Information, Figure S3a), however, almost-cylindrical NWs are also observed (Supporting Information, Figure S3b). To gain insight into possible growth mechanisms, we compared the distribution of gold nanoparticles with the growth products in the same area after a 5 min deposition of bismuth telluride at 470 °C (Figure 1a,b). The initial locations of the gold catalyst particles shown in Figure 1a are highlighted in Figure 1b with arrows. It can be seen that the gold nanoparticles moved during the growth process. Moreover, the starting points of the NWs coincide with the initial locations of the gold nanoparticles involved in the growth process. This indicates that crystal growth was nucleated at the gold nanoparticles, which are clearly visible at the edges and corners of NWs, and proceeds via the VLS mechanism. Additionally, we observe lateral growth at the

side facets of flat NWs (Figure 1c). We conclude that the formation of flat NWs proceeds via uniaxial VLS growth in combination with lateral VS-growth. By comparing of the VLS-grown NW segment with the shorter segment which grew in the opposite direction via a VS process in Figure 1c, it follows that the uniaxial VLS-growth rate exceeds the VS-growth rate by a factor of about 6. However, we do not observe tapered NWs, as could be expected from the VS-growth process. Possible explanations could be the layered crystal structure of bismuth telluride, in combination with a high surface diffusion rate of the adsorbed atoms. After a deposition process of 1 h at a 470 °C base temperature, the NWs reach lengths of up to 15 μm. The thickness of the NWs, which we define as the smallest length perpendicular to the wire axis, ranges from 30 nm to 150 nm. The minimum thickness of 30 nm, observed using scanning force microscopy, corresponds to the diameter of the gold nanoparticles. Statistical distributions of the length scales perpendicular to the wire axis are given in Figure S4 in the Supporting Information. The as-grown NWs were post-annealed in a Te atmosphere at 250 °C for 100 h inside a sealed quartz tube. The actual crystalline state of the nanowires during annealing is unclear. According to Han et al., the nanowires should change to the amorphous state, if the Te content approaches 60 at.% at 250 °C.^[30] If this were true, the nanowires could still recrystallize while the temperature is slowly decreased after the annealing step. The chemical composition and crystal structure of both as-grown and annealed NWs were analyzed using element-specific energy-dispersive X-ray (EDX) spectroscopy inside a high-resolution transmission electron microscope (HR-TEM). The accuracy of the employed EDX spectroscopy method lies between 5% and 10%. This accuracy can in principle be improved by using high-accuracy EDX spectroscopy chemical analysis.^[17,18] For as-grown nanowires, we obtain a composition of Bi_{0.46 ± 0.05}Te_{0.54 ± 0.05}, which corresponds to a composition between the Bi₄Te₅, Bi₆Te₇, Bi₈Te₉, and BiTe phases (Figure 2a). The specified confidence interval is due to the analysis method. At the surface of the as-grown NWs, we observe a clear increase of the Bi content up to about 60 at.% (Supporting Information, Figure S5).

The selected area electron diffraction (SAED) patterns show a hexagonal lattice (Trigonal, hR15, SpaceGroup R-3m, No.166) (insets of Figure 2c,d). The NW axes are parallel to the [110] direction—perpendicular to the *c* axis. However, the SAED pattern of as-grown NWs exhibits multiple spots (inset of Figure 2c),

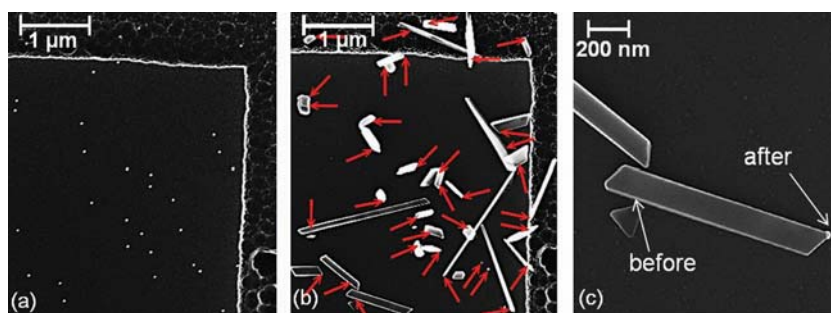


Figure 1. SEM images of: a) the distribution of gold nanoparticles (white spots) before deposition of bismuth telluride; b) the growth products after deposition of bismuth telluride for 5 min (the red arrows indicate the initial locations of the gold nanoparticles shown in (a)); and c) an enlarged part of the growth products shown at the bottom of (b).

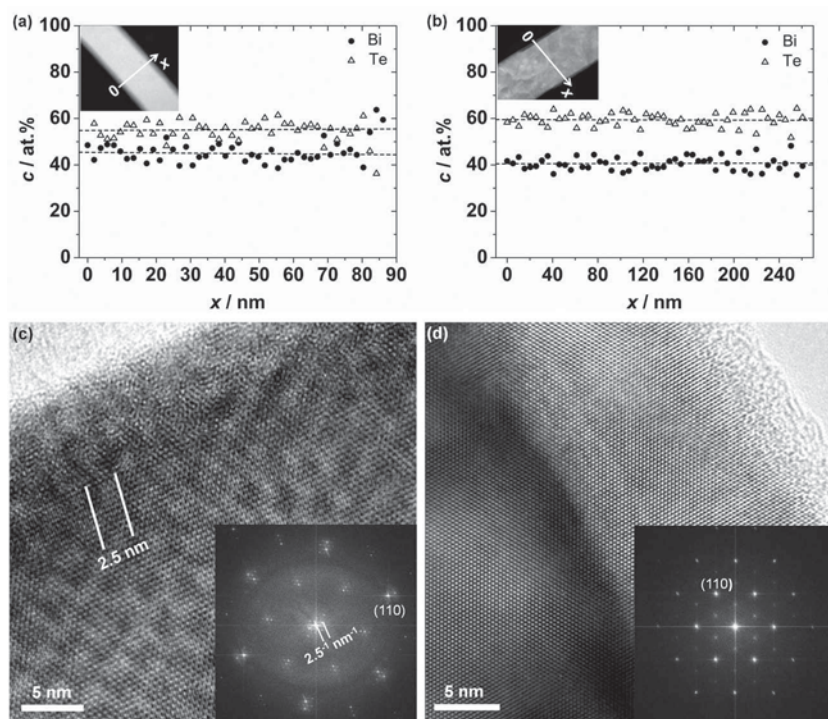


Figure 2. Representative compositional and structural results for as-grown nanowires (NWs) (a,c), and annealed NWs (b,d). The chemical compositions (a,b) were measured across the NW's cross-section, using EDX spectroscopy. The insets show high-angle annular dark-field scanning transmission electron microscopy (HAADF-STEM) images of the NWs indicating the EDX line-scans. The composition of as-grown NWs (a) clearly deviates from the Bi₂Te₃ phase, determined for annealed NWs (b). We observe Moiré patterns in the high-resolution transmission electron microscopy (HR-TEM) images of as-grown NWs (c), and multiple spots in the selected area electron diffraction (SAED) patterns (inset of (c)), which indicate a superlattice crystal structure. The HR-TEM images of the annealed NWs show a defect-free crystal structure (d), and the SAED patterns reveal single spots (inset of (d)), which indicates that the initial superlattice structure was removed during the annealing step.

Table 1. Electrical conductivity σ , Seebeck coefficient S and power factor $S^2\sigma$ of individual as-grown and annealed bismuth telluride nanowires (NWs), measured at 300 K. The data of Zhou et al. and Mavrokefalos et al. were obtained for individual cylindrical, electrochemically grown NWs. The last two rows provide bulk values for comparison.

Composition	Cross-sectional area [nm ²]	σ [$\times 10^4 \Omega^{-1} \text{ m}^{-1}$]	S [$\times 10^{-6} \text{ V K}^{-1}$]	$S^2\sigma$ [$\times 10^{-4} \text{ W m}^{-1} \text{ K}^{-1}$]	References
Bi _{0.46 ± 0.05} Te _{0.54 ± 0.05} (As-grown)	105 × 35	22.9 ± 1.8	-13.4 ± 1.6	0.4 ± 0.1	This work
	241 × 60	23.1 ± 1.3	-34.4 ± 1.4	2.7 ± 0.3	
	157 × 95	28.9 ± 1.8	-13.1 ± 1.1	0.5 ± 0.09	
	150 × 160	29.5 ± 2.1	-13.7 ± 1.03	0.6 ± 0.1	
Bi _{0.41 ± 0.03} Te _{0.59 ± 0.03} (Annealed)	108 × 47	2.10 ± 0.17	-89.1 ± 7.8	1.7 ± 0.3	This work
	120 × 48	1.68 ± 0.12	-128.7 ± 24.7	2.8 ± 1.1	
	389 × 48	2.08 ± 0.14	-140.8 ± 15.0	4.1 ± 0.9	
	96 × 60	2.05 ± 0.15	-156.9 ± 21.1	5.0 ± 1.4	
	$\pi (64/2)^2$	2.20 ± 0.69	-119.7 ± 6.4	3.2 ± 1.0	
	170 × 68	1.43 ± 0.08	-99.6 ± 5.2	1.4 ± 0.2	
Bi _{0.54} Te _{0.46}	$\pi (81/2)^2$	7	-9.4	0.06	Zhou et al. ^[10]
Bi _{0.74} Te _{0.26}	$\pi (52/2)^2$	21.5	-52	5.8	Mavrokefalos et al. ^[11]
Bi ₂ Te ₃	Bulk	6.9	-165.3	18.8	Bos et al. ^[9]
Bi ₄ Te ₅		52.4	-31.1	5.1	
Bi ₆ Te ₇		26.8	-26.1	1.8	
Bi ₈ Te ₉		26.2	-30.6	2.5	
BiTe		35.5	-28.9	3.0	
Bi ₂ Te ₃	Nearly intrinsic bulk	1.4	-	-	Nolas et al. ^[1]

which are particularly clear near the surfaces. This indicates a superlattice structure that could be related to the observed bismuth excess in that region. The superlattice structure leads to Moiré patterns in the corresponding HR-TEM images (Figure 2c). In contrast to the as-grown nanowires, the composition of annealed NWs appears uniform from the center of the NWs towards its sides with a ratio of Te to Bi atoms of 1.46 ± 0.13 , which matches the stoichiometry of Bi₂Te₃ (Figure 2b). Moreover, no Moiré patterns are observed in the HR-TEM images (Figure 2d), and the SAED patterns of the annealed NWs reveal clear spots, even of higher order (inset of Figure 2d). This indicates that the initial superlattice structure was removed during the transformation to the Bi₂Te₃ phase.

The observed differences in crystal structure and chemical composition between as-grown and annealed NWs under Te atmosphere are mirrored in their thermoelectric properties. We determined the electrical conductivity σ and the Seebeck coefficient S for several individual as-grown and annealed NWs at room temperature. From both quantities the power factor, defined as $S^2\sigma$, can be determined. The cross-sectional areas of the NWs for calculating σ were determined using a scanning electron microscope in combination with scanning force microscopy. The Seebeck coefficients were measured relative to Pt, which has a negligible Seebeck coefficient.^[37] The results are summarized in Table 1, along with the

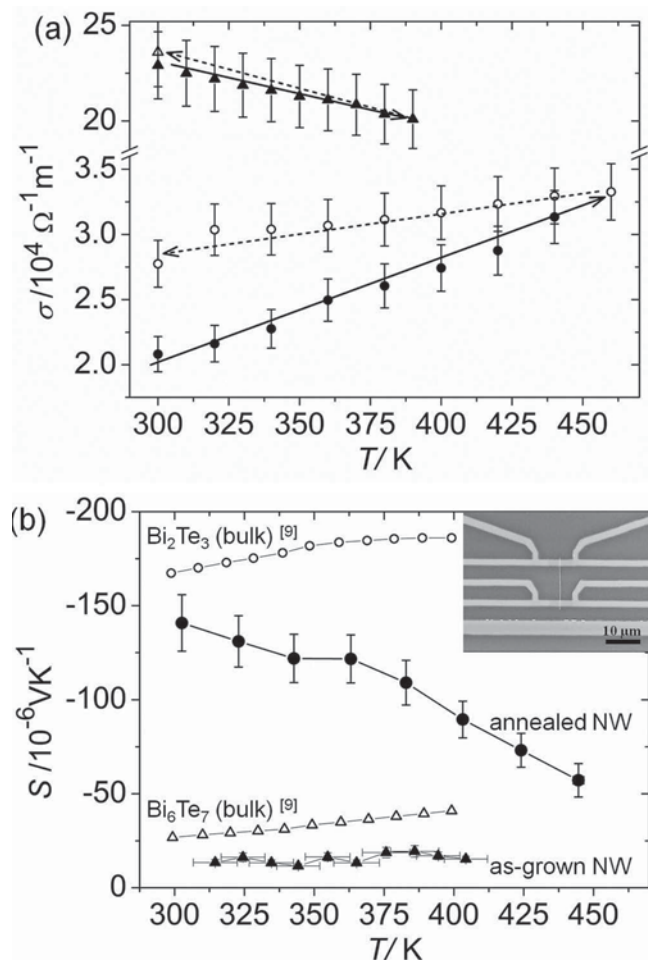


Figure 3. a) Temperature dependence of electrical conductivities, σ , of an as-grown NW (triangles) and an annealed NW (circles). The curves are irreversible during thermal cycling. The heating and cooling curves are indicated by the full and dashed arrows, respectively. The error bars are due to uncertainties in the determination of the sizes of the NWs. b) Temperature dependence of the Seebeck coefficients of an as-grown NW (filled triangles) and of an annealed NW (filled circles). The error bars are due to uncertainties in the determination of the temperature gradients. For the as-grown NW, due to the low S , a large temperature gradient was required, which increased the overall temperature of the NW, and led to large x -axis error bars. The inset shows a typical microdevice, including a heater-line and two four-point resistance thermometers, attached to a NW. For comparison, data from Bos et al., obtained for bulk Bi_2Te_3 (open circles) and for bulk Bi_6Te_7 (open triangles) are shown.^[9]

literature values for electrochemically synthesized bismuth telluride NWs,^[10,11] and bulk bismuth tellurides.^[1,9,38] For the as-grown NWs we obtain mean values of $\sigma = (26.1 \pm 3.6) \times 10^4 \Omega^{-1} \text{ m}^{-1}$ and $S = (-18.6 \pm 1.5) \times 10^{-6} \text{ V K}^{-1}$, while for the annealed NWs σ is reduced and S is enhanced to mean values of $\sigma = (1.9 \pm 0.3) \times 10^4 \Omega^{-1} \text{ m}^{-1}$ and $S = (-122.5 \pm 25.3) \times 10^{-6} \text{ V K}^{-1}$, respectively. The observed changes of σ and S between the as-grown phase and the Bi_2Te_3 phase are comparable to those between bulk bismuth tellurides with Bi-contents above 40% and bulk Bi_2Te_3 , although the bulk values of σ and S are larger (Table 1). However, the electrical conductivities measured on the annealed

NWs are close to $\sigma = 1.4 \times 10^4 \Omega^{-1} \text{ m}^{-1}$, which has been obtained from the purest bulk Bi_2Te_3 specimens.^[1,38] The enhanced values for σ and S reported for bulk specimens in work by Bos et al.^[9] could be explained by the presence of antisite defects.^[8]

The smallest geometric constriction of the investigated NWs (35 nm) lies well above 5 nm, below which quantum size effects may significantly enhance the power factor of Bi_2Te_3 .^[5] In the transition region between strong confinement and weak confinement ($\approx 5 \text{ nm}$ to $\approx 100 \text{ nm}$), calculations predict a decreasing power factor with decreasing diameter due to a decreasing number of nearly degenerate states.^[39] Within the accuracy of our measurements, we observe no diameter or thickness dependency of the power factor. The temperature dependencies of σ are depicted in Figure 3a, for representative NWs from each batch (as-grown and annealed). In non-stoichiometric Bi_2Te_3 , the charge carrier density is dominated by antisite defects with donor and acceptor states close to the conduction and valence band edges, respectively.^[8] The saturation range, in which all impurity states are activated, and in which intrinsic excitation of carriers is not yet significant, lies between about 100 K and about 300 K.^[38,40] In this range, the electrical conductivity of bulk Bi_2Te_3 decreases with increasing temperature due to thermal scattering. With increasing defect density the saturation range is extended to higher temperatures. Likewise we observe monotonically decreasing electrical conductivities of as-grown NWs (Figure 3a). In contrast, the electrical conductivities of annealed NWs, when starting at room temperature, monotonically increase with temperature. This is consistent with the low electrical conductivity, and indicates small concentrations of antisite defects. However, as shown in Figure 3a, the electrical conductivity shows irreversible changes during thermal cycling: the cooling curve of the annealed NW shows still decreasing conductivities with decreasing temperatures, but the values lie above the previously recorded heating curve. A possible explanation could be diffusion into or from the contact leads at elevated temperatures, leading to extrinsic conduction, which superimposes the activation process of intrinsic conduction.

The respective temperature dependencies of the Seebeck coefficients are depicted in Figure 3b. The absolute Seebeck coefficient of as-grown NWs slightly increases, while the absolute Seebeck coefficient of annealed NWs monotonically decreases over the temperature range of the measurement due to an increasing bipolar contribution from both charge carrier types, thermally excited electrons and holes.

This work demonstrates the possibility of achieving nearly intrinsic single-crystalline Bi_2Te_3 NWs via VLS-growth and post-annealing in a Te atmosphere. The near intrinsic electrical conductivity makes the Bi_2Te_3 NWs promising candidates for investigating topological insulating effects. Regarding thermoelectricity, the Bi_2Te_3 NWs could be used as a well-defined starting system for enhancing the thermoelectric performance, for example, by nanoscale doping,^[41] or by reduction of the cross-section area.^[5]

Experimental Section

Substrate Preparation: Si substrates with native oxide layers were treated in a piranha solution (H_2SO_4 :30% $\text{H}_2\text{O}_2 = 3:1$) at 90 °C for

15 min. Subsequently, the substrates were rinsed with isopropyl alcohol and deionized water, and dried using a nitrogen jet. The cleaned substrates were immersed in 0.1 wt% aqueous poly(L-lysine) solution (Ted Pella) for 60 s, and subsequently rinsed with deionized water. Finally the substrates were immersed in a solution containing gold nanoparticles (Ted Pella, diameter: 30nm) for 4 s. The negatively charged gold nanoparticles were spread evenly across the substrate surface due to attraction by the positive surface charges of the polymer film. The particle density was optimized to a value of about 0.5 μm^{-2} . After final rinsing with deionized water and drying with a nitrogen jet, the ready-prepared growth substrates were immediately mounted to the tube furnace for catalytic nanostructure growth.

Synthesis of Bi₂Te₃ Nanostructures: Bi₂Te₃ NWs were synthesized via physical vapor transport and gold-nanoparticle-assisted catalytic growth in a single heater zone tube furnace (MTI Inc. USA/OTF-1200X-25). The quartz tube of the furnace had a diameter of 25 mm and a length of 1 m. At the center of the tube furnace, 4 mg of Bi₂Te₃ powder was located for thermal evaporation. The growth substrate (Si with a native oxide layer, size: 30 mm x 10 mm x 530 μm , evenly covered with gold nanoparticles) was located at a distance of 20 cm to 23 cm from the center of the tube at the downstream zone of the furnace. Due to the inhomogeneous temperature profile across the tube furnace, the substrate temperature ranges from about 432 °C to about 355 °C. The charged furnace was evacuated to below 10 Torr and flushed several times with Ar gas to obtain an inert atmosphere. Then the Ar flow was adjusted to 30 sccm while the pressure was maintained at 10 Torr, and the base temperature was raised to 470 °C at a heating rate of 18 °C min⁻¹. After 1 h at 470 °C, the heating power was switched off. Under constant Ar flow and pressure, the furnace was returned to room temperature by natural cooling.

Annealing of the Growth Products: As-grown nanowires were annealed in Te atmosphere at 250 °C for 100 h. The annealing process was performed in a sealed evacuated quartz tube inside a tube furnace. More details about the annealing process can be found in work by Rostek et al.^[32]

Structural and Compositional Characterization: The distribution of gold nanoparticles on the growth substrate, and the morphology of growth products were analyzed using a scanning electron microscope (Zeiss, Sigma Gemini). Additionally, the thicknesses of the NWs were determined by scanning force microscopy. Information about the chemical composition and the crystal structure, as well as a closer look at the morphology of NWs were obtained inside a transmission electron microscope (Titan 80-300). For quantifying the EDX spectra, we used the Bi-L (10.837 keV) and the Te-L (3.769 keV) X-ray peaks. We used the Cliff-Lorimer *k*-factors of 6.327 (Bi-L) and 3.311 (Te-L), which were calibrated by the manufacturer of the device.

Thermoelectric Measurements: Metal electrodes for current injection and voltage detection across our NWs were fabricated using a laser-lithography system (Heidelberg Instruments, $\mu\text{pg}101$) with a minimum line-width of 1 μm . In situ sputter-etching with Ar was used to remove any surface oxide on the NWs directly before sputter-deposition of Ti (4nm) and Pt (50 nm). This was followed by a lift-off process. In Figure S6a in the Supporting Information and in the inset of Figure 3b, a typical microdevice for measuring the electrical resistance and the Seebeck coefficient is depicted. The microdevice comprised two four-point resistance thermometers, which also served as voltage probes, and a heater line to generate a temperature gradient across the specimen of the order of 1 K. The microdevices were fabricated on Si substrates, insulated with 300 nm thermally grown SiO₂, as well as on glass substrates. Due to the smaller thermal conductivity of the latter, less heating power was required to reach the same temperature gradient, which was obtained using a Si/SiO₂ substrate. As shown in Figure S7 in the Supporting Information, the temperature at the thermometers (a), as well as the generated thermovoltage across the specimen (b), were proportional to the applied heating power. The determined electrical resistances included the contact resistances between metal electrode and NW. By comparison with four-probe measurements (Supporting Information, Figure S6b), we found that contact resistances were negligible (below 1% of the total resistances).

Supporting Information

Supporting Information is available from the Wiley Online Library or from the author.

Acknowledgements

B.H. and J.K. contributed equally to this work. This work was supported by the German science foundation (DFG) within the German priority program SPP 1386, "Nanostructured Thermoelectrics". We thank C. Schumacher, S. Bäßler, R. Meißner, and L. Akinsinde for technical support.

Received: June 18, 2012

Revised: September 6, 2012

Published online: November 2, 2012

- [1] G. S. Nolas, J. Sharp, H. J. Goldsmid, in *Thermoelectrics* (Eds: A. Zunger, R. M. Osgood Jr., R. Hull, H. Sakaki), Springer-Verlag, Berlin Heidelberg, Germany **2001**, Ch. 5.
- [2] H. Zhang, C.-X. Liu, X.-L. Qi, Z. Fang, S.-C. Zhang, *Nat. Phys.* **2009**, *5*, 438.
- [3] Y. L. Chen, J. G. Analytis, J.-H. Chu, Z. K. Liu, S.-K. Mo, X. L. Qi, H. J. Zhang, D. H. Lu, X. Dai, Z. Fang, S. C. Zhang, I. R. Fisher, Z. Hussain, Z.-X. Shen, *Science* **2009**, *325*, 178.
- [4] M. Z. Hasan, C. L. Kane, *Rev. Mod. Phys.* **2010**, *82*, 3045.
- [5] L. D. Higgs, M. S. Dresselhaus, *Phys. Rev. B* **1993**, *47*, 16631.
- [6] H. Peng, K. Lai, D. Kong, S. Meister, Y. Chen, X.-L. Qi, S.-C. Zhang, Z.-X. Shen, Y. Cui, *Nat. Mater.* **2009**, *9*, 225.
- [7] D. M. Rowe, *CRC Handbook of Thermoelectrics*, CRC Press, Boca RatonFL, USA **1995**, Ch. 19.
- [8] G. R. Miller, C.-Y. Li, *J. Phys. Chem. Solids* **1964**, *26*, 173.
- [9] J. W. G. Bos, H. W. Zandbergen, M.-H. Lee, N. P. Ong, R. J. Cava, *Phys. Rev. B* **2007**, *75*, 195203.
- [10] J. Zhou, C. Jin, J. H. Seol, X. Li, L. Shi, *Appl. Phys. Lett.* **2005**, *87*, 133109.
- [11] A. Mavrokefalos, A. L. Moore, M. T. Pettes, L. Shi, W. Wang, X. Li, *J. Appl. Phys.* **2009**, *105*, 104318.
- [12] S. A. Sapp, B. B. Lakshmi, Charles R. Martin, *Adv. Mater.* **1999**, *11*, 402.
- [13] M. S. Sander, A. L. Prieto, R. Gronsky, T. Sands, A. M. Stacy, *Adv. Mater.* **2002**, *14*, 665.
- [14] J. Lee, S. Farhangfar, J. Lee, L. Cagnon, R. Scholz, U. Gösele, K. Nielsch, *Nanotechnology* **2008**, *19*, 365701.
- [15] R. Mannam, M. Agarwal, A. Roy, V. Singh, K. Varahramyan, D. Davis, *J. Electrochem. Soc.* **2009**, *156*, B871.
- [16] O. Picht, S. Müller, I. Alber, M. Rauber, J. Lensch-Falk, D. L. Medlin, R. Neumann, M. E. Toimil-Molares, *J. Phys. Chem. C* **2012**, *116*, 5367.
- [17] N. Peranio, E. Leister, W. Töllner, O. Eibl, K. Nielsch, *Adv. Funct. Mater.* **2012**, *22*, 151.
- [18] C. Frantz, N. Stein, Y. Zhang, E. Bouzy, O. Picht, M. E. Toimil-Molares, C. Boulanger, *Electrochim. Acta* **2012**, *69*, 30.
- [19] S. H. Kim, B. K. Park, *Mater. Lett.* **2010**, *64*, 938.
- [20] A. Purkayastha, Q. Yan, M. S. Raghuvver, D. D. Gandhi, H. Li, Z. W. Liu, R. V. Ramanujan, T. Borca-Tasciuc, G. Ramanath, *Adv. Mater.* **2008**, *20*, 2679.
- [21] R. J. Mehta, C. Karthik, W. Jiang, B. Singh, Y. Shi, R. W. Siegel, T. Borca-Tasciuc, G. Ramanath, *Nano Lett.* **2010**, *10*, 4417.
- [22] J. Ham, W. Shim, D. H. Kim, S. Lee, J. Roh, S. W. Sohn, K. H. Oh, P. W. Voorhees, and W. Lee, *Nano Lett.* **2009**, *9*, 2867.

- [23] R. S. Wagner, W. C. Ellis, *Appl. Phys. Lett.* **1964**, *4*, 89.
- [24] H. J. Fan, P. Werner, M. Zacharias, *Small* **2006**, *2*, 700.
- [25] J. S. Lee, S. Brittman, D. Yu, H. Park, *J. Am. Chem. Soc.* **2008**, *130*, 6252.
- [26] D. Kong, J. C. Randel, H. Peng, J. J. Cha, S. Meister, K. Lai, Y. Chen, Z.-X. Shen, H. C. Manoharan, Y. Cui, *Nano Lett.* **2010**, *10*, 329.
- [27] R. B. Yang, J. Bachmann, E. Pippel, A. Berger, J. Woltersdorf, U. Gösele, K. Nielsch, *Adv. Mater.* **2009**, *21*, 1.
- [28] G. Wang, S. K. Lok, G. K. L. Wong, I. K. Soua, *Appl. Phys. Lett.* **2009**, *95*, 263102.
- [29] Q. Wei, Y. Su, C. J. Yang, Z. G. Liu, H. N. Xu, Y. D. Xia, J. Yin, *J. Mater. Sci.* **2011**, *46*, 2267.
- [30] N. Han, S. I. Kim, J.-D. Yang, K. Lee, H. Sohn, H.-M. So, C. W. Ahn, K.-H. Yoo, *Adv. Mat.* **2011**, *23*, 1871.
- [31] J. Lee, A. Berger, L. Cagnon, U. Gösele, K. Nielsch, J. Lee, *Phys. Chem. Chem. Phys.* **2010**, *12*, 15247.
- [32] R. Rostek, V. Sklyarenko, P. Woias, *J. Mater. Res.* **2011**, *26*, 1785.
- [33] A. Prince, G. V. Raynor, D. S. Evans, *Phase Diagrams of Ternary Gold Alloy*, Institute of Metals, London **1990**, 172–178.
- [34] S. Kodambaka, J. Tersoff, M. C. Reuter, F. M. Ross, *Science* **2007**, *316*, 729.
- [35] D. Kong, W. Dang, J. J. Cha, H. Li, S. Meister, H. Peng, Z. Liu, Y. Cui, *Nano Lett.* **2010**, *10*, 2245.
- [36] R. J. Mehta, Y. Zhang, C. Karthik, B. Singh, R. Siegel, T. Borca-Tasciuc, G. Ramanath, *Nat. Mater.* **2012**, *11*, 233.
- [37] J. P. Moore, R. S. Graves, *J. Appl. Phys.* **1973**, *44*, 1174.
- [38] H. J. Goldsmid, *Proc. Phys. Soc.* **1958**, *71*, 633.
- [39] J. E. Cornett, O. Rabin, *Appl. Phys. Lett.* **2011**, *98*, 182104.
- [40] J. P. Fleurial, L. Galliard, R. Triboulet, H. Scherrer, S. Scherrer, *J. Phys. Chem. Solids* **1988**, *49*, 1237.
- [41] J. C. Ho, R. Yerushalmi, Z. A. Jacobson, Z. Fan, R. L. Alley, A. Javey, *Nat. Mater.* **2008**, *7*, 62.

4 3ω Method

While it is straightforward to perform electrical transport measurements, the situation is more challenging as concerns thermal transport measurements. This is because thermal insulation is usually worse than electrical insulation. Heat leakage through the substrate and by thermal radiation can pose big challenges when investigating thin films and nanowires. This chapter deals with the 3ω Method - a prevalent measuring technique for determining thermal properties of bulk materials [Cahi 90], thin films [Cahi 94], and nanowires [Lu 01, Ou 08]. An advantage of this method over the standard longitudinal steady-state method [Nola 01] is that errors due to thermal radiation are negligible, even at high temperatures of to order of 1000 K [Cahi 90]. Furthermore, due to its dynamic nature the 3ω method is fast compared to the times usually needed to reach thermal equilibrium in a static method. Concerning 3ω measurements on thin films, heat leakage through the substrate is not an issue, because the thermal wave is intended to penetrate into the substrate. Concerning nanowires, a microdevice for performing 3ω measurements is feasible within a rather small microfabrication effort.

Section 4.1 introduces the general concept of the 3ω method. Sections 4.2, 4.3, and 4.4 discuss common theoretical models for 3ω measurements on bulk materials, on thin films, and on wires, respectively. Section 4.5 gives estimates of the characteristic length- and time-scales of the different 3ω measurements and compares them with values of alternative measuring techniques. Section 4.6 discusses the significance of heat loss due to thermal radiation for 3ω measurements. The chapter closes with a detailed revision of the 3ω method in the context of voltage-driven setups, which has been published in Ref. [Kiml 11] reprinted in Sec. 4.7.

4.1 Concept of the 3ω Method

The following discussion is based on the general framework for 1ω , 2ω , and 3ω methods given by Dames and Chen [Dame 05]. The 3ω method can be applied to systems containing a single electrical heater that is simultaneously used as a temperature sensor through changes in its resistance. An alternating current

$$I = I_0 \sin(\omega_0 t), \quad (4.1)$$

which oscillates at angular frequency ω_0 is applied to a heater with resistance R_0 . To determine the temperature oscillations of the heater, it is assumed that R_0 is constant. In this approximation, the generated heating power oscillates at frequency 2ω :

$$P(t) \approx \frac{R_0 I_0^2}{2} (1 - \cos(2\omega_0 t)). \quad (4.2)$$

The resulting temperature oscillation can be related to the heating power using a thermal transfer function or thermal impedance $Z(\omega)$:

$$\Delta T(t) = P(t) \otimes \mathcal{F}^{-1}[Z(\omega)], \quad (4.3)$$

where \otimes denotes convolution and $F^{-1}[Z(\omega)]$ is the inverse Fourier transformation of $Z(\omega)$. In general, $Z(\omega)$ is a complex function that determines the thermal properties of the system. Inserting Eq. (4.2) into Eq. (4.3) and using a convolution theorem gives

$$\Delta T(t) \approx \frac{R_0 I_0^2}{2} (Z(0) - \operatorname{Re}[Z(2\omega_0)] \cos(2\omega_0 t) + \operatorname{Im}[Z(2\omega_0)] \sin(2\omega_0 t)). \quad (4.4)$$

The sinusoidal current leads to a stationary temperature rise of the heater (first term) that is superimposed by temperature oscillations at frequency $2\omega_0$. The real (imaginary) part of Z determines the in-phase (out-of-phase) temperature oscillations. In Eq. (4.2) we assumed that changes in the resistance of the heater are small compared to the total resistance: $\frac{\Delta R(t)}{R_0} \ll 1$. This approximation enabled us to obtain the temperature response of the system. Now, the changes in the resistance of the heater shall be used to determine $Z(\omega)$. This sounds contradictory, but it is a good approximation as long as $\frac{\Delta R(t)}{R_0} \ll 1$ holds. Assuming a constant temperature derivative in the temperature interval ΔT , the resistance of the heater is given by

$$R(t) = R_0 + \frac{dR}{dT} \Delta T. \quad (4.5)$$

The resistance of the heater determines the measuring voltage $U(t)$. Multiplying Eq. (4.1) with Eq. (4.5) using Eq. (4.4) one obtains

$$\begin{aligned} U(t) = & R_0 I_0 \sin(\omega_0 t) + R_0 \frac{dR}{dT} I_0^3 \left[\left(\frac{Z(0)}{2} + \frac{\operatorname{Re}[Z(2\omega_0)]}{4} \right) \sin(\omega_0 t) + \frac{\operatorname{Im}[Z(2\omega_0)]}{4} \cos(\omega_0 t) \right] \\ & - R_0 \frac{dR}{dT} I_0^3 \left[\frac{\operatorname{Re}[Z(2\omega_0)]}{4} \sin(3\omega_0 t) + \frac{\operatorname{Im}[Z(2\omega_0)]}{4} \cos(3\omega_0 t) \right]. \end{aligned} \quad (4.6)$$

According to this equation $Z(\omega)$ can be determined either from the first harmonic component, or from the third harmonic component of the measuring voltage. The latter choice corresponds to the 3ω method. The 1ω method is similar to the Völklein method [Vlkl 84, Vlkl 90, Vlkl 09a], which uses a DC source. If a sinusoidal current is applied in combination with a DC offset, the measuring voltage contains an additional 2ω component [Dame 05]. Using the 1ω method, small changes [the terms in the first square parenthesis in Eq. (4.6)] of a large measuring signal (dominated by the first term in Eq. (4.6)) have to be detected. Hence, large errors can be introduced if $Z(\omega)$ is determined from 1ω measurements.

4.2 Bulk Model

In the following we focus on the oscillations of the heating power and ignore the constant term in Eq. (4.2), which is irrelevant for the 3ω voltage in Eq. (4.6). The exact solution of the temperature oscillations at distance r from a periodically heated line located on a semi-infinite substrate was derived by Carslaw and Jaeger [Cars 59]:

$$\Delta T(r,t) = -\frac{P}{\pi \kappa_s l} K_0(qr) \exp(i2\omega_0 t), \quad q = \left(\frac{i2\omega_0}{D} \right)^{1/2}, \quad (4.7)$$

where $-\frac{P}{l} \exp(i2\omega_0 t)$ is the complex heating power per unit length, κ_s and D are thermal conductivity and thermal diffusivity of the infinite half-volume below the heater, and

$K_0(qr)$ is the zeroth-order modified Bessel function. The magnitude of $K_0(qr)$ rapidly decays for $qr > 1$, with $|1/q|$ being the characteristic length of the thermal diffusion process. The physical temperature oscillations are given by the real part of Eq. (4.7):

$$\text{Re}[\Delta T] = -\frac{P}{\pi\kappa_s l}(-\text{Re}[K_0] \cos(2\omega_0 t) + \text{Im}[K_0] \sin(2\omega_0 t)). \quad (4.8)$$

Comparison with Eq. (4.4) yields the thermal transfer function of a line heater on a semi-infinite substrate:

$$Z(\omega) = \frac{K_0(qr)}{\pi\kappa_s l}, \quad q = \left(\frac{i\omega}{D}\right)^{1/2}. \quad (4.9)$$

Using Eq. (4.7) Cahill calculated the mean¹¹ temperature oscillations at a heater line of finite width $2b$ [Cahi 90]. In this case, Eq. (4.9) becomes

$$Z(\omega) = \frac{1}{\pi\kappa_s l} \int_0^\infty \frac{\sin^2 kb}{(kb)^2 \sqrt{k^2 + q^2}} dk, \quad (4.10)$$

For real substrates the assumption of semi-infinite thickness is valid for $d_s \gg |1/q|$, where d_s is the thickness of the substrate. In the limit $d_s \gg |1/q| \gg b$ Eq. (4.10) can be approximated by [Cahi 90]

$$Z(\omega)_{\text{bulk}} \approx \frac{1}{\pi\kappa_s l} \left(-\frac{1}{2} \ln \omega - \frac{1}{2} \ln \frac{ib^2}{D} + \eta \right), \quad (4.11)$$

where $\eta \approx 0.923$ can be obtained by numerical integration in Eq. (4.10). It is convenient to perform a frequency dependent 3ω measurement. Then, κ_s can be determined from the change of the in-phase 3ω signal with $\ln \omega$. The approximations of the above model were discussed in detail by Raudzis [Raud 07].

Beside the standard longitudinal steady-state method and the 3ω method, also the laser-flash method [Nola 01] is frequently used for determining the thermal conductivity of bulk materials.

4.3 Thin-Film Model

The breakthrough of the 3ω method came along with its application to dielectric thin films in 1994 [Cahi 94]. The thin film with thickness d_f and thermal conductivity κ_f is located between heater line and substrate (compare Fig. 6.1), and considered to act as a thermal resistance increasing the temperature oscillations of the heater line. For $b \gg d_f$ and $\kappa_s > \kappa_f$ heat flow through the thin film can be considered one-dimensional. In this case, the following real offset adds to the thermal transfer function of the substrate due to the thin film [Cahi 94]:

$$\Delta Z_{\text{film}} = \frac{d_f}{2b\kappa_f l}. \quad (4.12)$$

For the experimental determination of ΔZ a reference 3ω measurement is performed on a heater line without a thin film underneath. The investigation of conductive thin films requires an additional dielectric layer for electrical insulation. The temperature offset due to the dielectric layer is canceled out after subtraction of the reference measurement. To

¹¹Averaged across the width of the heater line.

obtain reliable results, the temperature offset caused by the thin film investigated should be comparable to the temperature rise caused by the bare substrate. Furthermore, in the case of conducting thin films, the temperature offset caused by the electrically isolating layer should not overwhelm the one of the thin film investigated. These conditions restrict the minimum thickness of the thin film. The thermal conductivity of SiO₂ thin films ($\kappa_{300\text{ K}} \approx 1\text{W/mK}$) on Si substrates has been determined down to a thickness of 20 nm.[Cahi 94]

More general heat-diffusion models have been developed that consider two-dimensional and three-dimensional heat flow in multilayers including anisotropic conductivities, boundary resistances, and thermal properties of the heater line [Borc 01, Jacq 02, Batt 07]. The following multilayer model was derived by Borca-Tasciuc et al. [Borc 01]:

$$Z_{\text{film}}(\omega) = -\frac{1}{\pi\kappa_{z1}l} \int_0^\infty \frac{1}{A_1B_1} \frac{\sin^2(b\lambda)}{b^2\lambda^2} d\lambda, \quad (4.13)$$

where

$$A_n = -1, \quad A_{i-1} = \frac{A_i \frac{\kappa_{zi}B_i}{\kappa_{z(i-1)}B_{i-1}} - \tanh(\phi_{i-1})}{1 - A_i \frac{\kappa_{zi}B_i}{\kappa_{z(i-1)}B_{i-1}} \tanh(\phi_{i-1})}, \quad (4.14)$$

$$B_i = \sqrt{\frac{\kappa_{xi}}{\kappa_{zi}}\lambda^2 + \frac{i\omega}{D_{zi}}}, \quad \phi_i = B_i d_i, \quad i \in \{2, \dots, n\}. \quad (4.15)$$

In the above expressions, i indexes the layer number starting from the top, n is the total number of layers, κ_z and κ_x are cross-plane and in-plane thermal conductivities, and ω is the angular frequency of the heating current. Equation (4.14) assumes a semi-infinite substrate. Expressions for isothermal or adiabatic boundary conditions are given in Ref. [Borc 01]. A convenient fit algorithm for the above expressions was presented by Olson et al. [Olso 05], including an approximation for the influence of the thermal mass of the heater line. We have used this fit algorithm for the determination of the thermal conductivity of Co/Cu multilayers (see Sec. 6). The Matlab programs for data reduction can be found in Appendix E.

Apart from the slope method for bulk materials [Eq. (4.11)], the other models critically depend on the width $2b$ of the heater line. For example the finite thermal conductivity of a real heater line changes the temperature profile across the heater width. [Raud 07] This problem is enhanced by imperfections of the heater line, such as an inhomogeneous thickness profile and edge roughness. Consequently an effective heater width is required which represents an additional fit parameter. However, this is problematic because a change of the heater width results in a constant shift of the temperature oscillations - similar to the effect of the thin film. Only at high frequencies ($f > \sim 10\text{ kHz}$) this shift may become frequency dependent. Therefore, Lee and Cahill introduced the empirical value $\tilde{\eta} = 1.05$ for η in Eq. (4.11) instead of using an effective heater width [Lee 97]. However, this empirical value cannot be used as an universal constant for every 3ω measurement. The correct value may depend on the material combinations and on the sample geometry. Nanometer-scale depth resolution of the thermal conductivity of electrically conducting thin films, which cannot be achieved by the 3ω method, is provided by the time-domain thermoreflectance method [Koh 09].

4.4 Wire Model

In contrast to the bulk and thin film models, the specimen in the wire model serves itself as heater and thermometer of the experiment. An example of a typical sample geometry is depicted in Fig. 5.1. Heat is generated in the suspended part of the wire between the inner contacts, while the rest of the wire, as well as the contacts and the substrate are considered as heat sinks. A solution of the heat-diffusion equation of this problem was given by Lu et al. [Lu 01]. A solution of the same form but with slightly different coefficients was derived by Dames and Chen [Dame 05]. The mean temperature oscillation, averaged across the length of the suspended wire segment, is given by the following expression [Lu 01, Dame 05]:

$$Z_{\text{wire}}(\omega) = \frac{(1 - i\omega\tau/10)}{12\kappa_{\text{w}}A/l(1 + (\omega\tau/10)^2)}, \quad (4.16)$$

where κ_{w} , D , A and l are thermal conductivity, thermal diffusivity, cross-sectional area, and length of the suspended wire segment; $\tau = l^2/D$ is the characteristic time of the heat diffusion process. The measurements are performed at current frequencies of the order of 100 Hz. For nanowires the length of the suspended wire segment is typically a few μm , hence $\omega\tau \ll 1$. In this limit, the imaginary part of Eq. (4.16) vanishes, i.e. the temperature oscillates in-phase with the heating power:

$$Z_{\text{wire}} = \frac{l}{12\kappa_{\text{wire}}A}. \quad (4.17)$$

Alternative methods that are not restricted to electrically conducting nanowires have been achieved by using micrometer-sized measuring platforms that allow for applying the longitudinal steady-state method to nanowires [Shi 03], as well as via scanning thermal microscopy using microfabricated thermocouples [Shi 00]. The latter method can provide spacial resolution of the temperature distribution of the sample surface.

4.5 Characteristic Length- and Time-scales

The characteristic length of a diffusion process during the time t is of the order of $l_{\text{diff}} \propto \sqrt{Dt}$; its characteristic time over the length L is of the order of $\tau_{\text{diff}} \propto L^2/D$ [Pros 11]. The thermal diffusivity D of most engineering materials is in the range $0.005 \text{ cm}^2/\text{s} < D < 1 \text{ cm}^2/\text{s}$ [Cahi 03]. In the following, characteristic lengths and times of different measuring techniques are specified:

- For the nanowire 3ω method the typical sample length is $5 \mu\text{m}$;
hence, $0.25 \mu\text{s} < \tau_{\text{diff}} < 50 \mu\text{s}$.
- For the bulk and thin film 3ω method the typical heating frequency is $f \approx 200 \text{ Hz}$;
hence, $50 \mu\text{m} < l_{\text{diff}} < 700 \mu\text{m}$.
- For the time domain thermoreflectance method the typical pulse duration is 200 ps ;
hence, $10 \text{ nm} < l_{\text{diff}} < 140 \text{ nm}$.

4.6 Thermal Radiation

The significance of heat loss from the surface of the sample via thermal radiation (Q_{rad}) compared to the heat conduction through the sample (Q_{cond}) can be quantified by the

ratio $Q_{\text{rad}}/Q_{\text{cond}}$. For a cylindrical specimen of length L and radius r this ratio is given by [Vlkl 09a]

$$\frac{Q_{\text{rad}}}{Q_{\text{cond}}} \approx \frac{4\epsilon\sigma_{\text{B}}T_0^3L^2}{\kappa r}, \quad (4.18)$$

where ϵ is the emissivity of the sample surface and σ_{B} the Stefan-Boltzmann constant. According to this equation, the error due to thermal radiation is proportional to the length of the specimen, if the aspect ratio L/r remains fixed. For the bulk 3ω method Cahill found that [Cahi 90]

$$\frac{Q_{\text{rad}}}{Q_{\text{cond}}} \approx \frac{2\epsilon\sigma_{\text{B}}T_0^3l_{\text{diff}}}{\kappa}. \quad (4.19)$$

From these equations it follows that the error due to thermal radiation decreases as the characteristic length of the diffusion process drops. To quantify this error, we assume a worst case emissivity of $\epsilon = 1$, a high temperature of 1000 K, and thermal conductivities of the specimen in the range $1 \text{ W/mK} < \kappa < 100 \text{ W/mK}$. Then, the relative error due to thermal radiation is between 0.02% and 2.3% assuming a nanowire with $L = 5 \mu\text{m}$ and $r = 50 \text{ nm}$. For a bulk or thin film sample with $l_{\text{diff}} = 100 \mu\text{m}$ this error is between 0.01% and 1.13%. It follows that heat loss through thermal radiation is usually negligible for thermal conductivity measurements using 3ω methods, even at high temperatures of the order of 1000 K.

4.7 1ω and 3ω Methods Revisited for Voltage-Driven Setups

3ω measurements on bulk materials and thin films typically require current amplitudes of the order of 10 mA. Frequently, the voltage source provided by the lock-in amplifier used for detecting the 3ω voltage is used in combination with a large ballast resistor to simulate a current source. However, to reach the required current amplitudes, the ballast resistance is typically limited to values of the order of the heater resistance. In such cases the device acts more like a voltage source rather than a current source. For this situation, a correction factor has been suggested for the evaluation of the measuring voltages [Dame 05]. To revise the proposed correction factor, we have taken the trouble to perform a Fourier analysis of 1ω and 3ω measurements using voltage-driven setups, and corrected the small mistakes made in Ref. [Dame 05]. The theoretical results are confirmed by different 1ω - and 3ω -measurements. Our results have been published in Ref. [Kiml 11] reprinted in the following pages.

Thermal Conductivity Measurements Using 1ω and 3ω Methods
Revisited for Voltage-Driven Setups

Reprinted with permission from

Johannes Kimling, Stephan Martens, and Kornelius Nielsch

Review of Scientific Instruments **82**, 074903 (2011)

Copyright 2011 by the American Institute of Physics

The contributions of each author to the research study are indicated in the table below, using the following specifications:

Conception of the research study (1), sample preparation (2), measurements (3), data analysis (4), interpretation (5), and composition of the manuscript (6).

JK	SM	KN
1,2,3,4,5,6	4,5	1

Thermal conductivity measurements using 1ω and 3ω methods revisited for voltage-driven setups

J. Kimling, S. Martens, and K. Nielsch

Institute of Applied Physics, University of Hamburg, Jungiusstrasse 11, 20355 Hamburg, Germany

(Received 8 May 2011; accepted 8 June 2011; published online 13 July 2011)

1ω and 3ω methods are widely established transient measurement techniques for the characterization of thermal transport in bulk-materials, thin films, and 1D nano-objects. These methods are based on resistance oscillations of a heater caused by Joule-heating from a sinusoidal current at frequency 1ω which lead to changes in the 1ω voltage and produce a voltage component at 3ω . Although the usual formalism for analyzing the measurement data assumes an ideal current source, voltage-driven measurement setups are employed in many cases. In this context, we find that there has been lack of clarity if a correction generally has to be considered when analyzing the measurement data from voltage driven setups. In this work, Fourier-analysis is employed to show that a correction is not required for 1ω methods and for 3ω measurements that use common-mode-subtraction. Experimental results are presented for a line heater on a fused silica substrate with known thermal properties, and for an individual nickel wire with diameter of 150 nm. © 2011 American Institute of Physics. [doi:10.1063/1.3606441]

I. INTRODUCTION

The expression 3ω method was coined by Cahill, who employed the third harmonic component (3ω) of the voltage along a metal line, fabricated on top of a dielectric solid, to determine the thermal conductivity of the solid.¹ The approach was extended to thin films² and improved by considering two-dimensional and three-dimensional heat-conduction models,^{3,4} and numerical simulations⁵ to only mention a few. These approaches take into account various experimental constraints such as boundary conditions and thermal contact resistances. Furthermore, an approach of the 3ω method for wires⁶ was applied to nanowires⁷ and nanotubes.⁸ The versatile concept of the 3ω method was generalized together with 2ω and 1ω methods by Dames and Chen⁹ to describe thermal systems containing a line heater that is also used to sense the temperature. Using this generalization the methods developed by Völklein *et al.*^{10–12} to determine the thermal conductivity of thin films and nanowires can be called 1ω methods. Dames and Chen⁹ derived general electrical transfer functions that relate the harmonic components of the measurement voltage with the thermal transfer function of the system that is investigated for the case of sinusoidal current with a dc offset. The thermal transfer function contains information about the thermal properties of the system, such as thermal conductivity or specific heat or both of the heater or its adjacencies or of both. The expressions are of great benefit because they reveal that the various voltage components are rich with information about the thermal transfer function. Dames and Chen⁹ point out advantages and disadvantages of each voltage component for determining the thermal transfer function. Furthermore they discuss, in which extent a voltage source can be used for the experiment, although an ideal current source is assumed for the mathematical formalism. In this context they derive a correction factor that depends on the ratio of the sample resistance to the total electrical resistance

of the circuit. They conclude that “this correction applies to any 1ω , 2ω , or 3ω experiment that uses a voltage source but assumes a current source for analysis and data processing,” and that “... even with the widespread practice of common-mode-subtraction (CMS) it is still necessary to consider the correction.”⁹ The same correction factor was derived also by Yusibani *et al.*¹³ for 3ω measurements. They additionally employ an alternative correction by subtracting the voltage due to the measured 3ω current, which “removes the need for the correction factor (...) and makes the procedure mathematically equivalent to the experimental circuit used by Cahill.”¹³ Apart from this, the correction factor seems not to be considered by others in this context. We mention recent publications, the authors of which employed voltage-driven setups in combination with CMS,^{14–16} and without CMS.^{17,18} In the last two references the authors do not use the correction factor proposed by Dames and Chen, but state that their measurement setups were calibrated by measuring the thermal conductivities of sapphire and SiO₂. Other researchers employ CMS in combination with a current-driven setup, e.g.,^{19,20} as it was done originally by Cahill.¹

Apparently there exists disagreement in the literature about the interpretation of data obtained from 1ω or 3ω measurements by using voltage-driven setups. In this article we aim to give a clear answer to this problem. In Sec. II we recap the basic concept of 1ω and 3ω methods. In Sec. III the correction factor mentioned above is derived using leading-order Taylor expansion of the measurement voltage. Furthermore, using this approach, it is shown that the correction cancels out when using CMS. To gain further insight, a Fourier analysis of the 1ω and 3ω methods is performed in Sec. IV. It is shown that for 1ω methods the correction is not required, while for direct 3ω measurements the correction has to be considered. The results can be used to show that for 3ω measurements that use CMS a correction is not required, which was already shown in Sec. III by using Taylor approximations. 2ω

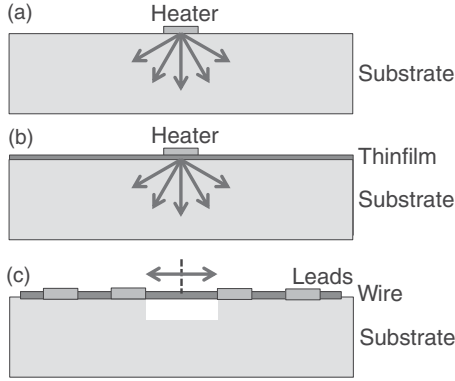


FIG. 1. The schematic cross-sectional drawings represent three typical systems for 3ω measurements. Arrows indicate the directions of heat flow.

measurements will not be considered in this work, as they are recommended only for niche applications.⁹ We present experimental data for a fused silica substrate with known thermal properties to confirm the analysis. Since 1ω and 3ω methods are increasingly the method of choice when investigating conducting wires with diameters in the sub-micrometer range, experimental data is presented for an individual suspended nickel nanowire. For all measurements we employed both, a current-driven setup and a voltage-driven setup. For each setup, 1ω and 3ω measurements with and without CMS were performed.

II. THE CONCEPT OF 1ω AND 3ω METHODS

Sketches of the most prominent systems for 3ω measurements are shown in Fig. 1. All systems contain a single Joule-heater that is also used as a temperature sensor by evaluating changes in its electrical resistance. For dielectric solids (Fig. 1(a)) and thin films (Fig. 1(b)) a thin heater line, typically 100 nm thick with large aspect ratio (typically $2\ \mu\text{m}$ to $20\ \mu\text{m}$ wide and 2 mm long) is fabricated on the surface of the sample. In this case heat is considered to flow perpendicular to the heater axis into the sample. For conducting wires (Fig. 1(c)) no external heater is required as the specimen itself serves as the heater and temperature sensor of the experiment. The heat is considered to flow from the center of the suspended wire segment parallel to the wire axis into the metal leads which serve as heat sinks.

For 1ω and 3ω measurements one assumes an ideal current source applying an alternating current

$$I(t) = I_0 \cos(\omega t) \quad (1)$$

to the heater. Due to the resistance R_H of the heater, the current produces Joule-heat

$$Q(t) = R_H(t)I^2(t) \approx \frac{R_{H0}I_0^2}{2}(1 + \cos(2\omega t)) \quad (2)$$

with a 2ω component. It is usually assumed that heating power fluctuations caused by resistance oscillations are small compared to the total heating power. For this reason, the time-dependent resistance can be replaced by the resistance in the limit of zero current, R_0 , on the right side of Eq. (2). The resulting temperature rise depends on the thermal properties of

the sample. The average temperature rise ΔT_{avg} of the heater is related to the Joule-heating via the thermal transfer function Z of the system.⁹ In the time domain

$$\Delta T_{avg}(t) = Q(t) \otimes Z_t, \quad (3)$$

where Z_t is the inverse Fourier-transform of Z and \otimes denotes convolution. In order that the 3ω method can be applied, the heater needs a considerable temperature coefficient of resistance $\alpha = \frac{1}{R_0} \frac{dR_H}{dT} |_{T_0}$, where R_0 is the resistance of the heater in the limit of zero current, and d/dT is the temperature derivative. If this condition is fulfilled, then the temperature rise results in a resistance change of the heater that oscillates with a dominating 2ω component,

$$R_H(t) = R_{H0} [1 + \alpha \Delta T_{avg}(t)]. \quad (4)$$

As a consequence of the 2ω component of R_H , the voltage along the heater contains a 3ω component which is typically 1000 times smaller than the 1ω component. Amplitude and Phase of both components depend on Z which contains information about the thermal properties of the system. The electrical transfer functions that relate the harmonic components of the voltage to Z were derived by Dames and Chen.⁹

III. 1ω AND 3ω MEASUREMENTS USING A VOLTAGE SOURCE

A. Derivation of the correction factor

The following derivation of the correction factor is similar to the derivation by Dames and Chen,⁹ but uses a general notation, because the derivation does not depend on the origin of the time-variation of the sample resistance. Consider the simple series circuit shown in Fig. 2(a). Resistance R_B is assumed constant over time, while for resistance R_A , small changes may occur: $R_A = R_{A0} + \Delta R$. We assume an ideal voltage source applying the voltage U , which leads to the current I . Then, according to Ohm's law, the voltage drop along R_A is

$$U_A = R_A I = (R_{A0} + \Delta R) \frac{U}{R_{A0} + \Delta R + R_B}. \quad (5)$$

It is helpful for the imagination to consider first two limiting cases for Eq. (5):

1. $R_B \ll R_A$:

$$U_A \approx U. \quad (6)$$

If R_A would be the only resistance in the circuit, then it is straightforward that the voltage drop along R_A is the source voltage U . Changes in R_A do not affect U_A and 1ω or 3ω methods cannot be applied.

2. $R_B \gg R_A$:

$$U_A \approx (R_{A0} + \Delta R) \frac{U}{R_{A0} + R_B}. \quad (7)$$

If R_B is much larger than R_A , influences of ΔR on the current are negligible. Then, changes in the voltage across R_A are proportional to changes in R_A , and 1ω or 3ω methods can be applied assuming an ideal current source.

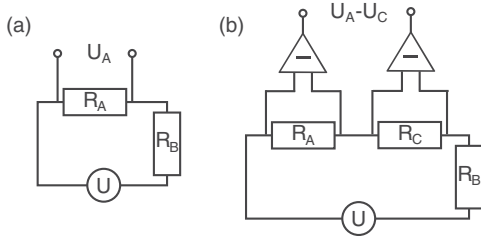


FIG. 2. (a) Circuit for direct measurements of the voltage U_A across resistor R_A . (b) Circuit for CMS. Both circuits are voltage-driven assuming an ideal voltage source. For real voltage sources, the finite output impedance needs to be included in R_B .

Because of practical reasons, the relative contribution of the sample resistance to the total resistance of the circuit is not negligible in many cases. Researchers, for example, often use the output of a lock-in amplifier, which in combination with large ballast resistances may not supply sufficiently large currents for the measurements. In this instance use can be made of the following approximation for Eq. (5). For 1ω and 3ω measurements at room-temperature, the temperature amplitude is typically below 1 K. Therefore fluctuations in the sample resistance can be assumed small compared to the sample resistance, and a leading-order Taylor-series expansion of Eq. (5) can be applied.

3. $R_B \sim R_A$, $\Delta R \ll R_{A0}$:

$$\begin{aligned} U_A &\approx \frac{R_{A0} U}{R_{A0} + R_B} + \frac{R_B \Delta R U}{(R_{A0} + R_B)^2} \\ &= \left(R_{A0} + \frac{R_B}{R_{A0} + R_B} \Delta R \right) \frac{U}{R_{A0} + R_B} \\ &= \left(R_{A0} + \frac{R_B}{R_{A0} + R_B} \Delta R \right) I_{as}, \end{aligned} \quad (8)$$

where I_{as} is the constant amplitude of the assumed current. Equation (8) is consistent with the two limiting cases discussed above. Comparing Eq. (8) with Eq. (7) reveals a correction factor that has to be considered when using a voltage source but assuming that the current amplitude would be constant. In this case the apparent resistance change ΔR_{ap} , when measuring the voltage and assuming a constant current amplitude, is smaller compared to the actual resistance change:

$$\Delta R_{ap} = \frac{R_B}{R_{A0} + R_B} \Delta R. \quad (9)$$

We should mention that for real voltage sources the output impedance is not zero. The output impedance, which is typically 50Ω , has to be considered for the calculation of the correction factor, i.e., needs to be included in R_B of Eq. (9).

B. Common-mode-subtraction

In Fig. 2(b) a circuit for common-mode-subtraction is shown. The circuit contains a reference resistance R_C , which is assumed constant over time, just like R_B . Again for resis-

tance R_A , small changes may occur: $R_A = R_{A0} + \Delta R$. We assume an ideal voltage source applying the voltage U , which leads to the current I . The voltage drop along R_A is obtained analog to Eq. (8). For the voltage drop along R_C Taylor-series expansion to leading order gives

$$\begin{aligned} U_C &= R_C \frac{U}{R_{A0} + \Delta R + R_B + R_C} \\ &\approx \left(R_C - \frac{R_C}{R_{A0} + R_B + R_C} \Delta R \right) I_{as}. \end{aligned} \quad (10)$$

The circuit subtracts U_A from U_C . Subtraction of the two voltages yields

$$U_A - U_C = \left(R_{A0} - R_C + \frac{R_B + 2R_C}{R_{A0} + R_B + R_C} \Delta R \right) I_{as}. \quad (11)$$

From Eq. (11) it follows that for equal resistances R_{A0} and R_C the differential signal contains the actual resistance change ΔR , which is identical as for an ideal current source:

$$R_{A0} = R_C \implies U_A - U_C = \Delta R I_{as}. \quad (12)$$

CMS is frequently used for 3ω measurements to remove the dominant in-phase 1ω component from the measurement signal, before the 3ω component is detected. In practice the reference resistor needs to be heat sunk and should have a negligible temperature coefficient of resistance. To adjust the 1ω voltage drops across the reference resistor and the heater prior to CMS, a series potentiometer can be used as reference resistor or a fixed reference resistor of arbitrary value in combination with an appropriate amplifying device, for example, a multiplying digital-to-analog converter. In the former case, the potentiometer is tuned to match the resistance of the heater. In the latter case, the voltage drop across the reference resistor is multiplied by the gain factor needed to make both 1ω voltages the same. The remaining signal after CMS contains a small out-of-phase 1ω signal and higher harmonic components. In contrast to the case of a current source errors are introduced if the 1ω component is not completely removed.

C. Relevance for 1ω and 3ω methods

Combining Eqs. (3) and (4), the time-dependent part of the resistance of interest for 1ω and 3ω measurements is given by

$$\Delta R_H = R_{H0} \alpha Q(t) \times Z_t. \quad (13)$$

With this it follows from Eq. (9) that the thermal transfer function Z^{VS} deduced from 1ω and direct 3ω measurements using a voltage source and assuming a current source for data analysis, needs a correction to obtain the actual thermal transfer function:

$$Z^{CS} = \frac{R_{H0} + R_B}{R_B} Z^{VS}. \quad (14)$$

Because of $\Delta R_H \ll R_{H0}$ the dominant contribution to Joule-heating stems from $I_{1\omega}$, the 1ω component of the current, which is usually measured using a precision resistor connected in series with the sample. In Sec. IV it is shown that

the amplitude of the $n\omega$ component of the current decays exponentially with index n . Therefore the contribution of higher harmonic components of the current to the Joule-heating can be neglected. Because of the same reason, also the difference between $I_{1\omega}$ and I_{as} is marginal. However $I_{1\omega}$ can be determined with higher accuracy. For this reason it seems natural to replace I_{as} with $I_{1\omega}$, which was actually done by Dames and Chen.⁹ In the following it is demonstrated that the replacement of I_{as} with $I_{1\omega}$ makes the correction redundant for 1ω measurements, while for 3ω measurements without CMS a negligible error is introduced but the correction still has to be considered. If CMS is employed, the correction factor disappears also for 3ω measurements, which was already shown in Sec. III B.

IV. FOURIER ANALYSIS

In Sec. III A a correction factor for the thermal transfer function when using a voltage source was derived by using leading-order Taylor approximation of the voltage across the heater. In this section the Fourier expansions of this voltage and of the current are derived. The ratio of the 1ω and 3ω components of the voltage to the first harmonic component of the current – these are the measured quantities – proves whether a correction is required or not. Consider an ideal voltage source with amplitude U_0 at frequency 1ω :

$$U(t) = U_0 \cos(\omega t). \quad (15)$$

As for the case of a current source discussed in Sec. II, small resistance oscillations are neglected when calculating the Joule heating,

$$Q(t) = R_{H0} \left(\frac{U_0 \cos(\omega t)}{R_{H0} + R_B} \right)^2, \quad (16)$$

where the ballast resistance R_B is assumed constant over time and includes any additional resistances to the resistance R_H of the heater. Combining Eqs. (3) and (16) the average temperature rise of the heater is

$$\Delta T(t) = \frac{R_{H0}}{2} \left(\frac{U_0}{R_{H0} + R_B} \right)^2 (Z(0) + \operatorname{Re}[Z(2\omega)] \cos(2\omega t) - \operatorname{Im}[Z(2\omega)] \sin(2\omega t)). \quad (17)$$

Then the resistance of the heater takes the form

$$\begin{aligned} R_H(t) &= R_{H0}(1 + \alpha(\vartheta_0 + \vartheta_a \cos(2\omega t) - \vartheta_b \sin(2\omega t))) \\ &= R_{H0}(1 + \alpha(\vartheta_0 + \vartheta_c \cos(2\omega t + \varphi))), \end{aligned} \quad (18)$$

where

$$\vartheta_c^2 = \vartheta_a^2 + \vartheta_b^2; \quad \tan(\varphi) = \frac{\vartheta_b}{\vartheta_a}, \quad (19)$$

with temperature coefficients $\vartheta_{0,a,b}$ that abbreviate the respective terms in Eq. (17).

A. Fourier-representation of $I(t)$

According to the Ohm law, the current is given by the expression

$$I(t) = \frac{U(t)}{R_H(t) + R_B}. \quad (20)$$

Consider no phase shift between the voltage and the resistance of the heater. Then, using Eqs. (15) and (18) the current takes the form

$$I(t) = g(t)f(t), \quad (21)$$

where g and f are defined as

$$g(t) \equiv \frac{U_0}{R_{H0}(1 + \alpha\vartheta_0) + R_B} \cos(\omega t) \equiv I_0 \cos(\omega t), \quad (22)$$

$$f(t) \equiv \frac{1}{1 + a \cos(2\omega t)}, \quad (23)$$

where

$$a = \frac{R_{H0}\alpha\vartheta_c}{R_{H0}(1 + \alpha\vartheta_0) + R_B} \ll 1. \quad (24)$$

The Fourier representation of Eq. (23) is

$$f(t) = a_0 + \sum_{k=1}^{\infty} a_k \cos(k2\omega t), \quad (25)$$

where

$$a_0 = \frac{1}{T} \int_{-T/2}^{T/2} f(t) dt, \quad (26)$$

$$a_k = \frac{2}{T} \int_{-T/2}^{T/2} f(t) \cos(k2\omega t) dt.$$

The following formula from Gradshteyn and Ryzhik²¹ can be used to evaluate these integrals:

$$\int_0^{\pi} \frac{\cos(nx)}{1 + a \cos(x)} = \frac{\pi}{\sqrt{1 - a^2}} \left(\frac{\sqrt{1 - a^2} - 1}{a} \right)^n, \quad (27)$$

which holds for

$$|a| < 1. \quad (28)$$

The phase shift φ between the resistance of the heater and the voltage in Eq. (20) is incorporated in the frequency domain using the shift theorem and the convolution theorem for Fourier transforms,²²

$$I_{\omega}(\tilde{\omega}) = g_{\omega}(\tilde{\omega}) \otimes f_{\omega}(\tilde{\omega}) e^{i t_0 \tilde{\omega}}, \quad (29)$$

where

$$t_0 = \frac{\varphi}{2\omega}. \quad (30)$$

After substitution of the Fourier-transforms of Eqs. (22) and (25) into Eq. (29) followed by inverse Fourier transformation, the following result is obtained for the Fourier-representation of $I(t)$:

$$\begin{aligned} I(t) &= \gamma I_0 [\cos(\omega t) + \sum_{k=1}^{\infty} (-1)^k \eta^k (\cos([2k - 1]\omega t + k\varphi) \\ &\quad + \cos([2k + 1]\omega t + k\varphi))], \end{aligned} \quad (31)$$

with

$$\gamma = \frac{1}{\sqrt{1-a^2}}, \quad (32)$$

and

$$\eta^k = \left(\frac{1 - \sqrt{1-a^2}}{a} \right)^k. \quad (33)$$

Besides the dominant 1ω component the current comprises higher harmonic components. As defined in Eq. (24), the parameter a is the ratio of the amplitude of the resistance oscillation to the total resistance in the circuit. For 1ω and 3ω measurements, the inequality in Eq. (24) holds, and the expression of Eq. (33) can be rewritten as

$$\eta^k \approx e^{-bk}; \quad e^{-b} \equiv \frac{a}{2}. \quad (34)$$

For small resistance oscillations the Fourier coefficients of the current decrease exponentially with the index k . It follows that for large ballast resistance $R_B \gg R_H$ the voltage source can be regarded as a current source at frequency 1ω . The in phase 1ω current is given by

$$I^{(1\omega)}(t) = \gamma I_0 \left(1 + \eta \frac{\vartheta_a}{\vartheta_c} \right) \cos(\omega t). \quad (35)$$

B. Fourier representation of $U_H(t)$

Making use of the results obtained in Sec. IV A, the Fourier representation of $U_H(t)$ is obtained by multiplying Eq. (18) with the Fourier representation of $I(t)$:

$$\begin{aligned} U_H(t) = & R_{H0}(1 + \alpha\vartheta_0)I(t) + \gamma \frac{R_{H0}\alpha\vartheta_c I_0}{2} (\cos(\omega t + \varphi) \\ & + \cos(3\omega t + \varphi)) + \gamma \frac{R_{H0}\alpha\vartheta_c I_0}{2} \sum_{k=1}^{\infty} (-1)^k \eta^k \\ & \times (\cos[(2k+1)\omega t + (k+1)\varphi] + \cos[(2k-3)\omega t \\ & + (k-1)\varphi] + \cos[(2k+3)\omega t + (k+1)\varphi] \\ & + \cos[(2k-1)\omega t + (k-1)\varphi]). \end{aligned} \quad (36)$$

Contributions to the 1ω voltage across the heater come from the 1ω and 3ω components of the current. After rearranging the terms the following expression is obtained for the in-phase 1ω voltage across the heater:

$$\begin{aligned} U_H^{(1\omega)}(t) = & I^{(1\omega)}(t) \left(R_{H0}(1 + \alpha\vartheta_0) + \frac{R_{H0}\alpha\vartheta_a}{2} \right. \\ & \left. \times \left[\frac{1 - \eta \frac{\vartheta_c}{\vartheta_a}}{1 - \eta \frac{\vartheta_a}{\vartheta_c}} - \eta \frac{\vartheta_c}{\vartheta_a} \right] \right) \\ & \approx I^{(1\omega)}(t) \left(R_{H0}(1 + \alpha\vartheta_0) + \frac{R_{H0}\alpha\vartheta_a}{2} \right). \end{aligned} \quad (37)$$

The approximation of the term in square parentheses holds because of Eqs. (24) and (34). Compared with the corresponding expression for the case of a current source derived by Dames and Chen,⁹ the expression of Eq. (37) is of the same form. We

conclude that if both the in-phase 1ω voltage and the in-phase 1ω current are measured no correction is required for determining the thermal transfer function. As a reminder, according to Eqs. (17)–(19), the thermal transfer function is included in the temperature coefficients ϑ_0 , ϑ_a , ϑ_b , and ϑ_c . This result is not in contradiction to Eq. (8) – the assumed current I_{as} used there has to be distinguished from the actual 1ω current used here. If I_{as} is used for analyzing the data the correction factor still has to be considered for 1ω measurement. If the actual 1ω component of the current is used – which is usually the one that is measured – no correction is required.

Contributions to the 3ω voltage across the heater come from the 1ω , 3ω , and 5ω components of the current. After rearranging the terms the following expression is obtained for the in-phase 3ω voltage across the heater:

$$\begin{aligned} U_H^{(3\omega)} = & \widehat{I}^{(1\omega)} \left[\frac{1 - \eta \left(1 - \left(\frac{\vartheta_b}{\vartheta_a} \right)^2 \right)}{1 - \eta \frac{\vartheta_a}{\vartheta_b}} \right] R_B \frac{\vartheta_a}{\vartheta_c} \eta \cos(3\omega t) \\ & \approx \widehat{I}^{(1\omega)} R_B \frac{\vartheta_a}{\vartheta_c} \eta \cos(3\omega t), \end{aligned} \quad (38)$$

where $\widehat{I}^{(1\omega)}$ is the amplitude of the in-phase 1ω current. The approximation of the term in square parentheses holds due to Eqs. (24) and (34), which are further used to approximate η which leads to

$$U_H^{(3\omega)} \approx \widehat{I}^{(1\omega)} \left(\frac{R_B}{R_{H0}(1 + \alpha\vartheta_0) + R_B} \right) \frac{R_{H0}\alpha\vartheta_a}{2} \cos(3\omega t). \quad (39)$$

This expression equates the one for the case of a current source derived by Dames and Chen⁹ multiplied with the ratio of the ballast resistance to the total resistance of the circuit, which is the correction factor derived in Sec. III A. This means that for direct 3ω measurements a correction is required for determining the thermal transfer function. To apply this correction the ballast resistance R_B has to be known. An alternative correction was employed by Yusibani *et al.* by measuring the 3ω component of the current using a reference resistance and subtracting the voltage due to the 3ω current from the measured 3ω voltage across the heater.¹³ This approach neglects the contribution of the 5ω current. A way to avoid a correction is to make use of CMS as already discussed in Secs. III B and III C. With the Fourier representations of $I(t)$ and $U(t)$ it is straightforward to calculate the resulting voltage after CMS. For ideal balancing the 3ω component of the current produces identical contributions to the 3ω components of both, the reference voltage and the voltage across the heater, which are canceled out after CMS. Therefore, to leading order, no correction is required for 3ω measurements that make use of CMS. In the same way imperfections of the source that produce additional distortions at 3ω are removed when using CMS, which improves the accuracy of this method.

V. EXPERIMENT AND DISCUSSION

To test the theoretical aspects of Secs. II–IV two different systems were investigated: the traditional line heater on a fused silica substrate, and the one-dimensional system in form

of a very thin metal wire. The former system is a typical reference system to test 3ω measurement setups. On this system 1ω and 3ω measurements were performed using three different sources: a function generator (“VS A,” Agilent Technologies 33220A), the internal voltage-source of a lock-in amplifier (“VS B,” Stanford Research Systems SR830) and an ac current source (“CS,” Keithley 6221). Additionally we have chosen the one-dimensional system because we think that the number of applications of 1ω and 3ω methods for investigating individual nanowires is going to increase. Compared to steady state techniques²³ the main advantages of these methods are their low microfabrication effort and the speed of the measurements. The nanowire system is very sensitive to electrostatic discharges, start-up peaks, and uncontrolled current peaks from the apparatus, which may lead to current densities that burn parts of the wire. To avoid electrostatic discharges the measurement apparatus was carefully grounded. A switch box between sample and measurement apparatus allows us to set the leads to ground potential before and after the measurements. To reduce the risk of critical current peaks, it is recommended to connect resistors in series adjacent to each lead and close to the nanowire.²⁴ The series resistances should be some orders of magnitudes larger than the resistance of the specimen. But then, as discussed in Sec. III A, the source dependent differences in the measurement signal would be hardly observable, because the voltage source would approximate a current source. Therefore the measurements were performed without such protecting resistors. On the other hand for the investigated system the output of the lock-in amplifier is sufficient to produce the required resistance oscillation of the nanowire even for large ballast resistances. Therefore for the suspended nanowire system we used the output of the lock-in amplifier connected to a $3\text{ k}\Omega$ resistor to approximate a current source and compare the results with those obtained without the $3\text{ k}\Omega$ resistor.

The 3ω voltage across the sample was measured both, directly using a lock-in amplifier (Stanford Research Systems SR830) and after CMS (compare Fig. 2). The measurement unit for CMS (3ω system, Fraunhofer IPM Freiburg) uses an analog/digital conversion board to record the data and a numerical lock-in technique to extract the 3ω components.²⁵ The maximum frequency of this measurement unit is 1 kHz , while the lock-in amplifier allows 3ω measurements up to 33 kHz . A $10\ \Omega$ precision resistor was used to measure the current with a second lock-in amplifier (Anfatec Instruments eLockIn 204/2). All measurements were performed at room temperature. The samples were connected to the measurement apparatus using a micro-manipulated probestation (Lake Shore TTPX). To avoid heat convection all measurements were performed under vacuum conditions.

A. Line heater on fused silica

Figure 3 shows a scheme of a typical heater geometry used for 3ω measurements. The heater line used for the experiment was $25\ \mu\text{m}$ wide and 4 mm long. For measurements using a current source edge effects of the temperature profile along the heater line do not have to be considered for

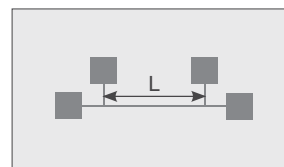


FIG. 3. Top-view scheme of a line heater with four bond pads for 3ω measurements on bulk samples or thin films. Along the length L between the inner contacts, the temperature profile is homogeneous.

appropriate distances between the outer contacts (typically 0.5 mm). If a correction has to be considered when using a voltage source, the whole heater line contributes to the correction factor. The resistance of the part between the inner contacts can be determined without influences from contact resistances. With this the total resistance of the heater line can be estimated via its total length by assuming constant width and thickness. Because of the decreasing temperature profile toward the ends of the heater line, the effective resistance that contributes to the correction factor is reduced. Nevertheless the experimental results indicate that, at least for the substrate and heater geometry investigated in this work, edge effects can be neglected for the calculation of the correction factor. For substrates of large thermal conductivity or small distances between the outer contacts, the edge effects may introduce considerable errors at low frequencies.⁵

The thermal transfer function for a line heater of length L on a semi-infinite substrate of thermal conductivity κ_S is given by¹

$$Z(\omega) = -\frac{1}{2\pi\kappa_S L} \left(\ln 2\omega + i\frac{\pi}{2} + C \right), \quad (40)$$

where the unknown constant C is purely real. The assumption of semi-infinite substrate holds if the thermal penetration depth $\lambda = (D/(2\omega))^{1/2}$, where D is the thermal diffusivity of the substrate, is small compared to the substrate dimensions. A further assumption is that λ is large compared to the width of the heater. The frequency range used for the measurements has to be chosen accordingly. As discussed by Dames and Chen⁹ for sinusoidal heating, κ_S can be determined from the slope of the in-phase 1ω and 3ω voltages with respect to $\ln \omega_H$. Figure 4 shows the thermal transfer function Z deduced from 3ω measurements, plotted against $\ln f$, where $f = \omega/2\pi$. The curves obtained for CMS (characters: filled squares (CS), open triangles pointing to the right (VS A), and open upward pointing triangles (VS B)) are identical within the precision of the measurement, independent of the source. The curves obtained for direct 3ω measurements clearly depend on the source. For the current source (characters: open circles) the resulting curve is close to the curves obtained for CMS with small deviations in the medium frequency range. To explain the small deviations we mention two possible reasons: First, the output signal of the current source contains a small 3ω component due to imperfections. Second, the 3ω measurement can be distorted by the large 1ω component, which is typically 1000 times as large as the 3ω component.¹ For voltage sources A and B the curves obtained for direct 3ω measurements (characters: open downward pointing triangles and open stars) need to be corrected.

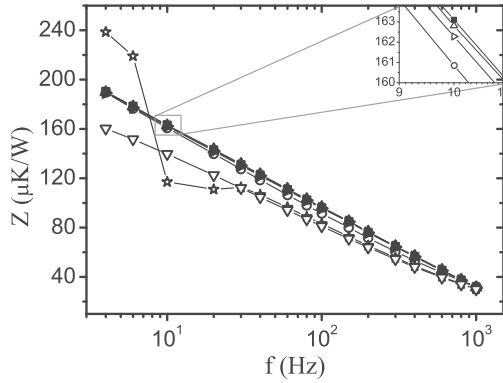


FIG. 4. Frequency-dependence of the thermal transfer functions obtained from the proposed 3ω measurements for a line heater on a fused silica substrate. Filled squares: CMS with current source (CS); open triangles pointing to the right: CMS with voltage source (VS) A; open upward pointing triangles: CMS with VS B; open circles: direct with CS; open downward pointing triangles: direct with VS A; open stars: direct with VS B.

In the frequency range above 30 Hz, both curves are identical within the precision of the measurement. Apparently the internal oscillator of voltage source B produces significant harmonic distortion at frequencies below 30 Hz. The thermal conductivity of the fused silica substrate determined from the 3ω measurements is $\kappa_S = 1.36\text{W}/(\text{mK})$, which is close to the literature value of $\kappa_{ref} = 1.31\text{W}/(\text{mK})$ (Schott Lithotec).

It was discussed by Dames and Chen⁹ that the demand on stability and phase accuracy of the current source is larger for 1ω methods than for 3ω methods. For this reason we present 1ω measurements at constant frequency and for varying current amplitudes, which is sufficient to demonstrate that no correction is required for 1ω methods. The voltages are expected to scale with $I_{1\omega}^3$, therefore as shown in Fig. 5 the measured resistances $U_{1\omega}/I_{1\omega}$ are plotted against $I_{1\omega}^2$. The intersection of the curves with the y-axis corresponds to the resistance of the heater line at the temperature of the heat sink of the experiment. The curve obtained for the current source (filled squares) and for the voltage source (open circles) are identical within the precision of the measurement. Only when using I_{as} , the assumed current introduced in Sec. III B, to calculate $U_{1\omega}/I_{1\omega}$ (open triangles) a correction is required for the voltage source. The total resistance of the circuit which is required for determining I_{as} and also for the correction factor, was determined from the ratio of the source voltage to the measured 1ω current.

Table I summarizes the total resistance of the circuit, the resistance of the total heater line, the correction factor derived from Eq. (9) and the actual correction factors derived from the measured curves. The correction factors obtained from 1ω and 3ω measurements are consistent within the precision of the measurement. However, this table should not create the impression that 1ω measurements are more precise than 3ω measurements – which usually is not the case.⁹ The small error for $CF_{1\omega}$ is a consequence from the current-dependent measurement at constant frequency, whereas the 3ω measurement was performed at constant current and variation of the frequency.

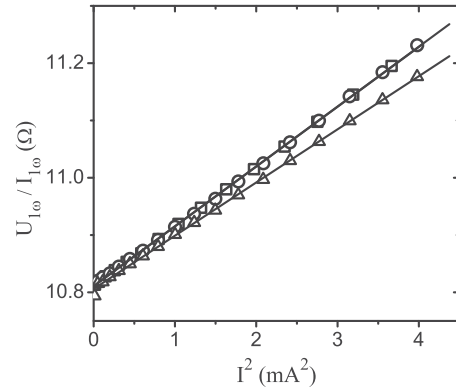


FIG. 5. 1ω voltage divided by 1ω current vs the square of the current for a line heater on a fused silica substrate. The three curves correspond to 1ω measurements using a current source (squares) and a voltage source (circles and triangles). For the latter, the 1ω voltage was divided by the assumed current (see Sec. III A), while for the others the measured current was used.

B. Suspended nickel nanowire

Figure 6 shows a scanning electron micrograph of the microdevice employed for the proposed 1ω and 3ω measurements that includes an individual nickel wire with diameter of 150 nm. The specimen is suspended over a trench and connected to four gold leads. The outer contacts are used to apply a current to the wire, while the inner contacts are used to measure the voltage along the wire. Additional heater and thermometer structures are not required, because the wire itself serves as heater and temperature sensor. Joule heating increases the temperature of the suspended segment of the wire. The metal leads at the edges of the groove are in intimate thermal contact with the wire and the substrate, and therefore can be regarded as heat sinks. Nickel nanowires were synthesized by filling the pore channels of a porous alumina template with nickel using electrodeposition from a Watts bath.^{26–29} After deposition, the nanowires were released from the template and suspended in isopropyl alcohol by selective chemical etching of alumina and filtration. The crystallinity of the nanowires was analyzed by x-ray diffraction. The nanowires are polycrystalline with an average grain size of about 35 nm. The employed microfabrication approach includes the following steps. At first parallel trenches (several mm long, 5 μm wide and 1 μm deep) were etched into a Si/SiO₂ substrate. The structured surface was wetted with a solution containing nickel nanowires and a magnetic field was applied to direct the nanowires perpendicular to the trenches. By choosing an appropriate concentration, usually five to ten nanowires cross the trenches after evaporation of the solvent. In the subsequent lithography step, the substrate including the nanowires crossing the trenches was spin-coated with photoresist. The areas

TABLE I. Resistance values to calculate the correction factor (CF) using Eq. (9). $CF_{1\omega}$ and $CF_{3\omega}$ are the actual correction factors derived from the 1ω measurements and the 3ω measurements, respectively.

R_{tot} (Ω)	R_H (Ω)	CF	$CF_{1\omega}$	$CF_{3\omega}$
99.2	12.35	1.142	1.147 ± 0.004	1.16 ± 0.04

074903-8 Kimling, Martens, and Nielsch

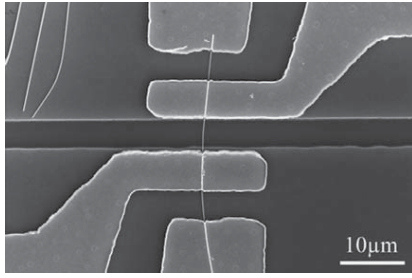
Rev. Sci. Instrum. **82**, 074903 (2011)

FIG. 6. Scanning electron micrograph of the measurement microdevice. A nickel wire (150 nm diameter) is suspended over a trench and connected to four gold electrodes. The length of the wire between the inner contacts is 5.4 μm .

designated for the metal leads were exposed using photo projection lithography. Directly before the metalization of the structure, controlled sputter etching was performed to open the native oxide surrounding the nickel wire. After the lift-off process the substrates were rinsed with water and dried using a N_2 -jet.

To derive the correction factor for a suspended wire, the outer parts of the wire are usually assumed to be heat sunk, so that only the suspended segment of the wire has to be considered.⁹ Although in our case the outer parts of the wire are not suspended, they are far from being heat sunk. The cylindrical shape of the wire and the roughness of substrate and wire result in an unknown thermal contact area between wire and substrate. Therefore the correction factor for the wire cannot be determined *ab initio*.

Using the lumped approximation from Dames *et al.*, the thermal transfer function for a suspended wire is given by⁹

$$Z = \frac{L}{12A\kappa} \left(\frac{1 - i\omega\gamma/10}{1 + (\omega\gamma/10)^2} \right), \quad (41)$$

where L , A , and κ are length, cross section, and thermal conductivity of the suspended wire segment, and $\gamma = 4 * L^2/D$ is the characteristic diffusion time (D : thermal diffusivity). In the low frequency range ($\omega\gamma \ll 1$) the term in parentheses of Eq. (41) can be approximated with the identity.⁶ For wire length of 5 μm and bulk values of nickel for the thermal diffusivity, the order of magnitude of γ is -7 . Therefore within the accessible frequency range of the measurement apparatus the term $\omega\gamma$ is of no importance, and the focus lies on the scaling of the measurement signal with the current. For sinusoidal heating the voltages are expected to scale with I^3 . Figure 7 shows the measured resistances $U_{1\omega}/I_{1\omega}$ and $U_{3\omega}/I_{1\omega}$ plotted against $I_{1\omega}^2$. The 1ω measurements do not depend on the source, while the direct 3ω measurements strongly depend on whether the source behaves as a voltage source (characters: triangles pointing downward) or as a current source (characters: circles). The latter curve and the curves obtained for CMS (squares: CS, upward pointing triangles: VS) are the same within the precision of the measurements. Small deviations are observed for large current amplitudes which produce large resistance oscillations. The correction factor obtained from the measured curves is 1.45 ± 0.02 . For thermally insulated outer wire segments and for heat sunk outer wire segments, the *ab initio* correction factor would be 1.89 and 1.19,

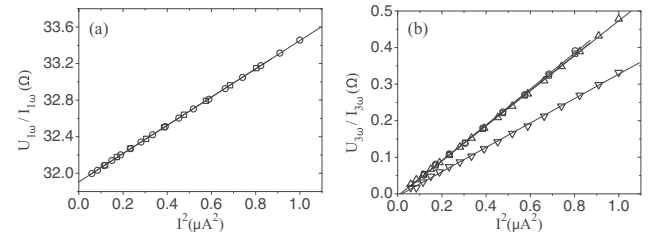


FIG. 7. (a): 1ω voltage divided by 1ω current vs the square of the current for a nickel wire with 150 nm diameter. Squares: current source; circles: voltage source. (b): 3ω voltage divided by 1ω current vs the square of the current. Squares: CMS with voltage source; triangles pointing upward: CMS with current source. Direct 3ω measurements depend on the source: triangles pointing downward: voltage source; circles: current source.

respectively. This confirms the above reasoning that the outer wire segments cannot be considered heat sunk nor thermally insulated which makes the *ab initio* determination of the correction factor at least awkward.

From both, 1ω and 3ω measurements the thermal conductance G of the wire can be determined,⁹

$$G^{(1\omega)} = \frac{R_{H0}^2 \alpha I_{1\omega}^2}{16(U_{1\omega}/I_{1\omega} - R_{H0})}, \quad (42)$$

$$G^{(3\omega)} = \frac{R_{H0}^2 \alpha I_{1\omega}^3}{48U_{3\omega}}. \quad (43)$$

The denominator of Eq. (42) yields a small number that is obtained by subtracting two large numbers. Therefore small errors in the 1ω measurements or in the determination of R_{H0} or both result in a significant error for G . By extrapolating the curves in Figure 7(a) to zero current we obtain $R_{H0} = 31.91 \pm 0.03 \Omega$. Figure 8 shows the scaling of the thermal conductance with the current obtained from 1ω measurements and 3ω measurements with CMS using a voltage source for both. It can be seen that increasing the current has two competing effects on 1ω measurements. On the one hand uncertainties in the determination of R_{H0} become more and more insignificant, while on the other hand the systematic error due to the approximation for the Joule heating (Eq. (2)) in the numerator of Eq. (42) results in an apparent thermal conductance which is smaller than the actual thermal conductance. For 3ω measurements the first effect is

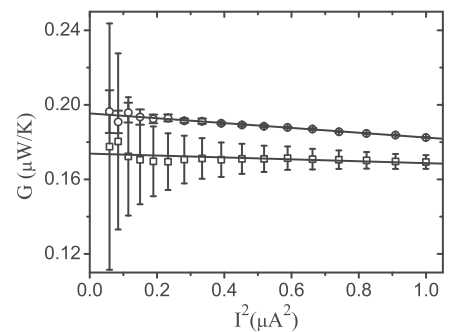


FIG. 8. Thermal conductance vs square of the current obtained from 1ω (squares) and 3ω (circles) measurements for a nickel wire with 150 nm diameter and a length of 5.4 μm .

TABLE II. Results obtained from 1ω and 3ω measurements for a nickel nanowire (diameter: 150 nm). R_{H0} : Resistance in the limit of zero current; ρ : electrical resistivity; G : thermal conductance; κ : thermal conductivity; LN : Lorenz number. For comparison the literature values of bulk nickel and of a nanocrystalline (NC) nickel nanowire are shown.

	R_{H0} Ω	ρ $10^{-8}\Omega\text{m}$	G 10^{-8}W/K	κ W/(mK)	LN $10^{-8}\text{V}^2/\text{K}^2$
1ω	31.91 ± 0.03	10.4 ± 2.3	17.4 ± 1.7	53 ± 13	1.87 ± 0.18
3ω	–	–	19.5 ± 0.2	60 ± 13	2.09 ± 0.02
Bulk (Ref. 31)	–	7	–	90.7	2.15
NC nickel nanowire (Ref. 7)	–	35	–	22	2.7

insignificant. Even in the low current range the error bars are small compared to the 1ω measurement. The second effect has to be considered for 3ω measurements as well – the obtained thermal conductance decreases about 7% over the applied current range. The almost linear decrease with the square of the current of the curves in Fig. 8 suggests that the extrapolation of the curves to zero current obtained from a linear fit is reasonable for the calculation of the thermal conductance of the wire. Table II summarizes the results and contains literature values for comparison. The electrical resistivity ρ and the thermal conductivity κ were calculated using the geometric properties of the wire segment. ρ is clearly larger and κ is clearly smaller than the corresponding values of bulk nickel, which is attributed to enhanced grain-boundary scattering in the polycrystalline wire.³⁰ An even stronger deviation from the bulk values was observed by Ou *et al.*⁷ for a nanocrystalline nickel nanowire which was patterned from a nickel thin film. The large error for the specific values mainly results from uncertainties in the determination of the diameter using scanning electron microscopy. The Lorenz ratio is not influenced by this error. It was calculated from the resistance and the thermal conductance of the suspended wire segment according to

$$L = \frac{GR}{T}, \quad (44)$$

where T is the temperature.

Stojanovic *et al.*³¹ recently calculated the thermal conductivity and the Lorenz ratio for rectangular metallic wires with characteristic sizes between 25 nm and 500 nm at room temperature by using the Boltzmann transport equation. They considered thermal conductivity contributions from electrons and phonons. Besides electron-phonon and phonon-phonon scattering, they addressed scattering at grain boundaries and at the surface. Concerning the Lorenz ratio, Stojanovic *et al.*³¹ find that it starts to rise significantly for characteristic sizes of the wires below 100 nm. If this is true, then a Lorenz ratio close to the one for bulk (or slightly increased) is expected for the investigated nickel wire which has a diameter of 150 nm. As listed in Table II, the determined values for $L_{3\omega}$ and $L_{1\omega}$ are close to, but smaller than the bulk value. The relative deviations from the bulk value are 3% for $L_{3\omega}$ and 13% for $L_{1\omega}$.

VI. SUMMARY

We have investigated the influence of a voltage source on the applicability of 1ω and 3ω methods that assume a cur-

rent source for data analysis. We have derived the Fourier representation of the current and the measurement voltage and obtained the following results:

- The harmonic components of the current ($I_{n\omega}$) decrease exponentially with index n .
- For 1ω methods using a voltage source, the data can be analyzed assuming a current source.
- For direct 3ω methods using a voltage source, the usual formalism assuming a current source can be applied if a correction factor is considered.
- For 3ω measurements using CMS and a voltage source, the data can be analyzed assuming a current source.

The results are based on the usual assumption for 1ω and 3ω methods – the assumption that resistance oscillations of the sample are small compared to the sample resistance. The current used for data analysis is the 1ω component of the actual current, which is measured. Only for direct 3ω measurements, the replacement of the current source with a voltage source can lead to significant effects on the measurement signal, which make a correction necessary. However the determination of the correction factor represents an additional error source. For certain sample geometries it is not possible to determine the correction factor. Consequently a current source should be used in such cases, or alternatively either 1ω measurements or 3ω measurements with CMS should be applied. A further disadvantage of direct 3ω measurements is due to harmonic distortions from the source (either voltage or current source), which would be removed from the measurement signal by using CMS.

ACKNOWLEDGMENTS

This work was supported by the German Research Council (DFG) in the framework of the priority program SPP1386 (Nanostructured Thermoelectrics: Theory, Model Systems, and Controlled Synthesis). We thank J. Gooth for the synthesis of nickel nanowires and B. Hamdou for assistance during measurements.

¹D. G. Cahill, Rev. Sci. Instrum. **61**, 802 (1990).

²D. G. Cahill, M. Katiyar, and J. R. Abelson, Phys. Rev. B **50**, 6077 (1994).

³T. Borca-Tasciuc, A. R. Kumar, and G. Chen, Rev. Sci. Instrum. **72**, 2139 (2001).

⁴J.-L. Battaglia, C. Wiemer, and M. Fanciulli, J. Appl. Phys. **101**, 104510 (2007).

⁵A. Jacquot, B. Lenoir, A. Dauscher, M. Stölzer, and J. Meusel, J. Appl. Phys. **91**, 4733 (2002).

⁶L. Lu, W. Yi, and D. L. Zhang, Rev. Sci. Instrum. **72**, 2996 (2001).

074903-10 Kimling, Martens, and Nielsch

Rev. Sci. Instrum. **82**, 074903 (2011)

- ⁷M. N. Ou, T. J. Yang, S. R. Harutyunyan, Y. Y. Chen, C. D. Chen, and S. J. Lai, *Appl. Phys. Lett.* **92**, 063101 (2008).
- ⁸T. Y. Choi, D. Poulidakos, J. Tharian, and U. Sennhauser, *Appl. Phys. Lett.* **87**, 013108 (2005).
- ⁹C. Dames and G. Chen, *Rev. Sci. Instrum.* **76**, 124902 (2005).
- ¹⁰F. Völklein and E. Kessler, *Phys. Status Solidi A* **81**, 585 (1984).
- ¹¹F. Völklein, *Thin Solid Films* **188**, 27 (1990).
- ¹²F. Völklein, H. Reith, T. W. Cornelius, M. Räuber, and R. Neumann, *Nanotechnology* **20**, 325706 (2009).
- ¹³E. Yusibani, P. Woodfield, M. Fujii, K. Shinzato, X. Zhang, and Y. Takata, *Int. J. Thermophys.* **30**, 397 (2009).
- ¹⁴P. B. Kaul, K. A. Day, and A. R. Abramson, *J. Appl. Phys.* **101**, 083507 (2007).
- ¹⁵S. Shin, T.-J. Ha, H.-H. Park, and H. H. Cho, *J. Phys. D: Appl. Phys.* **42**, 125404 (2009).
- ¹⁶T. Coquil, E. K. Richman, N. J. Hutchinson, S. H. Tolbert, and L. Pilon, *J. Appl. Phys.* **106**, 034910 (2009).
- ¹⁷B. N. Pantha, R. Dahal, J. Li, J. Y. Lin, H. X. Jiang, and G. Pomrenke, *Appl. Phys. Lett.* **92**, 042112 (2008).
- ¹⁸H. Tong, J. Zhang, G. Liu, J. A. Herbsommer, G. S. Huang, and N. Tansu, *Appl. Phys. Lett.* **97**, 112105 (2010).
- ¹⁹B. W. Olson, S. Graham, and K. Chen, *Rev. Sci. Instrum.* **76**, 053901 (2005).
- ²⁰J.-Y. Duquesne, *Phys. Rev. B* **79**, 153304 (2009).
- ²¹I. S. Gradshteyn and I. W. Ryzhik, *Summen-, Produkt- und Integraltafeln* (Verlag Harri Deutsch, Frankfurt, 1981).
- ²²I. N. Bronstein, K. A. Semendjaev, G. Musiol, and H. Mühlig, *Taschenbuch der Mathematik* (Verlag Harri Deutsch, Frankfurt, 2001).
- ²³L. Shi, D. Y. Li, C. H. Yu, W. Y. Jang, D. Y. Kim, Z. Yao, P. Kim, and A. Majumdar, *ASME Trans. J. Heat Transfer* **125**, 881 (2003).
- ²⁴E. Shapira, A. Tsukernik, and Y. Selzer, *Nanotechnology* **18**, 485703 (2007).
- ²⁵A. Jacquot, M. Stölzer, J. Meusel, O. Boffoue, B. Lenoir, and A. Dauscher, in *Proceedings of the Fifth European Workshop on Thermoelectrics*, Padubice, 1999, p. 31.
- ²⁶O. P. Watts, *Trans. Am. Electrochem. Soc.* **29**, 395 (1916).
- ²⁷T. M. Whitney, J. S. Jiang, P. C. Searson, and C. L. Chien, *Science* **261**, 1316 (1993).
- ²⁸L. Sun, P. C. Searson, and C. L. Chien, *Appl. Phys. Lett.* **74**, 2803 (1999).
- ²⁹K. Nielsch, F. Müller, A.-P. Li, and U. Gösele, *Adv. Mater.* **12**, 582 (2000).
- ³⁰A. F. Mayadas and M. Shatzkes, *Phys. Rev. B* **1**, 1382 (1970).
- ³¹N. Stojanovic, D. H. S. Maithripala, J. M. Berg, and M. Holtz, *Phys. Rev. B* **82**, 075418 (2010).
- ³²T. M. Tritt, *Thermal Conductivity: Theory, Properties, and Applications* (Kluwer, New York, 2004).

5 Ferromagnetic Nanowires

This chapter summarizes our results on Ni nanowires synthesized via electrodeposition in the pores of anodic aluminum oxide (AAO) membranes. Preparation steps and process parameters of the anodization of the AAO membranes and of the electrodeposition of Ni are given in Tables E.1 and E.2 in Appendix E. Millimeter-sized bundles of nanowires with diameters between 150 and 350 nm were dripped on a substrate and examined by x-ray diffraction at the Hamburg Synchrotron Radiation Laboratory to determine their average grain size. This was done by Dr. Andriy Zolotaryov who found that the wires are polycrystalline with an average grain size of about 30 nm. This value is well below the diameters of the wires, therefore we expect that the classical size effects are dominated by scattering at grain boundaries with a minor contribution from surface scattering.

Section 5.1 summarizes the preparation steps of the microdevice and introduces the measuring setup used for 3ω measurements on individual Ni nanowires under applied magnetic fields. Section 5.2 discusses the contact issues that may arise due to the width of the metal leads and due to the contact resistances between metal leads and nanowire in such microdevices. Section 5.3 discusses the influence of spurious 3ω currents due to nonlinearities of the current source or time-varying resistances that may contribute to the 3ω voltage. Section 5.4 presents experimental results on the diameter dependence of several transport properties measured on various Ni nanowires and discusses the impact of classical size effects. At the end of this chapter, we propose a simple model to describe a new effect – the anisotropic magnetothermal resistance effect – and present experimental results on it, which have been published in Ref. [Kim13a] reprinted in Sec. 5.5.

5.1 3ω Microdevice

Nanowires are transferred to Si substrates by dripping of a suspension containing electrodeposited Ni nanowires. The Si substrates are electrically isolated by a 300-nm-layer of SiO_2 . For thermal conductivity measurements the Si substrates are structured with micrometer-sized trenches using contact lithography and reactive ion-etching. The preparation steps and process parameters are summarized in Table E.4 in Appendix E. The Ni nanowires are aligned perpendicular to the trenches by applying magnetic fields, while the solvent evaporates. This enhances the chance for the nanowires to cross a trench. Microdevices that allow for 3ω measurements are fabricated either by photo-projection lithography¹² or by laser lithography, followed by sputter deposition and lift-off. The native-oxide shell surrounding the nanowires is removed via Ar-sputter etching in the same sputter chamber where the metalization takes place. Details of the preparation steps and process parameters used are summarized in Tables E.5 and E.6 in Appendix E. Figure 5.1(a) shows a light-microscope image of a sample after exposure and development of the photo resist. The reddish areas uncovered with photo resist define the later structure of the metal contacts. Figure 5.1(b) depicts a scanning electron micrograph of

¹²A detailed description of the photo-projection lithography microscope can be found in the Diploma thesis of Tim Böhnert [Bhne 09]

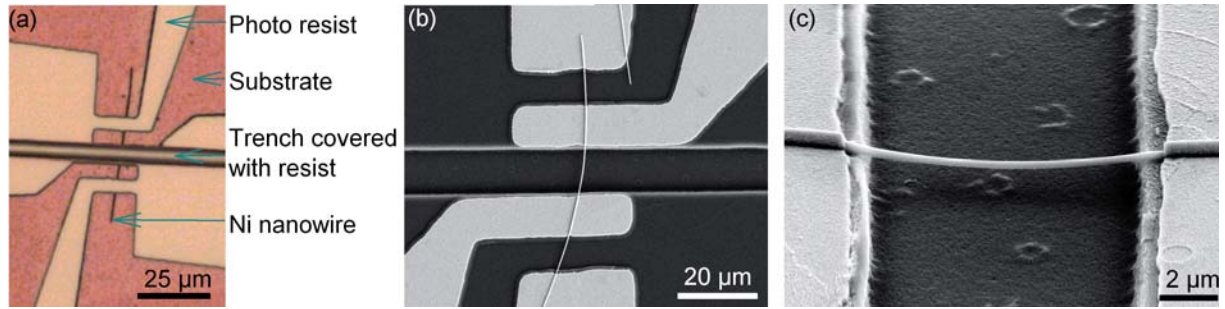


Figure 5.1: (a) Light-microscope image of a sample after exposure and development of the photo resist. The sample includes a Ni nanowire that crosses a trench etched into the substrate. (b) Scanning-electron micrograph of a similar device after the lift-off process. (c) Tilted view into the trench of the device shown in (b) using a tilt angle of 70 degrees.

another sample after the lift-off process. A tilted view into the trench under an angle of 70 degrees with respect to the surface normal is presented in Fig. 5.1(c). Wires with diameters below 150 nm that were suspended over the 3 to 5 μm wide trenches broke during the spin-coating process and could not be investigated using the present microfabrication approach. The nanowires investigated with diameters between 150 and 350 nm were electrodeposited in a single AAO membrane that exhibited this broad distribution of pore-channel diameters. The measuring principle of the 3ω method applied to wires is explained in Secs. 4.1 and 4.4. Figure 5.2 depicts the measuring setup employed. The sample is connected with the measuring apparatus using a micromanipulated probestation (Lakeshore EMPX), which is described Appendix E. The measuring voltage is dominated by a large 1ω component that disturbs the detection of the small 3ω voltage. The ratio of the two amplitudes is typically $U_{3\omega}/U_{1\omega} \approx 5 \times 10^{-3}$ for the nanowires investigated. In this case the dynamic reserve of the lock-in amplifier used is sufficient for detecting $U_{3\omega}$ with an accuracy $\Delta U_{3\omega}/U_{3\omega} \approx 0.1\%$ for typical temperature oscillations of the order of 1 K. The voltage output of a lock-in amplifier (Stanford Research Systems SR830) in combination with a 10 kΩ ballast resistor serves as the current source of the experiment. The sample is connected in series with a 10 Ω precision resistor that has a negligible temperature coefficient. $U_{3\omega}$ and $U_{1\omega}$ across the sample and across the precision resistor are measured directly using two lock-in amplifiers (Stanford Research Systems SR830). The voltages measured across the precision resistor are used to determine the 1ω - and 3ω -components of the applied current. The latter mainly arises from nonlinearities of

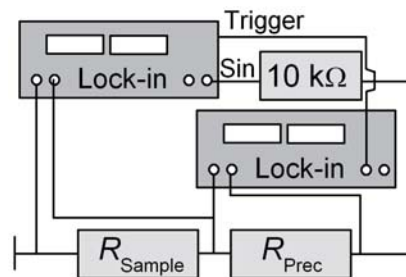


Figure 5.2: Measuring setup used for 3ω measurements on individual nanowires.

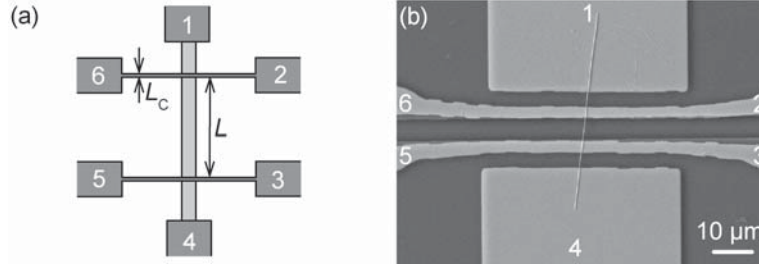


Figure 5.3: (a) Illustration of a four-point measuring device with thin voltage probes ($L_C \ll L$). (b) Scanning-electron micrograph of a four-probe measuring microdevice that includes a Ni nanowire suspended over a trench. Due to lithographic limits $L_C \approx L$.

the internal voltage generator of the lock-in amplifier (see Sec. 5.3). It generates a spurious 3ω voltage across the sample that needs to be subtracted from the measuring voltage.

5.2 Contact Issue

5.2.1 Four-point measurement

Figure 5.3(a) shows a sketch of a four-point measuring device with thin voltage probes in electrical contact with a wire (wire radius: r , resistivity: ρ , distance between the inner contacts: L , resistance of the wire between the inner contacts: R_W). The potential drop along the wire is not influenced by the presence of the inner contacts, because $L_C \ll L$. If a current I_0 is injected through the outer contacts, the voltage U_{1234} measured with the inner contacts can be used to determine ρ according to Ohm's law:

$$U_{1234} = R_W I_0 = \rho \frac{L}{\pi r^2} I_0. \quad (5.1)$$

5.2.2 Four-probe measurement

Figure 5.3(b) depicts a four-probe microdevice that includes a nanowire. It can be seen that the width L_C of each inner contact is now of the order of L . Therefore, a significant amount of the current can flow through the contacts making Eq. (5.1) inapplicable. The voltage measured with the inner probes can be expressed using an effective length L^* , which may assume values in the range $L < L^* < L + L_C$:

$$U_{1234} = R_W^* I_0 = \rho \frac{L^*}{\pi r^2} I_0. \quad (5.2)$$

The exact value of L^* is unknown. If the specific contact resistance between the contact material and the nanowire were known, L^* could in principle be determined by numerical simulations. Here, we are interested only in the two limiting cases. For large contact resistances, L^* can be replaced by $L + L_C$; for negligible contact resistances, L^* can be replaced by L . As shown in the following, comparison of four-probe measurements with pseudo four-probe measurements on the same sample can deliver a criterion for judging if one of the two limiting cases is applicable.

5.2.3 Pseudo four-probe measurements

If the same current I_0 as above is injected through the inner contacts, the voltage drop U_{6235} measured at the opposite sides between the inner contacts includes the potential drop due to the contact resistance $R_{C1} + R_{C2} \equiv 2R_C$:

$$U_{6235} = (R_W + 2R_C)I_0 = \left(\rho \frac{L}{\pi r^2} + 2R_C\right)I_0. \quad (5.3)$$

The measuring voltages for both types of measurements are equal if the following condition holds:

$$U_{6235} = U_{1234} \Leftrightarrow L^* = L \left(1 + \frac{2R_C}{R_W}\right). \quad (5.4)$$

We can distinguish the following three cases:

- (i) $U_{6235} = U_{1234} \wedge 2R_C \ll R_W \Rightarrow L^* = L$;
- (ii) $U_{6235} \sim U_{1234} \wedge 2R_C \sim R_W \frac{L_C}{L} \Rightarrow L \leq L^* \leq L + L_C$;
- (iii) $U_{6235} \gg U_{1234} \Rightarrow 2R_C \gg R_W \Rightarrow L^* = L + L_C$;

For a metal contact sputter deposited on a metal wire one can usually assume that $2R_C \ll R_W$. Due to spreading of the current into the wide contact metal of low longitudinal resistance, the potential drop over the width of the contact can become small compared to the one between the contact leads. If this is verified by $U_{6235} = U_{1234}$, it is reasonable to apply case (i) and set $L^* = L$. For a metal contact sputter deposited on a semiconducting wire it can happen that $2R_C \gg R_W$. In that case one measures $U_{6235} \gg U_{1234}$, which corresponds to case (iii), for which $L^* = L + L_C$ holds. In the indefinite case (ii), the uncertainty $L < L^* < L + L_C$ remains.

Table 5.1 compares four-probe voltages with pseudo four-probe voltages measured on three Ni nanowires with different diameters. The contact material used was Ti(5 nm)/Pt(150 nm), i.e. a metal on metal contact for which we expect $2R_C \ll R_W$. For each sample the different voltages measured show good agreement with each other. This indicates that case (i) is valid. We believe that the deviations, in particular for the 180-nm-wire, arose from shadowing effects due to the modification of the sputter coater used for depositing Pt (compare Table E.6 in Appendix E).

Table 5.1: Voltages $U_{(xxxx)}$, measured for the different contact configurations (1234), ..., (2653) on three Ni nanowires with diameters of 160 nm, 210 nm, and 180 nm. Details are given in the main text and in Fig. 5.3. The contact material used was Ti(5 nm)/Pt(150 nm).

	(1234)	(1654)	(6235)	(2653)	Diameter
$U_{(xxxx)}$ (mV)	13.79	13.85	13.94	13.95	160 nm
	10.66	10.72	10.41	10.39	210 nm
	14.64	14.56	12.00	14.09	180 nm

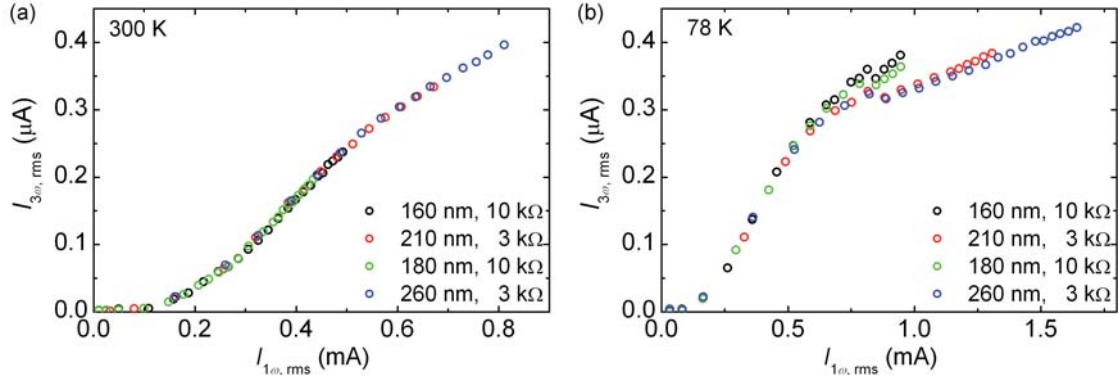


Figure 5.4: Amplitude of the 3ω current, $I_{3\omega}$, plotted against the amplitude $I_{1\omega}$, measured on several Ni nanowires using different ballast resistances, as indicated in the graphs. The measurements shown in (a) were performed at 300 K, those shown in (b) at 78 K.

5.3 Spurious 3ω Currents

In Sec. 4.7, different measuring setups used for 3ω measurements are discussed, and current-driven setups are compared with voltage-driven setups. It is mentioned that for direct 3ω measurements (without subtraction of the 1ω voltage) spurious 3ω and 5ω currents arising, e.g., from nonlinearities of the current source or time-varying resistances, may contribute to the 3ω voltage measured. However, there is a possibility to remove the dominant contribution that arises from the 3ω current, by simply measuring the 3ω current [Yusi 09]. We do this using a $10\ \Omega$ precision resistance with negligible temperature coefficient connected in series with the sample. It turns out that the 3ω current does neither depend significantly on the sample nor on the current-defining preresistor ($10\ \text{k}\Omega$ or $3\ \text{k}\Omega$), which indicates that the 3ω current mainly arises from nonlinearities of the signal generator, in this case the voltage source of the lock-in amplifier. This is demonstrated in Fig. 5.4, which shows the amplitude $I_{3\omega}$ of the 3ω current plotted against the amplitude $I_{1\omega}$ measured on several Ni nanowires using different ballast resistances, as indicated in the graphs. At 300 K the curves are identical, while at 78 K small sample-specific deviations occur for higher applied currents. The 3ω current is in-phase with the heating current, while the 3ω voltage oscillates out-of-phase to the heating current [see Eq. (4.6)]. Therefore, the amplitude of the spurious 3ω voltage across the sample resistance generated by $I_{3\omega}$ has to be added to the amplitude of the measured 3ω voltage. This gives the pure 3ω voltage used for determining the thermal conductance of the nanowire.

Inserting Eq. (4.16) into Eq. (4.6) one obtains the theoretical relation between the 3ω voltage $U_{3\omega}$ and the thermal conductance G of the nanowire on which a current $I_0 \sin(\omega_0 t)$ is imposed [Lu 01, Dame 05]:

$$U_{3\omega}(t) = -R_0 \frac{dR}{dT} I_0^3 \frac{1}{48G} \sin(3\omega_0 t), \quad (5.5)$$

where R_0 is the resistance of the wire at zero heating current and dR/dT is its temperature derivative. During the 3ω measurement the time-averaged resistance of the wire increases due to the heating current. Moreover, the resistance may change, e.g. by applying magnetic fields (compare Sec. 5.5). Then, it is convenient to approximate the time-averaged

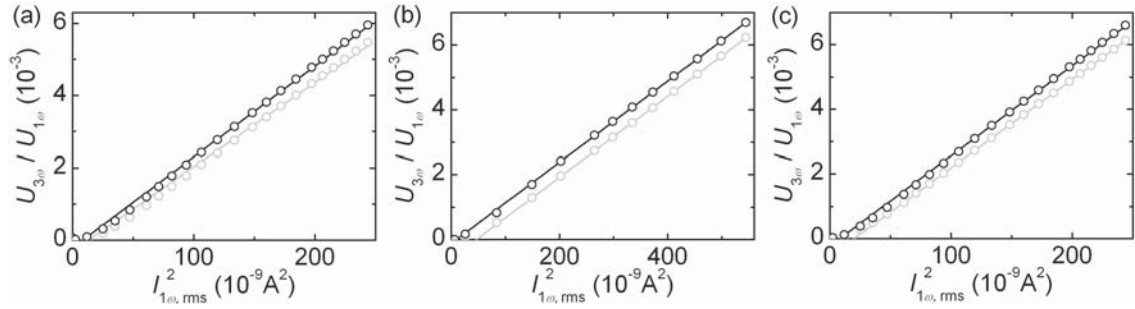


Figure 5.5: Data measured on three Ni nanowires with diameters of 160 nm (a), 210 nm (b), and 180 nm (c) plotted in the form of Eq. (5.6). The gray curves includes the contribution from the spurious 3ω voltage; the black curves are corrected by adding the amplitude of the spurious 3ω voltage.

resistance by $R \approx U_{1\omega}/I_{1\omega}$. Replacing R_0 in Eq. (5.5) by R and considering only the amplitude of $U_{3\omega}(t)$ yields

$$\frac{U_{3\omega}}{U_{1\omega}} = \frac{dR}{dT} I_0^2 \frac{1}{48G}. \quad (5.6)$$

Figure 5.5 shows measuring data for three Ni nanowires plotted in the form of Eq. (5.6). The gray curves correspond to the as-measured data; the black curves were corrected by adding the amplitude of the spurious 3ω voltage. It can be seen that the corrected curves run through the origin of the coordinate system as predicted by Eq. (5.6), while the non-corrected ones cut the negative y -axis.

5.4 Classical Size Effects in Ni Nanowires

Figure 5.6 summarizes room temperature values of electrical resistivity ρ , thermal conductivity κ , Lorenz number L , and temperature coefficient of resistivity α of the individual Ni nanowires investigated, and compares them with literature values for high purity bulk Ni (dotted lines) [Whit 59] and for polycrystalline to nanocrystalline bulk Ni (broken-dotted lines, numbers indicate the average grain sizes) [Aus 94]. The broken line in Fig. 5.6(c) indicates the Sommerfeld value L_0 .¹³ For some nanowires results only appear in Fig. 5.6(a), because the wires were destroyed by electrostatic discharges or transient voltages before the measurements for determining κ could be completed. The average grain size, determined by x-ray diffraction on millimeter-sized bundles of nanowires from the same batch, was about 30 nm. However, the comparison of the diameter dependence of ρ plotted in Fig. 5.6(a) with the literature values for polycrystalline to nanocrystalline bulk Ni indicates that the grain sizes of nanowires with diameters above 250 nm are between 15 nm and 35 nm, while the grain sizes of nanowires with diameters below 250 nm are above 35 nm and clearly exceed the diameters for the thinnest nanowires investigated. In the latter cases the classical size effects diminishing the conductivities are dominated by surface scattering. As most of the heat is carried by electrons, the diameter-dependence of κ shown in Fig. 5.6(b) follows the behavior of $\sigma = 1/\rho$. The Lorenz numbers determined are shown in Fig. 5.6(c). The values are in reasonable agreement with the Lorenz number

¹³The resistivity ρ was determined from four-probe measurements (compare Sec. 5.2); κ was obtained using 3ω measurements; L was calculated using ρ and κ ; and α was determined either from continuous resistance measurements under slowly raising sample temperatures (about 5 K/h), or from subsequent resistance measurements at different sample temperatures over a wide range of temperatures.

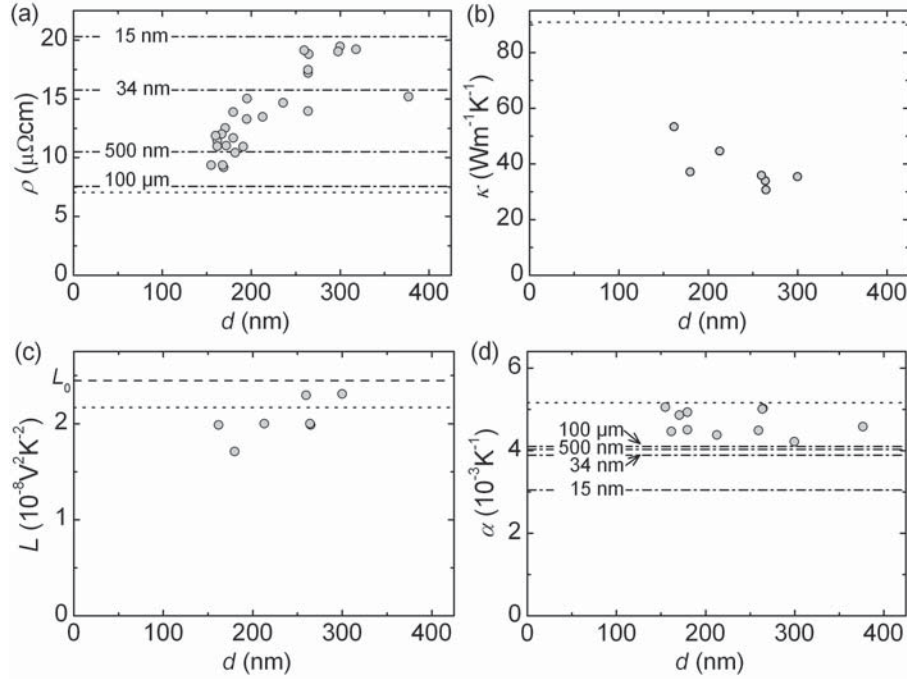


Figure 5.6: Room temperature data of (a) Electrical resistivity ρ , (b) thermal conductivity κ , (c) Lorenz number L , and (d) temperature coefficient of the resistance, plotted against the diameter of the different Ni nanowires investigated. The broken-dotted lines in (a) and (d) indicate data of polycrystalline to nanocrystalline bulk Ni determined by Aus *et al.* [Aus 94]. The dotted lines in (b) and (c) indicates data of high purity bulk Ni determined by White and Woods [Whit 59]. The broken line in (c) indicates the Sommerfeld value of L .

of bulk Ni. The plot may indicate a trend to smaller L 's with decreasing diameters. This could be explained by the crystallographic structure of the wires suggested: Reduced scattering of phonons and magnons at grain boundaries due to larger grain sizes in the thinner wires increases the inelastic scattering rate of electrons resulting in a drop of L . This conjecture is supported by the diameter-dependence of α shown in Fig. 5.6(d) that may indicate a trend to larger α 's with decreasing diameters - a behavior that also suggests that the inelastic scattering rate increases as the diameter drops. Apart from this, the determined values of α fall between the literature values for high purity bulk (dotted line) and bulk Ni with grain sizes of $100 \mu\text{m}$ (highest broken-dotted line).

5.5 Anisotropic Magnetothermal Resistance in Ni Nanowires

In ferromagnetic conductors, the two spin subsystems are characterized by different thermal conductivities and can have different temperatures (see Sec. 2.11). In a ferromagnetic metal, most of the heat is carried by electrons. Therefore, it is natural to expect that there is a thermal analogue to the anisotropic magnetoresistance effect (see Sec. 2.10) in such materials. We have observed this effect in individual Ni nanowires using a slightly modified 3ω method as already discussed in Sec. 5.3.

It has been suggested that the anisotropic magneto Seebeck effect in Ni nanowires would arise from interfaces [Wegr 06]. In our single-nanowire microdevice employed [see Figs. 5.1 and 5.3(b)], heat is generated at the center of the suspended wire segment and spreads into the heat sink at the edges of the trench. Due to the symmetry of the temperature profile along the nanowire the thermovoltage across the suspended nanowire segment is

zero. The heat sink is determined by the temperature of the substrate that does not change during the 3ω measurements. The nanowire is thermally anchored to the heat sink via large metal contacts with high thermal conductivities. Hence, we expect that the anisotropic magnetothermal resistance effect observed arises from the bulk, and not from interfaces.

The length of the suspended nanowire segment ($\sim 5 \mu\text{m}$) is much larger than the spin-diffusion length, and there are no temperature gradients through interfaces. In this case spin-dependent heat models can be developed in analogy to spin-dependent charge models [Slac 11]. Our results on the anisotropic magnetothermal resistance have been published in Ref. [Kim13a] reprinted in the following pages. The Supplemental Material to this publication is reprinted in Appendix D.

We propose that the modified 3ω technique used may also be applied for investigating the giant magnetothermal resistance (GMTR) effect in the current-perpendicular-to-the-planes geometry, e.g. in Co/Cu multilayered nanowires. By comparing the GMTR effect with the GMR effect on the same sample one could obtain information about the spin-heat diffusion length (compare Sec. 2.11).

Anisotropic Magnetothermal Resistance in Ni Nanowires

Reprinted with permission from

Johannes Kimling, Johannes Gooth, and Kornelius Nielsch

Physical Review B **87**, 094409 (2013)

Copyright 2013 by the American Physical Society.

The contributions of each author to the research study are indicated in the table below using the following specifications: Conception of the research study (1), sample preparation (2), measurements (3), data analysis (4), interpretation (5), and composition of the manuscript (6).

JK	JG	KN
1,2,3,4,5,6	2	1

Anisotropic magnetothermal resistance in Ni nanowires

Johannes Kimling,* Johannes Gooth, and Kornelius Nielsch

Institut für Angewandte Physik, Universität Hamburg, Jungiusstraße 11, D-20355 Hamburg (Germany)

(Received 15 January 2013; revised manuscript received 9 February 2013; published 8 March 2013)

We present measurements of the electrical and thermal transport properties of individual Ni nanowires as a function of the applied magnetic field, recorded in the temperature range between 78 and 380 K. In analogy to the anisotropic magnetoresistance (AMR) effect observed in ferromagnetic conductors, we find that the thermal resistance of Ni nanowires depends on the angle between magnetization vector and current direction. This anisotropic magnetothermal resistance effect turns out to be weaker than the AMR effect in Ni nanowires over the temperature range investigated. As a consequence, also the Lorenz number is found to be anisotropic with respect to the magnetization direction. To explain our observation, we propose a simple model that considers spin mixing due to electron-magnon scattering.

DOI: 10.1103/PhysRevB.87.094409

PACS number(s): 75.47.-m, 73.63.-b, 72.15.Gd

I. INTRODUCTION

In ferromagnetic metals the electrical resistivity depends on the direction of the current relative to the magnetization vector.¹ This effect is known as anisotropic magnetoresistance (AMR) and its physical origin has been ascribed to the spin-orbit interaction.^{2–7} The AMR effect in ferromagnetic nanowires has been used, for example, to determine the critical fields for magnetization reversal,^{8–11} or to detect magnetic domain walls.^{12,13} The work of Kamalakar *et al.* focused on the electrical transport properties of Ni nanowires.^{14,15} Thermal and thermoelectric transport measurements were reported for lithographically patterned thin films.^{16,17} Anisotropies similar to AMR have been observed in the Seebeck coefficient of ferromagnetic nanowires^{18,19} and of ferromagnetic thin films.²⁰ Research in the coupling of spin, charge, and heat currents in magnetic thin films and nanostructures is nowadays categorized in the field of spin caloritronics.²¹ Occasionally, the physical origin of the AMR effect is ascribed to spin-dependent scattering ignoring that the symmetry breaking element arises from the spin-orbit interaction.²⁰ In this context it is interesting to know that in 1999 Ebert *et al.* saw an upcoming trend in the literature to connect the AMR with the giant magnetoresistance and the colossal magnetoresistance.⁷ To emphasize the quite different physical origin of these effects they used the name “spontaneous magnetoresistance anisotropy” instead of AMR.⁷

We have measured the electrical and thermal transport properties of individual Ni nanowires as a function of the applied magnetic field in the temperature range between 78 and 300 K. Similar to the AMR effect, we observe an anisotropy of the thermal resistance that in the following will be called anisotropic magnetothermal resistance (AMTR) effect. Investigating the thermal conductivity requires accurate temperature measurements and control over heat generation and heat flow. Our experimental technique is based on the so-called 3ω method that has widely been used for determining the thermal properties of bulk materials,²² thin films,²³ and suspended wires.^{16,24} The characteristic heat diffusion lengths for 3ω measurements range from 100 μm for bulk materials and thin films, to a few micrometers for nanowires. Due to the small length scale, the 3ω method is insensitive to background thermal leakages caused by radiation.²² Likewise,

the corresponding time scales are short, of the order of 1 μs for the Ni nanowire device employed in our work. This is advantageous for observing the AMTR effect. Moreover, in the case of suspended wires, simultaneous measurements of the resistance of the wire, in principle, allows for the direct measurement of the field dependence of the Lorenz number.

The AMR and AMTR effects can be quantified using AMR and AMTR ratios. We define the ratios to be

$$\frac{\Delta R}{R^\perp} = \frac{R^\parallel - R^\perp}{R^\perp}; \quad \frac{\Delta W}{W^\perp} = \frac{W^\parallel - W^\perp}{W^\perp}, \quad (1)$$

where R^\parallel (R^\perp) is the electrical resistance and W^\parallel (W^\perp) is the thermal resistance at saturation fields applied parallel (perpendicular) to the wire axis; ΔR denotes the absolute AMR; and ΔW denotes the absolute AMTR. Before we discuss the experiment and present the results, we describe the AMTR effect in terms of a simple model that is developed in analogy to the AMR effect. To explain our measurement results, we recapitulate basic knowledge on the AMR effect.

II. ANISOTROPIC MAGNETOTHERMAL RESISTANCE

Most of the theoretical models on AMR are based on the two-current s - d scattering model.²⁵ This model separates the current into a contribution from majority-spin electrons with a resistivity ρ_M and a contribution from minority-spin electrons with a higher resistivity $\rho_m > \rho_M$. The spin-orbit interaction gives rise to mixing or hybridization of the two spin subsystems that causes anisotropic scattering probabilities, for example, of majority spin electrons into minority spin states.^{2–7} This mechanism results in a difference $\Delta\rho = \rho^\parallel - \rho^\perp$ between the resistivities parallel and perpendicular to the spontaneous magnetization. Although the semiclassical models are not rigorous, they provide intuitive understanding of the AMR effect. Campbell *et al.*³ assumed that ρ_m is solely due to s - d scattering arising from isotropic scattering potentials. They considered spin mixing due to electron-magnon scattering by using the spin-flip parameter ρ_{sf} .²⁶ The AMR ratio is given by³

$$\frac{\Delta\rho}{\rho^\perp} = \gamma \frac{(\rho_m - \rho_M)\rho_m}{\rho_M\rho_m + \rho_{sf}(\rho_M + \rho_m)}, \quad (2)$$

$$\rho_\sigma = \rho_\sigma^0 + \rho_\sigma^v(T), \quad \sigma \in \{m, M\},$$

where γ is a constant that is related to the spin-orbit coupling constant, ρ^0 is the residual resistivity, and ρ^v is the resistivity due to electron-phonon scattering. According to this model, the temperature dependence of the AMR ratio is due to inelastic scattering: electron-magnon scattering that tends to equalize the spin-dependent resistivities, and electron-phonon scattering that is characterized by a different spin asymmetry compared to the scattering at disordered magnetic impurities ($\alpha^0 \equiv \rho_m^0/\rho_M^0 \neq \rho_m^v/\rho_M^v \equiv \alpha^v$).

For ferromagnetic alloys, it was suggested that the main origin of the temperature dependence of the AMR ratio lies in an anisotropic scattering potential for electron-phonon scattering.²⁷ It was shown by Smit that for nonspherical scattering potentials arising from phonons, grain boundaries, and nonmagnetic impurities, the anisotropy of the transition probability is reduced compared to the transition probability arising from disordered magnetic impurities.² Therefore, the AMR ratio decreases as the number of phonons rises, and thus as the temperature rises. In this case the following expression allows for determining the different AMR ratios originating from electron-impurity scattering and from electron-phonon scattering:^{27,28}

$$\frac{\Delta\rho}{\rho^\perp}(T) = \left(\frac{\Delta\rho}{\rho^\perp}\right)_{\text{ph}} + \left[\left(\frac{\Delta\rho}{\rho^\perp}\right)_{\text{im}} - \left(\frac{\Delta\rho}{\rho^\perp}\right)_{\text{ph}}\right] \frac{\rho^\perp(0)}{\rho^\perp(T)}, \quad (3)$$

where $\rho^\perp(0) = \rho_{\text{im}}^\perp$ is the residual resistivity at zero temperature. While experimental data on ferromagnetic alloys follow the behavior predicted by Eq. (3), the situation is different for pure ferromagnets. There, due to the lack of magnetic impurities, electron scattering at grain boundaries and phonons lead to a small AMR ratio with a weak temperature dependence.² In this case, electron-magnon scattering is required to explain the weak decrease of AMR, which is typically observed at high temperatures.

A thermal analog of the two-current model has recently been proposed by Heikkilä *et al.*^{29,30} Within this spin-dependent heat model the two spin channels are characterized by spin-dependent thermal conductivities and temperatures. Assuming a homogeneous ferromagnet (no spin-dependent temperature), the AMTR ratio is given by the equivalent expression of Eq. (2), replacing electrical resistivities by thermal resistivities:

$$\frac{\Delta w}{w^\perp} = \gamma \frac{(w_m - w_M)w_m}{w_M w_m + w_{\text{sf}}(w_M + w_m)}. \quad (4)$$

In contrast to Campbell *et al.*³, who described ferromagnetic alloys, we assume that all spin-dependent scattering is intrinsically caused by the spin-polarized band structure of pure Ni. Therefore, we assume that all scattering mechanisms j are characterized by the same asymmetry parameter:

$$\alpha^j = \frac{\rho_m^j}{\rho_M^j} = \frac{w_m^j}{w_M^j} \equiv \alpha. \quad (5)$$

The equality between electrical and thermal resistance ratios in this equation is tantamount to the assumption that the Lorenz number $L^j = \rho^j/(w^j T)$, where T is the temperature, is solely determined by the nature of the scattering mechanism j , and thus equal for both spin subsystems. Inserting Eq. (5) into

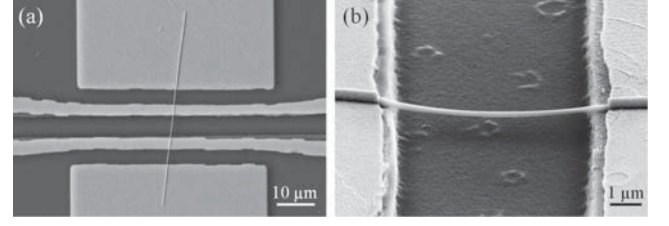


FIG. 1. Scanning electron micrographs of the microdevice used for 3ω measurements on individual nanowires. (a) Top view of a Ni wire with a diameter of 210 nm that is suspended over a trench and connected to four platinum electrodes. (b) Side view of a Ni wire with a diameter of 250 nm that is suspended over a trench (tilt angle: 70° with respect to the substrate normal). The depth of the trenches between the inner contacts is $1 \mu\text{m}$.

Eqs. (2) and (4) we obtain

$$\frac{\Delta\rho}{\rho^\perp} = \gamma \frac{\alpha(\alpha - 1)}{\alpha + \frac{\rho_{\text{sf}}}{\rho_M}(1 + \alpha)}, \quad (6)$$

$$\frac{\Delta w}{w^\perp} = \gamma \frac{\alpha(\alpha - 1)}{\alpha + \frac{w_{\text{sf}}}{w_M}(1 + \alpha)}. \quad (7)$$

If the major contribution to ρ_{sf} and w_{sf} comes from inelastic electron-magnon scattering, it can be expected that $\rho_M/w_M > \rho_{\text{sf}}/w_{\text{sf}}$. To summarize, the simple model developed above suggests two hypotheses: (i) there is an AMTR effect in ferromagnetic conductors due to the spin-orbit interaction, and (ii) in the presence of electron-magnon scattering the AMTR ratio is smaller than the AMR ratio.

III. EXPERIMENT

Nickel wires with diameters between 100 and 300 nm and lengths of $\sim 50 \mu\text{m}$ were grown by electrodeposition in porous alumina membranes.³¹ The wires are polycrystalline with an average grain size of $\sim 30 \text{ nm}$, as determined by x-ray diffraction on bundles of nanowires from the same batch. Figure 1 shows scanning electron micrographs of the microdevice employed for 3ω measurements. The device includes a Ni nanowire and four metal electrodes with ohmic contacts to the nanowire. Thermal isolation from the substrate is achieved by suspending the nanowire over a micrometer-sized trench. The specimen is connected to the measurement apparatus using a cryogenic probe station (LakeShore EMPX) that contains an electromagnet for applying horizontal fields up to 550 mT over a temperature range between 8 and 400 K. To avoid heat loss through convection the sample chamber is evacuated to pressures less than 5×10^{-5} mbar. Below we present results on three nanowires. Diameters and lengths of the suspended segment of the nanowires were determined using scanning electron microscopy. These values are summarized in Table I. Small contact resistances were achieved using rf

TABLE I. Geometrical properties of the nanowires investigated.

Wire number	Diameter (nm)	Suspended length (μm)
NW1	160 ± 10	5.8 ± 0.1
NW2	180 ± 10	5.5 ± 0.1
NW3	210 ± 10	5.8 ± 0.1

sputter etching with Ar gas to remove the native nickel oxide shell, directly before sputter deposition of the contact materials (4 nm Ti and 150 nm Pt). By comparing four probe measurements with pseudo four probe measurements, we confirmed that the contact resistances were negligible. The outer contacts are used to inject an alternating current at frequency 1ω into the nanowire that generates Joule heat at frequency 2ω . Due to the temperature-dependent resistivity of the nanowire, the temperature oscillation leads to a resistance oscillation at frequency 2ω that modulates the voltage measured between the inner contacts. The third harmonic component of this voltage, $U_{3\omega}$, is proportional to the amplitude of the temperature oscillation and therefore contains information about the thermal properties of the nanowire.^{22,24} The heating current at frequency 1ω is generated using the voltage output of a lock-in amplifier (Stanford Research Systems SR830) in combination with a 10 k Ω resistor. Due to imperfections, the voltage output contains a small component at frequency 3ω that generates a current at frequency 3ω . Furthermore, it is possible that besides the specimen, other time-varying resistances are included in the circuit that contribute to this spurious 3ω current.^{32,33} Across the resistance of the specimen, the spurious 3ω current generates a spurious 3ω voltage that contributes to the measurement signal. To obtain the pure 3ω voltage that arises from the temperature oscillations of the specimen, we determined the spurious 3ω voltages at each temperature by measuring the 3ω current using a heat sunk 10 Ω precision resistance that has a negligible temperature coefficient. The precision resistance is connected in series with the specimen. The amplitude of the 3ω voltage measured is typically of the order of 50 μV . The amplitude of the spurious 3ω voltage is of the order of 1–5 μV . The phase difference between the two signals is 180°, i.e., the amplitude of the pure 3ω voltage is obtained by adding both amplitudes. Given by the length of the suspended part of the wire ($\sim 5 \mu\text{m}$) the characteristic time of the heat diffusion process is of the order of 1 μs . The output frequency was 277 Hz; whence, the 3ω measurements are performed in the low-frequency limit where the thermal resistance is given by^{24,32}

$$W(H) = \frac{48U_{3\omega}(H)}{R(H)\frac{dR(H)}{dT}I^3}, \quad (8)$$

where R is the resistance of the suspended part of the nanowire, and d/dT denotes the temperature derivative; I is the amplitude of the applied current. In this equation we have indicated that besides $W(H)$, also $R(H)$ and $dR(H)/dT$ are functions of the applied magnetic field strength H . As a consequence, the heating and sensing properties of the device change in the presence of magnetic fields. To consider this we measured simultaneously the 3ω and the 1ω components of the voltage signal across the nanowire using two lock-in amplifiers (Stanford Research Systems SR830). Figures 2(a) and 2(b) show representative curves of $U_{3\omega}(H)$ and $U_{1\omega}(H)$ for fields applied perpendicular and parallel to the wire axis, measured at a temperature of 240 K. A comparison of the field dependence of $U_{3\omega}(H)$ and of $U_{1\omega}(H)$ at different temperatures is given in the Supplemental Material.^{34,35} The field dependence of $R(H)$ follows directly from $U_{1\omega}(H) = R(H)I$. The field dependence of $dR(H)/dT$ can, in principle, be determined from the

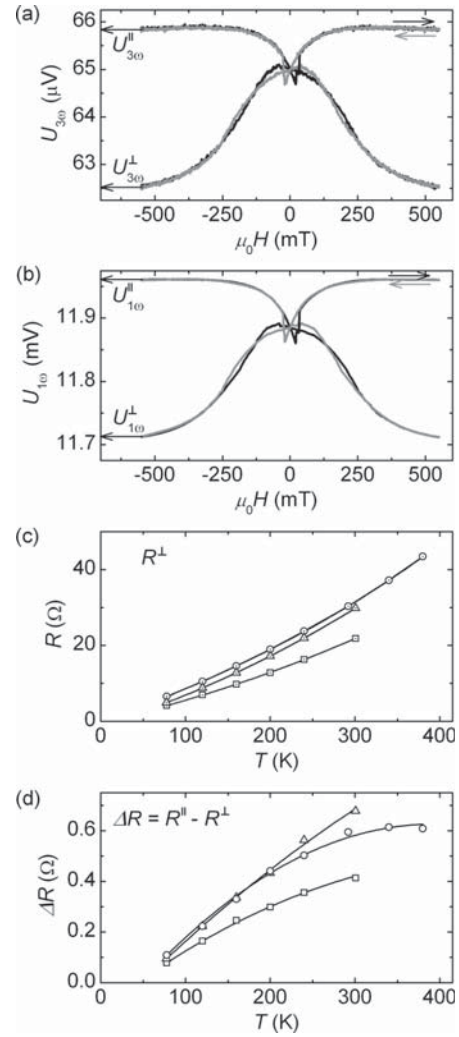


FIG. 2. (a) and (b) Field dependence of the third harmonic (a) and the first harmonic (b) components of the voltage signal at a temperature of 240 K, measured on NW1. The upper (lower) curves show the response to magnetic fields applied parallel (perpendicular) to the wire axis. (c) Temperature dependence of the resistance R^{\perp} at saturation fields applied perpendicular to the wire axis. (d) Temperature dependence of the difference $\Delta R = R^{\parallel} - R^{\perp}$, where R^{\parallel} denotes the resistance at saturation fields applied parallel to the wire axis. Circles, triangles, and squares in (c) and (d) indicate data measured on samples NW1, NW2, and NW3, respectively. Solid lines in (c) and (d) are fit curves to the measurement data using polynomial fits.

consecutive measurements of $R(H)$ at different temperatures. It was shown by Wegrowe *et al.* that the field dependence of $dR(H)/dT$ arises from two terms.³⁶ The first term considers the temperature variation of the absolute AMR, ΔR , and the second term is due to the thermal susceptibility of the magnetization.³⁶ At this point we should emphasize that with our work we aim to describe and observe the AMTR effect that is quantified by the AMTR ratio [Eq. (1)]. The interest of our work is not on the behavior of $W(H)$ during the magnetization reversal process. Therefore, we can focus on the saturation values denoted by W^{\perp} , R^{\perp} and W^{\parallel} , R^{\parallel} for saturation fields applied perpendicular and parallel to the wire

axis. At saturation fields, dR^{\parallel}/dT is given by³⁶

$$\frac{dR^{\parallel}}{dT} = \frac{dR^{\perp}}{dT} + \frac{d\Delta R}{dT}. \quad (9)$$

The temperature dependence of R^{\perp} and of ΔR of samples NW1, NW2, and NW3 are depicted in Figs. 2(c) and 2(d). The graphs include fit curves to the measurement data that were used to determine dR^{\perp}/dT and $d\Delta R/dT$. Due to the fact that the resistivity of Ni has a complicated temperature dependence in the temperature range under consideration,³⁷ we applied polynomial fits of second order. Inserting Eq. (8) into the second expression of Eq. (1) we can write the AMTR ratio in terms of the measurement quantities:

$$\frac{\Delta W}{W^{\perp}} = \frac{U_{3\omega}^{\parallel} U_{1\omega}^{\perp} \frac{dR^{\perp}}{dT}}{U_{3\omega}^{\perp} U_{1\omega}^{\parallel} \left(\frac{dR^{\perp}}{dT} + \frac{d\Delta R}{dT} \right)}. \quad (10)$$

It can be seen from Fig. 2(d) that the variation of ΔR becomes very small for temperatures between ~ 300 K and 380 K. Therefore, it is possible to neglect $d\Delta R/dT$ in Eq. (10) in this temperature range. This approximation was also used by Wegrowe *et al.* for determining the thermal susceptibility of the magnetization of Ni nanowires of diameters between 25 and 40 nm.³⁶ We return to this point when discussing the experimental results on the AMTR ratio.

IV. RESULTS AND DISCUSSION

We commence the presentation of the experimental results with the temperature dependence of the transport properties shown in Fig. 3. Depicted are the electrical resistivity ρ^{\perp} (a), the thermal conductivity κ^{\perp} (b), and the Lorenz number L^{\perp} (c), measured at saturation fields applied perpendicular to the wire axes. The usage of the specific quantities in (a) and (b) allows for the comparison of our results with literature values on bulk Ni,³⁸ which are plotted in the same graphs. As expected from the polycrystalline nature of the nanowires investigated, ρ^{\perp} is larger and κ^{\perp} is smaller than the bulk values of Ni (stars) measured by White and Woods.³⁸ The enhanced residual resistivity is also responsible for the lack of the low temperature peak of the thermal conductivity that is typically observed in pure bulk metals.³⁹ The Lorenz number can be written in the same form using either specific quantities or nonspecific quantities:

$$L = \rho\kappa/T = R/(WT). \quad (11)$$

Generally, at high temperatures ($T \gg T_{\text{Debye}}$) and at low temperature ($T \rightarrow 0$) elastic scattering of electrons predominates, and the Lorenz number of metals approaches the Sommerfeld value of $L_0 \approx 2.45 \times 10^{-8} \text{ V}^2 \text{ K}^{-2}$.³⁹ A constant L is known as the Wiedemann Franz law. In the intermediate temperature range, deviations from this law are observed due to inelastic scattering of electrons.³⁹ Figure 3(c) reveals that the determined values of L^{\perp} for samples NW1 and NW3 are in good agreement with the reference bulk values. L^{\perp} of sample NW2 shows some deviation, of which we have no clear explanation. Below 120 K the observed decrease of L^{\perp} is weaker compared to the bulk values due to the larger residual resistivity of the polycrystalline nanowires.

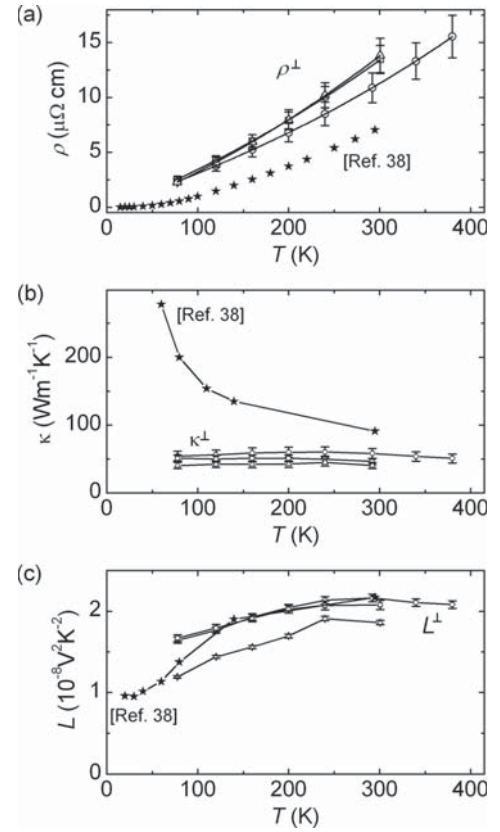


FIG. 3. Temperature dependence of electrical resistivity (a), thermal conductivity (b) and Lorenz number (c) of Ni nanowires, measured under saturation fields applied perpendicular to the wire axes. The bulk values for Ni (stars) were measured by White and Woods (Ref. 38). Circles, triangles, and squares indicate data measured on samples NW1, NW2, and NW3, respectively. Solid lines in (a) are fit curves to the measurement data using polynomial fits. Solid lines in (b) and (c) are guides to the eye.

The results on the AMTR effect, namely, the AMTR ratios defined in Eq. (10), are plotted against the temperature in Fig. 4. The error bars shown were calculated considering Gaussian error propagation of the standard deviations of $U_{3\omega}$, $U_{1\omega}$, dR^{\perp}/dT , and $d\Delta R/dT$. A quantitative comparison of the different contributions to the total error is given in the Supplemental Material.⁴⁰ As discussed in Sec. III it is possible to neglect the dominant contribution arising from the standard deviation of $d\Delta R/dT$ for temperatures above ~ 300 K. This would result in a reduction of the error shown in Fig. 4 by a factor of ~ 5 . For comparison we present the corresponding AMR ratios in the same graph. The curves are nonmonotonic with maxima at temperatures between 160 and 200 K. To explain the reduced AMR ratios at low temperatures, we can use Eq. (3) and consider electron-defect scattering instead of electron-impurity scattering:

$$\frac{\Delta\rho}{\rho^{\perp}}(T) = \left(\frac{\Delta\rho}{\rho^{\perp}} \right)_{\text{ph}} + \left[\left(\frac{\Delta\rho}{\rho^{\perp}} \right)_{\text{def}} - \left(\frac{\Delta\rho}{\rho^{\perp}} \right)_{\text{ph}} \right] \frac{\rho^{\perp}(0)}{\rho^{\perp}(T)}, \quad (12)$$

where $\left(\frac{\Delta\rho}{\rho^{\perp}} \right)_{\text{def}}$ is the AMR ratio due to electron-defect scattering. If $\left(\frac{\Delta\rho}{\rho^{\perp}} \right)_{\text{def}} < \left(\frac{\Delta\rho}{\rho^{\perp}} \right)_{\text{ph}}$, Eq. (12) predicts that the

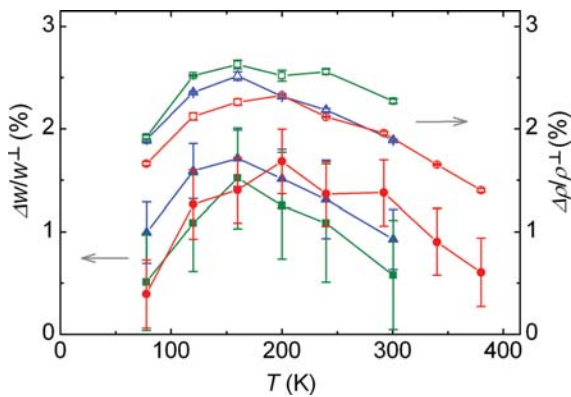


FIG. 4. (Color online) Temperature dependence of the AMR ratio (open symbols) and the AMTR ratio (solid symbols) of Ni nanowires. Red circles, blue triangles, and green squares indicate data measured on samples NW1, NW2, and NW3, respectively. Solid lines are guides to the eye.

AMR ratio increases as the temperature rises, before it saturates at temperatures where electron-phonon scattering dominates. A further effect that can cause a reduction of the AMR ratio at low temperatures is the Lorentz deflection of electrons due to the internal field $B = \mu_0 M_S$, where M_S is the saturation magnetization.^{27,41} The decrease of the AMR ratio at higher temperatures can be explained by electron-magnon scattering, using the model of Campbell *et al.*³ [Eq. (2)]. The AMTR ratios are smaller than the AMR ratios, which is in agreement with the prediction of the simple model presented in Sec. II. The inequality of the AMR and AMTR ratios results in an anisotropic Lorenz number. However, we have to point out

that the total thermal conductance that is measured contains isotropic contributions, for example, from phonons. Electrons contribute about 90% to the total thermal conductance in Ni wires with radii above 150 nm.⁴² Therefore, we expect that the corrected AMTR ratios would still be well below the AMR ratios.

V. CONCLUSION

We measured the field-dependent electrical and thermal transport properties of individual Ni nanowires in the temperature range between 78 and 380 K. In analogy to the AMR effect observed in ferromagnetic conductors, we found that the thermal resistance of Ni nanowires depends on the angle between magnetization vector and current direction. This anisotropic magnetothermal resistance effect turned out to be weaker than the AMR effect in Ni nanowires over the temperature range investigated. As a consequence, also the Lorenz number was found to be anisotropic with respect to the magnetization direction. Using a simple model, we proposed that spin mixing due to electron-magnon scattering is responsible for this observation. To extend the studies on AMTR we suggest similar measurements on nanowires from ferromagnetic alloys.

ACKNOWLEDGMENTS

We thank S. Martens and D. Görlitz for discussions, and R. Meissner and L. Akinsinde for technical support. This work was supported by the German science foundation (DFG) within the German priority program SPP 1538, “Spin-Caloric Transport”.

*johannes.kimling@physik.uni-hamburg.de

¹W. Thomson, Proc. R. Soc. London **8**, 546 (1857).

²J. Smit, Physica **16**, 612 (1951).

³I. A. Campbell, A. Fert, and O. Jaoul, J. Phys. C **3**, S95 (1970).

⁴O. Jaoul, I. A. Campbell, and A. Fert, J. Magn. Magn. Mater. **5**, 23 (1977).

⁵T. R. McGuire and R. I. Potter, IEEE Trans. Magn. **11**, 1018 (1975).

⁶J. Banhart and H. Ebert, Europhys. Lett. **32**, 517 (1995).

⁷H. Ebert, A. Vernes, and J. Banhart, Solid State Commun. **113**, 103 (1999).

⁸J.-E. Wegrowe, S. Gilbert, D. Kelly, B. Doudin, and J.-P. Ansermet, IEEE Trans. Magn. **34**, 903 (1998).

⁹J.-E. Wegrowe, D. Kelly, A. Franck, S. E. Gilbert, and J.-P. Ansermet, Phys. Rev. Lett. **82**, 3681 (1999).

¹⁰S. Pignard, G. Goglio, A. Radulescu, L. Piraux, S. Dubois, A. Declémy, and J. L. Duvail, J. Appl. Phys. **87**, 824 (2000).

¹¹Y. Rheem, B.-Y. Yoo, W. P. Beyermann, and N. V. Myung, Nanotechnology **18**, 015202 (2007).

¹²M. Bolte, M. Steiner, C. Pels, M. Barthelmeß, J. Kruse, U. Merkt, G. Meier, M. Holz, and D. Pfannkuche, Phys. Rev. B **72**, 224436 (2005).

¹³M. Hayashi, L. Thomas, C. Rettner, R. Moriya, X. Jiang, and S. S. P. Parkin, Phys. Rev. Lett. **97**, 207205 (2006).

¹⁴M. V. Kamalakar, A. K. Raychaudhuri, X. Wei, J. Teng, and P. D. Prewett, Appl. Phys. Lett. **95**, 013112 (2009).

¹⁵M. V. Kamalakar and A. K. Raychaudhuri, Phys. Rev. B **79**, 205417 (2009).

¹⁶M. N. Ou, T. J. Yang, S. R. Harutyunyan, Y. Y. Chen, C. D. Chen, and S. J. Lai, Appl. Phys. Lett. **92**, 063101 (2008).

¹⁷B. L. Zink, A. D. Avery, R. Sultan, D. Basser, and M. R. Pufall, Solid State Commun. **150**, 514 (2010).

¹⁸J.-E. Wegrowe, Q. A. Nguyen, M. Al-Barki, J.-F. Dayen, T. L. Wade, and H.-J. Drouhin, Phys. Rev. B **73**, 134422 (2006).

¹⁹R. Mitdank, M. Handweg, C. Steinweg, W. Töllner, M. Daub, K. Nielsch, and S. F. Fischer, J. Appl. Phys. **111**, 104320 (2012).

²⁰A. D. Avery, M. R. Pufall, and B. L. Zink, Phys. Rev. B **86**, 184408 (2012).

²¹G. E. W. Bauer, E. Saitoh, and B. J. van Wees, Nature Mater. **11**, 391 (2012).

²²D. G. Cahill, Rev. Sci. Instrum. **61**, 802 (1990).

²³D. G. Cahill, M. Katiyar, and J. R. Abelson, Phys. Rev. B **50**, 6077 (1994).

²⁴L. Lu, W. Yi, and D. L. Zhang, Rev. Sci. Instrum. **72**, 2996 (2001).

²⁵A. P. Malozemoff, Phys. Rev. B **34**, 1853 (1986).

²⁶A. Fert, J. Phys. C **2**, 1784 (1969).

KIMLING, GOOTH, AND NIELSCH

PHYSICAL REVIEW B **87**, 094409 (2013)

- ²⁷L. Berger, P-P-Freitas, J. D. Warner, and J. E. Schmidt, *J. Appl. Phys.* **64**, 5459 (1988).
- ²⁸R. Parker, *Proc. Phys. Soc. London, Sect. A* **64**, 447 (1951).
- ²⁹T. T. Heikkilä, M. Hatami, and G. E. W. Bauer, *Phys. Rev. B* **81**, 100408(R) (2010).
- ³⁰A. Slachter, F. L. Bakker, and B. J. van Wees, *Phys. Rev. B* **84**, 174408 (2011).
- ³¹K. Nielsch, F. Müller, A.-P. Li, and U. Gösele, *Adv. Mater.* **12**, 582 (2000).
- ³²C. Dames and G. Chen, *Rev. Sci. Instrum.* **76**, 124902 (2005).
- ³³J. Kimling, S. Martens, and K. Nielsch, *Rev. Sci. Instrum.* **82**, 074903 (2011).
- ³⁴ See Supplemental Material at <http://link.aps.org/supplemental/10.1103/PhysRevB.87.094409> for the field dependence of the first and third harmonic components of the measurement signal at different temperatures.
- ³⁵J. J. M. Franse and G. de Vries, *Physica* **39**, 477 (1968).
- ³⁶J.-E. Wegrowe, Q. A. Nguyen, and T. L. Wade, *IEEE Trans. Magn.* **46**, 866 (2010).
- ³⁷D. A. Goodings, *Phys. Rev.* **132**, 542 (1963).
- ³⁸G. K. White and S. B. Woods, *Philos. Trans. R. Soc. London, Ser. A* **251**, 273 (1959).
- ³⁹C. Uher, in *Thermal Conductivity of Metals*, edited by T. M. Tritt (Kluwer Academic/Plenum Publishers, New York, 2004).
- ⁴⁰ See Supplemental Material at <http://link.aps.org/supplemental/10.1103/PhysRevB.87.094409> for a quantitative comparison of the different contributions to the total error of the AMTR ratio.
- ⁴¹L. Berger and A. R. de Vroomen, *J. Appl. Phys.* **36**, 2777 (1965).
- ⁴²N. Stojanovic, D. H. S. Maithripala, J. M. Berg, and M. Holtz, *Phys. Rev. B* **82**, 075418 (2010).

6 Magnetic Multilayers

This chapter summarizes our results on Co/Cu multilayers that were sputter-deposited on fused silica substrates. The entire sample fabrication including the lithography of heater lines for 3ω measurements was accomplished by Dr. Karsten Rott in the group of Prof. Günter Reiss at the University of Bielefeld. Preparation steps and process parameters are summarized in Table E.8 in the Appendix E.

Section 6.1 describes the measuring setup used for 3ω measurements. The experimental results have been published in Ref. [Kim13b] reprinted in Sec. 6.2.

6.1 Sample Design and Measuring Setup

Figure 6.1 shows a photograph of a part of the sample investigated. The Co/Cu multilayer covers the largest part of the fused silica substrate. The stack comprises the following layers: $[\text{Co}(3\text{ nm})/\text{Cu}(1\text{ nm})]_{39}/\text{Co}(3\text{ nm})/\text{Ru}(5\text{ nm})$. The largest part of the multilayer is electrically isolated by a 200-nm- TaO_x layer. It can be seen that two edges of the multilayer are uncovered. These are used to perform van der Pauw measurements of the electrical resistivity on the entire multilayer. Two rows of heater lines for 3ω measurements are fabricated directly on the substrate, four rows of heater lines are fabricated above the multilayer. The heater lines comprise the following layers: $[\text{Ta}(\sim 2\text{ nm})/\text{Au}(\sim 50\text{ nm})]_2$. Compared to Ni nanowires (see Sec. 5.1) the much larger heater lines ($2\text{ mm} \times 5\text{--}10\ \mu\text{m}$

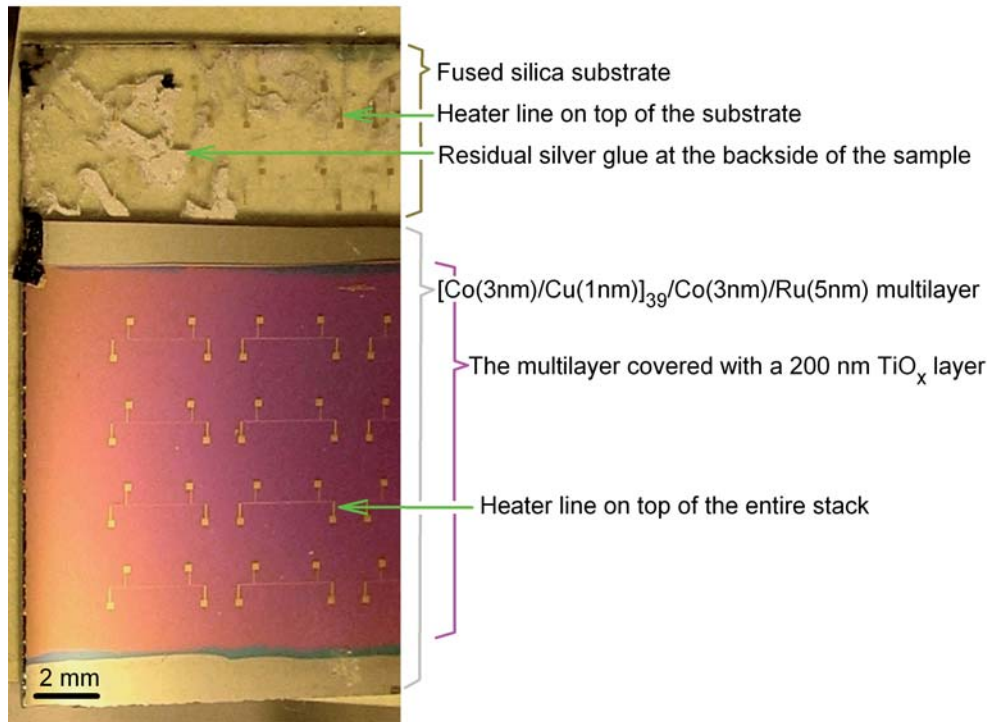


Figure 6.1: Photograph of a part of the sample investigated.

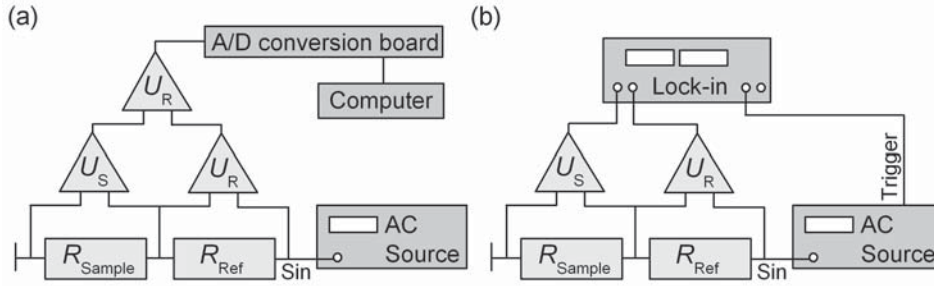


Figure 6.2: (a) 3ω measuring setup used in Chapter 4. (b) 3ω measuring setup used for investigating Co/Cu multilayers.

between the inner contacts) are less sensitive to electrostatic discharges and transient voltages. Therefore, a more complex experimental setup, which uses an active bridge circuit to subtract the 1ω voltage before measuring the 3ω voltage is employed (compare Sec. 4.7).¹⁴ The circuit of this measuring setup is illustrated in Fig. 6.2(b). It works similar to the setup depicted in Fig. 6.2(a), which is employed in Sec. 4.7, except for the following differences: instead of a potentiometer a precision resistance decade (Tinsley, ZX74) is used; instead of an A/D conversion board the measuring signals are recorded using a lock-in amplifier (Stanford Research Systems, SR830). By adjusting the precision resistance decade of negligible temperature coefficient, spurious 3ω voltages are automatically subtracted from the original 3ω signal (compare Secs. 4.7 and 5.3). The sample is connected with the measuring apparatus using a micromanipulated probestation, which is described in Appendix E. The rather complex measuring and data-evaluation procedure employed is described in Sec. 6.2.

6.2 Lorenz Number in Co/Cu Multilayers

Originally, The Wiedemann-Franz (WF) law (see Sec. 2.8) was an empirical law. It was observed to be valid for a large number of metals within deviations of the order of 50% [Wied 53, Lore 72].¹⁵ Later it was found theoretically that the WF law is strictly valid only in highly degenerate Fermi-electron gases under the assumption that all scattering processes are elastic [Somm 33, Ashc 76]. Hence, it can be concluded that deviations from the WF law in conventional metals may indicate inelastic scattering processes. This inference was used by several groups to judge about contributions to the giant magnetoresistance effect (GMR) that may arise from inelastic scattering processes [Sato 94, Shi 96, Tsui 97, Yang 06]. In the following, inconsistencies in earlier interpretations of the measurement data are revealed. It is pointed out that contributions from inelastic scattering not necessarily lead to deviations from the WF law in the context of GMR. To complement these findings a slightly modified 3ω method is applied for measuring field-dependent changes in the thermal conductivity of Co/Cu multilayers over a wide range of temperatures. The results are described in Ref. [Kim1 13b] preprinted in the following pages. The Matlab programs used for data evaluation and calculation procedures are given in the Appendix E.

¹⁴The reason why this setup could not be used for investigating Ni nanowires is simply because the nanowires immediately burned-out after connection with this setup.

¹⁵A review on experimental determinations of the Lorenz number was given by Kumar *et al.* [Kuma 93].

Field-dependent thermal conductivity and Lorenz number
in Co/Cu multilayers

Reprinted with permission from

Johannes Kimling, Karsten Rott, Günter Reiss, and Kornelius Nielsch

Physical Review B **87**, 134406 (2013)

Copyright 2013 by the American Physical Society.

The contributions of each author to the research study are indicated in the table below using the following specifications: Conception of the research study (1), sample preparation (2), measurements (3), data analysis (4), interpretation (5), and composition of the manuscript (6).

JK	KR	GR	KN
1,3,4,5,6	1,2	1	1

PHYSICAL REVIEW B **87**, 134406 (2013)**Field-dependent thermal conductivity and Lorenz number in Co/Cu multilayers**

Johannes Kimling* and Kornelius Nielsch

Institut für Angewandte Physik, Universität Hamburg, Jungiusstr. 11, D-20355 Hamburg, Germany

Karsten Rott and Günter Reiss

Fakultät für Physik, Universität Bielefeld, Postfach 100131, D-33501 Bielefeld, Germany

(Received 8 November 2012; revised manuscript received 18 February 2013; published 8 April 2013)

The influence of *inelastic* scattering mechanisms on the giant magnetoresistance (GMR) effect has been controversially discussed. This issue can be addressed, for example, by comparing charge currents with heat currents in magnetic multilayers that exhibit GMR. The interpretation of such experiments is based on the Wiedemann-Franz law. Due to the fact that this law only holds for elastic scattering, experimentally observed deviations from this law are usually attributed to the presence of inelastic scattering and vice versa. We develop two simple models to demonstrate that this interpretation can lead to wrong conclusions in the context of the GMR effect. We employ a measurement technique that is based on the so-called 3ω method to study the in-plane electrical and thermal conductivities of a Co/Cu multilayer in dependence on magnetic fields over a wide range of temperatures. Our experimental results indicate that the Wiedemann-Franz law holds over the temperature range investigated. Using the simple models developed, we conclude that the influence of electron-magnon scattering on the GMR effect in the Co/Cu multilayer is negligible. We further conclude that electron-phonon scattering is characterized by the same spin asymmetry as the predominant *elastic* scattering of electrons at interfaces in the Co/Cu multilayer.

DOI: 10.1103/PhysRevB.87.134406

PACS number(s): 75.70.Cn, 75.47.De, 72.10.Di, 66.70.Df

I. INTRODUCTION

Multilayers of nanoscale ferromagnetic and nonmagnetic metal layers can show significant changes in the electrical resistance as their magnetic configuration changes.^{1,2} This effect was called giant magnetoresistance (GMR) effect. Mainly driven by its technological importance for the data storage industry, this effect has been intensively studied. A comprehensive review about the theoretical and experimental work on the GMR effect carried out early after its discovery, has been given by Tsymbal and Pettifor.³ Analogous effects to GMR were observed for the thermoelectric power (giant magnetothermoelectric power, GMTP)^{4–7} and the thermal resistance (giant magnetothermal resistance, GMTR).^{8,9} Aiming at a complete understanding of the microscopic origins, some groups decided to perform combined measurements of GMR, GMTR, and GMTP effects on the same sample.^{10–12} However, the contribution to GMR from inelastic scattering, especially that from electron-magnon scattering, remained unclear: Sato *et al.* concluded that “conduction-electron scattering responsible for GMR in AgCo granular alloys is large angle in nature as well as in the magnetic multilayers”,¹⁰ while Shi *et al.* found that “scattering processes which contribute to GMR in layered systems have a significant inelastic component”.¹¹ The latter authors attributed the observed inelastic component to scattering of electrons at long-wavelength magnons. In both works, absolute values of the thermal conductivity could not be determined, because the measured thermal conductances included significant contributions from the substrate. Tsui *et al.*¹² and more recently Yang *et al.*¹³ tried to correct this deficiency by investigating freestanding magnetic multilayers. Again, the conclusions were different: Tsui *et al.* confirmed that an elastic scattering is responsible for GMR, while Yang *et al.* observed a difference between the GMR and GMTR ratios, which could indicate contributions from inelastic

scattering mechanisms. The more recent work of Heikkilä *et al.*¹⁴ points in another direction. They used the concept of spin-heat accumulation to calculate heat transport through a spin valve and found that GMTR can be very sensitive to inelastic scattering. However, this effect was derived for charge and heat transport perpendicular to the planes inside a spin valve, while the experiments mentioned before were carried out on magnetic multilayers in the current-in-plane geometry. Research that considers not only charge and spin transport but also heat transport in materials and nanoscale devices, is nowadays categorized in the field of *spin caloritronics*.^{15,16}

In this work, we revisit the concept of using thermal conductivity measurements to judge about the significance of inelastic scattering in magnetic multilayers. We employ a measurement technique that is based on the so-called 3ω method¹⁷ to study the in-plane electrical and thermal conductivities of a Co/Cu multilayer, deposited on a fused silica substrate. This method allows for determination of absolute values of the thermal conductivity of a thin film system without preparing free-standing specimens. Compared to steady-state techniques, the characteristic length over which the heat penetrates is small, typically below 100 μm . Therefore, the 3ω method is insensitive to background thermal leakages caused by radiation.¹⁷ Consequently, also the characteristic time scale is small, which is advantageous for detecting changes in the thermal conductivity and thus for observing the GMTR effect.

In Sec. II, the basic mechanisms that lead to spin-dependent scattering of electrons, and thus to GMR in magnetic multilayers, are briefly recapitulated. By analyzing the validity of the Wiedemann-Franz law in the context of the GMR effect in Sec. III, we revisit the concept of using thermal conductivity measurements to judge about the significance of inelastic scattering. In Sec. IV, the measurement technique used for detecting field-dependent changes in the thermal

conductivity is discussed. In Sec. V, we present and discuss our results and compare our findings with those obtained by others.

II. SPIN-DEPENDENT SCATTERING

In Co/Cu multilayers, ferromagnetic Co layers are separated by nonmagnetic Cu layers. The thickness of the Cu layer is chosen such that the coupling between adjacent Co layers is antiferromagnetic. By applying magnetic fields, the magnetization directions of the Co layers can be aligned parallel. During the alignment process, the electrical resistance of the multilayer drops significantly due to the GMR effect. This effect is observed for both current directions, current flowing in the plane of the multilayers (CIP transport) and perpendicular to them (CPP transport). Beside the different scaling lengths (electron mean free path for CIP transport,¹⁸ spin-diffusion length for CPP transport¹⁹), the main differences between the two current directions are spin-accumulation effects, which only appear for CPP transport.¹⁹ The GMR effect in Co/Cu multilayers can be intuitively understood in terms of the spin-dependent two current model that separates the total current into parallel contributions from majority-spin electrons and minority-spin electrons.^{3,20} In the parallel magnetic configuration, the total resistance of the two spin subsystems is governed by the low resistance of majority-spin electrons, while in the antiparallel configuration, the two current channels have the same high resistance. The various microscopic origins of spin-dependent scattering can be separated into intrinsic and extrinsic origins.³ Intrinsic spin-dependent scattering at the interfaces in Co/Cu multilayers arises from the spin-dependent band mismatch between magnetic and nonmagnetic layers. The spin-polarized band structure of the magnetic layers generates spin-dependent bulk scattering. Therefore all scattering mechanisms (also electron-phonon scattering) become spin dependent and can contribute to the GMR effect. Intrinsic spin dependent scattering potentials can arise from magnons. However, electron-magnon scattering involves spin-flip processes that diminish the GMR effect. Electron-electron scattering is only relevant in very pure metals at very low temperatures, and can be neglected in magnetic multilayers. Extrinsic spin-dependent scattering is associated to impurities in the layers and to roughness at the interfaces.

The strength of a spin-dependent scattering mechanism j is characterized by its spin-asymmetry parameter, which we define to be

$$\alpha^j = \frac{\rho_m^j}{\rho_M^j} = \frac{w_m^j}{w_M^j}, \quad (1)$$

where ρ_m^j and w_m^j are the electrical and thermal resistivities of minority-spin electrons, and ρ_M^j and w_M^j those of majority-spin electrons, which arise due to this scattering mechanism. The equality of α^j for electrical and thermal transport is tantamount to the assumption that the Lorenz number L^j does not depend on the magnetic configuration. However, in the presence of inelastic spin-flip scattering that diminishes the GMR effect, as well as for the case that both elastic and inelastic scattering mechanism are spin dependent and thus contribute to the GMR effect, the effective Lorenz number may depend on

the magnetic configuration. These two problems are analyzed separately in Sec. III.

III. WIEDEMANN-FRANZ LAW AND LORENZ NUMBER

In pure metals, heat transport is dominated by electrons.²¹ Comparison of electronic heat currents with charge currents can indicate if the scattering of electrons present in the specimen has a significant inelastic component.²¹ This argument is based on the Wiedemann-Franz law (WF law), which states that the ratio of electronic thermal conductivity κ to electrical conductivity σ is proportional to the temperature T :²²

$$\frac{\kappa}{\sigma} = LT, \quad L^0 = 2.44 \times 10^{-8} \text{ V}^2/\text{K}^2, \quad (2)$$

where L^0 is the Sommerfeld value of the Lorenz number L , calculated using Fermi-Dirac statistics. It can be shown that the WF law is valid for elastic electron scattering, i.e., in the limit of large-angle electron scattering.²³ The WF law usually holds at low temperatures, where scattering of electrons at impurities predominates, and at temperatures above the Debye temperature, where large-angle electron-phonon scattering predominates. In the intermediate temperature range, inelastic scattering at phonons can cause the Lorenz number to fall significantly below L^0 .²¹ In ferromagnetic metals, such as Co, inelastic electron-magnon scattering can contribute in decreasing L below the Curie temperature.^{24,25} In the following, we discuss the effect of inelastic scattering on the Lorenz number in the context of the GMR effect. If L is a constant with respect to the applied field, we say that the WF law is fulfilled, although L may be smaller than L^0 .

A. Electron-magnon scattering

Spin-flip scattering, such as electron-magnon scattering, suppresses GMR and GMTR. This fact has not been considered in the model of Shi *et al.*, which they developed to explain deviations from WF law for a Co/Cu multilayer due to scattering of electrons by long-wavelength magnons.¹¹ This model of Shi *et al.* is based on the two-current model. They derived electron-magnon scattering rates for majority spins and for minority spins that depend on the magnetic configuration, antiparallel (AP) or parallel (P). Assuming that these scattering rates add to the non-spin-flip scattering rates of the thermal relaxation process in the respective spin conduction channels, they found that $L_P > L_{AP}$ for magnon absorption rates below about one tenth of the non-spin-flip scattering rate of minority-spin electrons. In the following, we develop a phenomenological model for the Lorenz number of Co/Cu multilayers that is also based on the two-current model, but includes the spin-mixing term ρ_{sf} . The resistivities (electrical and thermal) of the P configuration are given by^{26,27}

$$\begin{aligned} \rho_P &= \frac{\rho_M \rho_m + \rho_{sf}(\rho_M + \rho_m)}{\rho_M + \rho_m + 4\rho_{sf}}, \\ w_P &= \frac{w_M w_m + w_{sf}(w_M + w_m)}{w_M + w_m + 4w_{sf}}, \end{aligned} \quad (3)$$

where the second equation is the thermal analog of the first one. The spin-mixing terms represent the tendency of spin-flip

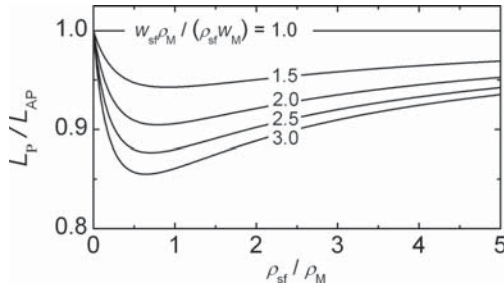


FIG. 1. In the presence of electron-magnon scattering, the Lorenz number L of magnetic multilayers can depend on the magnetic configuration (parallel: L_P , antiparallel: L_{AP}). The curves show the ratio L_P/L_{AP} according to Eq. (5) as functions of the significance of electron-magnon scattering that is quantified by the ratio ρ_{sf}/ρ_M .

scattering to equilibrate the two spin subsystems. With increasing spin-mixing terms, the resistivities of the P configuration approach the resistivities of the AP configuration. The latter are given by

$$\rho_{AP} = \frac{\rho_M + \rho_m}{4}, \quad w_{AP} = \frac{w_M + w_m}{4}. \quad (4)$$

To study the influence of the spin-mixing terms on L in magnetic multilayers, we assume at this point that all scattering mechanisms that contribute to GMR are characterized by the same spin-asymmetry parameter $\alpha = \frac{\rho_m}{\rho_M} = \frac{w_m}{w_M}$. Using Eqs. (3) and (4), we obtain the following Lorenz ratios for the two magnetic configurations:

$$L_{AP} = \frac{\rho_M + \rho_m}{(w_M + w_m)T}, \quad (5)$$

$$L_P = L_{AP} \frac{\left[\frac{\alpha}{(1+\alpha)} + \frac{\rho_{sf}}{\rho_M} \right] \left(1 + \alpha + 4 \frac{w_{sf}}{w_M} \right)}{\left(1 + \alpha + 4 \frac{\rho_{sf}}{\rho_M} \right) \left[\frac{\alpha}{(1+\alpha)} + \frac{w_{sf}}{w_M} \right]}.$$

For $\rho_{sf}/\rho_M = w_{sf}/w_M$, the Lorenz number does not depend on the magnetic configuration and the WF law holds. Due to its inelastic nature, electron-magnon scattering is more effective in suppressing GMTR than GMR, i.e., $\rho_{sf}/\rho_M < w_{sf}/w_M$. To demonstrate the effect of the spin-mixing terms for this case, we define $\alpha = 5$ and plot the ratio L_P/L_{AP} as a function of ρ_{sf}/ρ_M . The resulting curves are shown in Fig. 1 for $\frac{w_{sf}/w_M}{\rho_{sf}/\rho_M} \in \{1, 1.5, 2, 2.5, 3\}$. In contrast to Shi *et al.*,¹¹ we obtain $L_P < L_{AP}$ for the case that electron-magnon scattering is significant. After reaching a minimum L_P approaches L_{AP} for the case that electron-magnon scattering would dominate. However, in Co/Cu multilayers the spin-diffusion length is more than one order of magnitude larger than the mean free path,¹⁹ which makes the spin-mixing terms negligible. Moreover, the scaling length of GMR for CIP transport is given by the mean free path.¹⁸ Therefore we expect that electron-magnon scattering is negligible for GMR and GMTR of Co/Cu multilayers for CIP transport.

B. Electron-phonon scattering

In contrast to electron-magnon scattering, the scattering of electrons at phonons is usually spin conserving and therefore can contribute to GMR and GMTR. To investigate the influence of electron-phonon scattering on L , we use the above

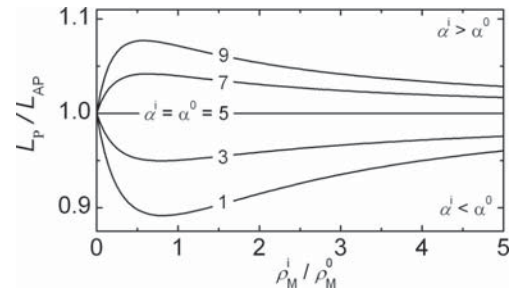


FIG. 2. In the presence of electron-phonon scattering, the Lorenz number L of magnetic multilayers can depend on the magnetic configuration (parallel: L_P , antiparallel: L_{AP}). The curves show the ratio L_P/L_{AP} according to Eq. (7) as functions of the significance of electron-phonon scattering that is quantified by ρ_M^i/ρ_M^0 .

model and neglect the spin-mixing terms. We assume that the Matthiessen rule is valid and distinguish between resistivities (electrical and thermal) that arise from elastic scattering (ρ^0 and w^0) and those that arise from electron-phonon scattering (ρ^i and w^i). The Lorenz number of the elastic scattering equals the Sommerfeld value L^0 , while the Lorenz number of the inelastic scattering is reduced:

$$L^i = \frac{\rho^i}{w^i T} < L^0. \quad (6)$$

The significance of elastic and inelastic scattering for GMR can be characterized using the respective spin-asymmetry parameters, abbreviated by $\alpha^0 = \rho_m^0/\rho_M^0 = w_m^0/w_M^0$ and $\alpha^i = \rho_m^i/\rho_M^i = w_m^i/w_M^i$. Using again Eqs. (3) and (4), we obtain the following Lorenz ratios for the two magnetic configurations:

$$L_{AP} = \frac{\rho_M + \rho_m}{(w_M + w_m)T},$$

$$L_P = L_{AP} \frac{\left(1 + \frac{\rho_M^i}{\rho_M^0} \right) \left(\alpha^0 + \alpha^i \frac{\rho_M^i}{\rho_M^0} \right) \left[\alpha^0 + 1 + (\alpha^i + 1) \frac{w_M^i}{w_M^0} \right]^2}{\left[\alpha^0 + 1 + (\alpha^i + 1) \frac{\rho_M^i}{\rho_M^0} \right]^2 \left(1 + \frac{w_M^i}{w_M^0} \right) \left(\alpha^0 + \alpha^i \frac{w_M^i}{w_M^0} \right)}. \quad (7)$$

According to Eq. (6), we know that $\frac{\rho_M^i}{\rho_M^0} < \frac{w_M^i}{w_M^0}$. To demonstrate the effect of electron-phonon scattering on L , we define $L^i = 0.5L^0$ and $\alpha^0 = 5$. Figure 2 shows the ratio L_P/L_{AP} as a function of ρ_M^i/ρ_M^0 for the values $\alpha^i \in \{1, 3, 5, 7, 9\}$. It turns out that for a negligible contribution of electron-phonon scattering to GMR and GMTR ($\alpha^i \approx 1$), the Lorenz number does depend on the magnetic configuration, and we obtain $L_P < L_{AP}$. With increasing significance of electron-phonon scattering to GMR and GMTR, L_P approaches L_{AP} . For $\alpha^0 = \alpha^i$ the WF law holds, i.e., $L_P = L_{AP}$, although inelastic scattering processes significantly contribute to GMR and GMTR. Deviations from the WF law in terms of $L_P > L_{AP}$ are obtained for $\alpha^i > \alpha^0$.

C. Spurious contributions in addition to κ

Besides the electronic thermal conductivity κ the total thermal conductivity of magnetic multilayers, κ_{tot} , includes contributions from other excitations, in particular from phonons and magnons. Additionally, the measured thermal conductivity κ_{meas} can differ from κ_{tot} due to thermal radiation, uncontrolled heat flow, and uncertainties of the measurement technique. In

the following, we abbreviate all additional contributions to κ_{meas} with κ_{off} :

$$\kappa_{\text{meas}} = \kappa + \kappa_{\text{off}}. \quad (8)$$

Unknown contributions to κ_{off} lead to an overestimation of L . However, the field dependence of κ_{meas} arises solely from κ . Inserting Eq. (2) into Eq. (8) gives

$$\kappa_{\text{meas}}(H) = LT\sigma(H) + \kappa_{\text{off}}, \quad (9)$$

where H is the magnetic field strength applied. If the measurement data $[\kappa_{\text{meas}}(H), \sigma(H)]$ plotted in the form of Eq. (9) result in a linear curve for constant temperatures, it follows that L is a constant. In this case, we say that the WF law holds, although L may be smaller than L^0 . The linear measurement curve can then be used to determine κ_{off} from the intercept with the y axis using extrapolation. On the other hand, deviations from linearity would indicate deviations from the WF law. This conclusion does not depend on κ_{off} .

IV. EXPERIMENT

The 3ω method was introduced by Cahill in 1990 for bulk thermal conductivity measurements on dielectric materials.¹⁷ The method was extended to dielectric thin films²⁸ and metallic wires.²⁹ For bulk materials and thin films, a heater line fabricated on top of the sample serves as both, heater and thermometer of the experiment. An alternating current at frequency 1ω is imposed to the heater line, generating Joule heat at frequency 2ω . The temperature oscillations result in resistance oscillations of the heater line that modulate the voltage measured across the heater line. The 3ω method makes use of the third harmonic component of the measurement voltage $U_{3\omega}$, which is proportional to the amplitude of the temperature oscillations ΔT and therefore contains the information for determining the thermal properties of the materials below the heater line:¹⁷

$$U_{3\omega} = \frac{dR}{dT} \frac{\Delta T}{2I_0}, \quad (10)$$

where $\frac{dR}{dT}$ is the temperature derivative of the resistance of the heater line and I_0 is the amplitude of the heating current. The thin film 3ω method is usually applied to dielectric thin films of low thermal conductivities (~ 1 W/mK), deposited on substrates of large thermal conductivities (~ 100 W/mK).²⁸ The thin film acts as a thermal resistance, increasing the temperature of the heater line relative to a reference sample without thin film. From the temperature offset between thin-film and reference samples, the cross-plane thermal conductivity of the thin film can be deduced. This method is known as the ‘‘differential 3ω method’’. For metallic thin films, there are three big challenges. First, due to the large thermal conductivity, the temperature offset of the metallic layer is small. Second, the thermal conductivity of the substrate must be larger than the thermal conductivity of the metallic layer. Otherwise, the simple thermal resistance model cannot be applied. Consequently, the heating power required to obtain typical temperature amplitudes of about 1 K is large. Third, a dielectric layer, typically SiO_2 , is required to electrically insulate the heater line from the metallic layer. Due to the large heating power, thicknesses of at least 100-nm SiO_2 are required

for obtaining reliable electrical insulation. Consequently, the small temperature offset produced by the metallic thin film is masked by a large temperature offset produced by the insulating layer.

We avoided these challenges by reversing the situation: we fabricated the metallic layer of interest onto a fused silica substrate with low thermal conductivity. Compared to the dominating thermal resistance of the substrate, the thermal resistance of interfaces and of the required insulating layer can be neglected. In this case, the generated heat spreads along the metallic layer before it enters the substrate, resulting in a negative temperature offset at the heater line. By fitting a two-dimensional multilayer model to the measurement data,^{30,31} the in-plane thermal conductivity of the metallic thin film can be determined. As discussed in Sec. IV B, this approach is insusceptible to offset errors of the temperature amplitude that can be caused by the finite thermal conductivity of the heater line, and by thermal resistances arising from the insulating layer and from interfaces. The measuring voltage is detected using a lock-in amplifier (Stanford Research SR830) after subtraction of the first harmonic component. This common-mode subtraction is accomplished using a precision resistance decade connected in series with the sample in combination with a simple measuring bridge, similar to those employed in Refs. 17 and 31. Our experiment uses a current source (Keithley 6221).

A. Substrate

Whereas other methods for determining the thermal conductivity of thin films consider heat conduction through the substrate as detrimental, it is a basic feature of the 3ω method. However, the variant employed in this work requires knowledge of the thermal properties of the substrate. Therefore we fabricated several gold heater lines directly on the bare substrate using electron-beam lithography in combination with a lift-off process (see Fig. 3). In contrast to steady-state methods, the geometry of the substrate does not influence the 3ω measurement, because the penetration depth of the thermal wave generated at the heater line is well below the thickness of the substrate. The amplitude of the temperature oscillations at the heater line, as derived by Cahill,¹⁷ are given by

$$\Delta T_{\text{sub}} = \frac{P}{l\pi\kappa_{\text{sub}}} \int_0^\infty \frac{\sin^2 kb}{(kb)^2(k^2 + q^2)^{1/2}} dk, \quad q^2 = \frac{2i\omega}{D_{\text{sub}}}, \quad (11)$$

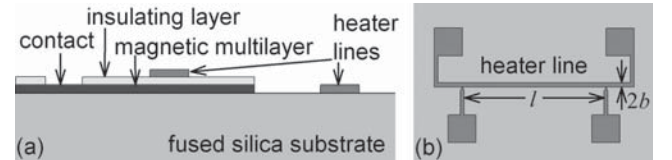


FIG. 3. Illustration of (a) the thin-film stack and (b) the heater geometry for 3ω measurements. The thin-film stack (magnetic multilayer, insulating layer, heater lines) is deposited on a fused silica substrate. Several heater lines are fabricated directly on the substrate, and above the Co/Cu multilayer. The lengths l of the heater lines are 2 mm; the widths $2b$ of the heater lines are 5 and 10 μm .

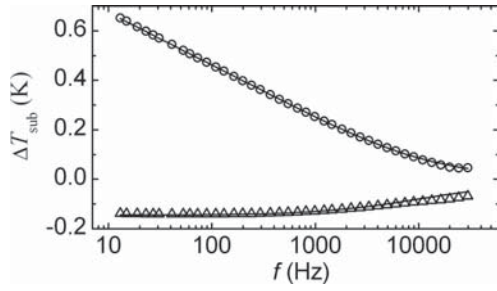


FIG. 4. In-phase (circles) and out-of-phase (triangles) components of the temperature oscillations of a heater line directly fabricated on a fused silica substrate, plotted against the logarithm of the frequency of the heating current. The fit curves (solid lines) are obtained using the model explained in the main text. The measurement was performed at a temperature of 300 K.

where l is the width, and $2b$ the length of the heater line; P is the power supplied to the heater line at angular frequency 2ω ; D_{sub} the thermal diffusivity, and κ_{sub} the thermal conductivity of the substrate. In the limit $|bq| \ll 1$, Eq. (11) can be approximated by¹⁷

$$\Delta T_{\text{sub}} = \frac{P}{l\pi\kappa_{\text{sub}}} \left(-\frac{1}{2} \ln \omega - \frac{1}{2} \ln \frac{ib^2}{D_{\text{sub}}} + \text{const} \right). \quad (12)$$

Combining Eqs. (10) and (12), the thermal conductivity of the substrate can be determined from the slope of the measurement data plotted against $\ln \omega$ (“slope method”). In Fig. 4, in-phase (circles) and out-of-phase (triangles) components of ΔT_{sub} , measured on a heater line that was fabricated directly on the substrate, are plotted against the logarithm of the frequency f of the heating current. For frequencies below about 2 kHz, the in-phase component of ΔT_{sub} decays linearly with $\ln f$, as predicted by Eq. (12). It has been observed that there exists a small frequency-independent offset between experiment and theoretical determination of the constant term in Eq. (12) using Eq. (11).^{28,32} This offset, which we define to be $\Delta T_{\text{off}} = \Delta T_{\text{sub}}^{\text{exp}} - \Delta T_{\text{sub}}^{\text{theo}}$, can be ascribed to various parameters that are not considered in Eq. (11), such as interfaces and thermal radiation. A critical contribution arises from the finite thermal conductivity of the heater line that alters the temperature profile across the heater width.³³ This problem is enhanced by imperfections of the heater line, such as an inhomogeneous thickness profile and edge roughness. The absolute value and the sign of ΔT_{off} can vary for different materials and geometries. Cahill *et al.* have observed a negative ΔT_{off} .²⁸ To account for this offset, they have used an effective width for the heater line that is 10% larger than the actual value. Lee and Cahill have observed a positive ΔT_{off} , which they considered directly in Eq. (12).³² As an alternative possibility to account for ΔT_{off} , we can use D_{sub} as a fit parameter in Eq. (11), because changing D_{sub} essentially results in a frequency independent offset of ΔT_{sub} . This procedure is convenient, because the temperature dependent specific heat capacity of the substrate is unknown. Frequency-dependent deviations from Eq. (11) are caused by the heat capacity of the heater line at high frequencies (typically above 10 kHz).^{30,31} The fit curves shown in Fig. 4, were obtained using Eq. (11) in combination with κ_{sub} determined from the slope method. The fit parameter was D_{sub} . Using typical values for D_{sub} at

room-temperature [specific heat capacity: $c_p = 964 \text{ J}/(\text{kg K})$, density $\rho_M = 2203 \text{ g}/\text{cm}^3$],³⁴ we find that ΔT_{off} is about 10 mK for this measurement. Additionally, we consider the thermal mass of the heater line to improve the fit in the high-frequency range.

B. Co/Cu multilayer

The Co/Cu multilayer was sputter deposited on a fused silica substrate. It comprises the following layers (from bottom to top): [Co(3 nm)/Cu(1 nm)]₃₉/Co(3 nm)/Ru(5 nm). Several gold heater lines (see Fig. 3) were fabricated above the Co/Cu multilayer using electron-beam lithography in combination with a lift-off process. The heater lines were electrically insulated from the Co/Cu multilayer using a 200-nm-thick TaO_x layer. A shadow mask was used during sputtering of the TaO_x layer to define windows in the oxide layer serving as contact areas for resistance measurements. The frequency dependence of in-phase and out-of-phase components of ΔT_{GMR} , measured at a heater line that was fabricated above the Co/Cu multilayer, is shown in Fig. 5. The dashed lines that were calculated, represent the temperature amplitude that would be observed under equal conditions, but without Co/Cu multilayer below the heater line. The presence of the Co/Cu multilayer significantly decreases the temperature amplitude and changes its frequency dependence. In contrast to ΔT_{sub} , the real part of ΔT_{GMR} decreases nonlinearly with $\ln f$ over the frequency range explored. The fit curves shown in Fig. 5 are obtained using the multilayer heat conduction model derived by Borca-Tasciuc *et al.*,³⁰ in combination with the fitting algorithm formulated by Olson *et al.*³¹ We consider two layers for this model: the substrate as layer 1, and the magnetic multilayer as layer 2. The thermal properties of layer 1 (κ_{sub} and D_{sub}) are fixed to the experimental values derived as explained in Sec. IV A. As fit parameters we use the thermal conductivity of layer 2 and a frequency-independent offset ΔT_{off} , the origin of which is discussed in Sec. IV A. Furthermore, ΔT_{off} includes the effect of the thermal resistance of the insulating layer. For the measurement shown in Fig. 5, we obtain a value of $\Delta T_{\text{off}} = 20 \text{ mK}$. We note that although ΔT_{off} is unknown, the proposed deduction of κ_{meas} is reliable due to the change in slope and curvature of the measurement curve, caused by

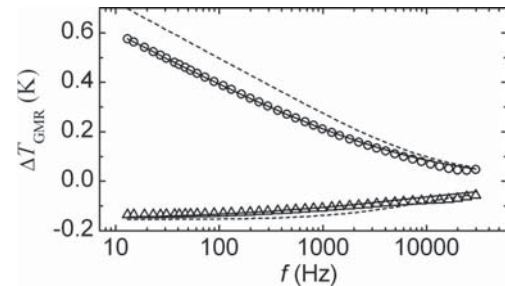


FIG. 5. In-phase (circles) and out-of-phase (triangles) components of the temperature oscillations of a heater line fabricated above a Co/Cu multilayer, plotted against the logarithm of the frequency of the heating current. The fit curves (solid lines) are obtained using the model explained in the text. The dashed lines show a simulation of the temperature oscillations without Co/Cu multilayer below the heater line. The measurement was performed at a temperature of 300 K.

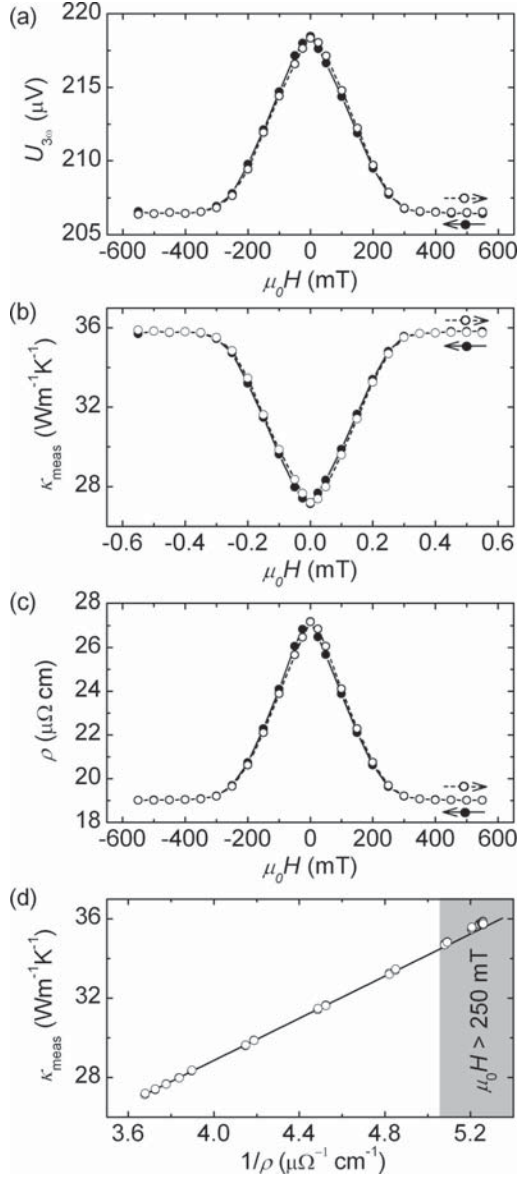


FIG. 6. (a) Field dependence of the 3ω voltage $U_{3\omega}(H)$ measured on a heater line, the resistance of which was 150Ω . The imposed heating current was 5 mA . (b) Field dependence of the thermal conductivity of the Co/Cu multilayer κ_{meas} deduced from the data shown in (a). The thermal conductivity changes due to the giant magnetothermal resistance effect. (c) Field dependence of the electrical resistivity $\rho(H)$ of the Co/Cu multilayer. (d) Thermal conductivity $\kappa(1/\rho)$ of the Co/Cu multilayer, plotted against its electrical conductivity $\sigma = 1/\rho$. The resulting curve is linear over the field-range of the giant magnetoresistance effect (between about -250 and 250 mT), and slightly deviates from linearity at saturation fields. The measurements were performed at 300 K .

the Co/Cu multilayer. The thermal diffusivity of the Co/Cu multilayer, D_{GMR} , is about two orders of magnitudes larger compared to D_{sub} that dominates the thermal penetration depth. Therefore variations of D_{GMR} have no measurable effect on the 3ω measurement.

The field-dependent 3ω measurement was performed at a constant frequency of 89 Hz . Using ΔT_{off} derived from

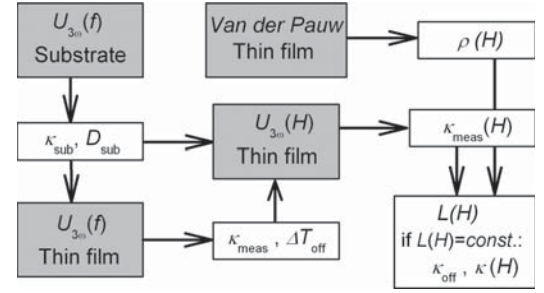


FIG. 7. Flow chart of the measurement procedure described Sec. IV.

the frequency-dependent 3ω measurement, fitting of the multilayer heat conduction model to the measurement data gives the field dependence of the thermal conductivity of the Co/Cu multilayer. Representative curves of the measurement data $U_{3\omega}(H)$ and the deduced thermal conductivity of the Co/Cu multilayer $\kappa_{\text{meas}}(H)$ are presented in Figs. 6(a) and 6(b). The field dependence of the electrical resistivity of the Co/Cu multilayer, $\rho(H)$, derived from van der Pauw measurements on the same sample³⁵ is depicted in Fig. 6(c). The data shown in Figs. 6(b) and 6(c) are combined to obtain the plot κ_{meas} versus $1/\rho$ shown in Fig. 6(d). This plot serves as a validity test of the WF law, as discussed in Sec. III. We observe a linear relation in the field range of GMR (between about -250 and 250 mT) and small deviations from linearity at saturation fields. We come back to these deviations in Sec. V. According to Eq. (9), it follows that the Lorenz number remains constant and is not influenced by the GMR effect. In this case, a linear fit to the measurement data can be used to obtain κ_{off} and consequently κ , and L (see Sec. III). For all measurements, κ_{off} comprises about 30% of κ_{meas} . The measurement procedure discussed in this section is summarized in the flow chart shown in Fig. 7.

V. RESULTS AND DISCUSSION

The temperature dependence of the thermal conductivity of the fused silica substrate is shown in Fig. 10 in the Appendix. The main results determined for the Co/Cu multilayer in the temperature range between 10 and 300 K are presented in Figs. 8 and 9. For comparison, we show results from Tsui *et al.* on an epitaxial $[\text{Co}(7 \text{ ML})/\text{Cu}(19 \text{ ML})]_{215}$ multilayer,¹² and from Yang *et al.* on a $[\text{Cu}(2.1 \text{ nm})/\text{CoFe}(1.2 \text{ nm})]_{40}$ multilayer,³⁶ along with our results (full black dots). Due to increasing electron-phonon scattering and to some extent electron-magnon scattering, the electrical resistivity ρ_{AP} increases over the temperature range investigated by a factor of 1.45 , and ρ_{P} by a factor of 1.74 [see Fig. 8(a)]. Electron-magnon scattering does not affect GMR, because the spin-diffusion length is much larger than the mean free path (compare Sec. III C). However, despite increasing electron-phonon scattering that can contribute to GMR (compare Sec. III B), the absolute GMR, $\rho_{\text{AP}} - \rho_{\text{P}}$, shows no temperature dependence within the accuracy of the measurement [see Fig. 8(a)]. Therefore, the GMR-ratio decreases from 41% to 30% as the temperature rises from 10 to 300 K [see Fig. 8(c)]. This can be explained by considering the electron mean free path that decreases as the temperature rises. As

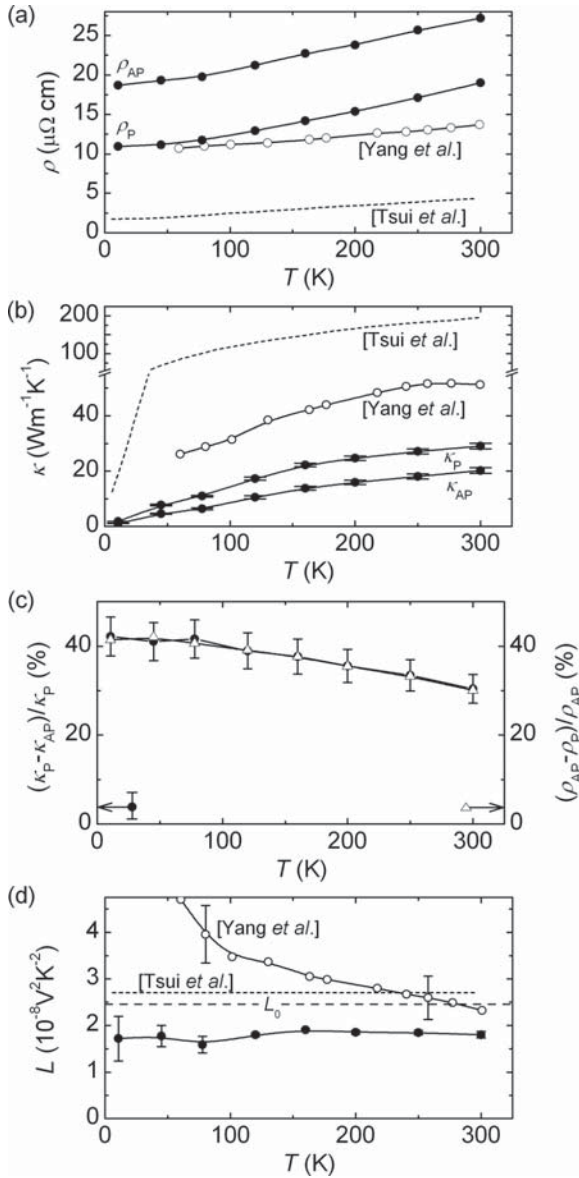


FIG. 8. Experimental results measured on a Co/Cu multilayer over the temperature range between 10 and 300 K (full black dots). (a) Electrical resistivity for the parallel magnetic configuration, ρ_p , and for the antiparallel one, ρ_{AP} . (b) Electronic thermal conductivity for the parallel magnetic configuration, κ_p , and for the antiparallel one, κ_{AP} . The data points represent the mean value averaged over the results from four heater lines. The error bars indicate the standard deviation. (c) Giant magnetothermal resistance ratio, $(\kappa_p - \kappa_{AP})/\kappa_p$ (full black dots) with error bars according to the standard deviation shown in (b), and giant magnetoresistance ratio, $(\rho_{AP} - \rho_p)/\rho_{AP}$ (white triangles). (d) Electronic Lorenz number L . For comparison, we show results from Tsui *et al.* on an epitaxial [Co(7 ML)/Cu(19 ML)]₂₁₅ multilayer¹² and from Yang *et al.* on a [Cu(2.1 nm)/CoFe(1.2 nm)]₄₀ multilayer.³⁶

the mean free path is the scaling length for GMR in the CIP geometry, the GMR ratio drops with rising temperatures.³⁷ Figure 8(b) depicts the electronic thermal conductivity of the Co/Cu multilayer, κ , that was derived as described in Sec. IV B. It can be seen that κ increases monotonically as the temperature

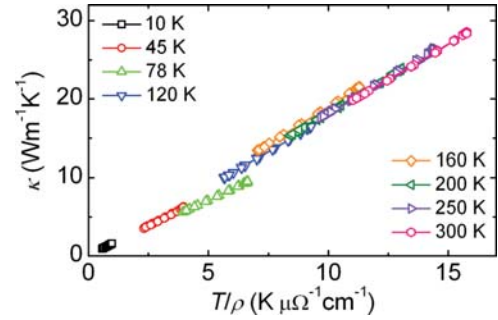


FIG. 9. (Color) Electronic thermal conductivity, κ , plotted against the product of temperature, T , and electrical conductivity, $\sigma = 1/\rho$. Different colors correspond to the respective temperatures during the measurements, as indicated in the legend. At each temperature, the curves are linear due to a constant Lorenz number that does not depend on the magnetic configuration of the Co/Cu multilayer.

rises. Similar to alloys, κ lacks a low-temperature peak that is typically observed for pure metals due to freeze-out of electron-phonon scattering. This can be explained by strong electron scattering at interfaces and defects inside the Co/Cu multilayer. The absolute GMTR, $\kappa_p - \kappa_{AP}$, scales with the temperature according to the WF law. From the observation that the WF law is valid in the context of GMR in our sample, it follows that the GMTR ratio equals the GMR ratio [see Fig. 8(c)]. In Fig. 9, κ is plotted against T/ρ for the entire temperature range investigated. The measurement curves at 300 K were already shown in Fig. 6(d). At each temperature, the relationship between thermal conductivity and electrical conductivity is linear in the field range of GMR. The slope of each curve yields the electronic Lorenz number, L , which is plotted in Fig. 8(d). In pure metals L exhibits a minimum at temperatures where inelastic electron-phonon scattering dominates over elastic electron-phonon and boundary scatterings ($T \approx 0.2 T_{\text{Debye}}$)²¹. With increasing impurity and defect concentration this minimum disappears. For the Co/Cu multilayer investigated, due to strong elastic scattering at interfaces and defects, only a small minimum of L can be guessed at in Figs. 8(d) and 9 at a temperature of 78 K. The error bars are larger at low temperatures due to increasing uncertainties of the temperature during 3ω measurements. The respective values reported by Yang *et al.*³⁶ and by Tsui *et al.*¹² are clearly above the Sommerfeld value of $L^0 = 2.44 \times 10^{-8} \text{ V}^2/\text{K}^2$. However, the authors do not give an explanation for such high values in magnetic multilayers. Our values for L are in agreement with those reported by Shi *et al.* for a [Co(1 nm)/Cu(1 nm)] multilayer.¹¹ The reduced values of L indicate that the scattering of electrons has a significant *inelastic* component, which comprises predominantly electron-phonon and to some extent electron-magnon scattering.

To summarize, our results indicate that in Co/Cu multilayers the WF law holds [see Figs. 6(d) and 9] in the presence of inelastic scattering [see Figs. 8(a) and 8(d)]. Using the simple models developed in Sec. III, we conclude first that electron-magnon scattering is negligible for GMR, and second that electron-phonon scattering is characterized by the same spin-asymmetry parameter as elastic scattering of electrons at impurities and interfaces, $\alpha^0 = \alpha^i$. We should note that the results can be different for Co/Cu multilayers with a different

microstructure due to interface roughness and interdiffusion at interfaces. These can result, e.g., in “loose” spins at the interfaces that may enhance spin-flip scattering.³ For different material combinations it is possible that different scattering mechanisms lead to deviations of the WF law in the context of GMR. For example, the influence of spin-flip scattering can become significant for the GMR effect in Fe/Cr multilayers at temperatures above 50 K,³⁸ which was ascribed to localized magnon modes at rough Fe/Cr interfaces.³⁹ It was shown on NiCr/Cu/Co/Cu multilayers by using different thicknesses of the NiCr layer that the GMR effect can reverse its sign due to spin-dependent scattering at Cr impurities ($\alpha_{Cr} < 1$).⁴⁰ In such a case, we expect deviations from the WF law (see Sec. III B).

In the following, we discuss the results from Shi *et al.*¹¹ and from Yang *et al.*,¹³ who concluded that *inelastic* scattering mechanisms significantly contributed to GMR. Yang *et al.* investigated a different material system: the ferromagnetic layers consisted of Co(90%)Fe(10%). Hence it is possible that different scattering mechanisms that were insignificant in our sample contributed to the GMR in their sample. However, Yang *et al.* directly calculated L without using $\kappa(H)$ versus $1/\rho(H)$ plots. Consequently, they did not account for a possible κ_{off} that could have contributed to the deviations from the WF law they claim to have observed. The argumentation of Shi *et al.* is based on $\kappa(H)$ versus $1/\rho(H)$ plots. They observe a clear deviation from linearity of the resulting curves above the saturation field of about 400 mT, which is tantamount to an increasing L in this field range (see Fig. 9 in Ref. 10). However, according to Fig. 7 in Ref. 10 the GMR effect occurs over a field range that is below 400 mT. Consequently, a conclusion from the observed deviations from linearity at high fields to the nature of the scattering processes responsible for GMR at low fields cannot be drawn. In fact, for applied fields below 400 mT, they explicitly presuppose that the WF law holds, and use a linear fit to obtain κ_{off} and L . Therefore the measurement data of Shi *et al.* on Co/Cu multilayers is in agreement with our results. As shown in Fig. 6(b), we also observe deviations from linearity at high fields. The deviations observed by Shi *et al.* appear larger due to stronger applied fields, up to about 1 T. These deviations could be ascribed to the presence of magnon magnetoresistance (MMR)^{25,41} that results in a linear decrease of ρ with increasing applied field due to diminishing of electron-magnon scattering. As this scattering process is *inelastic*, MMR is accompanied with a change of L . Below the saturation field, the small effect of MMR is masked by the much larger GMR effect.

VI. CONCLUSION

We have revisited the concept of using thermal conductivity measurements to judge about the significance of *inelastic* scattering for GMR in Co/Cu multilayers. We have found

that the usual interpretation in terms of the WF law can lead to wrong conclusions in the context of the GMR effect. For example, by assuming that electron-phonon scattering is spin-independent and thus insignificant for GMR, we found deviations from the WF law. On the other hand, we have shown that the WF law holds in the presence of spin-dependent electron-phonon scattering for the special case that inelastic and elastic scattering mechanisms are characterized by the same spin asymmetry. To complement the simple models developed, we have applied a modified 3ω method for detecting field-dependent changes of the in-plane thermal conductivity of a Co/Cu multilayer. The results indicate that the electronic thermal conductivity of the Co/Cu multilayer is a linear function of the electrical conductivity if both are changed by an external magnetic field. From this behavior, which we have observed over the temperature range between 10 and 300 K, we arrived at the following conclusions for the Co/Cu multilayer: electron-magnon scattering is negligible for GMR and electron-phonon scattering is characterized by the same spin asymmetry as the predominant elastic scattering of electrons at interfaces.

ACKNOWLEDGMENTS

We thank T. T. Heikkilä, Aalto University, for inspiring discussions. We thank J. Kimling, S. Martens, and D. Görlitz for discussions, and R. Meissner and L. Akinsinde for technical support. This work was supported by the German Research Foundation (DFG) within the Priority Program SPP 1538 “Spin-Caloric Transport.”

APPENDIX: THERMAL CONDUCTIVITY OF THE SUBSTRATE

The thermal conductivity of the fused silica substrate was determined using 3ω measurements as described in Sec. IV A. The results are shown in Fig. 10. The obtained values are in agreement with those determined by others⁴² for amorphous quartz.

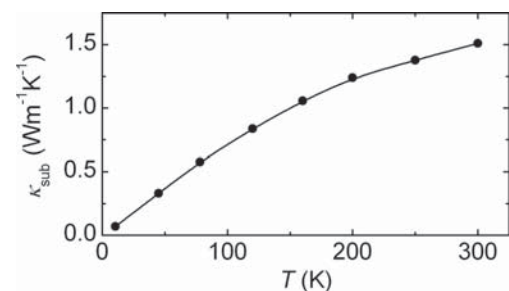


FIG. 10. Temperature dependence of the thermal conductivity of the fused silica substrate determined from 3ω measurements.

*johannes.kimling@physik.uni-hamburg.de

¹M. N. Baibich, J. M. Broto, A. Fert, F. Nguyen Van Dau, F. Petroff, P. Etienne, G. Creuzet, A. Friederich, and J. Chazelas, Phys. Rev. Lett. **61**, 2472 (1988).

²G. Binasch, P. Grünberg, F. Saurenbach, and W. Zinn, Phys. Rev. B **39**, 4828 (1989).

³E. Y. Tsymlal and D. G. Pettifor, *Perspectives of Giant Magnetoresistance*, edited by H. Ehrenreich and F. Spaepen,

- Solid State Physics Vol. 56 (Academic Press, London, 2001), pp. 113–237.
- ⁴J. Sakurai, M. Horie, S. Araki, H. Yamamoto, and T. Shinjo, *J. Phys. Soc. Jpn.* **60**, 2522 (1991).
- ⁵M. Conover, M. Brodsky, J. Mattson, C. Sowers, and S. Bader, *J. Magn. Magn. Mater.* **102**, L5 (1991).
- ⁶L. Piraux, A. Fert, P. Schroeder, R. Loloee, and P. Etienne, *J. Magn. Magn. Mater.* **110**, L247 (1992).
- ⁷J. Shi, R. C. Yu, S. S. P. Parkin, and M. B. Salamon, *J. Appl. Phys.* **73**, 5524 (1993).
- ⁸H. Sato, Y. Aoki, Y. Kobayashi, H. Yamamoto, and T. Shinjo, *J. Magn. Magn. Mater.* **126**, 410 (1993).
- ⁹L. Piraux, M. Cassart, J. S. Jiang, J. Q. Xiao, and C. L. Chien, *Phys. Rev. B* **48**, 638 (1993).
- ¹⁰H. Sato, H. Henmi, Y. Kobayashi, Y. Aoki, H. Yamamoto, T. Shinjo, and V. Sechovsky, *J. Appl. Phys.* **76**, 6919 (1994).
- ¹¹J. Shi, K. Pettit, E. Kita, S. S. P. Parkin, R. Nakatani, and M. B. Salamon, *Phys. Rev. B* **54**, 15273 (1996).
- ¹²F. Tsui, B. Chen, J. Wellman, C. Uher, and R. Clarke, *J. Appl. Phys.* **81**, 4586 (1997).
- ¹³Y. Yang, J.-G. Zhu, R. M. White, and M. Asheghi, *J. Appl. Phys.* **99**, 063703 (2006).
- ¹⁴T. T. Heikkilä, M. Hatami, and G. E. W. Bauer, *Phys. Rev. B* **81**, 100408(R) (2010).
- ¹⁵G. E. Bauer, A. H. MacDonald, and S. Maekawa, *Solid State Commun.* **150**, 459 (2010).
- ¹⁶G. E. W. Bauer, E. Saitoh, and B. J. van Wees, *Nat. Mater.* **11**, 391 (2012).
- ¹⁷D. G. Cahill, *Rev. Sci. Instrum.* **61**, 802 (1990).
- ¹⁸R. E. Camley and J. Barnas, *Phys. Rev. Lett.* **63**, 664 (1989).
- ¹⁹T. Valet and A. Fert, *Phys. Rev. B* **48**, 7099 (1993).
- ²⁰N. F. Mott, *Proc. Phys. Soc. (London), Ser. A* **153**, 699 (1936).
- ²¹C. Uher, *Thermal Conductivity of Metals*, edited by T. M. Tritt (Kluwer Academic/Plenum Publishers, New York, 2004), pp. 23, 85, 86.
- ²²G. Wiedemann and R. Franz, *Ann. Phys.* **89**, 497 (1853).
- ²³N. W. Ashcroft and N. D. Mermin, *Solid State Physics* (Thomson Learning, 1976), p. 322.
- ²⁴L. Colquitt, *Phys. Rev.* **139**, A1857 (1965).
- ²⁵B. Raquet, M. Viret, E. Sondergard, O. Cespedes, and R. Mamy, *Phys. Rev. B* **66**, 024433 (2002).
- ²⁶B. Dieny, *J. Magn. Magn. Mater.* **136**, 335 (1994).
- ²⁷A. Fert, *J. Phys. C: Solid State Phys.* **2**, 1784 (1969).
- ²⁸D. G. Cahill, M. Katiyar, and J. R. Abelson, *Phys. Rev. B* **50**, 6077 (1994).
- ²⁹L. Lu, W. Yi, and D. L. Zhang, *Rev. Sci. Instrum.* **72**, 2996 (2001).
- ³⁰T. Borca-Tasciuc, A. R. Kumar, and G. Chen, *Rev. Sci. Instrum.* **72**, 2139 (2001).
- ³¹B. W. Olson, S. Graham, and K. Chen, *Rev. Sci. Instrum.* **76**, 053901 (2005).
- ³²S.-M. Lee and D. G. Cahill, *J. Appl. Phys.* **81**, 2590 (1997).
- ³³S. P. Gurrum, W. P. King, and Y. K. Joshi, *J. Appl. Phys.* **103**, 113517 (2008).
- ³⁴Mechanical and thermal properties of fused silica were taken from www.heraeus-quarzglas.com.
- ³⁵L. J. van der Pauw, *Philips Res. Rep.* **13**, 1 (1958).
- ³⁶Y. Yang, W. Liu, and M. Asheghi, *Appl. Phys. Lett.* **84**, 3121 (2004).
- ³⁷S. S. P. Parkin, A. Modak, and D. J. Smith, *Phys. Rev. B* **50**, 9136 (1993).
- ³⁸F. Petroff, A. Barthélémy, A. Hamzic, A. Fert, P. Etienne, S. Lequien, and G. Creuzet, *J. Magn. Magn. Mater.* **93**, 95 (1991).
- ³⁹S. Zhang and P. M. Levy, *Phys. Rev. B* **43**, 11048 (1991).
- ⁴⁰C. Vouille, A. Barthélémy, F. Elokani Mpondo, A. Fert, P. A. Schroeder, S. Y. Hsu, A. Reilly, and R. Loloee, *Phys. Rev. B* **60**, 6710 (1999).
- ⁴¹A. P. Mihai, J. P. Attané, A. Marty, P. Warin, and Y. Samson, *Phys. Rev. B* **77**, 060401 (2008).
- ⁴²R. W. Powell, C. Y. Ho, and P. E. Liley, *Thermal Conductivity of Selected Materials* (U.S. Department of Commerce, National Bureau of Standards, Washington, 1966), p. 99.

7 Conclusion

We have examined various transport phenomena in thermoelectric and ferromagnetic nanostructures. We have synthesized Bi_2Te_3 nanowires via a gold-nanoparticle assisted vapor-liquid-solid mechanism and prepared single-nanowire microdevices for measuring the Seebeck coefficient and the electrical resistivity. Using micrometer-sized heater lines and thermometers we generated and measured temperature differences of the order of 1 K along individual nanowires with typical lengths of 10 μm . We demonstrated that by annealing in a Te atmosphere the Bi-rich as-grown nanowires can be transformed into nearly intrinsic single-crystalline Bi_2Te_3 nanowires. Structure and composition of as-grown and annealed nanowires were determined by high-resolution transmission electron microscopy and by energy-dispersive x-ray spectroscopy inside a transmission-electron microscope. The intrinsic behavior of individual annealed nanowires was confirmed by measuring their Seebeck coefficient and electrical resistance over a temperature range between 300 and 430 K. These nanowires may be used for studying quantum confinement effects, as well as for revealing their topological-insulating nature by means of transport measurements [Peng 09].

An important role in this thesis was assumed by the 3ω method, in particular for the detection of field-dependent changes of the thermal conductivity. We have revisited the concept of the 3ω method for voltage-driven measuring setups. The respective Fourier representations of the current and the measuring voltage were derived, and it was clarified that a correction factor proposed earlier by Dames and Chen [Dame 05] is not required for voltage-driven 1ω measurements, and also not necessarily required for voltage-driven 3ω measurements, if the 1ω current is measured. A correction factor is required for voltage-driven direct 3ω measurements, but not for voltage-driven 3ω measurements after subtracting the 1ω component from the measuring voltage.

Furthermore, we have synthesized Ni nanowires by electrodeposition in the pores of anodized aluminum oxide membranes and prepared microdevices including individual nanowires suspended over trenches for 3ω measurements. We determined the electrical resistance, the thermal conductance, and the Lorenz number of several Ni nanowires in the temperature range between 78 and 380 K. By using a slightly modified 3ω method under applied magnetic fields we succeeded in measuring the anisotropic magnetothermal resistance (AMTR) effect. Since this effect has not been described before, a simple model that ascribes its origin to the spin-orbit interaction was developed in analogy to the anisotropic magnetoresistance (AMR) effect. This model further suggests that due to electron-magnon scattering the AMTR effect in Ni nanowires is weaker than the respective AMR effect – a behavior that we have also observed experimentally. The study of the AMTR effect may be extended by performing similar measurements on nanowires from ferromagnetic alloys. Furthermore, our modified 3ω technique may be applied for investigating the giant magnetothermal resistance effect in the current-perpendicular-to-the-planes geometry, e.g. in Co/Cu-multilayered nanowires. Then, one could obtain information about the spin-heat diffusion length by comparing the GMTR effect with the GMR effect on the same sample.

In addition to that, we have investigated the in-plane thermal transport in Co/Cu multilayers. Applying the 3ω method to metal thin films is unusual, because the conventional cross-plane method works best for dielectric thin films deposited on substrates with thermal conductivities larger than the respective thermal conductivity of the thin film. We demonstrated that for the reversed situation – metallic thin film on dielectric substrate – 3ω measurements can be employed to determine the in-plane thermal conductivity of the metal thin film. We have revisited the Wiedemann-Franz law in magnetic multilayers and demonstrated, among others, that the presence of inelastic scattering not necessarily leads to a magnetic-field dependent Lorenz number. The reverse had been claimed earlier by other groups [Sato 94, Shi 96, Tsui 97, Yang 06]. We have measured the electrical resistivity and the electronic thermal conductivity of the Co/Cu multilayer as functions of the applied magnetic field, as well as the Lorenz number and the GMR and GMTR ratios over a temperature range between 10 and 300 K. It turned out that the Lorenz number in the Co/Cu multilayer investigated is a constant with respect to the applied magnetic field. Considering the simple models developed we concluded that the influence of electron-magnon scattering on the GMR effect in the Co/Cu multilayer is negligible. It was further found that electron-phonon scattering is characterized by the same spin asymmetry as the predominant elastic scattering of electrons at interfaces in the Co/Cu multilayer. In the presence of sizable electron-magnon scattering our model indicates that the Lorenz number of the parallel magnetic configuration would be larger than the one of the antiparallel configuration, while the model of Shi *et al.* suggests the opposite behavior [Shi 96]. This may for example be tested by performing similar measurements on Fe/Cr multilayers, for which electron-magnon scattering can play a significant role at temperatures above 50 K [Petr 91, Zhan 91].

A Review Article

Thermoelectric Nanostructures:
From Physical Model Systems towards Nanograined Composites

Reprinted with permission from

Kornelius Nielsch, Julien Bachmann, Johannes Kimling, and Harald Böttner

Advanced Energy Materials, **1**, 713–731 (2011)

Copyright 2011 by the WILEY-VCH Verlag GmbH & Co. KGaA, Weinheim.

Thermoelectric Nanostructures: From Physical Model Systems towards Nanograined Composites

Kornelius Nielsch,* Julien Bachmann, Johannes Kimling, and Harald Böttner

Thermoelectric materials could play an increasing role for the efficient use of energy resources and waste heat recovery in the future. The thermoelectric efficiency of materials is described by the figure of merit $ZT = (S^2\sigma T)/\kappa$ (S Seebeck coefficient, σ electrical conductivity, κ thermal conductivity, and T absolute temperature). In recent years, several groups worldwide have been able to experimentally prove the enhancement of the thermoelectric efficiency by reduction of the thermal conductivity due to phonon blocking at nanostructured interfaces. This review addresses recent developments from thermoelectric model systems, e.g. nanowires, nanoscale meshes, and thermionic superlattices, up to nanograined bulk-materials. In particular, the progress of nanostructured silicon and related alloys as an emerging material in thermoelectrics is emphasized. Scalable synthesis approaches of high-performance thermoelectrics for high-temperature applications is discussed at the end.

1. Introduction

More than half of the primary energy utilized is wasted in form of heat.^[1] The vast majority of this waste heat is produced in power stations, heating systems, and motor vehicles. Technologies for recovering this waste heat are a subject of great interest. In this regard, thermoelectric materials could make a significant contribution to improving the efficiency of power systems. To date, thermoelectric energy conversion has remained confined to niche applications due to the low efficiency of the known materials.^[2–5] The potential of individual materials for thermoelectric applications is usually quantified by the figure of merit $ZT = (S^2\sigma/\kappa)T$ (where S is the Seebeck coefficient [$\mu\text{V K}^{-1}$]; σ , electrical conductivity [$\Omega^{-1}\text{ cm}^{-1}$]; and κ , thermal conductivity $\text{W m}^{-1}\text{ K}^{-1}$). For the past five decades, the figure of merit of thermoelectric materials in industrial applications has remained static near $ZT \approx 1$, which corresponds to an efficiency of approx. 10% for a temperature difference $\Delta T = 300\text{ K}$.

Prof. K. Nielsch, Prof. J. Bachmann, J. Kimling
University of Hamburg
Institute of Applied Physics
Jungiusstr. 11, 20355 Hamburg, Germany
E-mail: kornelius.nielsch@physnet.uni-hamburg.de

Dr. H. Böttner
Fraunhofer Institute for Physical Measurement Techniques IPM
Department of Thermoelectrics and Integrated Sensor Systems
Heidenhofstrasse 8, 79110 Freiburg, Germany

DOI: 10.1002/aenm.201100207

According to a recent study, a doubling of the quality (that is, ZT value) of thermoelectric materials in industrial applications could lead to a tenfold increase in the number of their applications.^[1]

Beside waste heat recovery, thermoelectric converters can be used for cooling or refrigeration. They work silently and can be maintenance-free for extended periods of time. The first applications were discovered in the 1920s, for example, electricity generation using kerosene lamps.^[2] In the 1960s, thermoelectric converters took care of the energy supply for the moon landing, an event which prompted significant development effort in thermoelectricity. Nowadays, thermoelectric generators are still the first choice for missions to the edge of our solar system where the solar energy supply is insufficient. The potential of thermoelectrics might also be particularly important for miniature devices. Currently, temperature differences of few degrees can set watches running.

In the following areas future applications for thermoelectric generators based on high-performance thermoelectric materials (Figure 1) are expected and, in some cases already partially taking place:

- Miniaturized autarkic sensor systems powered by an integrated thermoelectric generator with a wireless data transmitter.
- Waste heat recovery in automobiles and other combustion-engine-powered vehicles for enhanced efficiency and electric current supply of the electronic system.
- Ventilated wood stove powered by a thermoelectric generator. Enhanced oxygen supply, improves burning process.
- Heating systems and water boilers with thermoelectric generator units which generate the electricity for the control units and pumping systems.
- On the long term perspective: waste heat recovery for medium-scale industrial facilities.

Thermoelectric cooling devices are operated at moderate temperatures below around $150\text{ }^\circ\text{C}$, whereas many potential applications for waste heat recovery utilize larger temperature differences of a few hundred degrees, up to a limit of $1000\text{ }^\circ\text{C}$. The development of novel thermoelectric materials and devices, especially for high temperature applications provides many research opportunities in materials science, solid-state physics, chemistry and device engineering in the current decade.

2. Physical Functionality

The direct conversion of heat to electricity in thermoelectric devices is based on the Seebeck effect (named for Thomas J. Seebeck, 1821). In thermoelectric cooling devices use is made of the Peltier effect (named for Jean C. A. Peltier, 1834).^[3–5] The thermoelectric effects were initially examined in metals. These generate only small thermovoltages of a few tens of microvolts per Kelvin. The electrical potential difference generated per degree of temperature difference is called Seebeck coefficient, S , or thermopower.

By using semiconductors, substantially higher thermovoltages of some hundreds of $\mu\text{V}/\text{K}$ can be achieved. For thermoelectric applications, low bandgap semiconductors, with typical charge carrier concentrations in the order of $10^{19}/\text{cm}^3$, are considered most suitable. Apart from a large Seebeck coefficient, a good thermoelectric material additionally needs to exhibit a high electrical conductivity and a low thermal conductivity to obtain a large figure of merit, ZT , at a certain temperature. The interdependence of these quantities has limited the ZT to values around one for the best conventional thermoelectric materials. For semiconductors and thermoelectric materials, the heat conductivity depends on both free charge carriers (holes or electrons) and phonons: $\kappa_{\text{tot}} = \kappa_{\text{El}} + \kappa_{\text{Ph}}$. The phonon-based thermal conductivity κ_{Ph} is decoupled from the electric conductivity. Thus, numerous attempts for the optimization of the thermoelectric efficiency ZT in nanostructures are based on a reduction of the heat transport by phonons.

3. Enhanced Efficiencies by Nanostructuring

The birth year for thermoelectric thin films and nanostructures was approximately 1992 and was directly connected to the proposals of Hicks and Dresselhaus^[13] regarding the utilization of quantum size effects for thermoelectric transport and on the other hand by R. Venkatasubramanian^[8] to enhance phonon scattering at nanoscale interfaces. These proposals have predicted huge improvements of the figure of merit (ZT) in low-dimensional materials, based on two different physical principles. In the race towards very high ZT values, nanotechnologically synthesized materials are currently regarded as particularly promising. The development of thermoelectric material systems can be divided into three categories:

- 1 Model systems: nanowires, nanomeshes, and quantum dot systems
- 2 Epitaxial multilayers and superlattices
- 3 Nanograined bulk materials

In this review, these categories will be presented in the same order. **Figure 2** shows a selection of landmark publications in each category of nanostructured thermoelectric materials. For single-crystalline nanowires based on highly doped silicon, enhanced ZT values of 0.6 and 1.2 near room temperature have been reported independently by two groups in 2008,^[6,7] although bulk single-crystalline silicon exhibits a more than two orders of magnitude lower ZT at room temperatures. Both research groups have demonstrated a substantial suppression of the thermal conductivity by reduction of the nanowire diameter and enhanced surface roughness, which significantly influenced the phonon propagation. The thermoelectric characterization was performed on individual nanowires by using microstructured measurement



Kornelius Nielsch studied physics at the Mercator University in Duisburg (1993–97) and conducted his diploma work at the University of Lund. His Ph.D. was carried out at the Max-Planck-Institute in Halle, Germany. From 2002 he worked as a postdoctoral associate at the MIT. From 2003 he was leading a research group on “Multifunctional

Nanowires and Nanotubes” at the Max-Planck-Institute in Halle. Nielsch was appointed as professor for Experimental Physics at the University of Hamburg in 2007. Since 2009 he coordinates the German Priority Program of Thermoelectric Nanostructures, funded by the German Science Foundation.



Julien Bachmann studied molecular chemistry at the University of Lausanne, Switzerland, and at the Massachusetts Institute of Technology. He then focused on materials science research as a postdoc at the Max Planck Institute of Microstructure Physics in Halle and at the University of Hamburg, Germany. He is now a Junior Professor in the

Physics and Chemistry departments in Hamburg. Julien’s research focuses on the preparation of nanostructured materials and their application to energy conversion.



Johannes Kimling studied physics at the University of Konstanz. He is now a PhD candidate at the Institute of Applied Physics at the University of Hamburg. The research of Johannes focuses on the synthesis of nanowires and their thermoelectric characterization.



Dr. Harald Böttner is head of the department “Thermoelectrics and Integrated Sensor Systems” of the Fraunhofer Institute for Physical Measurement Techniques IPM, Freiburg/Germany. He received his Ph.D. in 1977 at the University of Münster, Germany. In 1978 he joined the Fraunhofer Society and since

1980 he is with the Fraunhofer IPM, Freiburg. His research activities are focused on nanoscale thermoelectrics, industrializing thermoelectrics as materials and devices, thermoelectric metrology and systems. At Fraunhofer IPM Dr. Böttner was head of the development of the first completely wafer-based miniaturized thermoelectric devices known as MicroPelt.

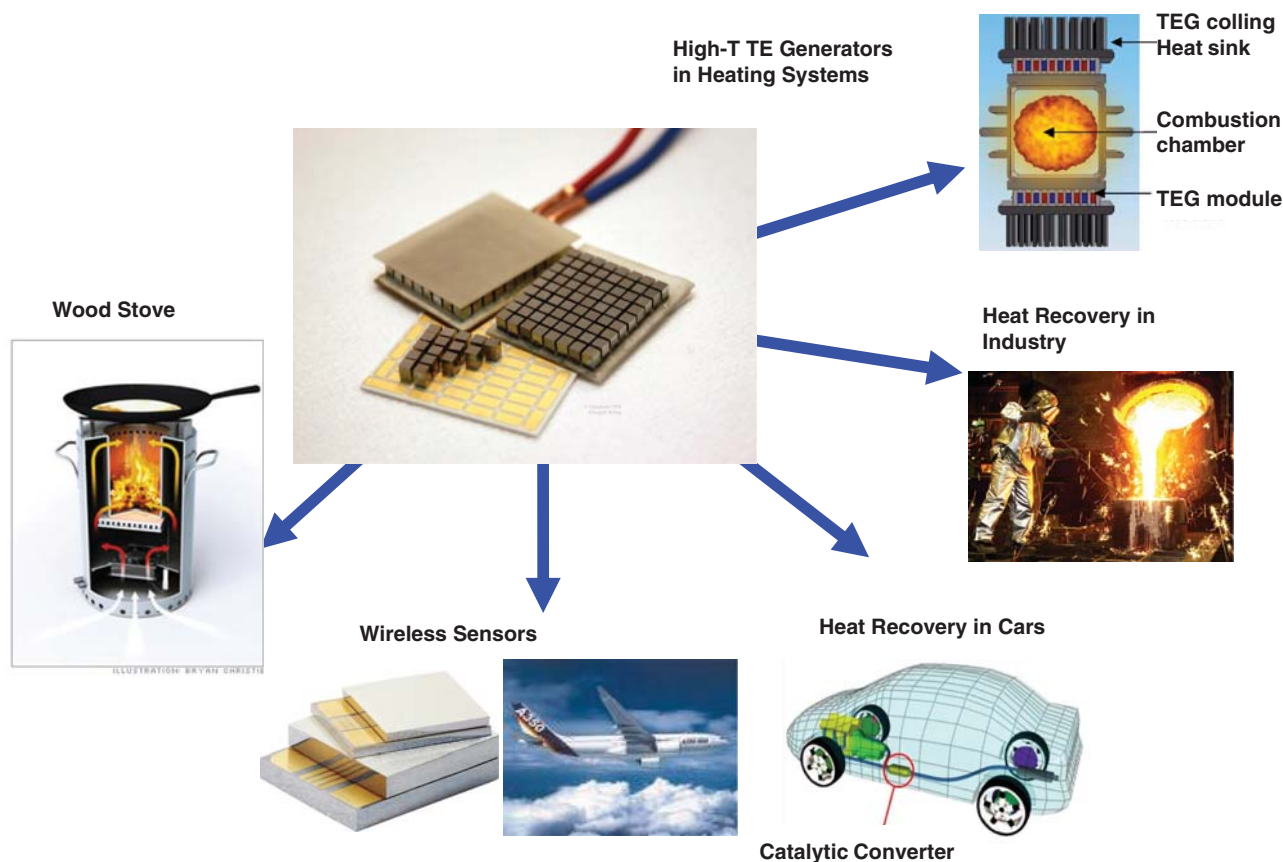


Figure 1. Overview of potential application of thermoelectric generators.

platforms. In this context we will also mention the thermoelectric performance of nanomeshes and quantum dot systems.

The highest thermoelectric performance was reported for epitaxial multilayer structures based on $\text{Sb}_2\text{Te}_3/\text{Bi}_2\text{Te}_3$ multilayers,^[8] and quantum dot superlattices based on PbTeSe dots in a PbTe matrix,^[9] which exhibited ZT values of 2.4 at 30 °C and 3.4 at 300 °C (575 K), respectively. Due to the restricted potentials of device application limited by sample thickness, area, and production costs, these epitaxial systems with record ZT values remained model systems until today. Nevertheless, they have strongly stimulated the worldwide research on thermoelectric nanostructures. Currently, the field of epitaxial multilayered systems is still very active on the development of artificial thermoelectrics, so-called thermionic systems. These are based on the physical principle of energy filtering of electrons for cross-plane transport to obtain enhanced power factors.

By refining established and scalable synthesis processes for thermoelectric bulk materials, the thermoelectric research is now focused on the development of nanograined bulk materials, by compacting of nanoparticles and/or by precipitation of nanoparticles in a bulk-system from different material phases. In 2004 Kanatzidis and co-workers reported on a nanostructured PbTe -matrix with precipitated AgSbTe_2 nanoparticles, fabricated by a conventional synthesis route in a quartz ampoule. The resulting ZT value was 2.2 at 530 °C.^[10] In the 1960s the company Siemens Schuckertwerke AG in Germany had already reported about remarkable ZT values

of 1.2 at 400 °C for this material system.^[11] By refining the grinding process for p-type $(\text{Sb}/\text{Bi})_2\text{Te}_3$ nanopowders from bulk ingots, a team from Boston Universities has achieved a nanograined nanocomposite after hot pressing, which revealed a maximum ZT value of 1.4 with a 100-degree increase of the temperature of highest efficiency for the same bulk material.^[12] Although a 50% increase of the thermoelectric efficiency seems to be moderate in comparison with many theoretic predictions for thermoelectric model systems, this approach is scalable, highly reproducible, and seems to be the most promising approach towards next-generation thermoelectric applications and devices. It has been applied to a wide range of thermoelectric materials over the last three years.

Step-by-step we will guide the reader through the three important areas of thermoelectric research depicted in Figure 2 and their development over the past decade. The survey starts with a discussion on thermoelectric nanowires as one kind of experimental model system.

4. General Considerations about Thermoelectric Nanowires

Research on nanowires with respect to thermoelectric properties was initiated by the calculations of Hicks and Dresselhaus,^[13] which predicted a large enhancement of ZT in bismuth telluride quantum wires. The confinement of electrons to move in a single dimension results in an increase of the density of states which in turn

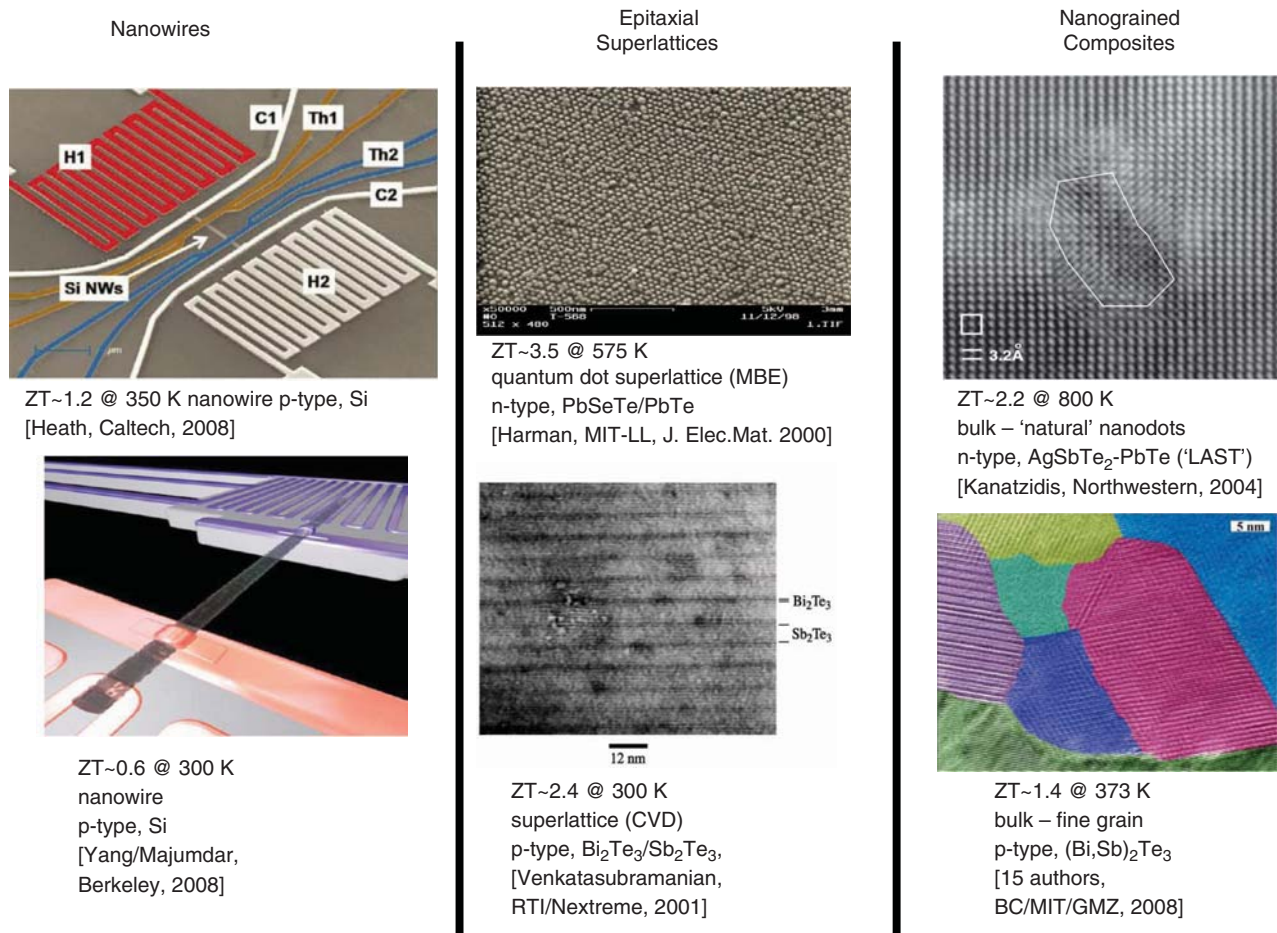


Figure 2. Research highlights on the development of thermoelectric nanostructure and their figure of merit ZT of the past decade (2001–2010). Reproduced with permission.^[6–8,10,62] Copyright 2000, Springer; 2004, Science; and 2008, Nature Publishing Group, respectively.

increases the thermoelectric power factor. In addition, the lattice thermal conductivity is reduced due to increased phonon scattering from the surface of the wire. The calculations are based on the Boltzmann transport equation in the relaxation time approximation, assuming a constant relaxation time. The results show a monotonically increasing ZT with decreasing wire diameters.^[13] To observe quantum confinement effects in a nanowire, its diameter must be similar to the Fermi wavelength, which is on the order of 1 nm for bismuth telluride. This critical diameter is enhanced in materials with small effective carrier masses and large carrier mean free paths. Both properties apply to bismuth on which subsequent theoretical and experimental work was focused.^[13–17] The ground state energy of the charge carriers inside the confinement potential leads to an increase of the effective bandgap. Consequently, a semimetal-to-semiconductor transition is predicted to occur in bismuth nanowires at experimentally attainable diameters around 50 nm at a temperature of 77 K.^[17] Temperature-dependent measurements of the resistance as well as magnetoresistance measurements were performed on single crystalline bismuth nanowire arrays.^[14,15,18,19] It was observed that the temperature dependence of the total resistance is very sensitive to the diameters of the individual nanowires included in the array, which was explained with a semimetal-to-semiconductor transition at

a diameter of around 65 nm. Similar trends in the temperature dependence of the resistance were observed in individual polycrystalline bismuth nanowires.^[20] However, with additional electric field-effect measurements they showed that the nanowires with diameters of 40 nm were still semimetallic. The single-crystalline bismuth nanowires were synthesized by using porous alumina templates, which were filled with bismuth either by high-pressure injection from the liquid phase^[14] or by using a vapor-phase technique.^[19] The nanowires can be released from their template by selective chemical etching of alumina. During this etching process a highly stable surface oxide layer of about 10-nm thickness is formed which makes it very difficult to create ohmic electrical contacts.^[21,22] This is the reason why systematic studies on the ZT of individual single-crystalline bismuth nanowires are still missing. Recently, a novel stress-induced method for growing single-crystalline bismuth nanowires with diameters down to 30 nm was introduced.^[23] By using argon sputter-etching of the bismuth oxide followed by in situ gold sputtering, it was possible to obtain ohmic electrical contacts to a wire with a diameter of 120 nm which was grown by this method.

Calculations on lead telluride and gallium arsenide quantum-well and quantum-wire superlattices performed by Broido and Reinecke showed that the thermoelectric powerfactor is still

enhanced for small diameters, but remains finite for all diameters if all frequency dependent scattering mechanisms are considered in the calculations.^[24] In contrast, previous theoretical works on bismuth telluride, bismuth and bismuth antimonide nanowires have reported a divergence in the thermoelectric powerfactor for decreasing diameters. Calculations on electrical and thermal transport in III–V semiconductor nanowires suggest that enhanced ZT values could be observed in indium antimonide nanowires with diameters around 10 nm.^[25] Recent calculations on bismuth telluride nanowires^[26] that considered a size- and energy-dependent expression for the relaxation time predict the strong increase in ZT to occur at diameters one order of magnitude larger compared to Ref. 13. However after reaching a sharp maximum, a rapid decrease of ZT is predicted for further decreasing diameters.^[26] Farhangfar further outlines contributions of higher-energy subbands to the thermoelectric properties of a 50-nm thick bismuth telluride nanowire. Many-subband models are required for wires with large diameters and thus weak confinement. Recently, Cornett and Rabin^[27] considered the lowest 300 energy subbands for power factor calculations of indium antimonide nanowires. For large wire radii, their model predicts power factor values that are in good agreement with experimental bulk values. Along the diameter range between strong and weak confinement (~100 to ~17 nm), they predict a monotonically decreasing power factor. Below ~17 nm confinement effects are significant and the many-subband model can be replaced by the single-subband model, which was already used by Higgs and Dresselhaus.^[13]

Measurements on thermoelectric nanowires can be divided into two categories: ensemble measurements on large arrays of nanowires and measurements on individual nanowires.

With regard to thermoelectric application nanowire arrays with high packing densities have been realized, but the matrix heat leakage needs to be further minimized, and the difficulty to obtain reliable ohmic contacts to all nanowires has to be solved. Absolute values of the various transport properties measured in nanowire arrays can only be roughly estimated. Substantial progress has been achieved in the fabrication of microdevices for thermoelectric measurements on individual nanowires. **Table 1** shows two prominent microdevices: a typical microdevice for Seebeck measurements and a suspended microdevice to determine ZT , both for individual nanowires. The microdevice shown below is patterned to the nanowire onto a silicon substrate which has an insulating layer (typically around 200 nm silicon dioxide) on top. Before the microfabrication process, individual nanowires are usually placed onto the substrate by drop-casting from a solution containing suspended nanowires. Small contact resistances to thermoelectric nanowires were usually achieved by either physical or chemical etching of native oxide shells that built up during the nanowire synthesis. Concerning the suspended microdevice the large effort to get the nanowire to the desired position and difficulties in creating reliable thermal and electrical contact to the nanowire so far prevented systematic studies on the ZT of individual nanowires. Reported values on the thermoelectric powerfactor of individual nanowires are far below the corresponding bulk values. This was mainly attributed to difficulties in controlling the chemical composition of nanowires. **Table 2** summarizes experimentally determined ZT values of individual nanowires. Only silicon nanowires show enhanced thermoelectric performance, however mainly due a reduction in the thermal conductivity, which will be discussed below.

Table 1. Two prominent measurement microdevices for thermoelectric characterization of individual nanowires are presented. Microdevice (i) is lithographically patterned onto the nanowire, whereas microdevice (ii) is prefabricated and the nanowire is integrated subsequently. Reproduced with permission Copyright 2008 American Chemical Society, and 2007 American Institute of Physics.


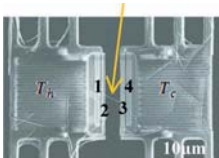
Micro Device	Accessible transport quantities	Brief description of the functionality
(i) ^[113] 	$\text{Electrical Resistance } R = \frac{U_{24}}{I}$ $\text{Seebeck Coefficient } S - S_l = \frac{U_{12}}{\Delta T_{12}}$ $U: \text{ Voltage,}$ $I: \text{ Current,}$ $\Delta T: \text{ Temperature difference,}$ $S_l: \text{ Seebeck coefficient of the metal leads.}$	A heating element is used to generate a temperature difference along the wire. ΔT_{12} is determined with two resistance thermometers, which have to be calibrated before the measurement. The thermovoltage U_{12} is measured using the contact leads of the thermometers. Additional leads are used for four-point resistance measurements.
(ii) ^[32,114] 	$\text{Electrical Resistance } R = \frac{U_{23}}{I}$ $\text{Thermal Conductance } G = G_b \frac{T_c - T_o}{T_h - T_c}$ $\text{Seebeck Coefficient } S - S_l = \frac{U_{12}}{T_h - T_c}$ $U: \text{ Voltage,}$ $I: \text{ Current,}$ $T_o, T_h, T_c: \text{ Temperatures of substrate,}$ $\text{heated membrane and unheated membrane,}$ $G_b: \text{ Thermal conductance of the SiN}_x \text{ beams.}$	Two adjacent SiN _x membranes, each of them contains two metal electrodes and a serpentine micro heater/ thermometer, are suspended with several SiN _x beams. A nanowire bridges the gap between the membranes and crosses the electrodes. Electrical and thermal contacts to the wire are improved by local deposition of a Pt layer. From the temperature difference of both membranes the thermal conductance of the wire can be determined if the thermal conductance of the SiN _x beams is known. The thermovoltage along the wire is measured using the two electrodes. Furthermore, the measurement device allows for structural characterization by transmission electron microscopy.

Table 2. Thermoelectric properties (electrical conductivity σ , Seebeck coefficient S , thermal conductivity κ and figure of merit ZT) measured on individual single-crystalline (*sc*) and polycrystalline (*pc*) nanowires summarized from selected references.

Material system	Diameter or Cross section [nm] or [nm ²]	Temperature [K]	Thermoelectric properties				Refs.
			σ [10 ⁶ /(Ω m)]	S [μ V/K]	κ [W/(mK)]	ZT	
Bi _x Te _{1-x} (<i>sc</i>)	81	300	0.07	-30	1.05	0.019	[115]
Bi _x Te _{1-x} (<i>pc</i>)	55	411	0.04	-90	1.2	0.13	[32]
Bi _x Te _{1-x} (<i>sc</i>)	52	306	0.22	-52	2.9	0.06	
CrSi ₂ (<i>sc</i>)	78	300	0.09	+125	7.7	0.060	[116]
	97	300	0.11	+120	7.7	0.062	
	103	300	0.05	+150	12	0.028	
Si* (<i>sc</i>), p-type (7×10^{19} /cm ⁻³)	20 × 20	200	-	-	-	1	[7]

* Ensemble measurement, results were averaged over 10 to 400 nanowires.

While an enhancement of the power factor in individual nanowires and nanowire arrays could not be observed so far, a reduction of the thermal conductivity is reported in several studies. For materials in which phonons with long mean free paths carry a significant amount of heat, a reduction of the thermal conductivity can be observed in their nanowire counterparts. For example for a lead telluride nanowire with a diameter of 182 nm, a reduction in the thermal conductivity of 50% with respect to the bulk value is reported.^[28] In polycrystalline bismuth nanowires a reduction of the thermal conductivity rather results from enhanced grain-boundary scattering which dominates over surface scattering for grain sizes smaller than the diameter.^[29] The thermal conductivity in silicon germanium alloys is reduced by alloy-scattering of high frequency phonons. In silicon germanium nanowires, the thermal conductivity can be further reduced by scattering of low-frequency phonons with long mean free paths from the surface of the wire.^[30,31] Because of the small effective phonon mean free path of bismuth telluride the thermal conductivity of bismuth telluride nanowires with diameters around 50 nm was reported to be close to the corresponding bulk value.^[32] The situation is different in nanowires in which the effective phonon mean free path is much larger than the diameter, such as silicon nanowires. Systematic measurements on the diameter dependence of the thermal conductivity were performed on single-crystalline silicon nanowires.^[33] They showed a drastic reduction in the thermal conductivity as the diameter was decreased. The nanowires in this study were grown by a vapour-liquid-solid method, in which molecular gaseous precursors thermally decomposed in a catalytic droplet, from which the desired solid compound crystallized continuously.^[34-36] A few years later Hochbaum *et al.* demonstrated that the lattice thermal conductivity of silicon nanowires can be even further reduced in nanowires with rough surfaces.^[6] They report that for nanowires with diameters around 50 nm, the lattice thermal conductivity is close to the amorphous limit of silicon, which is about 1 W/mK,^[37] even though the nanowires were single-crystalline. Using the electrical conductivity and the Seebeck coefficient measured on comparable nanowires from the same batch, they claim that the nanowires may reach ZT values of 0.6 near room temperature.^[6] The nanowires were fabricated from a silicon wafer by using

an aqueous electroless etching method. This top-down process enables the low-cost synthesis of silicon nanowires with a high control of the doping concentration in contrast to most bottom-up synthesis approaches for nanowire. A comprehensive review about the electrochemical synthesis of silicon nanowires from bulk-wafers has been recently published by Huang *et al.*^[38]

Using silicon as the material of interest is advantageous, because measurement microdevices with integrated nanowires of desired dimensions, controlled impurity doping level, crystallographic properties, and with monolithic contacts can be realized by top-down approaches. Such a measurement device was fabricated by Boukai *et al.*^[7] By tuning the diameter and p-doping level they were able to reach a ZT value of 1.0 in silicon nanowire arrays (at 200 K, wire cross-section 20 nm × 20 nm, doping level 7×10^{19} cm⁻³). Also in this study, the dominant improvement with respect to the bulk characteristics of silicon is a reduced (diameter-dependent) thermal conductivity. The optimum thermoelectric performance was achieved by additional tuning of the thermoelectric power factor by doping. A similar microdevice was fabricated by Hippalgaonkar *et al.*, but with integrated single-crystalline silicon nanowires having rough surfaces.^[39] In contrast to the nanowires obtained by electroless etching, only the sidewalls exhibited a rough surface, whereas the top and bottom surfaces of the nanowires were smooth. The reported thermal conductivity could be reduced to a level between the one for electroless etched Si nanowires and the one for vapour-liquid-solid grown nanowires (smooth surface), indicating that the suppression of the thermal conductivity in silicon nanowires increases with increasing degrees of surface roughness. **Figure 5** summarizes the experimental data for the thermal conductivity of the various silicon nanowires and silicon thin films.^[40]

The experimental findings on semiconducting nanowires were accompanied by theoretical work. The thermal conductivity of silicon nanowires with a germanium shell layer has been modelled by Yang *et al.*^[41] They found that the total thermal conductivity is dominated by the diameter of the silicon core. For a shell thickness around 0.5–1 times the core radius the thermal conductivity exhibits a minimum in thermal conductivity, but an enhancement of the phonon scattering by the germanium shell is moderate. Martin *et al.* modelled

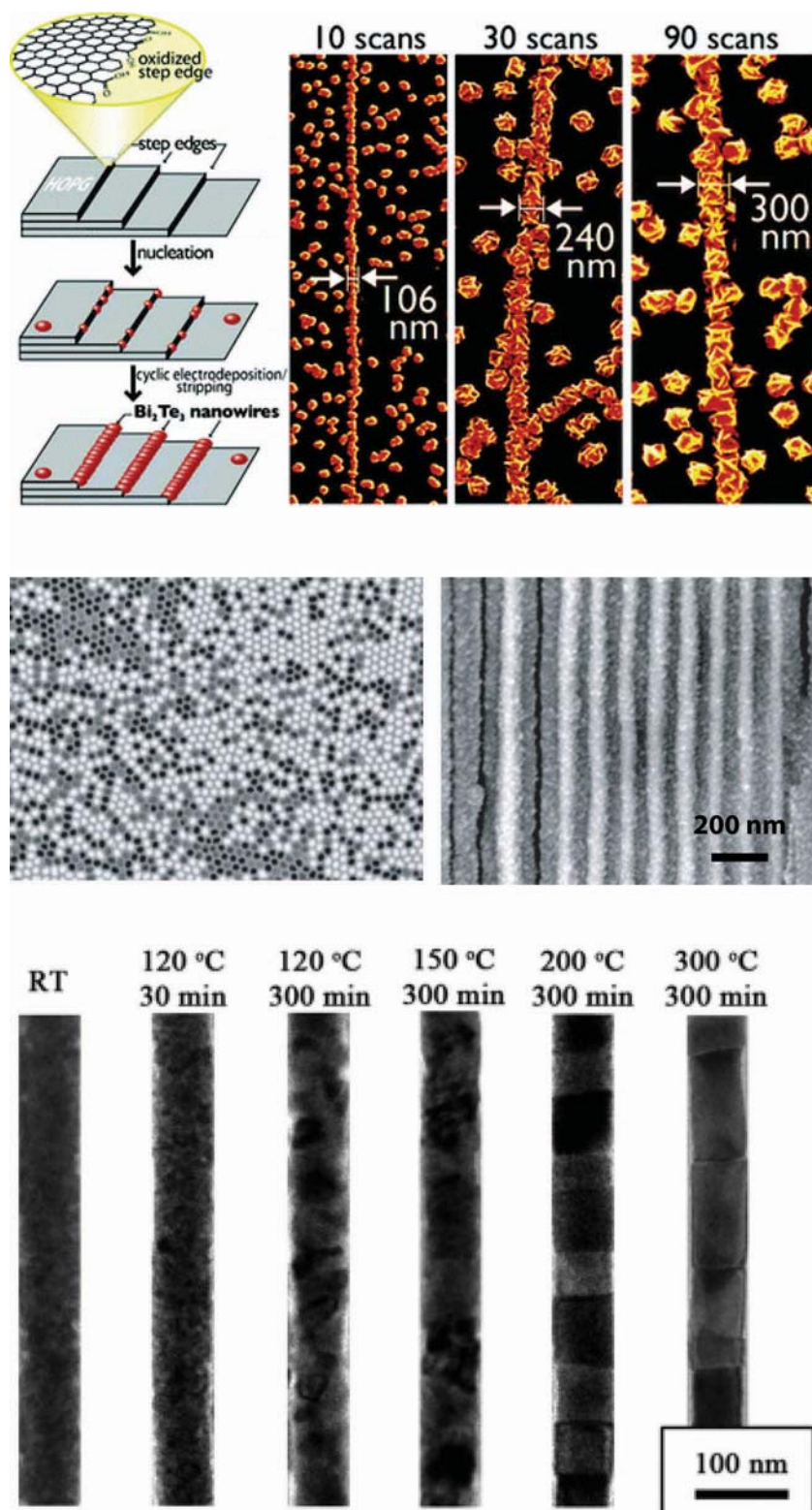


Figure 3. Nanowires of the V–VI compounds prepared by electrochemical methods. Top, a 'horizontal' system in which the step edges of a highly oriented pyrolytic graphite substrate serve as preferential nucleation sites.^[110] Center, an array of 'vertical' nanowires grown in an anodic alumina template.^[111] Bottom, thermal evolution of non-stoichiometric wires: phase separation leads to an additional level of structuring.^[112] Reproduced with permission. Copyright 2004 American Chemical Society, 2002 John Wiley and Sons, and 2007 American Chemical Society.

the thermal conductivity of silicon, germanium, and gallium arsenide nanowires with rough surfaces.^[42] Besides the drastic reduction of the thermal conductivity in silicon nanowires mainly due to phonon scattering from surface roughness, they predict remarkably low thermal conductivity values in rough nanowires of the latter two materials, several times lower than in rough silicon nanowires.^[49]

In conclusion, adopting the concept of surface roughness to nanowires of other semiconducting materials, for example germanium, gallium arsenide, silicon germanium alloys or indium antimonide, might reveal exciting new experimental results with respect to their thermoelectric properties in the near future.

The above mentioned suspended micro-devices with integrated silicon nanowires fabricated by using a top-down approach are model systems to systematically investigate phonon transport in silicon nanowires. Well-defined III–V semiconductor nanowires that include a double-barrier heterostructure can be used as model systems to study the thermoelectric properties of a quantum dot. Thermoelectric investigations of multilayered nanowires that include a quantum dot have been performed by the group of H. Linke at the University of Oregon and the University of Lund.^[43–45] An important advantage of confined semiconductor systems is the opportunity to tailor the thermoelectric properties by designing the energy spectrum at which electron transport can occur. An ideal case is provided by quantum dots, which can be designed such that electron transport takes place only within a very narrow energy range. When only electron heat flow is considered, such energy-filtering quantum dots convert heat to electricity with near Carnot efficiency,^[50] and their efficiency at maximum power approaches the fundamental Curzon-Ahlborn limit.^[51] Experiments using quantum dots defined by a double-barrier heterostructure embedded in a nanowire indeed demonstrate a very high Seebeck coefficient up to 3 mV K^{-1} if a single energy level contributes to transport (Figure 6). To determine the Seebeck coefficient, a novel thermometry technique was developed that uses the quantum dot itself as a thermometer.^[50] Comprehensive investigations on quantum dot systems based on 2D electron gases under the influence of heat gradients were performed by the group of H. Buhmann^[46,47] Although these fundamental studies have been performed at low temperatures (50 mK

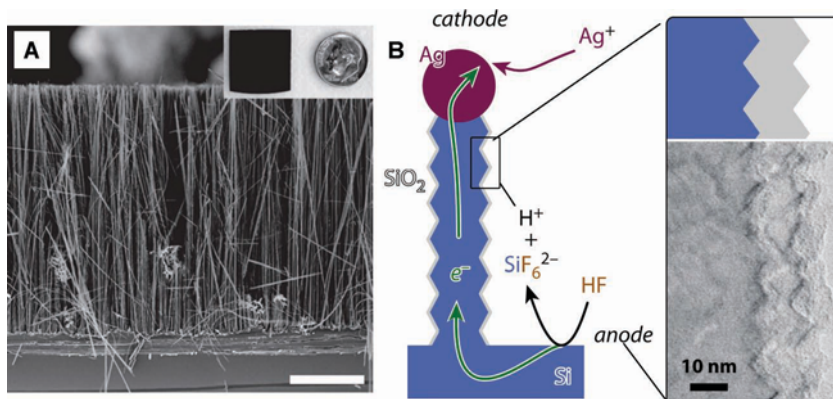


Figure 4. (a) Cross-sectional SEM of an electrochemically etched (EE) Si nanowire array. Dendritic Ag growth can be seen within the array—a product of Ag^+ reduction onto the wafer during reaction. Inset, an EE Si nanowire array Si wafer chip of the typical size used for the syntheses. Similar results are obtained on entire 4-inch wafers. The chip is dark and non-reflective owing to light scattering by, and absorbing into, the array. (b) Schematic description of the catalytic wet chemical etching of silicon used to generate rough Si nanowires:^[6] an electrochemical cell is generated between the bulk Si surface, which dissolves oxidatively in the hydrofluoric acid solution, and the wire tip, at which dissolved silver ions are reduced to the metallic state. The lateral surfaces of the wire are rendered inert by an oxide layer. Electron micrographs reproduced with permission. Copyright 2008 Nature Publishing Group.

to 5 K) and the material systems are not suitable for energy harvesting, these studies of the thermoelectric transport are a powerful spectroscopic tool to study the energy structure of the confined and interacting quantum systems. From the Kelvin-Onsager relation one can infer that the thermopower of an electronic system is directly related to the average energy transfer between two reservoirs. Additionally, it reflects the energy dependence of the conductance of a system and thus is much more sensitive than direct conductance measurements. This measurement technique has been successfully used to measure the influence of cotunnel contribution to the thermopower for a quantum dot system at very low temperatures.^[53] Recently, it was also possible to show that quantum dot state that couple asymmetrically to the reservoir can lead to thermal rectifying behavior.^[54]

There has been extensive work concerning the synthesis of nanowires and their characterization with respect to structural, chemical and thermoelectric properties. However, enhancements in the thermoelectric power factor could not be observed so far in nanowires. This can be explained in most cases with one simple fact: the diameters of the investigated nanowires were too large to observe quantum confinement effects. Furthermore, the structural and chemical compositions of the nanowires were not optimized in many cases and often modified during the lithographic contacting. If nanowires were available with the desired properties, for example bismuth nanowires, experimental problems such as difficulties in obtaining ohmic electrical contacts so far prevented the measurements of their thermoelectric properties. The approach to reduce the thermal conductivity in silicon nanowires was successful and led to ZT values of about 1 around room temperature, which is remarkable, compared to bulk silicon. However the same ZT is reached by conventional bulk thermoelectric materials and there is not much room for further enhancements, as the reported thermal

conductivity values are already close to the amorphous limit of silicon.

5. Nanomeshes and Phononic Crystals

In 2010 the Heath group from Caltech demonstrated a new record on the reduction of thermal conductivity in silicon nanostructures.^[48] By utilization of the so-called superlattice nanowire transfer process, they formed nanomesh structures with a period of 34 nm and pore diameter of 11 and 16 nm of single-crystalline silicon film with a thickness of 22 nm on SiO₂ wafers (Figure 7). The nanomesh systems exhibited a two times lower thermal conductivity ($1\text{--}2\text{ W mK}^{-1}$) than silicon nanowires with a cross-section of $20\text{ nm} \times 28\text{ nm}$, which were processed by the same lithographic technique and exhibited already a thermal conductivity of just $2\text{--}3.5\text{ W mK}^{-1}$. In comparison to reference samples based on single-crystalline silicon

films with similar thickness and mesh structures patterned by

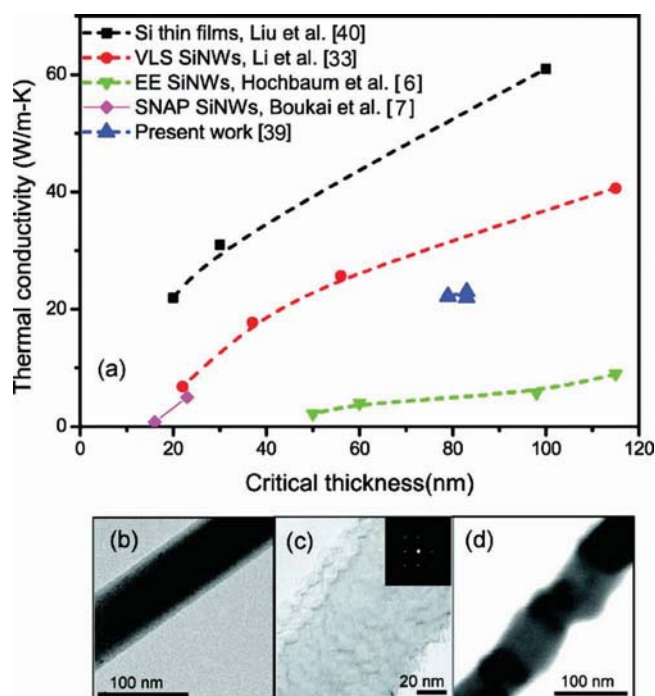


Figure 5. (a) Room temperature experimental data for confined silicon nanowires as a function of critical thickness. For thin films, $dc =$ thickness; for Si nanowires formed by VLS mode and by electrochemical etching (EE), $dc =$ diameter; for the integrated silicon nanowires (Integrated NWs), $dc = 2(wt)1/2/\pi1/2$. Dashed lines are added as guides to the eye. (b) TEM picture of smooth VLS Si Nanowires. (c) TEM pictures of EE Si NW from $0.1\ \Omega\text{ cm}$ presented in Hochbaum et al. (d) STEM image taken at 30 kV of EBL-based on integrated SiNW based on a SOI platform. Reproduced with permission.^[39] Copyright 2010, American Chemical Society.

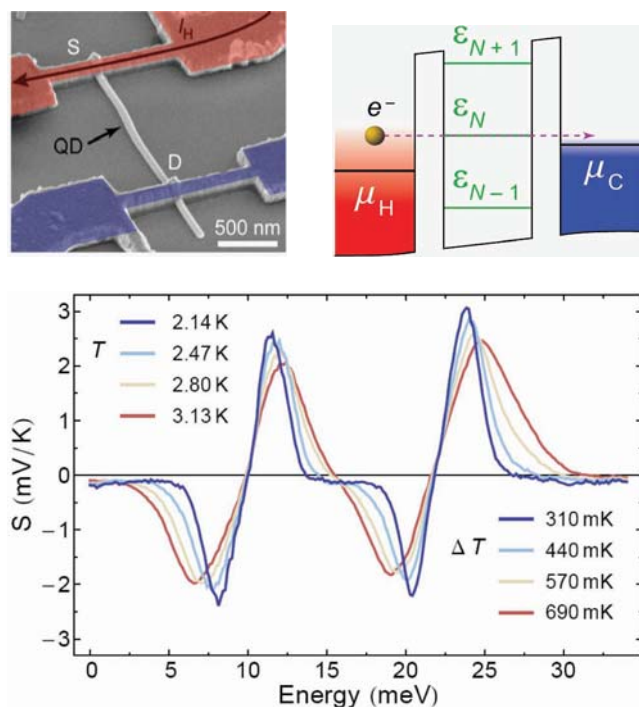


Figure 6. Top Left: Scanning electron microscope image of an InAs nanowire with embedded quantum dot formed by a pair of InP barriers (not resolved by the image). Driven by a balanced push-pull voltage arrangement, a heating current, I_H , through the contact S provides a temperature difference, ΔT , and thermovoltage, ΔV , is measured between S and D. Top Right: Using a backgate, the energy levels, ε_N , (separated by many kT) in the dot can be tuned relative to the hot and cold chemical potentials, $\mu_{H,C}$, in the nanowire leads. Bottom: Each energy level yields a characteristic line-shape of the thermopower, $S = \Delta V/\Delta T$, which changes sign whenever $\mu_H = \varepsilon_N$. Reproduced with permission of H. Linke (University Lund, Sweden)

electron beam lithography with a feature size >100 nm, the reduction of thermal conductivity was even of the order of one magnitude. For the nanowire and the nanomesh systems with feature in the sub-20 nm regime the thermal conductivity is significantly reduced by boundary scattering of phonons. Although the nanomeshes exhibit a substantially smaller ratio of surface to volume, the thermal conductivity is suppressed further by coherent phonon processes based on the periodic mesh structure which modify the phonon band structure and reduce the phonon group velocity. In analogy to photonic crystals, the silicon nanomeshes can be called phononic crystals, where a periodic array of scatters located in a homogeneous film matrix causes certain frequency of phonons to be reflected by the structure. In terms of applications, the nanomeshes might further outperform the silicon nanowires due to structural instability and challenges to contact the nanowire bundles after the electrochemical etching. Nevertheless, the silicon nanomeshes are far from device application but as a new class of model system in thermoelectric might stimulate new research activities related to the concept of phononic crystals.

Based on a collaboration between the groups led by P. Yang (Berkeley) and T. P. Russel (Univ. of Massachusetts, Amherst), the top single-crystalline layer with 100 nm thickness of SOI wafers was patterned based on self-organized block copolymers

down to periods of 55 nm with a porosity of 35%.^[49] The thermal conductivity of the single-crystalline and holey silicon layer with a hexagonal pore arrangement, which was 2 orders of magnitude lower than bulk materials and a maximum ZT of 0.4 at 300 K have been measured.

Shortly after Ref. 55, the thermal conductivity for two-dimensional phononic crystal structures with lattice pitches of 500 to 800 nm and hole diameters of 300 to 400 nm has been investigated with the same feature sizes as photonic crystals based on a SOI (silicon-on-insulator) platform with a (100)-orientation.^[50] Although the lattice period is in the sub- μm range, a reduction of the thermal conductivity (6.8 W/mK) of an order of magnitude in comparison to bulk-materials (148 W/mK) was reported. The authors have also demonstrated that in addition to boundary scattering, the thermal conductivity is in this experiment additionally reduced by the periodic nature of the silicon mesh which alters the phononic spectrum. The physical origins of the substantial reduction of the thermal conductivity in nanoporous silicon in comparison to bulk and nanowires has recently been discussed by means of molecular and lattice dynamic calculations by He et al.^[51]

The concept of nanomeshes has been applied also to polycrystalline and nanostructured $\text{Bi}_{0.4}\text{Sb}_{2.6}\text{Te}_3$ films, which have been fabricated by flash evaporation of 100 nm film onto self-ordered Al_2O_3 membranes with a pitch of 50 nm. The Japanese authors have reported about the achievement of $ZT = 1.8$ by the measurement of the thermal conductivity (0.25 W/mK) perpendicular to the film via time-domain thermal-reflection measurements.^[52] The Seebeck coefficient and the electrical conductivity for the in-plane direction were determined by conventional measurement techniques for thermoelectric thin films. The nanomeshes made from single-crystalline and polycrystalline thermoelectric materials seem to be an attractive model system, where film thickness, pitch and porosity can be tuned independently. In contrast to single nanowires, major thermoelectric quantities can be probed by conventional measurement techniques. Therefore, we assume a rapidly increasing number of publications of thermoelectric and phononic nanomeshed systems in the upcoming years.

6. Epitaxial Multilayered Systems with High Performance

Thermoelectric thin films and epitaxial multilayers have been reviewed in detailed previously.^[53–55] Here we want to mention briefly a few research highlights and most recent developments in the field. For the sake of clarity, we can define the type of samples reviewed here as thermoelectric films of thickness significantly below the micrometer range and deposited on an appropriate, thick substrate. This excludes preparation techniques from bulk materials, such as thinning by extrusion or melting.^[56] Films and multilayers of high quality are mostly prepared by ‘dry’ deposition methods such as molecular beam epitaxy (MBE) and chemical vapor deposition (CVD, or also called MOCVD if metal-organic precursors are used). For our purpose, a high quality implies (a) an accurate and homogeneous film thickness, (b) an accurate and homogeneous chemical composition and stoichiometry, and (c) a nearly perfect crystallinity,

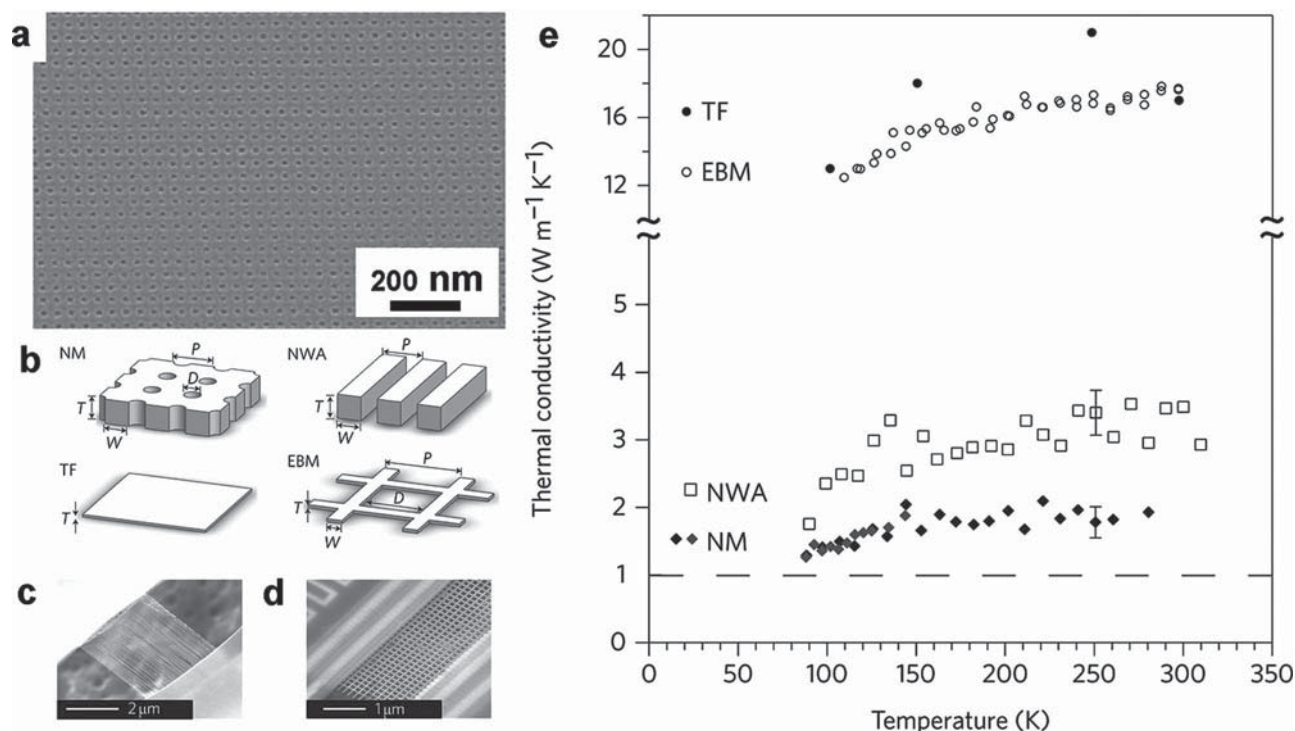


Figure 7. (a) Silicon nanomesh films with periods of 34 nm have been fabricated on SOI wafers. (b) Geometry of the two 22 nm thick nanomesh films (NM1 and NM2 with pore diameter of 11 and 16 nm, respectively) and three reference systems (TF: unpatterned silicon film with 25 nm thickness, EBM: nanomesh patterned by ebeam lithography with a period of 385 nm, a feature size of 165 nm and 22 nm thickness and NWA: nanowire arrays with a cross-section of 20 nm × 28 nm). (c,d) SEM images of suspended nanowires in the NWA device (c) and suspended EBM device (d). (e) Thermal conductivity versus temperature for two nanomesh devices (diamonds) and the three reference devices. The TF (solid circles) and EBM devices (open circles) have similar thermal conductivities as a result of their similar film thicknesses. The NWA nanowires (open squares) have lower thermal conductivities, a result of their larger surface-to-volume ratios compared to the TF and EBM devices (note the discontinuity in the y-axis). The nanomesh devices, although having significantly lower surface-to-volume ratios compared to the NWA device, exhibit a thermal conductivity that is factor of 2 lower. Reproduced with permission^[48] Copyright 2010, Nature Publishing Group.

including an epitaxial relationship between the thermoelectric film and the underlying substrate, as well as between the layers of the film.

In a multilayer system, the transport phenomena must be considered separately within the main plane of the sample and across it (Figure 8). In the latter configuration, significant improvements in the thermoelectric properties can be achieved by phonon scattering at each interface and thereby lowering the thermal conductivity, if the electronic transport remains uninfluenced. In-plane transport parameters may be affected by the layered structure, as well, albeit to a lesser extent,^[57] via the appearance of a quantum well structure within each layer between barriers. The pseudo-two-dimensional electron gas may give rise to larger electrical conductivity, although in many cases, thermal conduction increases as well.

The in-plane electrical conductivity of thin films can be determined via four-point probe techniques requiring electrically insulate the film from the substrate. In the cross-plane direction, the sample's small dimension necessitates a particularly low contact resistance between leads and sample. The cross-plane thermal conductivity of thin films and superlattices has often been measured by the 3ω method.^[58] In this method, a metal stripe is fabricated on the sample, and an AC current of frequency ω causes, by Joule heating, a temperature oscillation of frequency 2ω . The concomi-

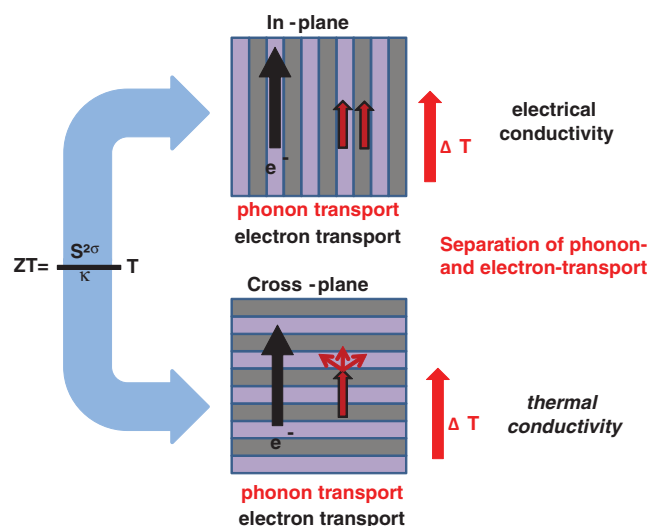


Figure 8. Quantum size effects can be exploited to some extent to control the transport properties along the planes of multilayered samples (top): if transport only occurs within one type of layers, the electrical conductivity and thereby the ZT value can be enhanced. Transport across the planes (bottom) can be characterized by enhanced phonon scattering at the interfaces. In this case, the thermoelectric efficiency (ZT) is improved via a reduction of the thermal conductivity.

tant 2ω resistance oscillation gives rise to a 3ω signal voltage along the metal stripe. The amplitude of the temperature oscillation in the metal stripe can be derived from this third harmonic of the measured AC voltage, and depends on the thermal conductivities of the materials underneath. In this technique, boundary conditions of the sample have to be considered carefully. The choice of the substrate material, the thickness of the film and the width of the metal stripe determine the frequency window over which this differential 3ω method can be applied. The cross-plane thermal conductivity of a thin film can also be derived from measurements in the time domain, in the form of an optical pump-probe method.^[59] A thin aluminium film deposited onto the surface of the sample serves as mirror, the reflectivity of which varies with temperature. The time trace of the reflection signal therefore contains the information on the thermal diffusion through the solid.

After the theoretical prediction of massive ZT increases for two-dimensional films,^[13] it took less than a decade until a figure of merit significantly beyond 1 was demonstrated near room temperature in a superlattice system for the cross-plane transport of charge carriers (Figure 8, lower conception). In Venkatasubramanian's p-type $\text{Bi}_2\text{Te}_3/\text{Sb}_2\text{Te}_3$ superlattice (1 nm/ 5 nm) grown by MOCVD, a reduction of the thermal conductivity by a factor 2.2 in the cross-plane direction (the crystal's c direction) resulted in a ZT value of 2.4.^[8] The electrical conductivity is hardly affected by the multilayer structure. Subsequent, systematic characterization of the thermal conductivity for various multilayer periods seemed to indicate that the unique success of this structure is not only due to phonon scattering at surfaces but may originate in part from some structural disorder within the films.^[60] This aspect might be one reason why Venkatasubramanian's most cited achievement does not seem to have been reproduced outside of his group to date.

Improvements in the in-plane thermoelectric properties of such multilayered systems have not been quite so impressive to date.^[57] The n-type bismuth-doped PbTe/Te system deposited by MBE and studied by Harman and Walsh could be tuned in terms of layer thicknesses and charge carrier concentrations. It does demonstrate significantly higher Seebeck coefficients and power factors than comparable bulk materials, but was not characterized in terms of thermal conductivity.^[61] Additional lateral structuring in the form of pyramidal quantum dots self-assembled by epitaxial strain during MBE growth can lead to further ameliorations. This was demonstrated experimentally in the case of Se-doped (n-type) $\text{PbSeTe}/\text{PbTe}$ superlattices.^[62] Thermoelectric figures of merit of 1.5 near room temperature and 3 at 550 K were articulated for this system even though the thermal properties have not been measured directly.^[63] The accuracy of those values has been debated.^[55] Independently of the trophy numbers, the physical phenomena leading to increases in S and σ could be modelled quite accurately.^[64] Table 3 summarizes experimentally determined ZT values of various superlattice systems.

In a Ge/Si superlattice, the thermal conductivity was found to depend on the superlattice period linearly, down to a value below $\kappa = 1 \text{ W m}^{-1} \text{ K}^{-1}$ for the smallest period of 3.7 nm (Figure 9).^[65] In this case, particular care was taken to reproduce the data by geographically and methodically independent measurements (a time-domain technique in the sub-picosecond range, on the one hand, and the frequency-domain 3ω method, on the other hand). Significantly, the models applied to this experimental system indicate for any given period, a significant contribution to the

Table 3. Overview of the thermoelectric properties of selected epitaxial thermoelectric multilayers and superlattice structures measured in the cross-plane direction in most cases.

Material system	κ [W/(mK)]	ZT	Reference
p-type $\text{Bi}_2\text{Te}_3/\text{Sb}_2\text{Te}_3$, MOCVD	0.22	2.4 (RT)	[8]
n-type $\text{Pb}(\text{Se},\text{Te})/\text{PbTe}$, MBE	0.62 (RT) 3.3 (300 °C)	1.3 (RT) 3.4 (300 °C)	[62,63]
Ge/Si , MBE	0.9	–	[65]
n-type $\text{Bi}_2\text{Te}_3/Bi_2(\text{Te}_x\text{Se}_{1-x})_3$, MBE	1.40	0.75 (RT)	[53]
$(\text{Zr},\text{W})\text{N}/\text{ScN}$, sputtered	2.1	–	[72]
n-type $(\text{In},\text{Ga},\text{Al})\text{As}/ErAs$, MBE	5.9 (RT) 1.3 (530 °C)	0.07 (RT) 1.1 (530 °C)	[76]

reduction of κ is brought in by lateral structuring. Perfectly planar multilayers are by far not as efficient at scattering phonons (even in the cross-plane direction) as their rough counterparts. This is reminiscent of the work carried out on Si nanowires, which demonstrated that surfaces with a well-defined roughness act as efficient phonon scatterers (see above).

The thermal conductivity has been minimized in so-called “misfit layer” compounds annealed after evaporating the elements in alternating manner (“modulated elemental reaction method”).^[66] Here, no epitaxial relationship exists between the individual layers, although each is highly crystalline, so that abrupt interfaces separate the layers. As a consequence, in superlattices of WSe_2 and $\text{W}_4(\text{WSe}_2)_{10}$, the thermal conductivity across the planes ($0.05 \text{ W m}^{-1} \text{ K}^{-1}$) is smaller than in plane by a factor 30.^[67] In the $\text{PbSe}/\text{MoSe}_2$ system, similarly low thermal conductivities can be accompanied by reasonable values of the

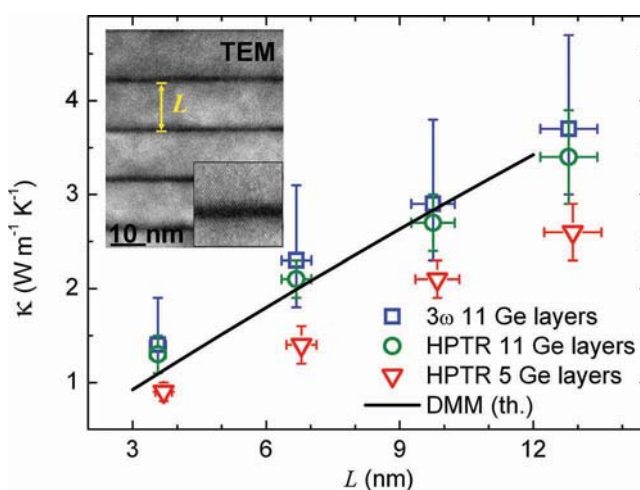


Figure 9. Thermal conductivity of Ge/Si nanodot multilayer, for the 5 and 11 layer systems, measured by HPTR, and the 11 layer system measured by the 3ω techniques, as a function of the average distance between layers, L .^[65] The solid line is the result of the diffuse mismatch model. The inset is a TEM image of a Ge/Si nanodot multilayer. Reproduced with permission of A. Rastelli (IFW Dresden, Germany).

electrical conductivity (on the order of $10 \Omega^{-1} \text{ m}^{-1}$) and of the Seebeck coefficient ($100 \mu\text{V K}^{-1}$ or better).^[68]

With this, the state of multilayered thermoelectric thin films can be summarized as follows:

- most studies have focused on a small number of materials systems, in particular the V–VI compounds (selenides and tellurides of antimony and bismuth), the IV–VI binaries (lead selenide and telluride), some III–V semiconductors (arsenides of aluminium, gallium and indium), and the group IV system (silicon and germanium);
- most efficiency gains have been claimed from reductions in thermal conductivity, even though an understanding of phonon transport and scattering is far from complete;
- further significant increases of ZT can only be derived from enhancements of the power factor, for example via energy filtering;
- some of the ‘trophy’ values of ZT have not been reproduced and/or have been questioned; this is likely related to the sensitivity of the thermoelectric properties to the preparation conditions.

The optimization of thermoelectric thin films has some relevance to applications, since very high cooling power densities could be obtained for minaturized electronic chip cooling.^[69] In this respect, challenges along the way are not only scientific but also of engineering nature: negligible electrical contact resistances, diamond-like substrate thermal conductivity, integration of the thermoelectric elements on the chip and in the classical vertical design with leg heights in the range of $10 \mu\text{m}$.^[57] Additionally, little work has been done concerning the long-term thermal stability of thin film and multilayer structures, interdiffusion, coarsening and ripening of nanocrystals. A superlattice structure can, however, survive the processing to a device.^[70] In this unique demonstration geared towards a thermoelectric sensor application, a $\text{Bi}_2\text{Te}_3/\text{Bi}_2(\text{Se},\text{Te})_3$ multilayer was transferred from a sacrificial BaF_2 substrate to a polyester foil, whereby the typical high-resolution X-ray diffraction superlattice pattern was only marginally affected due to the bending of the polyester foil.

7. Artificial Thermoelectrics: Thermionic Superlattices

In a recent development, systems structurally similar to those described above have been created in which a thermionic effect

is optimized instead of its thermoelectric counterpart.^[71] A thermionic superlattice combines a metal with a wide-bandgap semiconductor in a manner that causes an energy filtering of the charge carriers (**Figure 10**). In the metal, electrons and holes near the Fermi energy are most mobile, whereas only a small sample of the charge carrier population can transfer to the semiconductor and be transported through it, namely the warmest fraction. In this manner, the bulk of the charge carriers is effectively immobilized, whereas only those with the largest contribution to the Seebeck coefficient are mobile. From the practical viewpoint, the challenge lies in the epitaxial combination of a metal with a wide-bandgap semiconductor. This has been achieved in the case of a metallic IV/V compound and a III/V semiconductor, in particular in the TiN/GaN system,^[72] or based on ZrN and ScN .^[73] The possibility of tuning the thermal conductivity of such thermionic multilayers has been demonstrated, though a full characterization of their thermoelectric performance is missing.

An impressively lowered thermal conductance was observed in a quantum dot multilayer geometry. In samples of $\text{In}_x\text{Ga}_y\text{As}$ containing well-aligned ErAs quantum dots as epitaxial inclusions, the thermal conductivity of the host material was reduced to an extent that depended on the geometric parameters.^[74] While smaller multilayer periods resulted in lower κ , a limit was found whereby too small quantum dots can no longer function as efficient phonon scattering centers. The disordered system in which ErAs quantum dots with a broader size distribution were randomly distributed in the matrix displayed the most efficient decrease in κ (by a factor two for an Er content of 0.3%), this presumably due to the scattering of a broader range of phonon wavelengths.^[75] All three thermoelectric parameters of this system were later measured: the ZT value obtained is modest at 300 K (0.07), as expected in a III–V system, but increases sharply with temperature, with $ZT = 1.1$ reached by 800 K.^[76]

8. Nanograined Bulk Materials

During the last five years, a lot of empirical efforts were put into the development of thermoelectric nanocomposites with an enhanced interface-to-volume ratio and lower thermal conductivity. Nanocomposites are for example materials in which nanoparticles or nanocrystalline separations are in a more or less organized thermoelectrical matrix.^[17,18] At the moment,

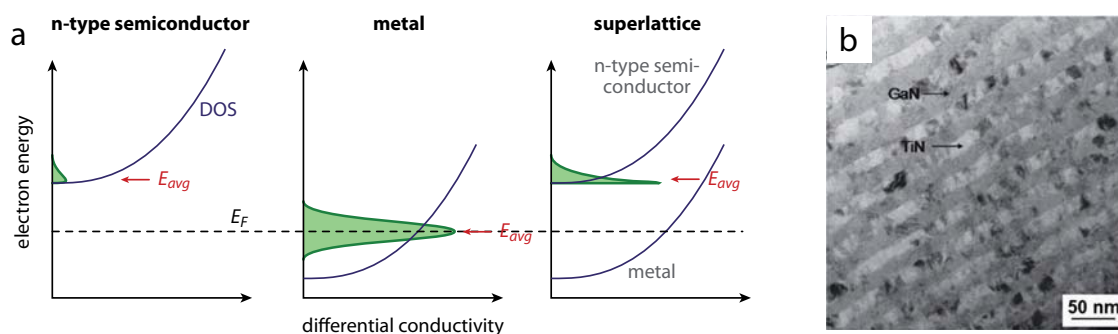


Figure 10. Principle of energy filtering in thermionic superlattices.^[72] “Hot” electrons are emitted from the metallic layer traverse the semiconductor, whereas the majority of electrons, featuring lower energy (near the Fermi energy), are ‘filtered out’ by the semiconductor’s bandgap. Reproduced with permission. Copyright 2006, American Institute of Physics.

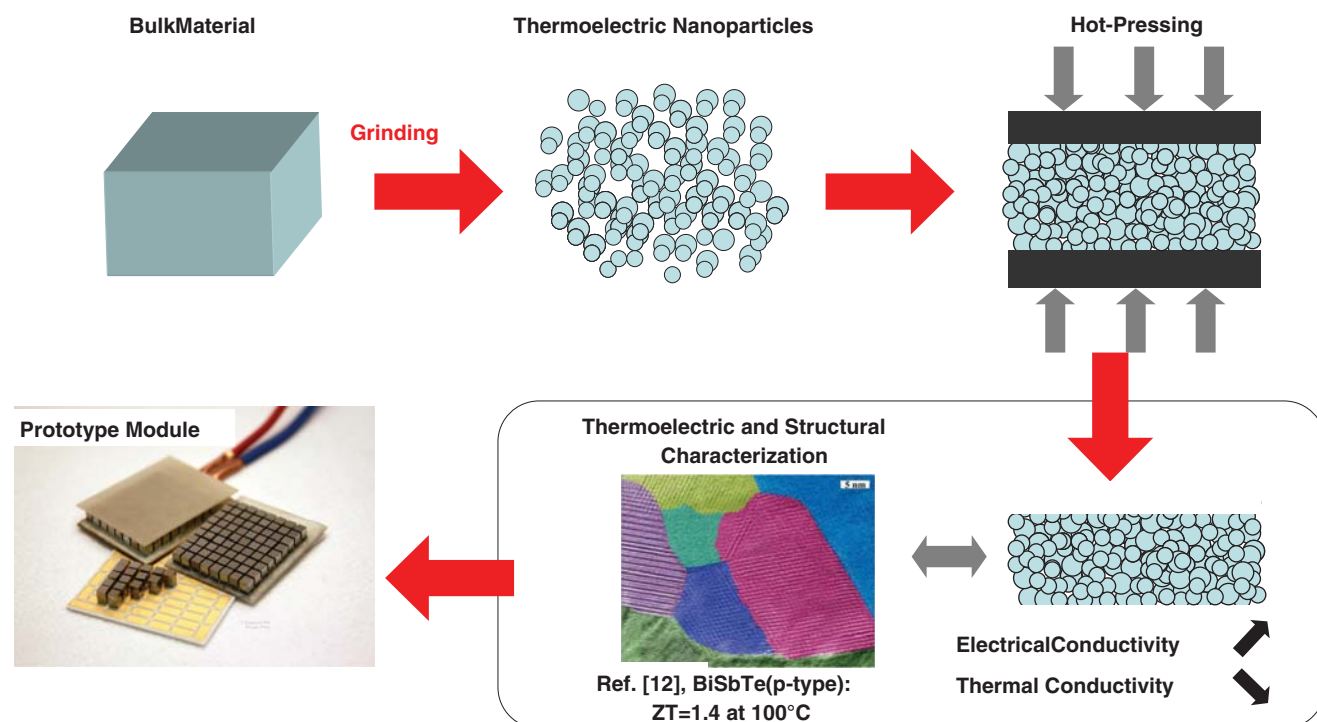


Figure 11. Cost-efficient production of high-power thermo-generator: Optimized thermo-electrical material will be ground into powder and compacted under heat treatment and pressure. 50% increase in efficiency could be reached by using this synthesis approach which can be transformed as soon as possible into new products as well as transferred to various material classes.

scientists mainly in the USA and China try to compact thermoelectric nanoparticles under high pressure and high temperature. By this process, nanoparticulate materials can be generated on the kg-scale, out of which subsequently classical thermo-electric components can be built. Despite current technological problems due to recrystallisation effects during the compaction, an efficiency increase by 40–75% compared to conventional thermoelectric components has been achieved.^[17] **Table 4** summarizes experimentally determined ZT values of nanograined nanocomposite materials ranging from room temperature to high temperature applications.

In 2007, a Chinese group has realized ZT values of 1.35 for p-type Bi_2Te_3 multi-layered nanostructures by melt-spinning and spark-plasma sintering (**Figure 11**).^[77] In the following year, a research team from MIT and Boston University has successfully produced nanoparticle powder of p-doped $\text{Bi}_x\text{Sb}_{2-x}\text{Te}_3$ by using a ball mill and hot-pressing.^[12,78] They measured a record value of $ZT = 1.4$. The size of the crystallites was around 5–50 nm. In comparison to bulk materials, the nanoparticulate structure exhibits an about 30% lower thermal conductivity around 100 °C which is quite stable up to 250 °C—although the thermal conductivity is nearly doubled over this temperature range. Surprisingly, the electrical conductivity is enhanced in the nanograined structure, which results in a slightly reduced Seebeck coefficient below 150 °C. It was assumed that the high density of interfaces and precipitations enhances the carrier concentration and electrical conductivity.

With similar results, the material synthesis was performed by grinding thermoelectrically optimized ingots,^[12] and by mechanical

alloying and grinding the pure chemical elements for $\text{Bi}_x\text{Sb}_{2-x}\text{Te}_3$.^[78] A similar ZT value of 1.47 has been reported for hot-pressed mixtures of hydro-thermally synthesized Bi_2Te_3 and Sb_2Te_3 nanoparticles.^[79] Probably, this synthesis approach can be transferred into lead-free products in the next five years. The Tritt group from Clemson University has successfully hot-pressed nanoparticulate materials out of $\text{Bi}_2\text{Te}_3/\text{Sb}_2\text{Te}_3$ compounds which were produced by nanoparticle synthesis based on melt spinning and set a new record of $ZT = 1.56$.^[80] In comparison to Ref. 78, a reduction of 30% of the thermal conductivity was achieved. Fundamental analysis of the researchers D.G. Cahill (University of Illinois) and D. Johnson (University of Oregon) have shown that the thermal conductivity of 0.3 W/mK for thin films with grain sizes <10 nm^[12,78] approaches the minimal reachable value of 0.2 W/mK,^[81] which is more than two times smaller than recent experiments with nanograined bulk materials.^[12,78–80] This work provides some evidences that further optimizations of nanograined (Bi/Sb)₂Sb₃ bulk materials might achieve potential ZT values around 2. Furthermore, the thermoelectric properties of squeezed nanoparticulate materials were also optimized by admixture of small amounts (<1%) of PbTe nanoparticles,^[82] which are suitable for high-temperature applications and do not mix with the SbBiTe matrix on thermal treatment.

The attempt to incorporate ceramic nanoparticles into $(\text{Bi}_{0.2}\text{Sb}_{0.8})_2\text{Te}_3$ prior to hot-pressing has not been successful for ZT enhancement.^[83] Although a slight increase of the thermo-power and decrease of the thermal conductivity were reported, the reduction of the electrical conductivity was very significant, therefore the overall ZT value decreased with the

Table 4. Overview of nanograined bulk materials with high thermoelectric performance: Selected references reporting $ZT > 1$ for nanocomposites based on Bi_2Te_3 and PbTe , or $ZT > 0.5$ for other materials such as SiGe and CoSb with are summarized in this table.

Material system	S [$\mu\text{V}/\text{K}$]	κ [$\text{W}/(\text{mK})$]	ZT	Methods* and comments	Reference
Bi_2Te_3 (p-type)	235	0.6	1.35 at 27 °C	MS + SPS	[77]
$(\text{Sb}/\text{Bi})_2\text{Te}_3$ (p-type)	210	0.95	1.4 at 100 °C	BM of ingots and MA + HP	[12,78]
$\text{Bi}_{0.52}\text{Sb}_{1.48}\text{Te}_3$ (p-type)	228	0.68	1.56 at 27 °C	MS + SPS	[80]
$\text{Bi}_2\text{Te}_{2.7}\text{Se}_{0.3}$ (n-type)	-220	0.8	1.04 at 125 °C	MA + 2x HP	[84]
$\text{GaSb}_{10}\text{Te}_{16}$ (p-type)	135	1.0	0.98 at 210 °C	BM of ingots + SPS	[88]
AgSbTe_2 (p-type)	200	0.39	1.59 at 400 °C	MA + SPS	[86]
PbTe (p-type)	320	1.0	0.4 at 100 °C	BM + SPS	[89]
$\text{PbTe}:\text{Tl}$ (2%) (p-type)	330	1.0	1.5 at 500 °C	Ingots synthesis	[90]
$\text{PbTe}:\text{Tl}$ (2%) (p-type)	295	0.95	1.3 at 400 °C	BM + HP	[91]
$(\text{Pb}_{0.95}\text{Sn}_{0.05}\text{Te})_{0.92}(\text{PbS})_{0.08}$ (n-type)	-260	1.0	1.5 at 380 °C	Ingots synthesis	[93]
$(\text{PbTe})_{0.98}(\text{SrTe})_{0.02}$ (p-type)	300	0.9	1.7 at 530 °C	Ingots synthesis	[94]
$\text{AgPb}_{18}\text{SbTe}_{20}$ (p-type)	380	0.95	2.1 at 530 °C	Ingots synthesis	[10]
$\text{Ag}_{0.8}\text{Pb}_{22}\text{SbTe}_{20}$ (p-type)	300	1.35 at RT	1.37 at 400 °C	MA + SPS	[95]
$\text{Co}_{0.8}\text{Ni}_{0.2}\text{Sb}_{3.05}$ (n-type)	-175	3	0.7 at 500 °C	BM + SPS	[107]
$\text{Yb}_{0.2}\text{Co}_4\text{Sb}_{12.3}$ (n-type)	-200	2.2	1.26 at 530 °C	MS + SPS	[105]
$\text{Yb}_{0.35}\text{Co}_4\text{Sb}_{12.3}$ (n-type)	-190	3.25	1.2 at 550 °C	BM + SPS	[106]
$\text{Mg}_2\text{Si}_{0.6}\text{Sn}_{0.4}:\text{Sb}$ (n-type)	-250	1.8	1.11 at 590 °C	(BM of ingots + SPS) \times 2	[104]
$\text{Zr}_{0.5}\text{Hf}_{0.5}\text{CoSb}_{0.8}\text{Sn}_{0.2}$ (p-type)	210	2.3	0.8 at 700 °C	BM + SPS	[108]
$\text{Si}_{80}\text{Ge}_{20}$ (p-type)	260	2.3	0.95 at 900 °C	BM + HP	[96]
$\text{Si}_{80}\text{Ge}_{20}$ (n-type)	-330	1.8	0.8 at 800 °C	NPS by gas phase + SPS	[101]
$\text{Si}_{80}\text{Ge}_{20}$ (n-type)	-280	1.8	1.3 at 900 °C	BM + HP	[96]
$\text{Si}_{95}\text{Ge}_5$ (n-type)	-230	3	0.95 at 900 °C	BM + HP	[98]
Si (n-type)	-200	4	0.7 at 900 °C	BM + HP	[99]

* Abbreviations: BM - Ball Milling; HP - Hot Pressing; MA - Mechanical Alloying; MS - Melt Spinning; NPS - Nanoparticle Synthesis from gas phase; SPS - Spark Plasma Sintering;

fraction of ceramic particles. In general, the selection of a secondary nanoparticle phase should be performed carefully; it should exhibit a certain epitaxial relation with the surrounding crystal structure of the matrix material and thus the flow of charge carriers remains nearly unaffected.

n-Type nanocomposites based on $\text{Bi}_2\text{Te}_{3-y}\text{Se}_y$ have also been developed by the groups from Boston College and MIT.^[84] Nanocrystalline powders were obtained from elemental source materials. All of the three important thermoelectric parameters were reduced in the resulting nanograined bulk-sample. Nevertheless, the resulting ZT value 0.85 at 125 °C after a first hot-pressing step corresponds to n-doped bulk materials. A second pressing procedure in a furnace resulted in an enhanced ZT value of 1.04 at 125 °C for the transport perpendicular to the press direction. In this publication the thermoelectric parameters have been analyzed for the first time in relation to the pressing direction. After first hot-pressing, the ZT value was nearly isotropic, whereas the repressed sample exhibited a strongly anisotropy with ZT values of 0.65 and 1.04 for the direction parallel and perpendicular to the press direction, respectively. As a consequence, more research is required on the influence of the pressing procedure on the thermoelectric anisotropy and the underlying evolution of the nano-grained morphology during the pressing process.

As a derivative material from p-doped Sb_2Te_3 , stoichiometric AgSbTe_2 has been proposed as a high performance p-type thermoelectric materials with a maximum ZT of 1.6 at 400 °C and a very low thermal conductivity of 0.35 to 0.5 W/mK ^[85] over the whole temperature range up to ZT_{max} .^[86] This system is similar to the famous TAGS-x alloys, which are a combination of GeTe and AgSbTe_2 in the form of $(\text{AgSbTe}_2)_{1-x}(\text{PbTe})_x$ and exhibits a similar thermoelectric performance.^[87] In this work, the authors applied ball-milling for the alloying process of AgSbTe_2 particles and spark plasma sintering for the compacting process. The resulting grained composite exhibited a porosity of nearly 20%, which might partially explain the efficient phonon scattering by nanovoids. Unfortunately, a detailed structural characterization by transmission electron microscopy is not provided.^[86] Thus, more detailed investigations of the AgSbTe_2 composites should be carried out with focus on the origin of the low thermal conductivity and the application potentials.

Nanograined bulk materials based on Sb_2Te_3 alloyed with concentrations of 10% of Ga_2Te_3 exhibited an improved TE performance of $ZT = 0.99$ at 210 °C,^[88] which indicates a significant improvement of 40%. An average grain size of less than 30 nm, lattice distortions originating from Ga atoms occupying Sb sites, and nanosized Ga_2Te_3 grains have been detected by TEM and

X-ray diffraction analysis. These factors contribute to an enhance phonon scattering and reduced thermal conductivity. In addition, a slight enhancement of the thermo power and the power factor was observed for the optimized composition of p-type GaSb₁₀Te₁₆.

For high-temperature materials, which are used for the generation of electricity at higher temperatures (>250 °C), first promising studies were carried out with ground PbTe nano-crystallites obtained by melt-spinning, which show an approximately 100 percent increase in efficiency ($ZT = 0.17\text{--}0.38$) at room temperature.^[89] By applying a bulk synthesis approach in a sealed quartz ampoule, J.P. Heremans et al. have achieved a significant ZT improvement of the PbTe by thallium doping.^[90] In this work, the power factor was significantly raised by introduction of a resonance level via the Tl doping in the valence band. The resulting p-type materials exhibited a record ZT value of 1.7 at 500 °C. For a nanograined PbTe structure doped with thallium, ZT values above 2 are predicted. One recent attempt has resulted in the reproduction of the thermoelectric performance of the previous bulk sample.^[91] Although initial ball-milled nanograins were utilized, uncontrolled grain growth during hot pressing was reported, resulting in bulk-like properties.

Intensive research activities on PbTe-based materials have been performed by alloying PbTe with other elements and binary components e.g. PbS, SrTe, SnTe and AgSbTe₂ with a remarkable set of ZT data ranging from 1.2 to 2.2.^[87,92–95] The Kanatzidis group from Northwestern University has done most of the pioneering work on the PbTe-based nanocomposites by applying a classic bulk synthesis approach with ingots in sealed glass ampoules and by utilizing strategies of spinodal decomposition and precipitation of nanoparticles epitaxially embedded in the PbTe matrix. Recently, a comprehensive review on this material system has been published by M.G. Kanatzidis,^[92] therefore a brief summary is given here on bulk nanostructured PbTe and related materials. For example, a very low thermal conductivity of the crystal lattice and a high mobility of the charge carriers have been achieved by spinodal decomposition of PbS inside the matrix of the solid solution, based on Pb_{1-x}Sn_xTe. This n-doped nanostructured bulk exhibited a maximum ZT value of 1.4 at 400 °C. As an example for a high-performance p-type nanostructured PbTe composite, endotaxially arranged SrTe nanoparticles were formed in a bulk-PbTe matrix.^[94]

Not only the thermal conductivity was reduced by the nanostructured interfaces, as reported in most publications on nanograined nanocomposites. Also the lattice strain of the SrTe/PbTe-based rocksalt structure affected the band offset, which lead to an enhancement of the power factor and improved ZT to a maximum value of 1.7 at 500 °C. Even more complex chalcogenide structures with natural quantum dots have also been studied, known under the abbreviation LAST (Pb-Sb-Ag-Te-connections),^[10] which is known for its high performance thermoelectric properties ($ZT > 1$) since the 1960s.^[11] In this case, a small volume fraction of AgSbTe₂ nanoparticles are formed by disalloying in a PbTe matrix. The Kanatzidis group reported on this so-called self-assembled nanoparticulate system with a record ZT value of 2.2 by a classic bulk synthesis approach in a sealed quartz ampoule.^[10] Motivated by previous reports on the bulk synthesis of the LAST system, The spark-plasma synthesis of nanograined Ag_nPb_{18-x}SbT₂₀ composite materials was reported with a maximum ZT of 1.37 at 400 °C.^[95] This

report of a powder-based synthesis method shows an about 17% lower ZT value than the previous reported value from the bulk approach by Kanatzidis at the same temperature. This deviation might originate from slightly different compositions in both reports and differences in the applied measurement techniques for the ZT determination. Since the LAST system already exhibits a so-called natural type of nanostructure that strongly scatters phonons, a higher degree of reproducibility in sample preparation than from the nanoparticle-based synthesis approach is assumed. Still, no significantly higher ZT value has been accomplished for this advanced material system.

The development of thermoelectric nanocomposited materials for high temperature applications based on silicon and silicon/germanium alloys has made a rapid progress in the last three years. The introduction to the market of novel thermoelectric generators for the elevated temperature range (400 to 1000 °C) seems to be in reach in the near future. In 2008, a team from Boston University and MIT applied the concept of nanostructured bulk materials for p- and n-doped Si₈₀Ge₂₀ alloys and achieved ZT values 0.95 and 1.3, respectively.^[96] These record values are due to the enhancement of phonon scattering at the grain boundaries and an increase of the power factor at elevated temperatures. The electron mobility was only moderately influenced by the high density of the grain boundaries. In combination with the enhancement of phonon scattering, the ZT value was enhanced by a factor of two and four in contrast to bulk materials. The significant amount of germanium will restrict the commercial applications due to the limited world supply (world production of a few hundreds of tons per year) and high market prizes (1600 US\$ per kg).^[97]

For the development of moderately prized silicon-based nanostructured materials, the above mentioned group of researchers from MIT and Boston College has explored the thermoelectric properties of p-type nanostructured silicon without and with a atomic ratio of 95/5 for germanium and achieved a ZT of 0.5 and 0.95 at 900 °C, respectively.^[98] This is a ZT enhancement of a factor of two in nanograined silicon and of a factor of four in Si₉₅Ge₅ in comparison to the related bulk materials. The pure and alloyed nanostructured materials exhibited quite similar values in the electrical conductivity σ and slightly elevated absolute thermopower S and power factor $\sigma \cdot S^2$ for the unalloyed material. In contrast to this, the nanostructured Si₉₅Ge₅ showed a thermal conductivity lowered by a factor of two, and therefore a significantly higher ZT . The small quantities of germanium can efficiently reduce the thermal conductivity in addition to phonon scattering at the grain boundaries, originated from point defects for phonon scattering by the germanium sites. Soon thereafter, a further improvement of $ZT = 0.7$ at 1000 °C was demonstrated by the same groups for n-typed nanograined silicon.^[99] As a consequence, the consumption of germanium can be drastically reduced or eventually be eliminated for device application in waste heat recovery.

In contrast to the batch synthesis of silicon based nanoparticles by ball milling, melt spinning or mechanical alloying, the utilization of a continuous synthesis process of Si₈₀Ge₂₀ nanoparticles in the gas phase has been demonstrated by a research team from the University of Duisburg/Essen.^[100] This gasphase process can be easily upscaled for industrial processes with material output ranging from kg to tonnes per days and provides a highly reproducible

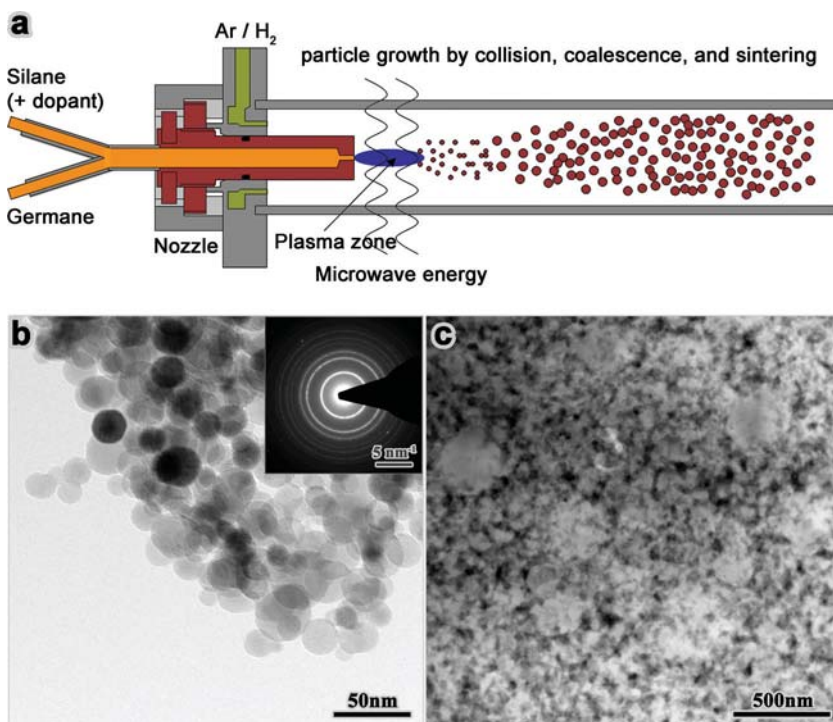


Figure 12. a) Microwave plasma reactor for the synthesis of alloyed SiGe nanoparticles. b) TEM image of the alloyed SiGe raw powder. c) Scanning TEM image of a SiGe nanocomposite obtained by current-assisted sintering around 1000 °C. Reproduced with permission.^[100] Copyright 2011, Cambridge University Press.

synthesis of nm-sized nanoparticles. A sketch of the reactor concept for the nanoparticle synthesis from the gas phase is shown in **Figure 12a**. Silane (SiH_4), germane (GeH_4), and the precursor materials for the intended doping (n-type doping: PH_3 , p-type doping: B_2H_6) are homogeneously mixed in the gas phase and subsequently injected into a microwave induced plasma through a nozzle. The precursors decompose in the non-thermal plasma and nuclei of alloyed SiGe particles form. The further growth is driven by collision, coalescence and sintering processes, while the particle growth is stopped by cooling the gas/particle mixture. The final mean diameter of the nanoparticles can be tailored by parameters like gas flow, pressure in the reaction chamber, energy of the microwave plasma and precursor concentration. The pyrolysis of the precursors is almost quantitative, so that the initial mixture of the gases determines the chemical composition of the nanoparticles.^[100] **Figure 12b** shows alloyed $\text{Si}_{80}\text{Ge}_{20}$ nanoparticles with a mean diameter around 20 nm. No separation of silicon and germanium was found. The nanoparticles are crystalline (inset of **Figure 12b**) and weakly agglomerated and typically show no crystal facets, due to kinetic control of the particle formation process. A subsequent current assisted sintering at temperatures around 1000 °C results in an alloyed nanocrystalline bulk with average crystallite size around 30 nm and typical densities between 95% and 98% of the respective single crystal; **Figure 12c** shows a scanning transmission electron micrograph of the obtained nanostructured bulk sample. The thermal conductivity of this $\text{Si}_{80}\text{Ge}_{20}$ sample is $1.8 \text{ W m}^{-1} \text{ K}^{-1}$ at room temperature and therewith comparatively low, demonstrating the potential of this synthesis route. The peak ZT of the same nanocomposite is 0.8

at 1000 °C.^[101] Most likely, this type of materials synthesis will be also applied soon for other classed of nanograined thermoelectric materials.

Natalio Mingo et al. recently performed some thorough calculations^[102] on the potential further improvements of nanostructured $\text{Si}_{1-x}\text{Ge}_x$ by comparing experimental results of this material system from major publications in this area.^[96] Based on the analysis of this co-author team, the degree of optimization for the sintered nanograined $\text{Si}_{1-x}\text{Ge}_x$ ($x = 20$ to 50) is already advanced and they predict only moderate further improvements (about 30%) of the thermoelectric efficiency of ZT of 2 for n-type and ZT 1.5 for p-type SiGe by variation of the doping concentration. Although the sizes of the nanograins are in the range of 5 to 20 nm, the sintered nanograined structures are fairly transparent for phonon scattering.

If the efficiency of the phonon scattering can be enhanced at the grain boundaries, for example by roughness enhancements of the grain surfaces, ZT values of 2 and more can be reached, as predicted for nanograined silicon germanium alloys. In a joint publication by Mingo and Shakouri,^[103] the embedding of silicide and germanide nanoparticles as low-density fillers of less than 1% in volume of the non-grained $\text{Si}_{50}\text{Ge}_{50}$ alloys has been

proposed as a strategy to enhance the figure of merit to $ZT = 1.7$ at around 600 °C and to a five times higher improvement of ZT at room temperature. The integration of monodisperse silicide and germanide nanoparticles, based on e.g. Ni_2Si in nanograined silicon and silicon germanium alloys might be also a very promising path for the future development of high performance thermoelectric materials for micro-generators.

Beside the established thermoelectric materials based on Bi_2Te_3 , PbTe and $\text{Si}_{100-x}\text{Ge}_x$, the synthesis approach of nanograined composites is currently adopted for silicides,^[104] Half-Heusler alloys and skutterudites. For the application in the medium temperature regime from 100 to 500 °C, $\text{Mg}_2\text{Si}_{0.6}\text{Sn}_{0.4}$ is a promising low-cost and environmental-friendly material system.^[104] Powders of this n-type silicide doped with 0.4 at% Sb have been compacted by spark plasma sintering and peak ZT values of 1.1 at 490 °C were achieved. In comparison to bulk materials, the reduction of the thermal conductivity due to nanograins has not been demonstrated. Thus, the $\text{Mg}_2\text{Si}_{0.6}\text{Sn}_{0.4}$ silicide seems to have great potentials for ZT enhancements by optimization of the preparation procedure of the nanograined structure.

The skutterudites are a further emerging and very low-cost material system for the medium temperature regime. Their open cage-like structure can be filled with foreign atoms acting as phonon rattlers. In this context, n-type $\text{Co}_4\text{Sb}_{12}$ skutterudites filled with Yb atoms have been studied as compacted grained composite. By spark-plasma sintering of melt-spun $\text{Yb}_{0.2}\text{Co}_4\text{Sb}_{12.3}$ flakes,^[105] and by hot pressing of high-energy ball milled $\text{Yb}_{0.35}\text{Co}_4\text{Sb}_{12}$ nanoparticles,^[106] ZT values of 1.26 at 530 °C and 1.2 at 550 °C have been obtained, respectively. A

solubility of Yb atoms twice as high in the nanograined system as in the bulk has been demonstrated, but due to large grain sizes, ranging from 50 nm up to 1 μm , a significant reduction of the thermal conductivity by phonon scattering at the grain boundaries has not been demonstrated in the Yb-filled $\text{Co}_4\text{Sb}_{12}$ skutterudite system. An unfilled $\text{Co}_{0.8}\text{Ni}_{0.2}\text{Sb}_{3.05}$ skutterudite system with sub- μm -sized pores exhibited an effectively reduced thermal conductivity and a maximum ZT value of up to 0.7 at 500 $^\circ\text{C}$ has been reached.^[107] The sub-micrometer pores were formed by a few percent Sb overload during the alloying, forming Sb inclusions embedded in the composite structure which volatilized during the processing at higher temperatures. By adding rattling atoms to this system, an additional ZT enhancement might be expected.

The approach of high-energy ball-milling has been successfully applied for so-called half-Heusler alloys based on $\text{Zr}_{0.5}\text{Hf}_{0.5}\text{CoSb}_{0.8}\text{Sn}_{0.2}$. The $ZT = 0.5$ for bulk was enhanced to 0.8 at 700 $^\circ\text{C}$.^[108] The power factor $\sigma \cdot S^2$ of the bulk ingots and the nanograined materials is similar. Although grain growth up to crystallite sizes of 20 to 500 nm from an initial average diameter of 5 to 10 nm after ball milling has been observed during the process of hot pressing, the thermal conductivity was reduced by 60%. If the small grain sizes can be preserved better during heat treatment and module operation, $ZT > 1$ can be expected for half-Heusler alloys, which are a promising and moderately priced replacement for the PbTe system in the future.

Currently, Bi_2Te_3 -based thermoelectric modules are used predominately for cooling applications and these modules are even employed as thermoelectric generators in exhaust lines of automobiles at a prototype level, although the long-term utilization at temperatures above 250 $^\circ\text{C}$ degrades the TE device. The application of Bi_2Te_3 -based nanograined bulk-composites in commercial products with a moderate improvement (30% to 60%) of the device efficiency and an introduction to the market is expected to take place within the next five years. For the regime near room temperature (-50 to 250 $^\circ\text{C}$), Bi_2Te_3 alloys will continue to be the benchmark materials in TE modules in the next one or two decades, due to the lack of low-cost alternatives in this temperature range.

For thermoelectric generators at medium temperatures from 200 to 600 $^\circ\text{C}$, improved modules based on nanostructured PbTe are projected in the near future, but can be named a transition technology. Based on the price, the limited supply of tellurium, and the regulations for lead-based consumer products, e.g. in the European Union, the field of potential applications might reasonably grow, but will be limited to certain areas. For the envisioned application in heat recovery on larger scale, e.g. in car and other exhaust-engine-based vehicles, the skutterudite, half-Heusler and silicide-based nanograined composites are potential candidates for the development of the next generation of thermoelectric generators. Their thermoelectric performance ZT is 30–40% less compared to the best PbTe-based materials, but the scalability to large-volume applications is not limited by the natural supply of the source substance. Also, most materials still exhibit large potential for further optimization. In all cases, the costs of precursor particles are at a low to moderate level (10–100 US\$ per kg).^[109]

Traditional SiGe alloys have been the materials of choice for applications at high temperature >800 $^\circ\text{C}$, especially for deep space missions. Fortunately, the material price has not been

a limitation for the development of the SiGe modules at the pioneering time in the 1960s. A new generation of moderately priced thermoelectric generators based on nanograined silicon with low concentrations of germanium exhibits great market potentials and might raise new application areas for thermoelectric devices. For even higher temperatures, oxide materials are under consideration for thermoelectric modules, although the development of p-doped high- ZT materials is challenging and new strategies for the module assembly and design are required for device applications under large temperature gradients.

9. Conclusions and Outlook

Currently, using nanostructured materials is considered to be a promising strategy for the development of thermoelectric materials with high efficiency ($Z \cdot T$). A large variety of thermoelectric materials have been developed in the last five years with a focus on high-temperature applications and high efficiency. Tellurium- and lead-free nanograined alternatives with a reasonable thermoelectric efficiency ($ZT > 0.5$) are now available. Although Bi_2Te_3 and related materials are still a dominating material system in thermoelectrics, more than hundred publications on silicon-based thermoelectric nanostructures and materials have been published based on Web of Science since 2005. Therefore, silicon and related alloys can be considered an emerging materials system in thermoelectrics. Other materials systems such as Heuslers and Skutterudites are following the same trend.

Novel nanostructures such as multilayered systems, nanowires, and nanotubes are of great interest for fundamental research of thermoelectric properties and in new emerging research fields such as topological insulators. Their fascinating properties are strongly influenced by nanoscale confinement, such as the reduction of heat conductivity and energy filtering of charge carriers. Recently, spin-dependent thermoelectric effects have also caught great general attention, which is not mentioned here. This fundamentally oriented and novel research area has been labelled spin-caloritronics. The currently intense interest in thermoelectric applications and thermoelectric effects at the nanoscale has led to numerous research activities on thermoelectric materials and model systems at many research institutions worldwide.

This review highlights the enormous progress in the theory, various technologies, and metrology of nanoscale thermoelectrics. The review also demonstrates impressively that the transfer of nanoscale thermoelectrics into thermoelectric products must be the next important step to stabilize nanoscale thermoelectrics to a research field with long-term sustainability. For small-scale energy harvesting devices, e.g., wireless sensors and on-spot cooling, high-performance thermoelectric nanostructures based on epitaxial multilayers and superlattice systems will be utilized and further development efforts are needed for the device integration. The authors suppose that the combination of different synthesis approaches of thermoelectric nanoparticles, e.g., ball-milling or continuous gas-phase synthesis and subsequent compacting processes based on hot-pressing or spark plasma sintering will have the best chance to create a material that is useful for implementation in outperforming standard vertical device designs for room temperature and e.g. high temperature applications.

Acknowledgements

The authors thank William Töllner, Bacer Hamdou, Stephanie Baer and Iris Klüver for discussions and manuscript modifications. For scientific discussions and making available of images for the review manuscript, we express particular thanks to Gabi Schierning and her collaborators at the University of Duisburg/Essen in Germany, Heiner Linke from the University of Lund/Sweden, Oded Rabin from the University of Maryland and Hartmut Buhmann from the University of Würzburg, Germany. Furthermore, the German Science Foundation is gratefully acknowledged in general for funding of the German Priority Program SPP 1386 "Nanostructured Thermoelectrics" since 2009 and specifically for financial support of the colored images via the coordination project of the SPP 1386.

Received: April 17, 2011

- [1] Lawrence Livermore National Laboratory, DOE, (2009). <https://publicaffairs.llnl.gov/news/energy/energy.html> (last accessed July 2011).
- [2] J. Sommerlatte, K. Nielsch, H. Böttner, *Phys. J.* **2007**, *6*, 35–41.
- [3] G. S. Nolas, J. Sharp, H. J. Goldsmid, *Thermoelectrics—Basic Principles and New Materials Developments*, Springer, Berlin, **2001**.
- [4] T. M. Tritt, M. A. Subramanian, *MRS Bull.* **2006**, *31*, 188.
- [5] A. F. Ioffe, *Semiconductor Thermoelements and Thermoelectric Cooling*, Infosearch Limited, London, **1957**.
- [6] A. I. Hochbaum, R. K. Chen, R. D. Delgado, W. J. Liang, E. C. Garnett, M. Najarian, A. Majumdar, P. D. Yang, *Nature* **2008**, *451*, 163.
- [7] A. I. Boukai, Y. Bunimovich, J. Tahir-Kheli, J. K. Yu, W. A. Goddard, J. R. Heath, *Nature* **2008**, *451*, 168.
- [8] a) R. Venkatasubramanian, T. Colpitts, E. Watko, M. Lamvik, N. ElMasry, *J. Cryst. Growth* **1997**, *170*, 817; b) R. Venkatasubramanian, *Phys. Rev. B* **2000**, *61*, 3091; c) R. Venkatasubramanian, E. Siivola, T. Colpitts, B. O'Quinn, *Nature* **2001**, *413*, 597.
- [9] T. C. Harman, P. J. Taylor, M. P. Walsh, B. E. Laforge, *Science* **2002**, *297*, 2229.
- [10] K. F. Hsu, S. Loo, F. Guo, W. Chen, J.S. Dyck, C. Uher, T. Hogan, Polychroniadis, M. G. Kanatzidis, *Science* **2004**, *330*, 818.
- [11] H. Fleischmann, *Z. Naturforsch.* **1961**, *16*, 765.
- [12] B. Poudel, Q. Hao, Y. Ma, Y. Lan, A. Minnich, B. Yu, X. Yan, D. Wang, A. Muto, D. Vashaee, X. Chen, J. Liu, M. S. Dresselhaus, G. Chen, Z. Ren, *Science* **2008**, *320*, 634.
- [13] L. D. Hicks, M. S. Dresselhaus, *Phys. Rev. B* **1993**, *47*, 12727.
- [14] Z. Zhang, X. Sun, M. S. Dresselhaus, J. Y. Ying, J. P. Heremans, *Appl. Phys. Lett.* **1998**, *73*, 1589.
- [15] Z. Zhang, X. Sun, M. S. Dresselhaus, J. Y. Ying, J. Heremans, *Phys. Rev. B* **2000**, *61*, 4850.
- [16] X. Sun, Z. Zhang, M. S. Dresselhaus, *Appl. Phys. Lett.* **1999**, *74*, 4005.
- [17] Y.-M. Lin, X. Sun, M. S. Dresselhaus, *Phys. Rev. B* **2000**, *62*, 4610.
- [18] J. Heremans, C. M. Thrush, Z. Zhang, X. Sun, M. S. Dresselhaus, J. Y. Ying, D. T. Morelli, *Phys. Rev. B* **1998**, *58*, 10091.
- [19] J. Heremans, C. M. Thrush, Y.-M. Lin, S. Cronin, Z. Zhang, M. S. Dresselhaus, J. F. Mansfield, *Phys. Rev. B* **2000**, *61*, 2921.
- [20] A. Boukai, K. Xu, J. R. Heath, *Adv. Mater.* **2006**, *18*, 864.
- [21] S. B. Cronin, Y.-M. Lin, O. Rabin, M. R. Black, J. Y. Ying, M. S. Dresselhaus, P. L. Gai, J.-P. Minet, J.-P. Issi, *Nanotechnology* **2002**, *13*, 653.
- [22] A. L. Moore, M. T. Pettes, F. Zhou, L. Shi, *J. Appl. Phys.* **2009**, *106*, 034310.
- [23] W. Shim, J. Ham, K.-I. Lee, W. Y. Jeung, M. Johnson, W. Lee, *Nano Lett.* **2009**, *9*, 18.
- [24] D. A. Broido, T. L. Reinecke, *Phys. Rev. B* **2001**, *64*, 045324.
- [25] a) N. Mingo, *Appl. Phys. Lett.* **2004**, *84*, 2652; b) N. Mingo, *Appl. Phys. Lett.* **2006**, *88*, 139901.
- [26] S. Farhangfar, *J. Phys. D: Appl. Phys.* **2011**, *44*, 125403.
- [27] J. E. Cornett O. Rabin, *Appl. Phys. Lett.* **98**, 182104.
- [28] J. W. Roh, S. Y. Jang, J. Kang, S. Lee, J.-S. Noh, W. Kim, J. Park, W. Lee, *Appl. Phys. Lett.* **2010**, *96*, 103101.
- [29] A. L. Moore, M. T. Pettes, F. Zhou, L. Shi, *J. Appl. Phys.* **2009**, *106*, 034310.
- [30] H. Kim, I. Kim, H.-J. Choi, W. Kim, *Appl. Phys. Lett.* **2010**, *96*, 233106.
- [31] Z. Wang, N. Mingo, *Appl. Phys. Lett.* **2010**, *97*, 101903.
- [32] A. Mavrokefalos, A. L. Moore, M. T. Pettes, L. Shi, W. Wang, X. Li, *J. Appl. Phys.* **2009**, *105*, 104318.
- [33] D. Li, Y. Wu, P. Kim, L. Shi, P. Yang, A. Majumdar, *Appl. Phys. Lett.* **2003**, *83*, 2934.
- [34] R. S. Wagner, W. C. Ellis, *Appl. Phys. Lett.* **1964**, *4*, 89.
- [35] A. M. Morales, C. M. Lieber, *Science* **1998**, *279*, 208.
- [36] M. Law, J. Goldberger, P. Yang, *Annu. Rev. Mater. Res.* **2004**, *34*, 83.
- [37] C. Kittel, *Phys. Rev.* **1949**, *75*, 972.
- [38] Z. Huang, N. Geyer, P. Werner, J. d. Boor, U. Gösele, *Adv. Mater.* **2011**, *23*, 285.
- [39] K. Hippalgaonkar, B. Huang, R. Chen, K. Sawyer, P. Ercius, A. Majumdar, *Nano Lett.* **2010**, *10*, 4341.
- [40] W. Liu, M. Asheghi, *J. Appl. Phys.* **2005**, *98*, 123523.
- [41] R. Yang, G. Chen, M. S. Dresselhaus, *Nano Lett.* **2005**, *5*, 1111.
- [42] P. N. Martin, Z. Aksamija, E. Pop, U. Ravaioli, *Nano Lett.* **2010**, *10*, 1120.
- [43] E. A. Hoffmann, H. A. Nilsson, J. E. Matthews, N. Nakpathomkun, A. I. Persson, L. Samuelson, H. Linke, *Nano Lett.* **2009**, *9*, 779.
- [44] T. E. Humphrey, R. Newbury, R. P. Taylor, H. Linke, *Phys. Rev. Lett.* **2002**, *89*, 116801.
- [45] N. Nakpathomkun, H. Q. Xu, H. Linke, *Phys. Rev. B* **2010**, *82*, 235428.
- [46] R. Scheibner, E. G. Novik, T. Borzenko, M. König, D. Reuter, A. D. Wieck, H. Buhmann, L. W. Molenkamp, *Phys. Rev. B* **2007**, *75*, 041301 (2007).
- [47] R. Scheibner, M. König, D. Reuter, A. D. Wieck, C. Gould, H. Buhmann, L. W. Molenkamp, *New J. Phys.* **2008**, *10*, 083016.
- [48] J.-K. Yu, S. Mitrovic, D. Tham, J. Varghese, J. R. Heath, *Nat. Nanotechnol.* **2010**, *5*, 718.
- [49] J. Tang, H.-T. Wang, D. H. Lee, M. Fardy, Z. Huo, T. P. Russell, P. Yang, *Nano Lett.* **2010**, *10*, 4279.
- [50] P. E. Hopkins, C. M. Reinke, M. F. Su, R. H. Olsson III, E. A. Shaner, Z. C. Leseman, J. R. Serrano, L. M. Phinney, I. El-Kady, *Nano Lett.* **2011**, *11*, 107.
- [51] Y. He, D. Donadio, J.-H. Lee, J. C. Grossman, G. Galli, *ACS Nano* **2011**, *5*, 1839.
- [52] M. Kashiwagi, S. Hirata, K. Harata, Y. Zheng, K. Miyazaki, M. Yahiro, C. Adachi, *Appl. Phys. Lett.* **2011**, *98*, 023114.
- [53] J. Nurnus, H. Böttner, A. Lambrecht, *Nanoscale Thermoelectrics*, in: *Thermoelectrics Handbook: Macro to Nano-structured Materials* (Ed: D.M. Rowe), Taylor & Francis, Boca Raton, FL **2006**, 48.1–48.23.
- [54] H. Böttner, G. Chen, R. Venkatasubramanian, *MRS Bull.* **2006**, *31*, 211.
- [55] C. J. Vineis, A. Shakouri, A. Majumdar, M. G. Kanatzidis, *Adv. Mater.* **2010**, *22*, 3970.
- [56] V. Semenyuk, *Proc. 25th Int. Conf. Thermoelectrics*, August 6-10, 2006, Vienna, Austria, **2006**, 322–326.
- [57] a) H. Böttner, J. Nurnus, A. Gavrikov, G. Kühner, M. Jägler, C. Künzel, D. Eberhard, G. Plescher, A. Schubert, K.-H. Schlereth, *IEEE J. Microelectromech. Syst.* **2004**, *13*, 414; b) H. Böttner, J. Nurnus, A. Schubert, F. Volkert, *Proc. 26th Int. Conf. Thermoelectrics*, June 3-7, 2007, Jeju Island, Korea, **2007**, 311–314.
- [58] D. G. Cahill, M. Katiyar, J. R. Abelson, *Phys. Rev. B* **1994**, *50*, 6077.
- [59] W. S. Capinski, H. J. Maris, T. Ruf, M. Cardona, K. Ploog, D. S. Katzer, *Phys. Rev. B* **1999**, *59*, 8105.
- [60] M. N. Touzelbaev, P. Zhou, R. Venkatasubramanian, K. E. Goodson, *J. Appl. Phys.* **2001**, *90*, 763.
- [61] T. C. Harman, D. L. Spears, M. P. Walsh, *J. Electron. Mater.* **1999**, *28*, L1-L4.
- [62] a) T. C. Harman, P. J. Taylor, D. L. Spears, M. P. Walsh, *J. Electron. Mater.* **2000**, *29*, L1-L4; b) T. C. Harman, P. J. Taylor, M. P. Walsh, B. E. LaForge, *Science* **2002**, *297*, 2229.

- [63] T. C. Harman, M. P. Walsh, B. E. Laforge, G. W. Turner, *J. Electron. Mater.* **2005**, *34*, L19.
- [64] C. J. Vineis, T. C. Harman, S. D. Calawa, M. P. Walsh, R. E. Reeder, R. Singh, A. Shakouri, *Phys. Rev. B* **2008**, *77*, 235202.
- [65] G. Pernot, M. Stoffel, I. Savic, F. Pezzoli, P. Chen, G. Savelli, A. Jacquot, J. Schumann, U. Denker, I. Mönch, Ch. Deneke, O. G. Schmidt, J. M. Rampoux, S. Wang, M. Plissonnier, A. Rastelli, S. Dilhaire, N. Mingo, *Nat. Mater.* **2010**, *9*, 491.
- [66] F. R. Harris, S. Standridge, C. Feik, D. C. Johnson, *Angew. Chem. Int. Ed.* **2003**, *42*, 5296.
- [67] a) C. Chiritescu, D. G. Cahill, N. Nguyen, D. Johnson, A. Bodapati, P. Koblinski, P. Zschack, *Science* **2007**, *315*, 351; b) A. Mavrokefalos, N. T. Nguyen, M. T. Pettes, D. C. Johnson, L. Shi, *Appl. Phys. Lett.* **2007**, *91*, 171912.
- [68] C. L. Heideman, R. Rostek, M. D. Anderson, A. A. Herzing, I. M. Anderson, D. C. Johnson, *J. Electron. Mater.* **2010**, *39*, 1476.
- [69] J.-P. Fleurial, A. Borshchevsky, M. A. Ryan, W. Philips, E. Kolawa, R. Ewell, "Thermoelectric Microcoolers for Thermal Management Applications", *Proc. 16th Int. Conf. Thermoelectrics*, August **1997**, Dresden, Germany, 641.
- [70] J. Nurnus, H. Böttner, C. Künzel, U. Vetter, A. Lambrecht, *Proc. 21st Int. Conf. Thermoelectrics*, August 25-29, **2002**, Long Beach, USA, 323-527 (**2002**).
- [71] a) A. Shakouri, J. E. Bowers, *Appl. Phys. Lett.* **1997**, *71*, 1234; b) D. Vashaee, A. Shakouri, *Phys. Rev. Lett.* **2004**, *92*, 106103; c) T. E. Humphrey, M. F. O'Dwyer, H. Linke, *J. Phys. D: Appl. Phys.* **2005**, *38*, 2051.
- [72] a) V. Rawat, T. Sands, *J. Appl. Phys.* **2006**, *100*, 064901; b) V. Rawat, Y. K. Koh, D. G. Cahill, T. D. Sands, *J. Appl. Phys.* **2009**, *105*, 024909.
- [73] a) M. Zebarjadi, Z. X. Bian, R. Singh, A. Shakouri, R. Wortman, V. Rawat, T. Sands, *J. Electron. Mater.* **2009**, *38*, 960; b) V. Rawat, Y. K. Koh, D. G. Cahill, T. D. Sands, *J. Appl. Phys.* **2009**, *105*, 024909.
- [74] W. Kim, S. L. Singer, A. Majumdar, D. Vashaee, Z. Bian, A. Shakouri, G. Zeng, J. E. Bowers, J. M. O. Zide, A. C. Gossard, *Appl. Phys. Lett.* **2006**, *88*, 242107.
- [75] W. Kim, J. Zide, A. Gossard, D. Klenov, S. Stemmer, A. Shakouri, A. Majumdar, *Phys. Rev. Lett.* **2006**, *96*, 045901.
- [76] a) R. Singh, Z. Bian, A. Shakouri, G. Zeng, J.-H. Bahk, J. E. Bowers, J. M. O. Zide, A. C. Gossard, *Appl. Phys. Lett.* **2009**, *94*, 212508; b) G. Zeng, J.-H. Bahk, J. E. Bowers, H. Lu, A. C. Gossard, S. L. Singer, A. Majumdar, Z. Bian, M. Zebarjadi, A. Shakouri, *Appl. Phys. Lett.* **2009**, *95*, 083503.
- [77] X. F. Tang, W. J. Xie, H. Li, W. Y. Zhao, Q. J. Zhang, M. Niino, *Appl. Phys. Lett.* **2007**, *90*, 012102.
- [78] Y. Ma, Q. Hao, B. Poudel, Y. Lan, B. Yu, D. Wang, G. Chen, Z. Ren, *Nano Lett.* **2008**, *8*, 2580.
- [79] Y. Q. Cao, X. Zhao, T. J. Zhu, X. B. Zhang, J. P. Tu, *Appl. Phys. Lett.* **2008**, *92*, 143106.
- [80] a) W. Xie, X. Tang, Y. Yan, Q. Zhang, T. M. Tritt, *Appl. Phys. Lett.* **2009**, *94*, 102111; b) W. Xie, X. Tang, Y. Yan, Q. Zhang, T. M. Tritt, *J. Appl. Phys.* **2009**, *105*, 113713.
- [81] C. Chiritescu, C. Mortensen, D. G. Cahill, D. Johnson, P. Zschack, *J. Appl. Phys.* **2009**, *106*, 073503.
- [82] D. G. Ebling, A. Jacquot, M. Jäggle, H. Böttner, U. Kühn, L. Kirste, *Phys. Status Solidi – Rapid Res. Lett.* **2007**, *1*, 238.
- [83] J. S. Lee, T. S. Oh, D.-B. Hyun, *J. Mater. Sci.* **2005**, *35*, 881.
- [84] X. Yan, B. Poudel, Y. Ma, W. S. Liu, G. Joshi, H. Wang, Y. Lan, D. Wang, G. Chen, Z. F. Ren, *Nano Lett.* **2010**, *10*, 3373.
- [85] D. T. Morelli, V. Jovovic, J. P. Heremans, *Phys. Rev. Lett.* **2008**, *101*, 035901.
- [86] H. Wang, J.-F. Li, M. Zou, T. Sui, *Appl. Phys. Lett.* **2008**, *93*, 202106.
- [87] K. F. Hsu, S. Loo, F. Guo, W. Chen, J. S. Dyck, C. Uher, T. Hogan, E. K. Polychroniadis, M. G. Kanatzidis, *Science* **2004**, *303*, 818.
- [88] J. Cui, X. Liu, W. Yang, D. Chen, H. Fu, P. Ying, *J. Appl. Phys.* **2009**, *105*, 063703.
- [89] C.-H. Kuo, M.-S. Jeng, J.-R. Ku, S.-K. Wu, Y.-W. Chou, C.-S. Hwang, *J. Electron. Mater.* **2009**, *38*, 1956.
- [90] J. P. Heremans, V. Jovovic, E. S. Toberer, A. Saramat, K. Kurosaki, A. Charoenphadee, S. Yamanaka, G. J. Snyder, *Science* **2008**, *321*, 554.
- [91] B. Yu, Q. Zhang, H. Wang, X. Wang, H. Wang, D. Wang, H. Wang, G. J. Snyder, G. Chen, Z. F. Ren, *J. Appl. Phys.* **2010**, *108*, 016104.
- [92] M. G. Kanatzidis, *Chem. Mater.* **2010**, *22*, 648.
- [93] J. Androulakis, C.-H. Lin, H.-J. Kong, C. Uher, C.-I. Wu, T. Hogan, B. A. Cook, T. Caillat, K. M. Paraskevopoulos, M. G. Kanatzidis, *J. Am. Chem. Soc.* **2007**, *129*, 9780.
- [94] K. Biswas, J. He, Q. Zhang, G. Wang, C. Uher, V. P. David, M. G. Kanatzidis, *Nat. Chem.* **2011**, *3*, 160.
- [95] H. Wang, J.-F. Li, C.-W. Nan, M. Zhou, W. Liu, B.-P. Zhang, T. Kita, *Appl. Phys. Lett.* **2006**, *88*, 092104.
- [96] a) G. Joshi, H. Lee, Y. Lan, X. Wang, G. Zhu, D. Wang, R. W. Gould, D. C. Cuff, M. Y. Tang, M. S. Dresselhaus, G. Chen, Z. Ren, *Nano Lett.* **2008**, *8*, 4670; b) X. W. Wang, H. Lee, Y. C. Lan, G. H. Zhu, G. Joshi, D. Z. Wang, J. Yang, A. J. Muto, M. Y. Tang, J. Klatsky, S. Song, M. S. Dresselhaus, G. Chen, Z. Ren, *Appl. Phys. Lett.* **2008**, *93*, 193121.
- [97] www.metal-pages.com/metalprices/germanium
- [98] G. H. Zhu, H. Lee, Y. C. Lan, X. W. Wang, G. Joshi, D. Z. Wang, J. Yang, D. Vashaee, H. Guilbert, A. Pillitteri, M. S. Dresselhaus, G. Chen, Z. F. Ren, *Phys. Rev. Lett.* **2009**, *102*, 196803.
- [99] S. K. Bux, R. G. Blair, P. K. Gogna, H. Lee, G. Chen, M. S. Dresselhaus, R. B. Kaner, J.-P. Fleurial, *Adv. Funct. Mater.* **2009**, *19*, 2445.
- [100] N. Petermann, N. Stein, G. Schierning, R. Theissmann, B. Stoib, M. Brandt, C. Hecht, C. Schulz, H. Wiggers, *J. Phys. D: Appl. Phys.* **2011**, *44*, 174034.
- [101] N. Stein, N. Petermann, R. Theissmann, G. Schierning, R. Schmechel, H. Wiggers, *J. Mater. Res.* **2011**, *26*, 1872.
- [102] C. Bera, M. Soulier, C. Navone, G. Roux, J. Simon, S. Volz, N. Mingo, *J. Appl. Phys.* **2010**, *108*, 124306.
- [103] N. Mingo, D. Hauser, N. P. Kobayashi, M. Plissonnier, A. Shakouri, *Nano Lett.* **2009**, *9*, 711.
- [104] W. Liu, X. Tang, J. Sharp, *J. Phys. D: Appl. Phys.* **2010**, *43*, 085406.
- [105] H. Li, X. Tang, X. Su, Q. Zhang, *Appl. Phys. Lett.* **2008**, *92*, 202114.
- [106] J. Yang, Q. Hao, H. Wang, Y. C. Lan, Q. Y. He, A. Minnich, D. Z. Wang, J. A. Harriman, V. M. Varki, M. S. Dresselhaus, G. Chen, Z. F. Ren, *Phys. Rev. B* **2009**, *80*, 115329.
- [107] Q. He, S. Hu, X. Tang, Y. Lan, J. Yang, X. Wang, Z. Ren, Q. Hao, G. Chen, *Appl. Phys. Lett.* **2008**, *93*, 042108.
- [108] X. Yan, G. Joshi, W. Liu, Y. Lan, H. Wang, S. Lee, J. W. Simonson, S. J. Poon, T. M. Tritt, G. Chen, Z. F. Ren, *Nano Lett.* **2011**, *11*, 556.
- [109] www.metal-pages.com/metalprices
- [110] E. J. Menke, Q. Li, R. M. Penner, *Nano Lett.* **2004**, *4*, 2009.
- [111] M. S. Sander, A. L. Prieto, R. Gronsky, T. Sands, A. M. Stacy, *Adv. Mater.* **2002**, *14*, 665.
- [112] W. Wang, X. Lu, T. Zhang, G. Zhang, W. Jiang, X. Li, *J. Am. Chem. Soc.* **2007**, *129*, 6702.
- [113] Y. M. Zuev, J. S. Lee, C. Galloy, H. Park, P. Kim, *Nano Lett.* **2010**, *10*, 3037.
- [114] A. Mavrokefalos, M. T. Pettes, F. Zhou, L. Shi, *Rev. Sci. Instrum.* **2007**, *78*, 034901.
- [115] J. Zhou, C. Jin, J. H. Seol, X. Li, L. Shi, *Appl. Phys. Lett.* **2005**, *87*, 133109.
- [116] F. Zhou, J. Szczech, M. T. Pettes, A. L. Moore, S. Jin, L. Shi, *Nano Lett.* **2007**, *7*, 1649.

B Philosophical Article

Über die Metaphysische oder Kosmologische Bedeutungslosigkeit der Erde

Reprinted with permission from

Johannes Kimling

Aufklärung und Kritik, Heft **43**, 205 (2012)

Copyright 2012 by the Gesellschaft für kritische Philosophie Nürnberg.

Johannes Kimling (Hamburg)

Über die metaphysische oder kosmologische Bedeutungslosigkeit der Erde Anmerkungen zu Klaas Schüllers Kritik der These von der objektiven Bedeutungslosigkeit der Erde.

In seinem Beitrag „Nur ein ‚Staubkorn im Weltall‘?“ kritisiert Klaas Schüller die „These von der objektiven Bedeutungslosigkeit der Erde und der auf ihr stattfindenden Ereignisse“.¹ Er bezeichnet diese These als „naturalistische These“, die „gegen konkurrierende Weltbilder in Stellung gebracht“ werde, „die die Erde und die auf ihr lebenden Menschen als Zentrum allen Seins ansehen“. In seiner Analyse der These erklärt Schüller, welches Verständnis Naturalisten vom Begriff „Bedeutung“ hätten. Für sie sei die Bedeutung eines Dinges bestimmt durch „dessen ‚Größe‘“, „ergänzt durch den Aspekt der ‚räumlichen Lage innerhalb eines Systems““. Schüller meint „anders als durch dieses Begriffsverständnis“ sei „nicht zu erklären, warum die Fakten der geringen Größe der Erde und ihrer Lage am ‚Rande der Milchstraße‘ von den Naturalisten immer wieder suggestiv mit dem Hinweis auf die Bedeutungslosigkeit dieses Planeten verknüpft werden“. Weiter behauptet Schüller, Naturalisten würden mittels dieser Definition des Begriffs „Bedeutung“ suggerieren, „über unparteiische Indikatoren für die Bestimmung von Bedeutung zu verfügen“. Dieser, so Schüller, „radikal-objektivistische erkenntnistheoretische Ansatz der Naturalisten“ führe dazu, dass „ihr Bedeutungsverständnis die gleiche Schwäche aufweist wie jenes ihrer theistischen Gegenspieler“. Diese bestehe darin, dass „‚Bedeutung‘ von beiden Parteien als etwas objektiv-faktisches rekonstruiert wird“. Schließlich stellt Schüller fest, Bedeutung

sei „eine relationale Eigenschaft und keine Eigenschaft des Dinges an sich“. Da die Erde „kein alleinstehendes Ding ist, sondern von Milliarden bewusster Lebewesen bewohnt wird“, die die Erde „selbst mit Bedeutung ausfüllen“, kommt Schüller zu dem Schluss, die Erde sei mitsamt ihrer Bevölkerung „in der Tat das Sinnzentrum des Kosmos“, denn nirgendwo sonst sei „das Netz der Bedeutung nach derzeitiger Kenntnis so dicht geknüpft wie auf diesem Planeten“.

Schüller versucht die naturalistische Kritik an religiösen Bedeutungszuschreibungen der Erde und der auf ihr stattfindenden Ereignisse auf eine Stufe mit diesen zu stellen. Damit ihm dieses Vorhaben gelingen kann, muss er voraussetzen, dass es sich um voneinander unabhängige Thesen handelt. Anstatt dies zu belegen suggeriert er nur die Eigenständigkeit der „naturalistischen These“, indem er in seinem zweiten Abschnitt schreibt: „Diese These wird nun gegen konkurrierende Weltbilder in Stellung gebracht“. Damit zerreißt er folgenden geschichtlichen Zusammenhang: Die „naturalistische These“ entstand unter dem Einfluss der Entwicklung neuzeitlicher Wissenschaften aus der Kritik an überholten religiösen Sinn- und Wertzusammenhängen. Aus diesem Grund haben die von Schüller kritisierten Autoren auch keine explizite „naturalistische These“ aufgestellt, sondern sprechen von *Kränkungen*, die wissenschaftliche Erkenntnisse der menschlichen Selbstverliebtheit zugefügt haben sollen^{2,3,4,5} – im Rahmen der

„naturalistischen These“ sprechen sie von der *kosmologisch-eschatologischen Kränkung*. Wollte man eine „naturalistische These“ in diesem Zusammenhang aufstellen, könnte diese richtiger lauten, dass religiöse Bedeutungszuschreibungen der Erde und der auf ihr stattfindenden Ereignisse falsch sind.

Um die beiden Thesen inhaltlich voneinander zu trennen, versucht Schüller in seinen Abschnitten vier bis acht, den Begriff „Bedeutung“ für den Naturalismus und für monotheistische Religionen unterschiedlich zu definieren. Schüller schreibt (S. 245): „Sind es bei den theistischen Religionen die Existenz „Gottes“ und eines objektiven Heilsgeschehens, die die Bedeutung bestimmter Dinge konstatieren, so sind es im Naturalismus gewisse objektiv gegebene Merkmale dieser Dinge.“ Um beide Thesen auf einer Stufe zu halten behauptet er weiter: „In beiden weltanschaulichen Systemen wird der Eindruck vermittelt, dass die Dinge ihre Bedeutung gewissermaßen in sich tragen oder die Bedeutung ihnen zumindest faktisch anhaftet.“ Schüller behauptet, „die Befürworter der naturalistischen These“ würden „die Bedeutungslosigkeit der Erde als objektive, auf wissenschaftlichen Befunden fußende Tatsache präsentieren“. Diese Aussage belegt er mit einer Fußnote, in der er behauptet, Kanitscheider würde „ausdrücklich von der ‚szientistischen‘ Dekonstruktion von objektiver Bedeutung“ sprechen. Hier wird Kanitscheider von Schüller unvollständig zitiert. Der eigentliche Inhalt des Satzes geht dadurch verloren und kann in der Art und Weise, wie Schüller es tut, missverstanden werden. Um dies ersichtlich zu machen müssen wir hier einen weitaus größeren Abschnitt zitieren. Kanitscheider schreibt:⁶

„Wenn das christlich-platonische Gedankengebäude den Menschen in der scala naturae in eine ausgezeichnete Position rückte, ihn mit einem über aller Materie stehenden Geist ausstattete, (...), dann sind es diese historischen Rollen, welche den Menschen in die fatale Lage der Zentralitätsenttäuschung gebracht haben. Diese historische Hinterlassenschaft ist die Bürde, die der moderne, von der Wissenschaft vereinnahmte Mensch tragen muss. Er steht in der Spannung zwischen geschichtlich bedingter ontologischer Sinnhaftigkeit und szientistischer Dekonstruktion von objektiver Bedeutung. Hätten Religion und Metaphysik den Menschen niemals mit der Last der objektiven Sinnhaftigkeit beladen, wäre diese Erwartungshaltung nicht entstanden und dann hätte es auch nicht zu dieser Enttäuschung durch die Wissenschaften kommen können.“

Offensichtlich bezieht Kanitscheider „objektive Bedeutung“ auf das christlich-platonische Gedankengebäude, das unter szientistischer Dekonstruktion stehe. Damit erweist sich der einzige Beleg, den Schüller für die Haltbarkeit seiner obigen Behauptung präsentiert, als falsch. Es handelt sich bei genauer Betrachtung folglich nur um Interpretationen und Eindrücke von Schüller selbst. Man kann genauso gut zu anderen Eindrücken gelangen, insbesondere wenn man die von Schüller kritisierten Bücher von Anfang bis Ende gelesen hat. Die drei von Schüller kritisierten Autoren geben beispielsweise an, einen kritischen Rationalismus zu vertreten. Vollmer grenzt sich deutlich von einem Naturalismus in der Ethik „in einem Sinne, wonach *Normen und Werte in der Natur ‚da draußen‘ auffindbar oder aus auffindbaren Fakten gewinnbar sein soll-*

ten“, ab.⁷ Kanitscheider schreibt nur wenige Seiten vor Schüllers Zitat: „Neben der kosmologischen Situation, in der sich der Mensch befindet, gibt es noch eine methodologische Begründung, warum der Mensch mit noch so viel Anstrengung in der Welt selber keine objektive Sinnhaftigkeit entdecken wird. Es war Max Weber, der darauf hingewiesen hat, dass die Wertfreiheit der Wissenschaft es grundsätzlich unmöglich macht, die Frage zu beantworten, ob diese Welt, die sie beschreibt, wert ist zu existieren, ob sie einen Sinn hat und ob es einen Sinn hat, in ihr zu existieren“.⁸ Und bei Schmidt-Salomon lesen wir, dass „das philosophische Denken sehr wohl präskriptive Sätze (ethische Regeln) und existentielle Sinndeutungen mit einschließt, die im strengen wissenschaftlichen Sinne nicht überprüfbar sind und daher aus dem Geltungsbereich der exakten Wissenschaften ausgeschlossen werden“.⁹ Alle drei Autoren werden sich davor hüten, den von Schüller unterstellten naturalistischen Fehlschluss zu begehen.¹⁰

In seinen Abschnitten neun und zehn stellt Schüller seine eigene These zur Bedeutung der Erde und der auf ihr stattfindenden Ereignisse vor. Diese Schüller'sche These basiert auf der Erkenntnis, dass „Bedeutung“ eine *relationale* Eigenschaft ist (*jemandem ist etwas von Bedeutung*). Nachdem Schüller meint gezeigt zu haben, dass sowohl innerhalb der monotheistischen Religion als auch innerhalb des Naturalismus „Bedeutung“ keine *relationale* Eigenschaft sei, fällt es ihm auch nicht schwer, sich nun von diesen abzugrenzen. Allerdings bleibt schon im Falle der monotheistischen Religion der *relationale* Charakter von „Bedeutung“ erhalten, denn die Erde und die auf ihr stattfindenden Ereignisse erhalten erst vom Gott der Re-

ligion im Rahmen dessen Heilsplans eine Bedeutung. Ob dieser Gott wiederum eine absolute und objektive Werte darstellen soll, oder nicht, spielt für den *relationalen* Charakter keine Rolle. Der Vertreter einer monotheistischen Religion begeht nicht den Fehler, den Begriff „Bedeutung“ falsch zu interpretieren. Sein Fehler liegt vielmehr darin, dass er mit seinem Gott eine Letztbegründung für eigene Bedeutungszuschreibungen der Wirklichkeit behauptet.¹¹ Beim Naturalismus fehlt nun dieser Gott, und damit auch jegliche über die Erde hinausgehende (metaphysische oder kosmologische) Bedeutung. Anders formuliert, da die Voraussetzung für metaphysische oder kosmologische Bedeutung fehlt (die Relation), kann ohne weiteres gefolgert werden, dass die Erde und die auf ihr stattfindenden Ereignisse metaphysisch oder kosmologisch bedeutungslos sind. Dieser Schluss widerspricht nicht einmal Schüllers These, der wir uns im Folgenden widmen wollen.

Schüller drückt sich nicht eindeutig aus. Er schreibt: „Aus diesem Blickwinkel“ (in Hinblick auf die relationalen Eigenschaft von „Bedeutung“) „ist die Erde mitsamt ihrer Bevölkerung in der Tat das Sinnzentrum des Kosmos, ...“. Er verwendet in seinem Text häufig die Wörter „objektiv“ und „Objektivität“, allerdings weiß der Leser nicht, was Schüller damit genau meint. Weiter ist unklar, ob für Schüller die Redewendung „in der Tat“ im oben zitierten Satz gleichbedeutend mit seiner Vorstellung von „objektiv“ ist. Im Folgenden sollen mehrere Möglichkeiten untersucht werden.

Zunächst wollen wir annehmen dass Schüllers „in der Tat“ oben gleichbedeutend ist mit „objektiv“, und auf die Definition von Karl Popper zurückgreifen. In

seiner Logik der Forschung schreibt Popper zunächst treffend: „Die Worte >objektiv< und >subjektiv< gehören zu jenen philosophischen Ausdrücken, die durch widerspruchsvollen Gebrauch und durch unentschiedene, oft uferlose Diskussionen stark belastet sind.“¹² Nach seiner Definition liegt die *Objektivität* der wissenschaftlichen Sätze darin, dass sie *intersubjektiv kritisierbar* sein müssen.¹³ Außerdem finden wir, dass „subjektive Überzeugungserlebnisse niemals die Wahrheit wissenschaftlicher Sätze begründen, sondern innerhalb der Wissenschaft nur die Rolle eines Objekts der wissenschaftlichen, nämlich empirisch-psychologischen Forschung spielen können.“¹⁴ Nun hat Schüller aber festgestellt, dass „Bedeutung“ eine relationale Eigenschaft ist, die nur durch ein solches subjektives Überzeugungserlebnis festgestellt werden kann. Wird „Objektivität“ im Sinne von Popper verstanden, so kann aus Schüllers „Blickwinkel“ nicht geschlossen werden, die Erde und die auf ihr stattfindenden Ereignisse seien objektiv bedeutend.

Soll Schüllers „in der Tat“ oben nicht gleichbedeutend mit „objektiv“ sein, und möchte man eine dritte Möglichkeit ausschließen, so lautete seine These sinngemäß: Die Erde und alle auf ihr stattfindenden Ereignisse sind *subjektiv* von Bedeutung, weil sie subjektiv von Bedeutung sind. Dann wäre die These eine Tautologie und somit trivial.

In seinem letzten Abschnitt deutet Schüller an, dass es noch eine dritte Möglichkeit geben müsse. Er schreibt: „Es ist also die Ebene des Sozialen und nicht die Ebene des Weltalls, die bei der Analyse von Bedeutung zu betrachten wäre.“ Doch dies widerspricht dem naturalistischen Weltbild der von Schüller kritisierten Autoren nicht

unbedingt. So schreibt Kanitscheider: „Vielleicht ist es ja wirklich so, dass man in verschiedenen Sachzusammenhängen am besten mit einem unterschiedlichen Wahrheitsbegriff auskommt: in den Naturwissenschaften die Übereinstimmung eines Satzes mit der Wirklichkeit, in den Sozialwissenschaften die Zustimmung aller Beteiligten und im Alltag die Überflüssigkeit, da ohnehin nicht auf der linguistischen Metaebene reflektiert wird.“¹⁵

Um die Ergebnisse unserer Kritik zusammenzufassen: Schüllers Versuch den Naturalismus (in der Version der von Schüller kritisierten Autoren) auf eine Stufe mit religiösen Behauptungen zu stellen, wenn es um Sinn- und Wertzuschreibungen der Erde und der auf ihr stattfindenden Ereignisse geht, ist fehlgeschlagen. Schüllers Vorwurf, die „Bedeutungslosigkeit der Erde“ würde von den Naturalisten als „objektive, auf wissenschaftlichen Befunden fußende Tatsache“ präsentiert werden, hat sich als Fehlinterpretation von Seiten Schüllers herausgestellt. Schüllers eigene These, die der Erde und der auf ihr stattfindenden Ereignisse „in der Tat“ Bedeutung verleihen soll, wurde als entweder falsch, trivial, oder widerspruchsfrei zur „naturalistischen These“ entlarvt – je nach Interpretation von Schüllers Ausdruck „in der Tat“. Damit ist es Schüller nicht gelungen, sich von den Ansichten der von ihm kritisierten Vertreter des Naturalismus abzugrenzen.

Dennoch kann man Schüllers Aufsatz als Warnung an all jene Naturalisten ansehen, die wissenschaftliche Ergebnisse dazu missbrauchen, eine eigene und neue, „absolut“ geltende Weltanschauung zu stützen.

Anmerkungen:

¹ Schüller, Klaas: *Nur ein ‚Staubkorn im Weltall‘?*

In: *Aufklärung und Kritik* 1/2012 S. 243-248.

² Vollmer, Gerhard: *Auf der Suche nach Ordnung. Beiträge zu einem naturalistischen Welt- und Menschenbild.* Hirzel Verlag Stuttgart 1995, S. 43-59.

³ Kanitscheider, Bernulf: *Die Materie und ihre Schatten.* Naturalistische Wissenschaftsphilosophie. Alibri Verlag Aschaffenburg 2007, S. 206-210.

⁴ Schmidt-Salomon, Michael: *Manifest des evolutionären Humanismus. Plädoyer für eine zeitgemäße Leitkultur.* Alibri Verlag Aschaffenburg 2005, S. 10-12.

⁵ Schmidt-Salomon, Michael: *Jenseits von Gut und Böse. Warum wir ohne Moral die besseren Menschen sind.* Pendo Verlag München 2009, S. 309.

⁶ Kanitscheider, Bernulf: *Die Materie und ihre Schatten*, a. a. O. S. 211.

⁷ Vollmer, Gerhard: *Auf der Suche nach Ordnung*, a. a. O., S. 24, siehe auch S. 29.

⁸ Kanitscheider, Bernulf: *Die Materie und ihre Schatten*, a. a. O., S. 200.

⁹ Schmidt-Salomon, Michael: *Manifest des evolutionären Humanismus. Plädoyer für eine zeitgemäße Leitkultur.* Alibri, Aschaffenburg 2005, S. 44.

¹⁰ Vgl. Kanitscheider, Bernulf: *Die Materie und ihre Schatten*, a. a. O., S. 91ff.

¹¹ Vgl. Hans Albert, *Das Elend der Theologie*, Alibri Verlag Aschaffenburg 2005, S. 166f.

¹² Popper, Karl: *Logik der Forschung*, Mohr Siebeck Verlag Tübingen 2005, S. 21.

¹³ Vgl. Popper, Karl: *Logik der Forschung*, a. a. O., S. 21 und Fußnote 36.

¹⁴ Popper, Karl: *Logik der Forschung*, a. a. O., S. 23.

¹⁵ Kanitscheider, Bernulf: *Die Materie und ihre Schatten*, a. a. O., S. 40.

Zum Autor:

Johannes Kimling hat an der Universität Konstanz Physik studiert und arbeitet derzeit am Institut für Angewandte Physik der Universität Hamburg an seiner Doktorarbeit.

C Supporting Information [Hamd 13]

Thermoelectric Characterization of Bismuth Telluride Nanowires,
Synthesized Via Catalytic Growth and Post-Annealing
-Supporting Information-

Reprinted with permission from

Bacel Hamdou*, Johannes Kimling*, August Dorn, Eckhard Pippel,
Raimar Rostek, Peter Woias, and Kornelius Nielsch

Advanced Materials, **25**, 239 (2013)

Copyright 2013 by the WILEY-VCH Verlag GmbH & Co. KGaA, Weinheim.

The contributions of each author to the research study are indicated in the table below using the following specifications: Conception of the research study (1), sample preparation (2), measurements (3), data analysis (4), interpretation (5), and composition of the manuscript (6).

BH	JK	AD	EP	RR	PW	KN
1,2,3,4,5	1,3,4,5,6	5	3,4,5	2	1	1

* Both authors contributed equally to the research study.

Submitted to
**ADVANCED
MATERIALS**

Supporting Information

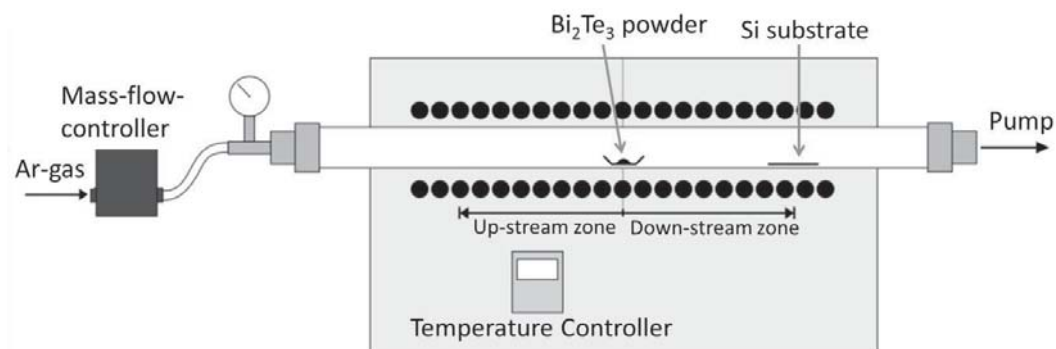


Figure S1. Scheme of the tube furnace used for the vapor-liquid-solid growth of Bi_2Te_3 nanowires.

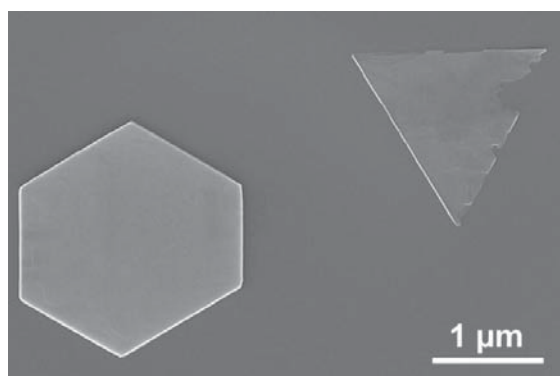


Figure S2. SEM images of nanoplates which grow in the absence of catalyst nanoparticles.

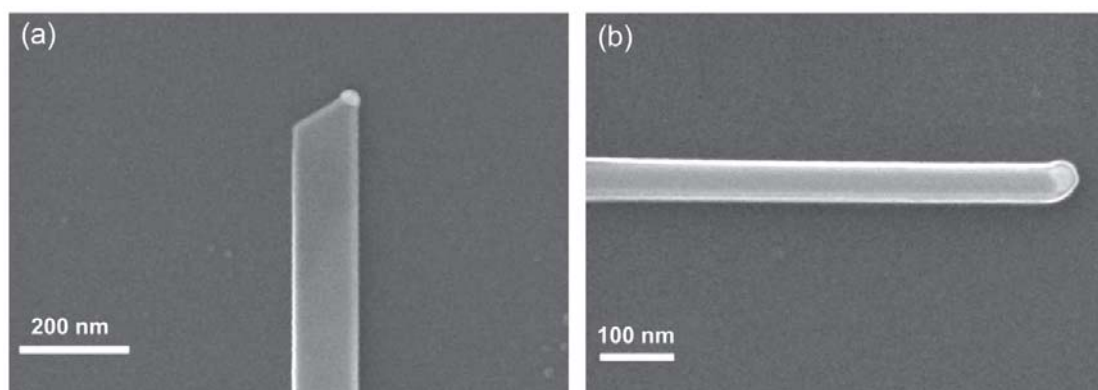


Figure S3. SEM images of a flat nanowire (a) and a cylindrical nanowire (b).

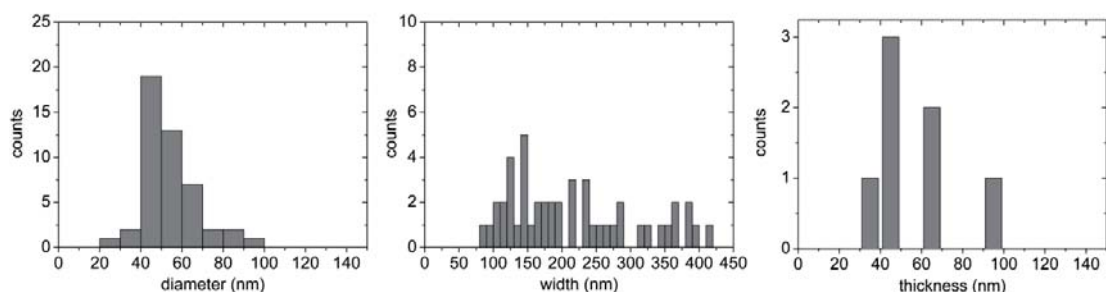


Figure S4. Statistical distributions of the diameter of cylindrical nanowires (a), the width of flat nanowires (b), and the thickness of flat nanowires (c). For (a) and (b) the total number of counts was 50, while for (c) due to the slowness of scanning force microscopy, the total number of counts was reduced to seven.

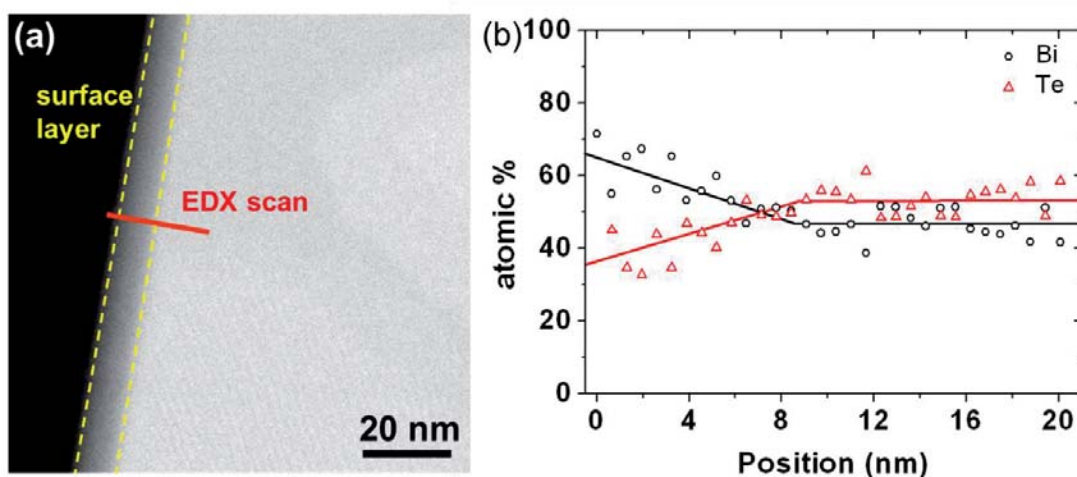


Figure S5. (a) HAADF-STEM (high angle annular dark field scanning transmission electron microscopy) image of an as-grown NW indicating the EDX-line-scan shown in (b). We observe a Bi-rich surface layer of about 10 nm (b).

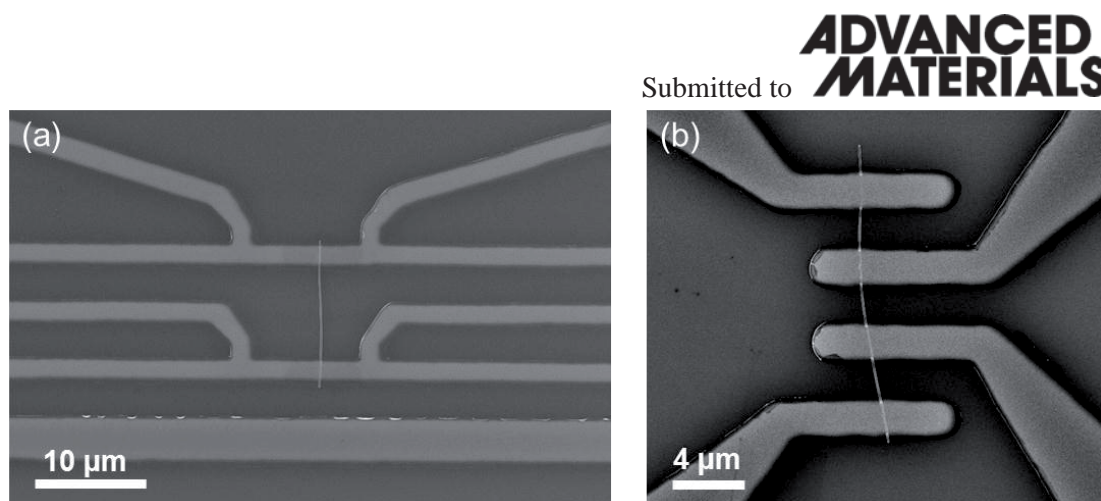


Figure S6. SEM images of: (a) Micro-device for Seebeck measurements on individual NWs. The NW is electrically connected to two four-point resistance thermometer. Adjacent to thermometer 1 runs a heater line which is used to generate a temperature gradient across the NW. (b) Four-probe configuration for determining the electrical resistivity of a NW without the influence of contact resistances between metal leads and NW.

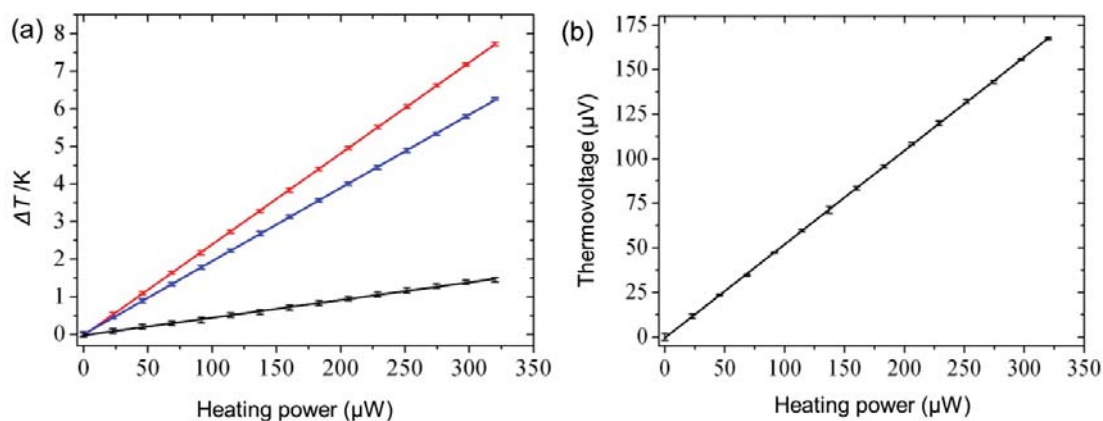


Figure S7. Performance of a Seebeck-device fabricated on a glass substrate. (a) Temperature increase vs applied heating power of thermometer 1, which is adjacent to the heater line, (red curve) and thermometer 2 (blue curve). The black curve gives the temperature difference between both thermometers. (b) Resulting thermovoltage vs applied heating power for an annealed NW.

D Supplemental Material [Kiml 13a]

Anisotropic Magnetoresistance in Ni Nanowires -Supplemental Material-

Reprinted with permission from

Johannes Kimling, Johannes Gooth, and Kornelius Nielsch

Physical Review B **87**, 094409 (2013)

Copyright 2013 by the American Physical Society.

The contributions of each author to the research study are indicated in the table below using the following specifications: Conception of the research study (1), sample preparation (2), measurements (3), data analysis (4), interpretation (5), and composition of the manuscript (6).

JK	JG	KN
1,2,3,4,5,6	2	1

I. FIELD DEPENDENCE OF $U_{3\omega}(H)$ AND $U_{1\omega}(H)$ AT DIFFERENT TEMPERATURES

Figure 1 depicts measurement data of $U_{3\omega}(H)$ (a) and $U_{1\omega}(H)$ (b) of sample NW1 at different temperatures. The upper (lower) curves shown in the graphs were measured for fields applied parallel (perpendicular) to the wire axis. For each temperature T_i the relation $U_{1\omega}(H, T_i) = R(H, T_i)I$ is used to determine the saturation resistances $R^\perp(T_i)$, $R^\parallel(T_i)$, and $\Delta R = R^\parallel(T_i) - R^\perp(T_i)$. It can be seen from Fig 1 (b) that the ratio $R(H = 0)/R^\perp$ increases as the temperature rises.** This means that the remanence magnetization parallel to the wire axis increases as the temperature rises. The magnetization configuration of Ni nanowires in the absence of external fields is determined by a competition between the shape anisotropy and the magnetocrystalline anisotropy. The observed behavior can be explained by the magnetocrystalline anisotropy of Ni, which decreases as the temperature rises.³⁵

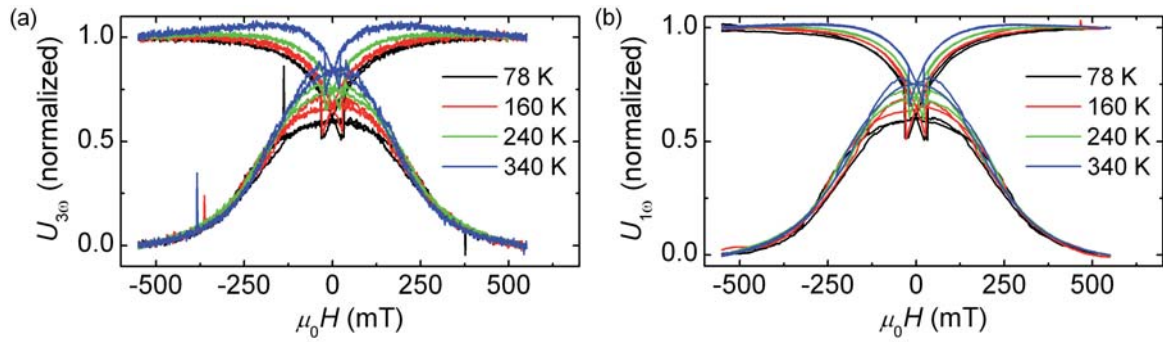


FIG. 1. (Color online) Field dependence of $U_{3\omega}(H)$ and $U_{1\omega}(H)$ of sample NW1 measured at different temperatures.

II. ERROR ANALYSIS

In this section we give a quantitative comparison of the different contributions to the total error of the AMTR ratio shown in Fig. 4 of the main text. The AMTR ratio is defined in Eq. (10) of the main text. Table I lists the relative errors of $U_{3\omega}$ and $U_{1\omega}$, averaged over all measurements at saturation fields. The relative error is the same for both field directions (parallel and perpendicular to the wire axis). It is defined to be $\frac{\sigma}{\langle U_{x\omega} \rangle}$, where σ is the standard deviation of the measurement data, and $\langle U_{x\omega} \rangle$ is the mean value of the measurement data.

TABLE I.

	$U_{3\omega}$	$U_{1\omega}$
Relative error (%)	0.05 ± 0.02	0.01 ± 0.009

Figure 2 depicts dR^\perp/dT (a) and $d\Delta R/dT$ (b) plotted against the temperature as determined from the polynomial fits of second order to the $R^\perp(T)$ and $\Delta R(T)$ data (see Fig. 2 (c) and (d) in the main text). The graphs include error bars that were calculated from the standard deviations of the fit parameters considering Gaussian error propagation.

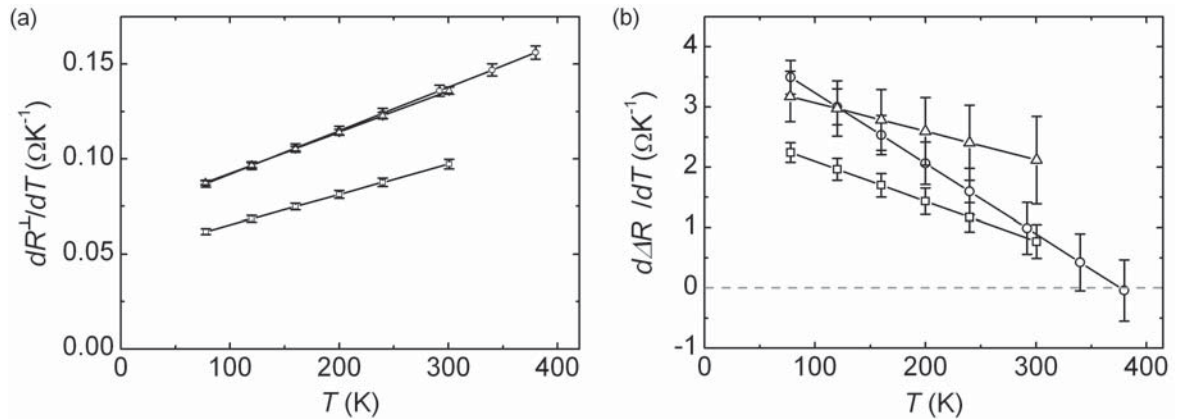


FIG. 2. Field dependence of $U_{3\omega}(H)$ and $U_{1\omega}(H)$ of sample NW1 measured at different temperatures.

* johannes.kimling@physik.uni-hamburg.de

³⁵ J. J. M. Franse and G. de Vries, Physica 39, 477 (1968).

** There is an error: the meant ratio is $(R(H = 0) - R^\perp)/R^\perp$.

E Experimental Details

Micro-Manipulated Probestations

The samples are connected to the measuring setup using two micro-manipulated probestations from LakeShore. The LakeShore TTPX model provides six low-frequency micro probes that can be moved across an area of about $30 \times 30 \text{ mm}^2$. The Lakeshore EMPX model provides four low-frequency micro probes and allows for applying in-plane fields of up to 550 mT. The sample chambers of both models can be evacuated below 1×10^{-5} mbar by a turbo molecular pump. Both probestations include a cryostat for cooling with liquid nitrogen or liquid helium. The sample stage can be stabilized at temperatures between 4 and 450 K with deviations below 50 mK. Both models are equipped with a pneumatic vibration isolation system.

An advantage over wire bonding is that many structures can be investigated consecutively without removing of the sample. However, the maximum number of contacts to one sample is limited by the number of micro probes. Another drawback is that measurements during temperature sweeps are not possible, because the components of the probe arms are extending as the temperature rises. A big issue with probestations is condensation on the sample during cooling, which results in unreliable contacts between probe tip and contact pad. Evacuating the sample chamber to the minimum pressures reachable with the system (about 1×10^{-7} mbar) is not sufficient to prevent condensation. The solution to this problem was to favor condensation on the radiation shields instead of the sample stage. This can be achieved by maintaining the temperature of the sample stage above room temperature during cooling of the system, until the radiation shields reached temperatures well below 0°C .

For measurements on nanowires, due to the small cross-sectional area of nanowires, small voltages can generate high current densities that may destroy parts of the nanowire (see Fig. E.1). Therefore, extreme care has to be taken concerning electrostatic discharges (e.g., when touching the measurement devices), transient voltages (e.g., when switching on or off of electrical equipment), and possible ground loops that may pick-up noise.

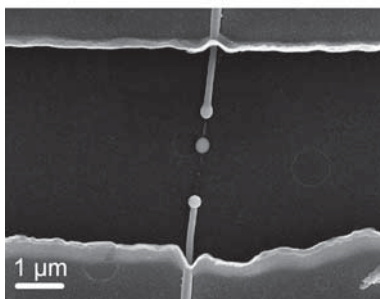


Figure E.1: Scanning electron micrograph of a destroyed Ni nanowire.

Process Parameters

Table E.1: Preparation of anodized aluminum oxide membranes.

Process		Parameters
1	Degrease Al foil with C ₂ H ₅ OH	2 min with tissue
2	Electropolish in HClO ₄ :C ₂ H ₅ OH (25:75 vol%)	20V, 10°C, 4 min
3	0.3 M H ₂ SO ₄	25 V, 8 °C, 24 h
	0.3 M H ₂ C ₂ O ₃	40 W, 8 °C, 24 h
	1 w% H ₃ PO ₄	195 V, -5 °C, 18h
3	Dissolve oxide film in H ₃ PO ₄ :H ₂ CrO ₄ :H ₂ O (1.8:6:92.2 w%)	45 °C, 24 h
4	0.3 M H ₂ SO ₄	25 V, 8 °C, 7 h
	0.3 M H ₂ C ₂ O ₃	40 W, 8 °C, 15 h
	1 w% H ₃ PO ₄	195 V, -5 °C, 25 h
5	37 w% HCl (100 ml)	23°C, ~30 min
	6.8 g CuCl ₄	
	100 ml H ₂ O	
6	Open pores in H ₃ PO ₄	32°C, ~10 min

Table E.2: Electrodeposition of Ni nanowires in AAO membranes.

Process		Parameters	
1	Prepare electrolyte [Watt 16]	NiSO ₄ · 6H ₂ O	30 w%
		NiCl ₂ · 6H ₂ O	4.5 w%
		H ₃ BO ₃	4.5 w%
2	Potentiostatic deposition	-1.2 V, 30°C, ~1 h	
3	Dissolve AAO membrane	H ₃ PO ₄ :H ₂ CrO ₄ :H ₂ O 1.8:6:92.2 w% 45 °C, ~120 h	

Table E.3: Preparation of Si₂N₃ membranes from Si substrates covered with low-stress Si₂N₃ on both sides. Before step 1, the sample was dried on a hot plate at 160 °C for 2 min. After step 4, the sample was rinsed with H₂O and blow-dried with N₂; after step 10, the sample was rinsed with isopropanol and H₂O, followed by blow-drying with N₂. The thickness of the Si₂N₃ layers is 1.5 μm, the thickness of the Si substrate is 530 μm.

Process		Parameters
1	Spin-coat ma-P 1205 resist (micro resist techn.)	500 rpm, 5 s, ramp 30 3500 rpm, 30 s, ramp 155
2	Soft-bake on hot plate	100 °C, 30 s
3	Exposure Mask aligner (Karl Süss MJB3)	280 W, 4 s
4	Development in ma-D 331 (micro resist techn.)	30 s
5	Reactive-ion etching of Si ₂ N ₃ (Sentech SI-220)	CHF ₃ 25 sccm, 10 mTorr, 75 W
6	Wet-chemical etching of Si	35 w.% KOH 70°C

Table E.4: Preparation of Si substrates with micrometer-sized trenches. Before step 1, the sample was dried on a hot plate at 160 °C for 2 min. After step 4, the sample was rinsed with H₂O and blow-dried with N₂; after step 10, the sample was rinsed with isopropanol and H₂O, followed by blow-drying with N₂.

Process		Parameters
1	Spin-coat ma-P 1205 resist (micro resist techn.)	500 rpm, 5 s, ramp 30 3500 rpm, 30 s, ramp 155
2	Soft-bake on hot plate	100 °C, 30 s
3	Exposure Mask aligner (Karl Süss MJB3) Laser (Heidelberg Instruments, μpg101)	280 W, 4 s 15 W, 65%
4	Development in ma-D 331 (micro resist techn.)	30 s
5	Reactive-ion etching (Sentech SI-220)	CHF ₃ 25 sccm, 10 mTorr, 75 W, 30 min CF ₄ /O ₂ 25/3.1 sccm, 100 mTorr, 100 W, 13 min
6	Ar- <i>rf</i> -magnetron sputtering of SiO ₂ (Torr CRC-600)	7.43 mTorr, 300 W, 25 min

Table E.5: Definition of Au contacts. Before step 1, nanowires were transferred to the sample, followed by a careful rinse with isopropanol, blow-drying with N₂, and drying on a hot plate at 160 °C for 2 min. After step 6, the sample was rinsed with H₂O and blow-dried with N₂; after step 10, the sample was rinsed with isopropanol and H₂O, followed by blow-drying with N₂. ((*) Sputtering was done in a sputter chamber in the clean room facility of the Institute of Applied Physics, University of Hamburg [Pels 04]. This sputter process is rather anisotropic (due to the relatively large active sputter area at the target and the centering of the sample below this area) and therefore avoids shadowing effects.

Process		Parameters
1	Spin-coat LOR 3B resist (MicroChem Corp)	500 rpm, 5 s, ramp 30 3500 rpm, 45 s, ramp 155
2	Soft-bake on hot plate	160 °C, 5 min
3	Spin-coat ma-P 1205 resist (micro resist techn.)	500 rpm, 5 s, ramp 30 3500 rpm, 30 s, ramp 155
4	Soft-bake on hot plate	100 °C, 30 s
5	Exposure Optical microscope	max, yellow, 0, 0, 45 s
	Laser (Heidelberg Instruments, μ pg101)	15 W, 65%
6	Development ma-D 331 (micro resist techn.)	30 s
	Microposit mf-319 (Shipley)	2 s
7	Ar-sputter etching (*)	0.01 mbar, 20 W, 5 min
8	Ar- <i>dc</i> -magnetron sputtering of Al (*)	0.01 mbar, 30 W, \sim 2 nm
9	Ar- <i>dc</i> -magnetron sputtering of Au (*)	0.01 mbar, 10 W, \sim 200 nm
10	Lift-off in Microposit Remover 1165 (Shipley)	45 °C, 24 h

Table E.6: Definition of Pt contacts. Before step 1, nanowires were transferred to the sample, followed by a careful rinse with isopropanol, blow-drying with N₂, and drying on a hot plate at 160 °C for 2 min. After step 6,, the sample was rinsed with H₂O and blow-dried with N₂; after step 10, the sample was rinsed with isopropanol and H₂O, followed by blow-drying with N₂. The sputter deposition of Pt was done in a Torr CRC-600 sputter coater, which was modified for allowing sputter etching at the sample. This modification forbids rotating the sample holder. Due to the tilted sputter head and the sample neither centered below the active sputter area at the target, nor aligned parallel to the target, the sputter process is rather isotropic and may lead to inhomogeneities of the deposited film due to shadowing effects.

Process		Parameters
1	Spin-coat LOR 3B resist (MicroChem Corp)	500 rpm, 5 s, ramp 30 3500 rpm, 45 s, ramp 155
2	Soft-bake on hot plate	160 °C, 5 min
3	Spin-coat ma-P 1205 resist (micro resist techn.)	500 rpm, 5 s, ramp 30 3500 rpm, 30 s, ramp 155
4	Soft-bake on hot plate	100 °C, 30 s
5	Exposure Optical microscope Laser (Heidelberg Instruments, μ pg101)	max, yellow, 0, 0, 45 s 15 W, 65%
6	Development ma-D 331 (micro resist techn.) Microposit mf-319 (Shipley)	30 s 2 s
7	Ar-sputter etching (Torr CRC-600)	7.43 mTorr, 20 W, 10 min
8	Ar- <i>rf</i> -magnetron sputtering of Ti (Torr CRC-600)	7.43 mTorr, 80 W, \sim 5 nm
9	Ar- <i>dc</i> -magnetron sputtering of Pt (Torr CRC-600)	7.43 mTorr, 50 A, \sim 150 nm
10	Lift-off in Microposit Remover 1165 (Shipley)	45 °C, 24 h

Table E.7: Definition of Pt heater lines and thermometers. Before step 1, nanowires were transferred to the sample, followed by a careful rinse with isopropanol, blow-drying with N₂, and drying on a hot plate at 160 °C for 2 min. After step 6, the sample was rinsed with H₂O and blow-dried with N₂; after step 10, the sample was rinsed with isopropanol and H₂O, followed by blow-drying with N₂. The sputter deposition of Pt was done in a Torr CRC-600 sputter coater, which was modified for allowing sputter etching at the sample. This modification forbids rotating the sample holder. Due to the tilted sputter head and the sample neither centered below the active sputter area at the target, nor aligned parallel to the target, the sputter process is rather isotropic and may lead to inhomogeneities of the deposited film due to shadowing effects.

Process		Parameters
1	Spin-coat LOR 3B resist (MicroChem Corp)	500 rpm, 5 s, ramp 30 3500 rpm, 45 s, ramp 155
2	Soft-bake on hot plate	160 °C, 5 min
3	Spin-coat ma-P 1205 resist (micro resist techn.)	500 rpm, 5 s, ramp 30 3500 rpm, 30 s, ramp 155
4	Soft-bake on hot plate	100 °C, 30 s
5	Exposure Laser (Heidelberg Instruments, μ pg101)	15 W, 65%
6	Development ma-D 331 (micro resist techn.) Microposit mf-319 (Shipley)	30 s 2 s
7	Ar-sputter etching (Torr CRC-600)	7.43 mTorr, 20 W, 10 min
8	Ar- <i>rf</i> -magnetron sputtering of Ti (Torr CRC-600)	7.43 mTorr, 80 W, \sim 5 nm
9	Ar- <i>dc</i> -magnetron sputtering of Pt (Torr CRC-600)	7.43 mTorr, 50 A, \sim 150 nm
10	Lift-off in Microposit Remover 1165 (Shipley)	45 °C, 24 h

Table E.8: Preparation of the Co/Cu multilayer sample for 3ω measurements. The entire sample fabrication was accomplished by Dr. Karsten Rott in the group of Prof. Günter Reiss at the University of Bielefeld.

Process		Parameters
1	Ar- <i>dc</i> -magnetron sputtering	Co Cu 1.5×10^{-3} mbar, 115 W
2	Ar/O ₂ - <i>dc</i> -sputtering	TaO _x 1.5×10^{-3} mbar, 50 W
3	Ar- <i>dc</i> -sputtering	Ta/Au 1.5×10^{-3} mbar, 25 W
4	Spin-coat	e-beam resist 40nm
5	e-beam exposure and development	
6	Ar-Ion etching of the Ta/Au layer	Controlled using a mass spectrometer
8	Lift-off	

```

function [Z, Tsim] = Heater_on_Substrate(f,b,L,I,R)
% Simulation of the temperature oscillations of a heater line on a substrate during 3 omega
% measurements.
% f: frequency array, b: heater half width, L: heater length, I: current amplitude, R: heater resistance.
format long g;
Pm=[1 1052 2203 550e-6]; % [thermal conductivity W/(mK) heat capacity J/(kg K) density kg/m^3
                        thickness m] of the substrate.
[n m]=size(Pm); % n: Number of layers, m: number of parameters
Dv = 8E-7; % Thermal diffusivity of the substrate; I varied this value manually for
           obtaining a good fit to the measurement data
TM=6; % TM ==  $4\pi H_e \rho C_e$  in the denominator of Eq. (3) in Ref. [Olso 05]
           (measure of the thermal mass)
x=[0:0.001:8*pi]; % Integration interval
x(1)=1e-22; % Avoid dividing by zero
Lx = length(x);
dx = abs(x(3)-x(2));
simpson=zeros(1,Lx);
simpson(1)=1;
for i=1:2:Lx-2
simpson(i+1)=4;
simpson(i+2)=2;
end
simpson(Lx)=1;
simpson=simpson*dx/3; % calculation of the coefficients of the Simpson rule for integration

for ii=1:length(f)
Phi=complex((x/b).^2, 4*pi*f(ii)/Dv(1));
Phi=sqrt(Phi); % Eq. (6) in Ref. [Olso 05]
z(1,1:length(x))=-1./(Pm(1,1)*Phi); % semi-infinite boundary conditions
% z(1,1:length(x))=-1./(Pm(1,1)*Phi.*1./tanh(Phi*Pm(1,4))); % adiabatic boundary conditions
% z(1,1:length(x))=-1./(Pm(1,1)*Phi).*tanh(Phi*Pm(1,4)); % isothermal boundary conditions
for jj=2:n
Phi=complex((x/b).^2, 4*pi*f(ii)/Dv(jj)); %kx = ky !!
Phi=sqrt(Phi);
z(jj,1:length(x))=1./(Pm(jj,1)*Phi).*(Pm(jj,1)*Phi.*z(jj-1,:)-tanh(Phi.*Pm(jj,4)))./(1-(Pm(jj,1)*Phi.*z(jj-1,:)).*tanh(Phi.*Pm(jj,4))); % Eq. (5) in Ref. [Olso 05]
end
Za(ii)=2*z(n,:).*sin(x).^2./(x.^2*pi)*simpson'; % Eq. (4) in Ref. [Olso 05]
Z(ii)=1/(1/Za(ii)-1)*f(ii)*TM; % Eq. (3) in Ref. [Olso 05]
end
Tsim = -Z*R*I^2/(4*b*L);

user_entry = input('Save Data? Then enter "1"');
if user_entry==1
[file,path] = uiputfile('Sim.dat','Save as...');
RTsim=real(Tsim);
ITsim=imag(Tsim);
ATsim=[log(f) RTsim ITsim];
save([path,file],'ATsim','-ASCII','-tabs');
end

```

```

function [Tsim,NVAL] = Heater_on_Film_on_Substrate(f,RdT,IdT,R,b,L,I)
% Simulation of the temperature oscillations of a heater line on thinfilm on a substrate during 3 omega
% measurements.
% f: frequency array, RdT: Amplitude of the real part of the measured temperature oscillations, IdT:
% Amplitude of the imaginary part of the measured temperature oscillations, R: heater resistance, b: heater
% half width, L: heater length, I: current amplitude.
format long;
Pm=[1 1052 2203 550e-6; 20 1 1 162.05e-9];
      % [thermal conductivity W/(mK)  heat capacity J/(kg K)  density kg/m^3  thickness m] of the
      % substrate (first row) and of the thin film (second row)
[n m]=size(Pm);      % n: Number of layers, m: number of parameters
Dv = [8.5E-7 4E-5];  % Thermal diffusivity of the substrate and of the thin film;
os= -0.01;          % Offset start value (should not be zero)
TM=5.5;            % TM == 4*pi H_e \rho C_e in the denominator of Eq. (3) in Ref. [Olso 05]
                    % (measure of the thermal mass)
x=[0:0.001:8*pi];  % Integration interval
x(1)=1e-22;        % Avoid dividing by zero
Lx = length(x);
dx = abs(x(3)-x(2));
simpson=zeros(1,Lx);
simpson(1)=1;
for i=1:Lx-2
simpson(i+1)=4;
simpson(i+2)=2;
end
simpson(Lx)=1;
simpson=simpson*dx/3;  % calculation of the coefficients of the Simpson rule for integration

for it=1:6          % number of iterations for fit
    lll=length(f);
    for ii=1:lll;
        Phi(1,1:length(x))=complex((x/b).^2, 4*pi*f(ii)/Dv(1));      % Eq. (6) in Ref. [Olso 05]
        Phi(1,1:length(x))=sqrt(Phi(1,:));
        z(1,1:length(x))=-1./(Pm(1,1)*Phi(1,:));      % semi infinite boundary conditions
        %z(1,1:length(x))=-1./(Pm(1,1)*Phi(1,:)).*1./tanh(Phi(1,:)*Pm(1,4)); % adiabatic boundary conditions
        %z(1,1:length(x))=-1./(Pm(1,1)*Phi(1,:)).*tanh(Phi(1,:)*Pm(1,4)); % isothermal boundary conditions
        S(1,1:length(x))=0;
        for jj=2:n
            Phi(jj,1:length(x))=complex((x/b).^2, 4*pi*f(ii)/Dv(jj));  % kx = ky !! Eq. (6) in Ref. [Olso 05]
            Phi(jj,1:length(x))=sqrt(Phi(jj,:));
            z(jj,1:length(x))=1./(Pm(jj,1)*Phi(jj,:)).*(Pm(jj,1)*Phi(jj,:).*z(jj-1,:)-tanh(Phi(jj,:)*Pm(jj,4))./(1-
            (Pm(jj,1)*Phi(jj,:)).*z(jj-1,:)).*tanh(Phi(jj,:)*Pm(jj,4)));  % Eq. (5) in Ref. [Olso 05]
            S(jj,1:length(x))=(1-Pm(jj,1)^2*Phi(jj,:).^2.*z(jj,:).^2)./(1-Pm(jj,1)^2*Phi(jj,:).^2.*z(jj-1,:).^2);
            % Eq.(11)
        end
        Za(ii)=2*z(n,:).*sin(x).^2./(x.^2*pi)*simpson';      % Eq. (4) in Ref. [Olso 05]
        Z(ii)=1/(1/Za(ii)-1*f(ii)*TM);      % Eq. (3) in Ref. [Olso 05]
        Tsim(ii) = -Z(ii)*R*I^2/(4*b*L);
        Tsim(ii) = Tsim(ii)-os;      % offset correction
    end
end

```

```

jj=2;

dzdk(1:length(x))=1/Pm(n,1)*(S(jj,:).*z(jj-1,:)-z(jj,:)); % Eq. (12) in Ref. [Olso 05]
dZdk(ii)=2*dzdk.*sin(x).^2./(x.^2*pi)*simpson'; % Eq. (10) in Ref. [Olso 05]
dTsimdk(ii)=-dZdk(ii)*R*I^2/(4*b*L);
D(1,ii)=Pm(n,1)*dTsimdk(ii); % Eq. (16) in Ref. [Olso 05]
dTsimdos(1,ii) = -1;
D(2,ii) = os*dTsimdos(1,ii);
end
A=real(D)*real(D)'+imag(D)*imag(D)'; % Eq. (19) in Ref. [Olso 05]
% B=real(D)*(RZ-real(Z))'+imag(D)*(IZ-imag(Z))'; % Eq. (20) in Ref. [Olso 05]
B=real(D)*(RdI(1:lll)'-real(Tsim))'+imag(D)*(IdI(1:lll)'-imag(Tsim))';
c=A^(-1)*B; % Eq. (21) in Ref. [Olso 05]
Pm(n,1)=(c(1)*1+1)*Pm(n,1); % Eq. (22) in Ref. [Olso 05]
os = (c(2)*1+1)*os;
NVAL(it,1:2)=[Pm(n,1)',os];
end

if lll==length(f)
[file,path] = uinputfile('Sim_frequ.dat','Save as...');
RTsim=real(Tsim)';
ITsim=imag(Tsim)';
ATsim=[f RdI IdI RTsim ITsim];
save([path,file],'ATsim','-ASCII','-tabs');
end

```



```

function [TT,NVAL] = Heater_Field(f,RdT,IdT,R,b,L,I)
% Simulation of the temperature oscillations of a heater line on thinfilm on a substrate during field-dependent
% 3 omega measurements. This program is used within the program Heater_Field_master.m
% f: frequency array, RdT: Amplitude of the real part of the measured temperature oscillations, IdT:
% Amplitude of the imaginary part of the measured temperature oscillations, R: heater resistance, b: heater
% half width, L: heater length, I: current amplitude.
format long;
Pm=[1 1052 2203 550e-6; 20 1 1 162.05e-9];
      % [thermal conductivity W/(mK)  heat capacity J/(kg K)  density kg/m^3  thickness m] of the
      % substrate (first row) and of the thin film (second row)
[n m]=size(Pm);      % n: Number of layers, m: number of parameters
Dv = [8.5E-7 4E-5];  % Thermal diffusivity of the substrate and of the thin film;
os= -0.01;          %Offset start value (should not be zero)
TM=5.5;            % TM == 4*pi H_e \rho C_e in the denominator of Eq. (3) in Ref. [Olso 05]
                    % (measure of the thermal mass)
x=[0:0.001:8*pi];  % Integration interval
x(1)=1e-22;        % Avoid dividing by zero
Lx = length(x);
dx = abs(x(3)-x(2));
simpson=zeros(1,Lx);
simpson(1)=1;
for i=1:2:Lx-2
simpson(i+1)=4;
simpson(i+2)=2;
end
simpson(Lx)=1;
simpson=simpson*dx/3;  % calculation of the coefficients of the Simpson rule for integration

for it=1:6          % number of iterations for fit
Phi(1,1:length(x))=complex((x/b).^2, 4*pi*f(it)/Dv(1));  % Eq. (6) in Ref. [Olso 05]
Phi(1,1:length(x))=sqrt(Phi(1,:));
z(1,1:length(x))=-1./(Pm(1,1)*Phi(1,:));  % semi infinite boundary conditions
%z(1,1:length(x))=-1./(Pm(1,1)*Phi(1,:)).*1./tanh(Phi(1,:)*Pm(1,4)); % adiabatic boundary conditions
%z(1,1:length(x))=-1./(Pm(1,1)*Phi(1,:)).*tanh(Phi(1,:)*Pm(1,4)); % isothermal boundary conditions
S(1,1:length(x))=0;
for jj=2:n
Phi(jj,1:length(x))=complex((x/b).^2, 4*pi*f(it)/Dv(jj));  % kx = ky !! Eq. (6) in Ref. [Olso 05]
Phi(jj,1:length(x))=sqrt(Phi(jj,:));
z(jj,1:length(x))=1./(Pm(jj,1)*Phi(jj,:)).*(Pm(jj,1)*Phi(jj,:).*z(jj-1,:)-tanh(Phi(jj,:)*Pm(jj,4))./(1-
(Pm(jj,1)*Phi(jj,:).*z(jj-1,:)).*tanh(Phi(jj,:)*Pm(jj,4)));  % Eq. (5) in Ref. [Olso 05]
S(jj,1:length(x))=(1-Pm(jj,1)^2*Phi(jj,:).^2.*z(jj,:).^2)/(1-Pm(jj,1)^2*Phi(jj,:).^2.*z(jj-1,:).^2);
                    % Eq.(11)
end
Za(it)=2*z(n,:).*sin(x).^2./(x.^2*pi)*simpson';  % Eq. (4) in Ref. [Olso 05]
Z(it)=1/(1/Za(it)-1*f(it)*TM);  % Eq. (3) in Ref. [Olso 05]
Tsim(it) = -Z(it)*R*I^2/(4*b*L);
Tsim(it) = Tsim(it)-os;  % offset correction

```

```

jj=2;

dzdk(1:length(x))=1/Pm(n,1)*(S(jj,:).*z(jj-1,:)-z(jj,:));           % Eq. (12) in Ref. [Olso 05]
dZdk(ii)=2*dzdk.*sin(x).^2./(x.^2*pi)*simpson';                 % Eq. (10) in Ref. [Olso 05]
dTsimdk(ii)=-dZdk(ii)*R*I^2/(4*b*L);
Pm(n,1)=Pm(n,1)+(RdT-real(Tsim))/real(dTsimdk); %new values for new iteration
NVAL(it,1)=Pm(n,1)';
end
TT=Tsim;

```

```

function [H,kappa,T]=Heater_Field_master(data)

[RZ,IZ,RdT,IdT,R,b,L,I,f]=Measurement_data(data);
clear f;
f=89;
H=data(:,1);
Z=zeros(length(H));

for ii=1:length(H)
    [Tnew,NVAL] = Heater_Field(f,RdT(ii),IdT(ii),R,b,L,I);
    T(ii)=Tnew;
    kappa(ii)=NVAL(length(NVAL));
end

[file,path] = uiputfile('Sim_field_.dat','Save as...');
RTsim=real(T);
ITsim=imag(T);
ATsim=[H RTsim ITsim kappa];
save([path,file],'ATsim','-ASCII','-tabs');

function [RZ,IZ,RdT,IdT,R,b,L,I,f]=Measurement_data(data)
% data: Matrix with measurement data imported (see below)

R=56.57481; % Time-averaged resistance of the heater
dRdT=0.11032; % Temperature derivative of R
b=5E-6; % heater half-width
L=2e-3; % heater length
I=7e-3; % current amplitude

f=data(:,1); % Frequency values of the heating current

RZ=-8*b*L*data(:,2).*cos(data(:,4))/(R*I^3*dRdT); % Eq. (2) in Ref. [Ols02]
IZ=-8*b*L*data(:,2).*sin(data(:,4))/(R*I^3*dRdT);

RdT=-2*data(:,2).*cos(data(:,4))/(dRdT*I);
IdT=-2*data(:,2).*sin(data(:,4))/(dRdT*I);

```


Bibliography

- [Adac 13] H. Adachi, K. Uchida, E. Saitoh, and S. Maekawa. “Theory of spin Seebeck effect”. *Rep. Prog. Phys.*, Vol. 76, p. 036501, 2013. 2
- [Ashc 76] N. W. Ashcroft and N. D. Mermin. *Solid State Physics*. Thomson Learning, Inc., 1976. 8, 14, 18, 19, 70
- [Aus 94] M. J. Aus, B. Szpunar, U. Erb, A. M. El-Sherik, G. Palumbo, and K. T. Aust. “Electrical resistivity of bulk nanocrystalline nickel”. *J. Appl. Phys.*, Vol. 75, p. 3632, 1994. 58, 59
- [Aver 12] A. D. Avery, M. R. Pufall, and B. L. Zink. “Observation of the Planar Nernst Effect in Permalloy and Nickel Thin Films with In-Plane Thermal Gradients”. *Phys. Rev. Lett.*, Vol. 109, p. 196602, 2012. 2
- [Bade 10] S. Bader and S. Parkin. “Spintronics”. *Annu. Rev. Condens. Matter Phys.*, Vol. 1, p. 71, 2010. 2
- [Baib 88] M. N. Baibich, J. M. Broto, A. Fert, F. N. Van Dau, F. Petroff, P. Etienne, G. Creuzet, A. Friederich, and J. Chazelas. “Giant Magnetoresistance of (001)Fe/(001)Cr Magnetic Superlattices”. *Phys. Rev. Lett.*, Vol. 61, p. 2472, Nov 1988. 17
- [Banh 97] J. Banhart, H. Ebert, and A. Vernes. “Applicability of the two-current model for systems with strongly spin-dependent disorder”. *Phys. Rev. B*, Vol. 56, p. 10165, 1997. 15
- [Batt 07] J.-L. Battaglia, C. Wiemer, and M. Fanciulli. “An accurate low-frequency model for the 3ω method”. *J. Appl. Phys.*, Vol. 101, p. 104510, 2007. 38
- [Baue 10] G. E. Bauer, A. H. MacDonald, and S. Maekawa. “Spin Caloritronics”. *Solid State Commun.*, Vol. 150, No. 11–12, p. 459, 2010. 2
- [Baue 12] G. E. W. Bauer, E. Saitoh, and B. J. van Wees. “Spin caloritronics”. *Nat. Mater.*, Vol. 11, No. 5, p. 391, 2012. 2
- [Bhne 09] T. Böhnert. *Magneto-Widerstandsmessungen an fotolithografisch kontaktierten Nickel-Nanodrähten*. Master’s thesis, Diplomarbeit, Universität Hamburg, 2009. 53
- [Bina 89] G. Binasch, P. Grünberg, F. Saurenbach, and W. Zinn. “Enhanced magnetoresistance in layered magnetic structures with antiferromagnetic interlayer exchange”. *Phys. Rev. B*, Vol. 39, p. 4828, Mar 1989. 17
- [Bloc 28] F. Bloch. *Z. Phys.*, Vol. 52, p. 555, 1928. 13
- [Borc 01] T. Borca-Tasciuc, A. R. Kumar, and G. Chen. “Data reduction in 3ω method for thin-film thermal conductivity determination”. *Rev. Sci. Instrum.*, Vol. 72, No. 4, p. 2139, 2001. 38

- [Cahi 03] D. G. Cahill, W. K. Ford, K. E. Goodson, G. D. Mahan, A. Majumdar, H. J. Maris, R. Merlin, and S. R. Phillpot. “Nanoscale thermal transport”. *J. Appl. Phys.*, Vol. 93, p. 793, 2003. 39
- [Cahi 90] D. G. Cahill. “Thermal conductivity measurement from 30 to 750 K: the 3 omega method”. *Rev. Sci. Instrum.*, Vol. 61, No. 2, p. 802, 1990. 35, 37, 40
- [Cahi 94] D. G. Cahill, M. Katiyar, and J. R. Abelson. “Thermal conductivity of *a*-Si:H thin films”. *Phys. Rev. B*, Vol. 50, p. 6077, Sep 1994. 35, 37, 38
- [Caml 89] R. E. Camley and J. Barnas. “Theory of Giant Magnetoresistance Effects in Magnetic Layered Structures with Antiferromagnetic Coupling”. *Phys. Rev. Lett.*, Vol. 63, p. 664, 1989. 17
- [Cars 59] H. S. Carslaw and J. C. Jaeger. *Conduction of Heat in Solids*. Oxford Univ. Press, 1959. 36
- [Chen 05] G. Chen. *Nanoscale Energy Transport and Conversion*. Oxford Univ. Press, New York, 2005. vii, 19
- [Chow 09] I. Chowdhury, R. Prasher, K. Lofgreen, G. Chrysler, S. Narasimhan, R. Mahajan, D. Koester, R. Alley, and R. Venkatasubramanian. “On-Chip cooling by Superlattice-based Thin-Film Thermoelectrics”. *Nat Nanotechnol*, Vol. 4, p. 235, 2009. 1
- [Corn 11] J. E. Cornett and O. Rabin. “Thermoelectric figure of merit calculations for semiconducting nanowires”. *Applied Physics Letters*, Vol. 98, No. 18, p. 182104, 2011. 20
- [Czyc 08] G. Czycholl. *Theoretische Festkörperphysik*. Springer-Verlag Berlin Heidelberg, 2008. 12, 13, 14, 15
- [Dame 05] C. Dames and G. Chen. “ 1ω , 2ω , and 3ω methods for measurements of thermal properties”. *Rev. Sci. Instrum.*, Vol. 76, p. 124902, 2005. 35, 36, 39, 40, 57, 81
- [Dres 07] M. S. Dresselhaus, G. Chen, M. Y. Tang, R. Yang, H. Lee, D. Wang, Z. Ren, J.-P. Fleurial, and P. Gogna. “New Directions for Low-Dimensional Thermoelectric Materials”. *Adv. Mater.*, Vol. 19, p. 1043, 2007. 1
- [Eber 00] H. Ebert, A. Vernes, and J. Banhart. “The influence of spin-orbit coupling and a current dependent potential on the residual resistivity of disordered magnetic alloys”. *Solid State Commun.*, Vol. 113, p. 103, 2000. 15
- [Eber 97] H. Ebert, H. Freyer, and M. Deng. “Manipulating of the spin-orbit coupling using the Dirac equation for spin-dependent potentials”. *Phys. Rev. B*, Vol. 56, p. 9454, 1997. 15
- [Fert 68] A. Fert and I. A. Campbell. “Two-current conduction in Nickel”. *Phys. Rev. Lett.*, Vol. 21, p. 1190, 1968. 15
- [Fleu 88] J. P. Fleurial, L. Gailliard, R. Triboulet, H. Scherrer, and S. Scherrer. “Thermal properties of high quality single crystals of bismuth telluride - part I: experimental characterization”. *J. Phys. Chem. Solids*, Vol. 49, p. 1237, 1988. 26
- [Fuch 38] K. Fuchs. “The conductivity of thin metallic films according to the electron theory of metals”. *Proc. Cambridge Philos. Soc.*, Vol. 34, p. 100, 1938. 18

- [Furl 99] R. R. Furlong and E. J. Wahlquist. “U.S. Space Missions Using Radioisotope Power Systems”. *Nuclear News*, Vol. 42, p. 26, 1999. 1
- [Garg 09] A. Garg, D. Rasch, E. Shimshoni, and A. Rosch. “Large Violation of the Wiedemann-Franz Law in Luttinger Liquids”. *Phys. Rev. Lett.*, Vol. 103, p. 096402, Aug 2009. 15
- [Gasi 02] S. Gasiorowicz. *Quantenphysik*. Oldenburg Wissenschaftsverlag GmbH, 2002. 5, 18
- [Giaz 07] F. Giazotto, F. Taddei, P. D’Amico, R. Fazio, and F. Beltram. “Nonequilibrium spin-dependent phenomena in mesoscopic superconductor–normal metal tunnel structures”. *Phys. Rev. B*, Vol. 76, p. 184518, Nov 2007. 16
- [Gold 58] H. J. Goldsmid. “The electrical conductivity and thermoelectric power of bismuth telluride”. *Proc. Phys. Soc.*, Vol. 71, p. 633, 1958. 26
- [Good 63] D. A. Goodings. “Electrical Resistivity of Ferromagnetic Metals at Low Temperatures”. *Phys. Rev.*, Vol. 132, p. 542, 1963. 13
- [Grne 33] E. Grüneisen. “Die Abhängigkeit des elektrischen Widerstandes reiner Metalle von der Temperatur”. *Ann. Phys.*, Vol. 408, p. 530, 1933. 13
- [Hamd 11] B. Hamdou. *VLS-Synthese und Charakterisierung Thermoelektrischer Nanodrähte*. Master’s thesis, Diplomarbeit, Universität Hamburg, 2011. 21
- [Hamd 13] B. Hamdou, J. Kimling, A. Dorn, E. Pippel, R. Rostek, P. Woias, and K. Nielsch. “Thermoelectric Characterization of Bismuth Telluride Nanowires, Synthesized Via Catalytic Growth and Post-Annealing”. *Advanced Materials*, Vol. 25, No. 2, pp. 239–244, 2013. x, 21, 27, 109, 110, 112
- [Hata 07] M. Hatami, G. E. W. Bauer, Q. Zhang, and P. J. Kelly. “Thermal Spin-Transfer Torque in Magnetoelectronic Devices”. *Phys. Rev. Lett.*, Vol. 99, p. 066603, Aug 2007. 2, 16, 17
- [Heik 10] T. T. Heikkilä, M. Hatami, and G. E. W. Bauer. “Spin heat accumulation and its relaxation in spin valves”. *Phys. Rev. B*, Vol. 81, p. 100408(R), 2010. 16, 17
- [http 11] <http://nanohub.org/resources/5475>. 2011. 12
- [Jacq 02] A. Jacquot, B. Lenoir, and A. Dauscher. “Numerical simulation of the 3ω method for measuring the thermal conductivity”. *J. Appl. Phys.*, Vol. 91, p. 4733, 2002. 38
- [Jawo 12] C. M. Jaworski, R. C. Myers, E. Johnston-Halperin, and J. P. Heremans. “Giant spin Seebeck effect in a non-magnetic material”. *Nature*, Vol. 487, p. 210, 2012. 2
- [John 87] M. Johnson and R. H. Silsbee. “Thermodynamic analysis of interfacial transport and of the thermomagnetolectric system”. *Phys. Rev. B*, Vol. 35, pp. 4959–4972, Apr 1987. 18
- [Kana 10] M. G. Kanatzidis. “Nanostructured Thermoelectrics: The New Paradigm?”. *Chem. Mater.*, Vol. 22, p. 648, 2010. 1
- [Kane 96] C. L. Kane and M. P. A. Fisher. “Thermal Transport in a Luttinger Liquid”. *Phys. Rev. Lett.*, Vol. 76, pp. 3192–3195, Apr 1996. 15

- [Kiml 11] J. Kimling, S. Martens, and K. Nielsch. “Thermal conductivity measurements using 1ω and 3ω methods revisited for voltage-driven setups”. *Rev. Sci. Instrum.*, Vol. 82, No. 7, p. 074903, 2011. 35, 40
- [Kiml 13a] J. Kimling, J. Gooth, and K. Nielsch. “Anisotropic magnetothermal resistance in Ni nanowires”. *Phys. Rev. B*, Vol. 87, p. 094409, 2013. x, 53, 60, 113, 114
- [Kiml 13b] J. Kimling, K. Nielsch, K. Rott, and G. Reiss. “Field-dependent thermal conductivity and Lorenz number in Co/Cu multilayers”. *Phys. Rev. B*, Vol. 87, p. 134406, 2013. 69, 70
- [Koh 09] Y. K. Koh, S. L. Singer, W. Kim, J. M. O. Zide, H. Lu, D. G. Cahill, A. Majumdar, and A. C. Gossard. “Comparison of the 3ω method and time-domain thermoreflectance for measurements of the cross-plane thermal conductivity of epitaxial semiconductors”. *J. Appl. Phys.*, Vol. 105, p. 054303, 2009. 38
- [Kuma 93] G. S. Kumar, G. Prasad, and R. O. Pohl. “Experimental determinations of the Lorenz number”. *J. Mater. Sci.*, Vol. 28, p. 4261, 1993. 70
- [Lder 12] S. Lüders. “Physikgeschichte ins Studium!”. *Physik Journal*, Vol. 11, p. 3, 2012. 3
- [Lee 97] S.-M. Lee and D. G. Cahill. “Heat transport in thin dielectric films”. *J. Appl. Phys.*, Vol. 81, No. 6, pp. 2590–2595, 1997. 38
- [Lore 72] L. Lorenz. “Bestimmung der Wärmegrade in absolutem Maasse”. *Ann. Phys.*, Vol. 223, p. 429, 1872. 14, 70
- [Lu 01] L. Lu, W. Yi, and D. L. Zhang. “ 3ω method for specific heat and thermal conductivity measurements”. *Rev. Sci. Instrum.*, Vol. 72, No. 7, pp. 2996–3003, 2001. 35, 39, 57
- [Malo 86] A. P. Malozemoff. “Anisotropic magnetoresistance with cubic anisotropy and weak ferromagnetism: A new paradigm”. *Phys. Rev. B*, Vol. 34, p. 1853, 1986. 15
- [Mavr 09] A. Mavrokefalos, A. L. Moore, M. T. Pettes, L. Shi, W. Wang, and X. Li. “Thermoelectric and structural characterizations of Individual electrodeposited bismuth telluride nanowires”. *J. Appl. Phys.*, Vol. 105, p. 104318, 2009. 26, 27
- [Maya 70] A. F. Mayadas and M. Shatzkes. “Electrical-resistivity model for polycrystalline films: the case of arbitrary reflection at external surfaces”. *Phys. Rev. B*, Vol. 1, p. 1382, 1970. 18
- [McGu 75] T. R. McGuire and R. I. Potter. “Anisotropic Magnetoresistance in Ferromagnetic 3d Alloys”. *IEEE Trans. Magn.*, Vol. 11, p. 1018, 1975. 18
- [Mill 65] G. R. Miller and C.-Y. Li. “Eviences for the existence of antistructure defects in bismuth telluride by density measurements”. *J. Phys. Chem. Solids*, Vol. 26, p. 173, 1965. 26
- [Minn 09] A. J. Minnich, M. S. Dresselhaus, Z. F. Ren, and G. Chen. “Bulk nanostructured thermoelectric materials: current research and future prospects”. *Energy Environ. Sci.*, Vol. 2, p. 466, 2009. 1
- [Moor 10] J. E. Moore. “The birth of topological insulators”. *Nature*, Vol. 464, p. 194, 2010. 1, 27

- [Mott 36a] N. F. Mott. “The electrical conductivity of transition metals”. *Proc. R. Soc. Lond. A*, Vol. 153, p. 699, 1936. 15, 16
- [Mott 36b] N. F. Mott. “The resistance and thermoelectric properties of the transition metals”. *Proc. R. Soc. Lond. A*, Vol. 156, p. 368, 1936. 15
- [Naga 10] N. Nagaosa, J. Sinova, S. Onoda, A. H. MacDonald, and N. P. Ong. “Anomalous Hall Effect”. *Rev. Mod. Phys.*, Vol. 82, p. 1539, 2010. 2, 15
- [Nard 11] D. Narducci. “Do we really need high thermoelectric figures of merit? A critical appraisal to the power conversion efficiency of thermoelectric materials”. *Appl. Phys. Lett.*, Vol. 99, No. 10, p. 102104, 2011. 1
- [Niel 11] K. Nielsch, J. Bachmann, J. Kimling, and H. Böttner. “Thermoelectric Nanostructures: From Physical Model Systems towards Nanograined Composites”. *Adv. Energy Mater.*, Vol. 1, No. 5, p. 713, 2011. 21
- [Nola 01] G. S. Nolas, J. Sharp, and H. J. Goldsmid. *Thermoelectrics*. Springer-Verlag Berlin Heidelberg, 2001. 1, 4, 10, 11, 26, 27, 35, 37
- [Olso 05] B. W. Olson, S. Graham, and K. Chen. “A practical extension of the 3 omega method to multilayer structures”. *Rev. Sci. Instrum.*, Vol. 76, No. 5, p. 053901, 2005. 38
- [Ou 08] M. N. Ou, T. J. Yang, S. R. Harutyunyan, Y. Y. Chen, C. D. Chen, and S. J. Lai. “Electrical and thermal transport in single nickel nanowire”. *Appl. Phys. Lett.*, Vol. 92, p. 063101, 2008. 35
- [Pels 04] C. Pels. *Ferromagnetic electrodes for spin-polarized transport-Technology and experiments*. PhD thesis, Dissertation, Universität Hamburg, 2004. 120
- [Peng 09] H. Peng, K. Lai, D. Kong, S. Meister, Y. Chen, X.-L. Qi, S.-C. Zhang, Z.-X. Shen, and Y. Cui. “Aharonov–Bohm interference in topological insulator nanoribbons”. *Nat. Mater.*, Vol. 9, p. 225, 2009. 81
- [Petr 91] F. Petroff, A. Barthélémy, A. Hamzic, A. Fert, P. Etienne, S. Lequien, and G. Creuzet. “Magnetoresistance of Fe/Cr superlattices”. *J. Magn. Magn. Mater.*, Vol. 93, p. 95, 1991. 82
- [Pich 10] P. Pichanusakorn and P. Bandaru. “Nanostructured Thermoelectrics”. *Mater. Sci. Eng.*, Vol. R 67, p. 19, 2010. 1
- [Popp 05] K. Popper. *Logik der Forschung*. Mohr Siebeck in Tübingen, 2005. 1
- [Popp 96] K. Popper. *Alles Leben ist Problemlösen*. Piper Verlag GmbH, München, 1996. 1
- [Pros 11] A. Prosperetti. *Advanced Mathematics for Applications*. Cambridge University Press, 2011. 39
- [Raqu 02] B. Raquet, M. Viret, E. Sondergard, O. Cespedes, and R. Mamy. “Electron-magnon scattering and magnetic resistivity in 3d ferromagnets”. *Phys. Rev. B*, Vol. 66, p. 024433, Jul 2002. 13
- [Raud 07] C. E. Raudzis. *Anwendung und Erweiterung der 3ω Methode zur Charakterisierung komplexer Mehrschichtsysteme in der Mikrosystemtechnik*. PhD thesis, Institut für Angewandte Physik, Universität Tübingen, 2007. 37, 38

- [Rowe 06] D. M. Rowe. “Thermoelectric Waste Heat Recovery as a Renewable Energy Source”. *Int. J. of Innovations in En. Syst. and Power*, Vol. 1, p. 13, 2006. 1
- [Sato 94] H. Sato, H. Henmi, Y. Kobayashi, Y. Aoki, H. Yamamoto, T. Shinjo, and V. Sechovsky. “Giant magnetoresistance related transport properties in multilayers and bulk materials (invited)”. *J. Appl. Phys.*, Vol. 76, No. 10, p. 6919, 1994. 70, 82
- [Satt 57] C. B. Satterthwaite and R. W. Ure. “Electrical and Thermal Properties of Bi_2Te_3 ”. *Phys. Rev.*, Vol. 108, p. 1164, Dec 1957. 26
- [Shap 07] E. Shapira, A. Tsukernik, and Y. Selzer. “Thermopower measurements on individual 30 nm nickel nanowires”. *Nanotechnology*, Vol. 18, p. 485703, 2007. 22
- [Shi 00] L. Shi, S. Plyasunov, A. Bachtold, P. L. McEuen, and A. Majumdar. “Scanning thermal microscopy of carbon nanotubes using batch-fabricated probes”. *Appl. Phys. Lett.*, Vol. 77, No. 26, p. 4295, 2000. 39
- [Shi 03] L. Shi, D. Li, C. Yu, W. Jang, D. Kim, Z. Yaoh, P. Kim, and A. Majumdar. “Measureing Thermal and Thermoelectric Properties of One-Dimensional Nanostructures Using a Microfabricated Device”. *J. Heat Transfer*, Vol. 125, p. 881, 2003. 39
- [Shi 05] L. Shi, C. Yu, and J. Zhou. “Thermal Characterization and Sensor Applications of One-Dimensional Nanostructures Employing Microelectromechanical Systems”. *J. Phys. Chem. B*, Vol. 109, p. 22102, 2005. 23
- [Shi 96] J. Shi, K. Pettit, E. Kita, S. S. P. Parkin, R. Nakatani, and M. B. Salamon. “Field-dependent thermoelectric power and thermal conductivity in multilayered and granular giant magnetoresistive systems”. *Phys. Rev. B*, Vol. 54, p. 15273, Dec 1996. 70, 82
- [Slac 11] A. Slachter, F. L. Bakker, and B. J. van Wees. “Modeling of thermal spin transport and spin-orbit effects in ferromagnetic/nonmagnetic mesoscopic devices”. *Phys. Rev. B*, Vol. 84, p. 174408, 2011. 16, 17, 60
- [Smit 51] J. Smit. “Magnetoresistance of Ferromagnetic Metals and Alloys at Low Temperatures”. *Physica*, Vol. 16, p. 612, 1951. 15
- [Snyd 08] G. J. Snyder and E. S. Toberer. “Complex thermoelectric materials”. *Nat. Mater.*, Vol. 7, p. 105, 2008. 1
- [Somm 33] A. Sommerfeld and H. Bethe. *Elektronentheorie der Metalle*. Springer Verlag, Heidelberg, 1933. 70
- [Sond 01] E. H. Sondheimer. “The mean free path of electrons in metals”. *Adv. in Phys.*, Vol. 50, p. 499, 2001. 18
- [Sthr 06] J. Stöhr and H. C. Siegmann. *Magnetism - From Fundamentals to Nanoscale Dynamics*. Springer-Verlag Berlin Heidelberg, 2006. 5, 6, 7, 18
- [Stoj 10] N. Stojanovic, D. H. S. Maithripala, J. M. Berg, and M. Holtz. “Thermal conductivity in metallic nanostructures at high temperature: Electrons, phonons, and the Wiedemann-Franz law”. *Phys. Rev. B*, Vol. 82, p. 075418, 2010. 18

- [Tsui 97] F. Tsui, B. Chen, J. Wellman, C. Uher, and R. Clarke. “Heat conduction of (111) Co/Cu superlattices”. *J. Appl. Phys.*, Vol. 81, No. 8, p. 4586, 1997. 70, 82
- [Tsymb 01] E. Y. Tsymbal and D. G. Pettifor. *Perspectives of Giant Magnetoresistance*. Vol. 56 of *Solid State Physics*, Academic Press, London, 2001. 17, 18
- [Uchi 08] K. Uchida, S. Takahashi, K. Harii, J. Ieda, W. Koshibae, K. Ando, S. Maekawa, and E. Saitoh. “Observation of the spin Seebeck effect”. *Nature*, Vol. 9, p. 455, 2008. 2
- [Uchi 10] K. Uchida, J. Xiao, H. Adachi, J. Ohe, S. Takahashi, J. Ieda, T. Ota, Y. Kajiwara, H. Umezawa, H. Kawai, G. E. Bauer, S. Maekawa, and E. Saitoh. “Spin Seebeck insulator”. *Nat. Mater.*, Vol. 9, p. 894, 2010. 2
- [Uher 04] C. Uher. *Thermal Conductivity of Metals*. Kluwer Academic / Plenum Publishers, New York, 2004. 8, 9, 12, 13, 14
- [Vale 93] T. Valet and A. Fert. “Theory of the perpendicular magnetoresistance in magnetic multilayers”. *Phys. Rev. B*, Vol. 48, p. 7099, 1993. 16, 18
- [Vine 10] C. J. Vineis, A. Shakouri, A. Majumdar, and M. G. Kanatzidis. “Nanostructured Thermoelectrics: Big Efficiency Gains from Small Features”. *Adv. Mater.*, Vol. 22, p. 3970, 2010. 1
- [Vlkl 09a] F. Völklein, H. Reith, T. W. Cornelius, M. Rauber, and R. Neumann. “The experimental investigation of thermal conductivity and the Wiedemann–Franz law for single metallic nanowires”. *Nanotechnology*, Vol. 20, p. 325706, 2009. 36, 40
- [Vlkl 09b] F. Völklein, M. Schmitt, T. W. Cornelius, O. Picht, S. Müller, and R. Neumann. “Microchip for the Measurement of Seebeck Coefficients of Single Nanowires”. *J. Electron. Mater.*, Vol. 38, p. 1109, 2009. 23
- [Vlkl 84] F. Völklein and E. Kessler. “A Method for the Measurement of Thermal Conductivity, Thermal Diffusivity, and Other Transport Coefficients of Thin Films”. *Phys. Stat. Sol.*, Vol. 81, p. 585, 1984. 36
- [Vlkl 90] F. Völklein. “Thermal conductivity and diffusivity of a thin film SiO₂-Si₃N₄ sandwich system”. *Thin Solid Films*, Vol. 188, p. 27, 1990. 36
- [Wake 11] N. Wakeham, A. F. Bangura, X. Xu, J.-F. Mercure, M. Greenblatt, and N. E. Hussey. “Gross violation of the Wiedemann-Franz law in a quasi-one-dimensional conductor”. *Nat. Commun.*, Vol. 2, p. 396, 2011. 15
- [Watt 16] O. P. Watts. *Trans. Am. Electrochem. Soc.*, Vol. 29, p. 395, 1916. 118
- [Wegr 06] J.-E. Wegrowe, Q. A. Nguyen, M. Al-Barki, J.-F. Dayen, T. L. Wade, and H.-J. Drouhin. “Anisotropic magnetothermopower: Contribution of interband relaxation”. *Phys. Rev. B*, Vol. 73, p. 134422, Apr 2006. 59
- [Whit 59] G. K. White and S. B. Woods. “Electrical and Thermal Resistivity of the Transition Elements at Low Temperatures”. *Phil. Trans. R. Soc. Lond. A*, Vol. 251, p. 273, 1959. 14, 58, 59
- [Whit 60] G. K. White and R. J. Tainsh. “Lorenz Number for High-Purity Copper”. *Phys. Rev.*, Vol. 119, p. 1869, 1960. 14

- [Wied 53] G. Wiedemann and R. Franz. “Ueber die Wärme-Leitungsfähigkeit der Metalle”. *Ann. Phys.*, Vol. 89, p. 497, 1853. 14, 70
- [Wolf 01] S. A. Wolf, D. D. Awschalom, R. A. Buhrman, J. M. Daughton, S. von Molnár, M. L. Roukes, A. Y. Chtchelkanova, and D. M. Treger. “Spintronics: A Spin-Based Electronics Vision for the Future”. *Science*, Vol. 294, No. 5546, pp. 1488–1495, 2001. 17
- [wwwc 08] www.commons.wikimedia.org/wiki/File:Thermoschema.svg. 2008. 10
- [Xiao 10] J. Xiao, G. E. W. Bauer, K.-c. Uchida, E. Saitoh, and S. Maekawa. “Theory of magnon-driven spin Seebeck effect”. *Phys. Rev. B*, Vol. 81, p. 214418, Jun 2010. 2
- [Yang 06] Y. Yang, J.-G. Zhu, R. M. White, and M. Asheghi. “Field-dependent thermal and electrical transports in Cu/CoFe multilayer”. *J. Appl. Phys.*, Vol. 99, No. 6, p. 063703, 2006. 70, 82
- [Yu 10] H. Yu, S. Granville, D. P. Yu, and J.-P. Ansermet. “Evidence for Thermal Spin-Transfer Torque”. *Phys. Rev. Lett.*, Vol. 104, p. 146601, Apr 2010. 8
- [Yusi 09] E. Yusibani, P. L. Woodfield, M. Fujii, K. Shinzato, X. Zhang, and Y. Takata. “Application of the Three-Omega Method to Measurement of Thermal Conductivity and Thermal Diffusivity of Hydrogen Gas”. *Int. J. Thermophys.*, Vol. 30, p. 397, 2009. 57
- [Zhan 91] S. Zhang and P. M. Levy. “Enhanced temperature-dependent magnetoresistivity of Fe/Cr superlattices”. *Phys. Rev. B*, Vol. 43, p. 11048, 1991. 82
- [Zhou 05] J. Zhou, C. Jin, J. H. Seol, X. Li, and L. Shi. “Thermoelectric properties of individual electrodeposited bismuth telluride nanowires”. *Appl. Phys. Lett.*, Vol. 87, p. 133109, 2005. 27
- [Zuev 10] Y. M. Zuev, J. S. Lee, C. Galloy, H. Park, and P. Kim. “Diameter Dependence of the Transport Properties of Antimony Telluride Nanowires”. *Nano Lett.*, Vol. 10, p. 3037, 2010. 22

Danksagung

Ich bedanke mich zutiefst bei

- Prof. Dr. Kornelius Nielsch für die freundliche Aufnahme in seiner Gruppe sowie für die fortwährende Betreuung und Unterstützung während der Doktorarbeit.
- Prof. Dr. Günter Reiss für die freundliche Zusammenarbeit und für die Übernahme des Zweitgutachtens der Dissertation.
- PD Dr. habil. Guido Meier für die Übernahme des Zweitgutachtens der Disputation.
- Prof. Dr. Tero T. Heikkilä, Dr. August Dorn, Dr. Detlef Görlitz, Dr. Toru Matsuyama und Dr. Alexandre Jacquout für hilfreiche Diskussionen.
- Bacel Hamdou für hervorragende Laborarbeiten während seiner Diplomarbeit.
- Dr. Karsten Rott für die schönen GMTR Proben.
- Johannes Gooth für die Unterstützung bei der Ni Nanodrahtsynthese.
- Dr. Eckhard Pippel für die TEM Aufnahmen an unseren thermoelektrischen Nanodrähten.
- Stephan Martens für unermüdliche Hilfe, vor allem bei technischen Fragen.
- Michael Martens, der als Onkel Michi schon fast zur Familie gehört und unser (vor allem Sophies) Leben bereichert.
- Lewis Akinsinde und Reinhold Meißner für präzise technische Unterstützung.
- Horst Biedermann und der E-Werkstatt für die Anfertigung der 3ω Messbrücke.
- Stephanie Baer und Iris Klüver für die Hilfe bei bürokratischen Hindernissen.
- allen Kollegen in der Arbeitsgruppe für die freundliche Hilfsbereitschaft.
- meiner liebsten Frau Judith und unseren herrlichen Töchtern Sophie und Reija für alles.
- meiner gesamten Familie und allen meinen Freunden für den Rückhalt.
- Sensei Toribio Osterkamp für grandioses Karatetraining, was mir besonders half einen klaren und kühlen Kopf zu behalten.

